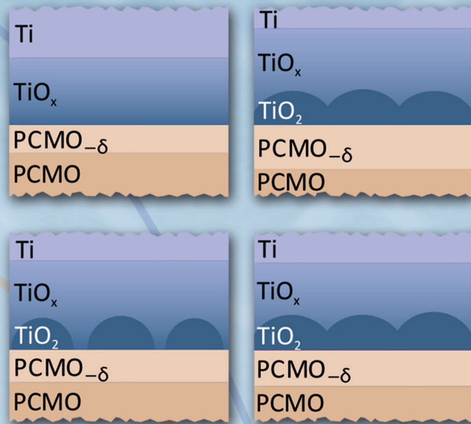

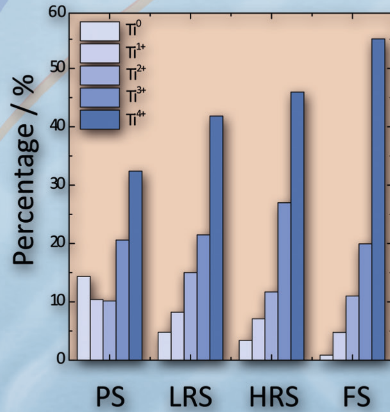

Electrical characterization of manganite and titanate heterostructures

Anja Herpers

Member of the Helmholtz Association

JÜLICH FORSCHUNGSZENTRUM

Schriften des Forschungszentrums Jülich
Reihe Information / Information	Band / Volume 32

Forschungszentrum Jülich GmbH
Peter Grünberg Institute (PGI)
Electronic Materials (PGI-7)

Electrical characterization of manganite and titanate heterostructures

Anja Herpers

Schriften des Forschungszentrums Jülich
Reihe Information / Information

Band / Volume 32

ISSN 1866-1777

ISBN 978-3-89336-948-5

Bibliographic information published by the Deutsche Nationalbibliothek.
The Deutsche Nationalbibliothek lists this publication in the Deutsche Nationalbibliografie; detailed bibliographic data are available in the Internet at http://dnb.d-nb.de.

Publisher and Distributor:	Forschungszentrum Jülich GmbH Zentralbibliothek 52425 Jülich Tel: +49 2461 61-5368 Fax: +49 2461 61-6103 Email: zb-publikation@fz-juelich.de www.fz-juelich.de/zb
Cover Design:	Grafische Medien, Forschungszentrum Jülich GmbH
Printer:	Grafische Medien, Forschungszentrum Jülich GmbH
Copyright:	Forschungszentrum Jülich 2014

Schriften des Forschungszentrums Jülich
Reihe Information / Information, Band / Volume 32

D 82 (Diss.,RWTH Aachen University, 2014)

ISSN 1866-1777
ISBN 978-3-89336-948-5

The complete volume is freely available on the Internet on the Jülicher Open Access Server (JUWEL) at www.fz-juelich.de/zb/juwel

Neither this book nor any part of it may be reproduced or transmitted in any form or by any means, electronic or mechanical, including photocopying, microfilming, and recording, or by any information storage and retrieval system, without permission in writing from the publisher.

Kurzfassung

Da die aktuelle Speichertechnologie in den nächsten Jahrzehnten ihr physikalisches Limit erreichen wird, müssen innovative Konzepte entwickelt werden, um weitere Verbesserungen in Größe, Stromverbrauch und Kosten sicherzustellen. Ein vielversprechender Kandidat unter den "Beyond CMOS" Technologien ist das resistive RAM, das auf dem nichtflüchtigen und reversiblen Schalten des Widerstandes eines Bauelements mithilfe einer externen Anregung basiert. Genauer formuliert scheinen schnelle Schreib- und Lesevorgänge in resistiv schaltenden Übergangsmetalloxiden durch Redox-basierte Mechanismen ermöglicht zu werden, die üblicherweise mit der Bildung eines leitenden Filaments einhergehen, das die isolierende Umgebung kurzschließt. Bei einigen Materialien tritt das Schalten homogen über der kompletten Bauelement-Fläche auf, was einen zusätzlichen Freiheitsgrad beim Bauelement-Design ermöglicht. Für diesen Schalt-Typ spielen Grenzflächeneffekte zwischen dem involvierten resistiv-schaltenden Oxid und der aktiven Elektrode die Schlüsselrolle.

Die Hauptthematik dieser Arbeit ist das Redox-basierte Wechselspiel zwischen einem komplexen Oxid und dem oxidierbaren Elektrodenmaterial in einem flächig-schaltenden ReRAM Bauelement. Als epitaktisches Modellsystem wird das quaternäre Übergangsmetalloxid (Pr,Ca)$MnO_{3\pm\delta}$ untersucht.
Um mittels gepulster Laser Deposition hoch-qualitative epitaktische Dünnschichten zu erhalten, wurden ausführliche Wachstumsstudien durchgeführt. Trotz der recht großen Gitterfehlanpassung von $-2.39\,\%$ zu dem $SrTiO_3$ Substrat, konnte defektarmes (Pr,Ca)$MnO_{3\pm\delta}$ erfolgreich in verschiedenen Schichtabfolgen gewachsen werden. Ab einer Schichtdicke von 40 nm wird die elastische Verformungsenergie groß genug für Relaxationseffekte. Es konnten zwei konkurrierende Relaxationsprozesse identifiziert werden, Rissbildung und Einbau von Stufenversetzungen, die jeweils in entscheidend unterschiedlichen strukturellen und elektrischen Eigenschaften der (Pr,Ca)$MnO_{3\pm\delta}$ Dünnschichten resultieren.

Nach einem ersten Elektroformierschritt zeigt (Pr,Ca)$MnO_{3\pm\delta}$ mit Ti als oberer Elektrode stabile resistive Schalteigenschaften, für die ein Widerstandsverhältnis von einer Größenordnung und Retention Zeiten von mindestens 300 Tagen erzielt werden konnten. Es wurde eine Redox-Reaktion an der Grenzfläche nachgewiesen, die einen Sauerstofftransfer von (Pr,Ca)$MnO_{3\pm\delta}$ zu Ti beinhaltet. Ein Valenzwechsel auf der Ti-Seite während des Formier- und den Schaltprozessen konnte mittels Photoelektronspektroskopie gezeigt werden. Der Stromtransport in den Bauelementen konnte für die symmetrischen Zustände mit kleinem Widerstand mit einem Beitrag aus Polaron-Hopping und einem ohmschen Serienwiderstand beschrieben werden. Für die Zustände mit großem Widerstand musste das Modell um eine trapezförmige Tunnelbarriere erweitert werden. Durch die Kombination aller Ergebnisse konnte ein schlüssiges Modell abgeleitet werden, um den Schalteffekt in (Pr,Ca)$MnO_{3\pm\delta}$/Ti Bauelementen durch die Bildung und Überbrückung einer natürlich entstandenen TiO_2 Tunnelbarriere an der Grenzfläche zu erklären.

Abstract

As the current memory technology will reach its physical limit within the next decades, innovative concepts have to be developed to ensure future improvements in size, power consumption and costs in data storage. A promising candidate among "Beyond CMOS" technologies is resistive RAM, which is based on the non-volatile and reversible switching of the resistance of a device with the help of an external stimulus. More specific, fast writing and reading operations in resistively switching transition metal oxides seem to be enabled by redox-based mechanisms, which usually go along with the formation of a conducting filament to bridge the insulating matrix. For a few materials, the switching occurs homogeneously over the entire device area, which offers one more degree of freedom in device design. For this switching type, the interface effects between the involved resistively switching oxide and the active electrode play the key role.

The main topic of this work is this redox-based interplay between the oxidizable electrode material and a complex oxide in a homogeneously switching ReRAM device, realized for the quaternary transition metal oxide (Pr,Ca)$MnO_{3\pm\delta}$ as epitaxial model system.
In order to obtain high quality epitaxial thin films by pulsed laser deposition, detailed growth studies were performed. In spite of the rather high lattice mismatch of $-2.39\,\%$ to the $SrTiO_3$ substrate, defect-poor (Pr,Ca)$MnO_{3\pm\delta}$ could be successfully grown in various layer stacks. For film thicknesses larger than 40 nm, the elastic strain energy becomes sufficient high for relaxation effects. We identified two concurring processes for relaxation, crack formation and the incorporation of edge dislocations, which result in crucially different structural and electrical properties of the (Pr,Ca)$MnO_{3\pm\delta}$ thin film.

After an initial electroforming step, (Pr,Ca)$MnO_{3\pm\delta}$ with Ti as active top electrode exhibits stable resistive switching properties, for which we could obtain a resistance ratio of one order of magnitude and retention times of at least 300 days. A redox reaction was found to occur at the interface involving an oxygen transfer from the (Pr,Ca)$MnO_{3\pm\delta}$ to the Ti. A change of the valence state on the Ti-side was identified during the forming and also the switching processes by X-ray spectroscopy. The current transport in the devices could be described by a polaron hopping contribution and a serial ohmic resistor for the symmetric low resistive states, and with the presence of a trapezoidal tunnel barrier for the high resistive states. Combining both results, a coherent model was derived to explain the switching effect in (Pr,Ca)$MnO_{3\pm\delta}$/Ti devices by the formation and bridging of a TiO_2 tunnel barrier, naturally formed at the (Pr,Ca)$MnO_{3\pm\delta}$/Ti interface.

Contents

Introduction 1

1 Basics 5
- 1.1 Resistive switching in oxides . . . 5
- 1.2 Mixed-valence manganites . . . 12
  - 1.2.1 Defect chemistry of mixed-valence manganites . . . 12
  - 1.2.2 Effects of correlated electronics . . . 17

2 Epitaxial growth of perovskite thin film heterostructures 25
- 2.1 Basics . . . 25
  - 2.1.1 Epitaxial thin film growth . . . 25
  - 2.1.2 Deposition and characterization methods . . . 26
    - 2.1.2.1 Pulsed laser deposition . . . 26
    - 2.1.2.2 RHEED . . . 27
    - 2.1.2.3 Target and substrate preparation . . . 29
    - 2.1.2.4 Atomic force microscopy . . . 30
    - 2.1.2.5 X-ray diffraction . . . 31
- 2.2 Growth of perovskite heterostructures . . . 33
  - 2.2.1 Growth of SRO . . . 33
  - 2.2.2 Growth of BTO heterostructures . . . 36
    - 2.2.2.1 Growth of BTO . . . 36
    - 2.2.2.2 Interface engineering of BTO/SRO heterostructures . . . 41
  - 2.2.3 Growth of mixed-valence manganites . . . 46
    - 2.2.3.1 Growth of PCMO in various layer stacks . . . 46
    - 2.2.3.2 Chemical analysis of PCMO . . . 50
    - 2.2.3.3 Growth of different manganite stoichiometries . . . 53
    - 2.2.3.4 Growth of different manganites on BTO . . . 55

3 Electrical properties of BTO 59
3.1 Principle of ferroelectricity 59
3.2 PFM measurements on BTO 62
3.3 Ferroelectric properties of BTO 65
3.3.1 Measurement setup 65
3.3.2 SRO/BTO/Pt devices 67
3.3.2.1 Separation of ferroelectricity from leakage in BTO devices 67
3.3.2.2 Annealing series 72
3.3.2.3 Low temperature measurements 74
3.3.2.4 C-V Measurements 75
3.3.3 Symmetric SRO/BTO/SRO devices 77
3.3.4 Discussion 78
3.4 ReRAM switching in BTO 80

4 Transport properties of PCMO 83
4.1 Interplay between structural and transport properties 83
4.1.1 Resistance measurements 83
4.1.2 Appearance of a line structure on the surface of PCMO 84
4.1.3 Thickness series of PCMO on SRO 85
4.1.4 XRD investigation: (hkl)-meshes 88
4.1.5 SEM-assisted micro-probe measurements 91
4.1.6 TEM investigations of domain walls 94
4.1.7 Discussion of the line structure 97
4.2 Bulk transport in PCMO 100
4.2.1 Resistivity measurements at room temperature 100
4.2.2 Hall measurements 101
4.2.3 Temperature dependence of resistance 103
4.2.4 High temperature measurements in miscellaneous oxygen ambience 105

5 Resistive switching of PCMO 109
5.1 Surface and interface contacts of PCMO 109
5.1.1 LC-AFM measurements 109
5.1.2 Nb:STO/PCMO 110
5.1.3 High and low work function metals 112
5.2 Forming and switching in PCMO/Ti devices 114

5.3 The forming process of PCMO/Ti 116
5.3.1 Impedance spectroscopy 116
5.3.2 TEM investigations 118
5.3.3 HAXPES experiments 120
5.4 The switching process of PCMO/Ti 125
5.4.1 HAXPES experiments 126
5.4.2 Modeling of read-out sweeps 128
5.5 Second forming step and switching 134

6 Conclusions 137

A Appendix 139
A.1 Additional information to Section about (hkl)-meshes 139
A.2 LC-AFM measurements on PCMO 140
A.3 Additional information to Section about TEM on domains in PCMO . . . 141
A.4 Additional information to Section about PFM on BTO 142
A.5 Electrical properties of PCMO/BTO stack 142

Figures 145

Tables 149

References 151

Acknowledgements 165

Introduction

In 1965 Gordon E. Moore documented his observation that the number of transistors on integrated circuits doubles approximately every two years, known as "Moore's law" [1]. The prediction of an exponential dependence of the transistor density on the time has proven to be accurate up to these days. For each reduction in size and thus costs of a functional device, a lot of research effort is necessary. This approach of further miniaturization according to "Moore's law" is known as "More Moore". As the standard density of an integrated function is nowadays already $\frac{4\cdot(20\,\mathrm{nm})^2}{2\,\mathrm{bit}}$ for Flash, the possibility of further size reduction is limited, as for the length scale of the elementary material components quantum mechanical effects occur, which might not be compatible with the current complementary metal oxide semiconductor (CMOS) technology. That is why, other concepts have to be developed to keep the opportunities of further device improvement.
One set of technologies for facing this challenge is "More than Moore", which bets on the functional diversification of semiconductor-based devices. The idea behind is that they do not necessarily scale according to "Moore's Law". Another concept is called "Beyond CMOS" and deals with nanometer-size functionalities, which are not necessarily based on semiconductors. Here, new state variables such as spin, molecular state, photons, phonons, nano-structures, mechanical state, resistance, quantum state (including phase) and magnetic flux are investigated for their suitability in electronic devices [2].

One of the most promising technologies is the concept of resistive random-access memory (RRAM), which is based on the non-volatile and reversible switching of the resistance of a device with the help of an external stimulus. Different materials and mechanisms have been considered for RRAM. Beyond them, resistive switching in a variety of oxide materials has gained much interest because of fast writing and reading operations and has already been successfully integrated in commercially available products [3]. The most convincing explanation for this type of resistive switching is the field-driven oxygen migration, which affects the valence state of the cations in complex transition metal oxides and thus influences the electronic properties of the system. However, the details of the redox-processes, which

are expected to occur at the nanoscale, are still only partly understood.
Most of the Redox-based resistive RAM effects are based on the formation of a conducting filament within an insulating matrix. For proceeding device design, a larger amount of degrees of freedom is indispensable and thus material systems are of great interest, that exhibit a homogeneously distributed switching effect over the entire device area and thereby allow for the tuning of the device parameters with the area. For these materials, the involved redox-process is typically located at the interface to an electrode material. However, one drawback of this approach is that there exists some hints from the literature [4] that the retention of interface-type switching devices is clearly worse than for filamentary switching systems.

In this work, the quaternary transition metal oxide $Pr_{1-x}Ca_xMnO_3$ is investigated as epitaxial model system for homogeneously switching complex oxides. The key role for this redox-based effect is thereby played by the interface between the involved oxide and the active oxidizable electrode. Resistive switching phenomena are reported for this mixed-valence manganite.
Besides the investigation of the switching effect itself, one aim of this work is to enhance the retention of the $Pr_{1-x}Ca_xMnO_3$ devices. One concept to improve the conservation of the states in interface-type devices is to stabilize the charged species at the interface by the insertion of a depolarization field of a neighboring ferroelectric like $BaTiO_3$.
Before combining both complex oxides, the resistive switching properties of $Pr_{0.48}Ca_{0.52}MnO_3$ and the ferroelectric switching properties of $BaTiO_3$ have to be investigated individually. As complex oxide systems, a suitable technique to deposit these materials as thin films is pulsed laser deposition, because the stoichiometric transfer from the ceramic target to the single crystal substrate is enabled by non-equilibrium processes. In order to receive high quality epitaxial thin films, detailed growth studies have to be performed to control the deposition process. For epitaxial thin films, tensile or compressive strain is induced into the film according to its lattice mismatch to the substrate. Relaxation effects can have an immense impact on the structural properties of a thin film and thus also influence its electrical properties. This impact has to be considered, especially because $Pr_{0.48}Ca_{0.52}MnO_3$ differs by $-5.14\,\%$ from $BaTiO_3$ in its lattice constant.
For the formation of a strong depolarization field, a large polarization of $BaTiO_3$ is important, which should not be screened by mobile charge carriers. Free electrons as compensating defects for oxygen vacancies are known to lead to screening effects in $BaTiO_3$, which can be visualized as leakage currents and need to be considered in this work.
For the observation of resistive switching, $Pr_{0.48}Ca_{0.52}MnO_3$ has to be integrated into

a metal-insulator-metal structure to build a device. The influence of different electrode materials has to be examined to select a good material combination for the appearance of homogeneous resistive switching. Detailed studies on the switching effect are necessary to identify the main properties of the switching heterostructures. To further clarify the origin of the redox-based switching effect, structural, chemical and electrical investigation methods are applied and evaluated to receive a deep understanding of the underlying processes and be able to develop a consistent model for the switching effect.

A detailed introduction into the basics of resistive switching can be found in Section 1.1. The studied material system $Pr_{1-x}Ca_xMnO_3$ as a member of the class of mixed-valence manganites offers a large diversity of structural, magnetic and transport properties. The origin of its nature is illuminated in Section 1.2, as well as its defect chemistry.
The growth study and optimization for titanates and manganites in various layer stacks is reported in Chapter 2.
Strategies to avoid leakage currents in $BaTiO_3$, which might screen the dipole moments and thus disable the depolarization field, are the topic of Chapter 3.
The bulk transport through $Pr_{0.48}Ca_{0.52}MnO_3$ as well as the identification of relaxation effects are reported in Chapter 4. The resistive switching mechanism of $Pr_{0.48}Ca_{0.52}MnO_3$ and its origin will be addressed in Chapter 5.
All results are summarized and concluded in Chapter 6.

1 Basics

The principle of redox-based resistive switching will be discussed in the framework of general data storage concepts.
The homogeneously switching material system $Pr_{1-x}Ca_xMnO_3$ is the main center of interest in this work. Its defect chemistry and its physical properties are depicted as one candidate of the material class of mixed-valence manganites.

1.1 Resistive switching in oxides

In current information technologies many different possibilities of data storage are available. The magnetic data storage used for hard disc drives requires a relatively complicated actor system, but is fast and the information is kept over a long time.
Devices with a much easier access to the stored data are based on electronic effects, which can be written and read on the basis of electric circuits. In this category, there also exist different device types. Mostly used as main memory in computers are dynamic random access memories (DRAM). These devices are based on capacitance effects and allow writing, erasing and reading times of less then 10 ns. In addition, they can be cycled more than 10^{16} times. But for these extremely fast devices, the written states constantly have to be refreshed due to a short retention time of 64 ms. Thus, the data storage is volatile and highly power-consuming during usage [5, 6].
On the opposite, NAND-Flash memories are available, where the charge is trapped in the floating gate of a transistor. These devices offer a non-volatile data storage with a retention time of 10 yrs and a non-destructive read-out. But the data storage is relatively slow with a reading time of 100 µs, an erasing time of 0.1 ms and a writing time of 1 ms. Furthermore, they show an endurance of only 10^4 cycles and hence can only be used to store data, but not for frequent storage during arithmetic computer processing. These devices are used in USB-sticks, SD-cards and portable solid-state drives [5, 6].

For future information technology it would be indispensable to combine the advantages of the given device types. But an electronic storage device, which saves the data non-volatilely but fast with a large endurance has to overcome a certain time-voltage dilemma. To compete with flash, the writing pulse should be in the range of 1-5 V and below 100 ns, while the data should be stored for more than 10 yrs and is read-out non-destructively at 0.1-0.5 V. This gap requires a non-linearity in the switching kinetics of more than 15 orders of magnitude in time for only one order of magnitude change in voltage, known as time-voltage dilemma [7].

Beside ferromagnetic, ferroelectric [8], molecular [9] and nanomechanical RAM concepts, especially the resistive switching is an interesting candidate for new generation RAM devices.
Here, the resistance of a material or device is switched between two or more resistive states due to a thermal, chemical or electronic stimulus, as shown in Figure 1.1. For phase change materials [10] the thermal heat is the primary stimulus to switch the material, whereas also a pure electronic mechanism exists. Within the redox-process related chemical mechanism three further different mechanisms can be found.

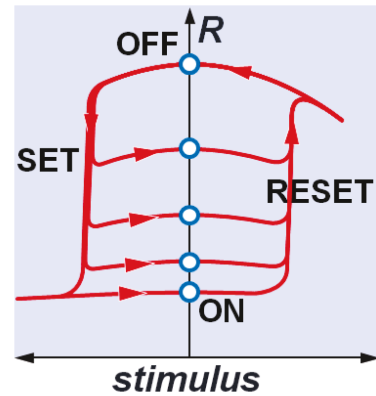

Figure 1.1: Working principle of resistive RAM, taken from [11].

The good conducting state is normally identified with the binary "1" and called ON or low resistance state (LRS), while the less conducting state is identified with "0" and called OFF or high resistance state (HRS). The process, which forms an OFF state into an ON state is called SET process, while RESET causes the opposite effect (Figure 1.1).

Going back to the switching mechanism itself, basically two different types can be found: Unipolar and bipolar resistive switching [7]. As depicted in Figure 1.2(a), for unipolarly switching materials, the SET and RESET process can both be achieved with the same polarity of the stimulating voltage, but at different amplitudes. For these materials, the direction of the voltage is not crucial, only the absolute value. Negative voltages can be used in the same manner. In contrast, for bipolarly switching systems the absolute value and the direction of the stimulus is decisive for the switching effect. As shown in the example in Figure 1.2(b), the SET process takes place for positive voltages, while a certain negative voltage is needed to RESET the device. This switching polarity is called "eight-wise",

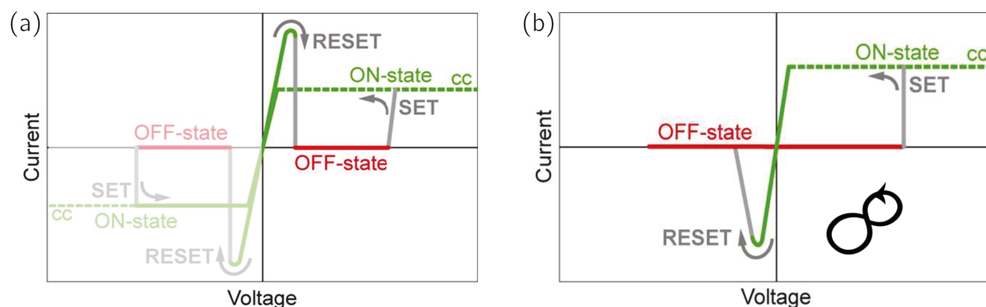

Figure 1.2: Polarity of switching in RRAM, based on [7]: (a) Unipolar resistive switching: The SET and RESET process are realized with the same voltage polarity, but different amplitude. (b) Bipolar resistive switching: For the SET and RESET process two different polarities are obliged. In this case, "eight-wise" switching is depicted. CC stands for current compliance.

because it has the drawing direction of the handwriting of a tilted "8" [12]. Other systems show a "counter-eight-wise" behavior with SET for negative voltages, corresponding to a counter-clockwise switching of the resistance, as depicted in Figure 1.1. Some systems indeed show both switching polarities [13].

Within the redox-based resistive RAM concepts, also know as "ReRAM", three different mechanisms are known so far, i.e. thermochemical memory effect (TCM), valence change mechanism (VCM) and electrochemical metallization (ECM) [7]. The TCM [14] is a unipolar switching mechanism, in which the controlled dielectric breakdown by thermal runaway is used. ECM [15] is based on the migration of cations due to redox-processes and thus is bipolar. A solid electrolyte is stacked between two different metal electrodes, one electrochemically active and the other one as inert counter electrode. With the application of a voltage, the electrochemical metal deposition and dissolution is utilized to form a conducting filament through the insulating ion-conductor by active electrode material [7]. The VCM devices show a bipolar resistive switching behavior, which is not electrode dominated as for ECM, but a result of the active material itself. This effect has mainly been observed for binary transition metal oxides or multinary oxides with transition metal content. Different models are available as explanation, including pure electronic effects as the charge-trap model [16], trapping at interface states [17], metal-insulator transition [18], polaron ordering [19] and resistance changes caused by ferroelectric polarization flip [8]. Besides, anion migration is assumed to be the main mechanism in this class of materials. Oxygen-related defects, as oxygen vacancies, are known to be much more mobile in these

materials than the cations. An enrichment or depletion of oxygen vacancies according to $O_O \rightleftharpoons \frac{1}{2} O_2(g) + V_O^{\bullet\bullet} + 2\,e^{/}$ might affect the valence state of the transition metal cation and consequently influence the electronic properties of the system. Therefore the mechanism is called VCM [7].

In addition to this classification of the switching effect, one has to distinguish two fundamentally different switching geometries: A filamentary switching scenario like for ECM cells and a homogeneous switching mechanism [20, 7]. This issue is not only relevant for the understanding of the switching procedure itself, but also for the scaling potential of future memory devices.

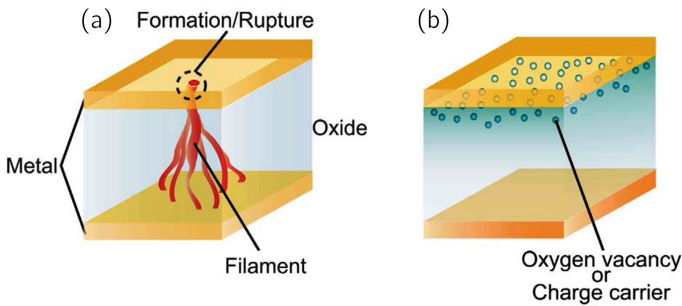

Figure 1.3: Classification of VCM, taken from [20]: (a) Filamentary type: As for ECM cells, a conducting filament is formed within the insulating matrix and during switching its connection to the electrode is interrupted and reconnected. (b) Homogeneous type: The switching takes place at the interface of the oxide to one electrode.

For the filamentary type, depicted in Figure 1.3(a), a conducting path is formed in the insulating matrix of the oxide, which connects the two electrodes. For devices with a single filament, especially the ON state is independent of the electrode area. It has been shown that only the filament itself is switched locally, while the other parts behave almost pristine. Thus, a parallel circuit arises out of the conducting filament resistance and the insulating matrix. A down-scaling of the pad size will only affect the highly-resistive part of the circuit, which is generally not dominant and therefore the influence of area scaling on the resistance is rather small. In this respect, filamentary switching devices show a good scaling potential, especially if the OFF state shows an area dependence of the resistance and hence the R_{ON}/R_{OFF} ratio is increased with decreasing cell size.
The homogeneous switching type in Figure 1.3(b) shows a switching effect distributed over the entire area of the electrode of the memory cell. The result is an electrode

area dependent resistance for the ON and the OFF state [20]. The change in resistance is attributed to a field-induced change of the Schottky-barrier at the metal-electrode interface, as it is also the case for several filamentary switching systems. Here it takes place homogeneously over the entire electrode area due to another field distribution. For these interface type devices, the R_{ON}/R_{OFF} ratio is not influenced by the pad size, as it might be the case for filamentary switching devices. However, these devices are not based on the random filament formation and the current and thus the power consumption for switching and reading also scales with the area. Moreover, in homogeneously switching systems the area is an additional screw to tune the device properties and it offers one more degree of freedom for sophisticated device designs.
In addition to these two extreme cases, there might be several types in-between. Coming from the single filament type, multiple filaments could be formed in the insulating oxide. On top of that, a spotty type has been observed, showing a conducting pattern of relatively regular spots of uniform distance. In the interface type, the affected layer is not necessarily completely homogeneous, but might show some irregularities, which could influence the area scaling as well.

For VCM and ECM based ReRAM cells, usually an initial electroforming cycle is required to activate the switching properties. For filamentary type switching devices, this can be understood in the framework of filament formation. It takes a certain DC voltage to form the filament between the two electrodes by a soft breakdown of the material, while during the switching effect itself only the last few nanometers of the filament are ruptured and reconnected. For homogeneously switching devices, such a breakdown is not necessarily needed and in this case a homogeneous oxidation process is behind.

In literature $Pr_{1-x}Ca_xMnO_3$ is found to show resistive switching behavior already in 1997 [18]. Here, the explanation is the magneto-resistive response of $Pr_{0.7}Ca_{0.3}MnO_3$, stimulated by an electrical field. The current induces a dielectric breakdown of the insulating charge-ordered into the metallic ferromagnetic state. A pure electronic effect is also reported in [19], where the ordering mechanisms of a polaron melt are said to be responsible for the resistance changes.
A widely spread explanation for the resistive switching is the movement of oxygen anions in the region of an enhanced electrical field. A first theoretical model for electrically induced resistance switching in manganites is proposed in [21], where oxygen vacancies are assumed to control the doping of the electronic state. In 2004 resistive switching of PCMO was observed to happen at the interface to low work function metals [22]. Intense studies suggest, that the Schottky barrier at the interface is modified during the oxidation and

reduction of the topmost layer of PCMO due to high electric fields [17, 20, 23]. As illustrated in Figure 1.4, an enrichment with oxygen vacancies is meant to create a highly resistive state, while an oxidized interface should be better conducting. Therefore, an enhanced electrical field, caused by the Schottky-like barrier, provides enough energy to move oxygen and, as a result, to change the barrier height and/or depletion layer width.

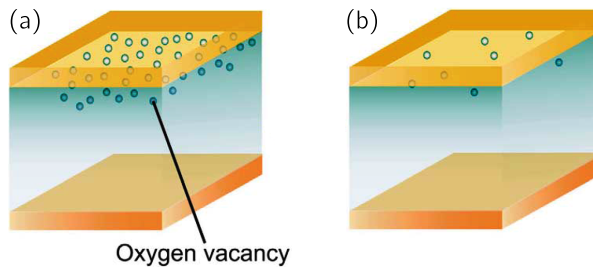

Figure 1.4: Resistive switching via homogeneous oxygen movement, taken from [20]: (a) A reduced interface results in a high resistance state. (b) An oxidized interface is meant to form the low resistance state.

One remaining question is, where the oxygen for switching of the Schottky barrier on PCMO side comes from or rather goes to. A first hint is given in [23], where an amorphous TiO_y layer is observed at the interface to PCMO by cross-sectional TEM. Still it is unclear, if this is connected to the switching effect. Many different electrode materials were tested in [24, 25] and the proposition of the influence of the work function is confirmed. For Ti and Ta top electrodes TEM and EELS studies also indicate the formation of oxidized electrode material and a redox-based switching mechanism [26, 27, 28].

Although a lot of studies have been done on the system $Pr_{1-x}Ca_xMnO_3$ and a redox-based effect is very likely, a detailed understanding on the mechanism is not yet existing. One crucial question is, to what extent the switching is influenced by the oxidized electrode material and if the switching effect is taking place homogeneously over the entire device area.

The interplay between ferroelectric properties and resistive switching is the topic of a large number of publications. One concept is based on a ferroelectric tunnel junction, which is used to switch the resistance of the stack by changing the barrier height in dependence of the polarization [29, 30, 31, 32, 33]. A similar idea is presented in [34], where a dead layer is assumed to be the origin of resistive switching.
Besides the usage of the ferroelectrics itself for resistance changes, the impact of the

ferroelectric on neighboring materials is also used, in terms of the piezoelectric field-induces strain or the depolarization field [4, 35, 36, 37]. One idea is to use the depolarization field of a ferroelectric layer to stabilize the charged oxygen vacancies at the interface to a homogeneously resistive switching material like $Pr_{1-x}Ca_xMnO_3$ for a better retention of the states. Thus, the combination of these two effects is of great interest.

1.2 Mixed-valence manganites

Mixed-valence manganites form a class of oxide materials, which excel in their large diversity in properties [38]. Generally, these materials form a distorted perovskite structure ABO_3, where Mn is positioned on B-site and the A-site is shared by trivalent rare earth cations (R) such as La, Ce, Pr or Nd and divalent alkaline earth cations (A) like Ca, Sr or Ba. The composition $R_{1-x}A_xMnO_3$ can be regarded as a solid solution of $RMnO_3$ and $AMnO_3$, while A^{2+} acts as acceptor dopant for the $RMnO_3$ host crystal due to the formal charges $(R^{3+}_{1-x}A^{2+}_x)(Mn^{3+}_{1-x}Mn^{4+}_x)O^{2-}_3$. Depending on the cation species, stoichiometry and temperature, these oxides exhibit different structural, magnetic and transport properties.

1.2.1 Defect chemistry of mixed-valence manganites

Smith defines defect chemistry as the study of deviations from perfect order in crystalline inorganic compounds, and the effects of such disorder on their properties [39].
In terms of defect chemistry, the most simple way to describe manganites is to first consider pure $RMnO_3$, referring to Section 1.2. In addition, R^{3+} and Mn^{3+} are assumed to be chemically equal, as the valence state has a more dominant impact on defect chemistry than the ion size. Thus the system $M^{3+}_2O^{2-}_3$ is discussed according to [39], where M stands for the metal cations R and Mn. Still the perovskite structure is conserved, so that interstitial oxygen anions are not allowed and Schottky disorder is favored over Frenkel disorder. Furthermore, for the stoichiometric composition the intrinsic electronic disorder is favored over the intrinsic ionic disorder, which are indeed the vacancies $V_M^{///}$ and $V_O^{\bullet\bullet}$, while /, $\bullet$ and x indicate a negative, positive and neutral charge of the defect relative to the perfect crystal, according to the Kröger-Vink notation [39, 40]. The relevant chemical reactions and corresponding mass-action equations, including the temperature dependent equilibrium constants $K_{eq,i}(T)$, as well as the charge neutrality equation to calculate the carrier density for each species are listed below:

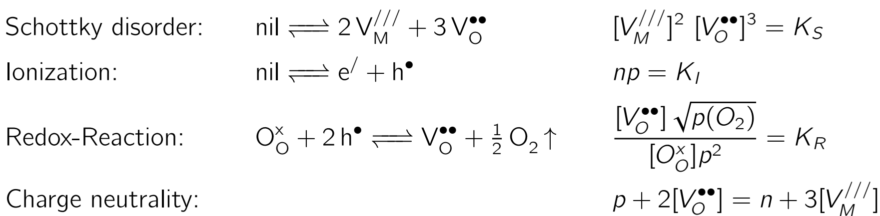

Schottky disorder:	$\mathrm{nil} \rightleftharpoons 2\,V_M^{///} + 3\,V_O^{\bullet\bullet}$	$[V_M^{///}]^2\,[V_O^{\bullet\bullet}]^3 = K_S$
Ionization:	$\mathrm{nil} \rightleftharpoons e^{/} + h^{\bullet}$	$np = K_I$
Redox-Reaction:	$O_O^x + 2\,h^{\bullet} \rightleftharpoons V_O^{\bullet\bullet} + \frac{1}{2}\,O_2\uparrow$	$\frac{[V_O^{\bullet\bullet}]\sqrt{p(O_2)}}{[O_O^x]p^2} = K_R$
Charge neutrality:		$p + 2[V_O^{\bullet\bullet}] = n + 3[V_M^{///}]$

From this set of equations, all different defect concentrations can be calculated in dependence of the ambient oxygen partial pressure $p(O_2)$. $n = [e^{/}]$ and $p = [h^{\bullet}]$ denote the electronic charge carrier densities. To solve these equations manually, one can distinguish between certain pressure regions, where different chemical processes are dominant, and neglect the contributions of the other species. In the case of M_2O_3 three different regions can be found:

- Near stoichiometric region: $n = p = n/p_0 = \sqrt{K_I}$ is valid for the stoichiometric composition. As the concentration of intrinsic electronic defects exceeds the one of ionic defects, the charge neutrality is reduced to $p \approx n$.
- Reduction region: The reduction process becomes the major source of defects, leading to a charge neutrality of $2[V_O^{\bullet\bullet}] \approx n$.
- Oxidation region: The oxidation process becomes the major source of defects, resulting in $p \approx 3[V_M^{///}]$.

Applying the mass-action constants $K_S = 10^{-23}$, $K_I = 10^{-4}$ and $K_R = 10^{-6}$, according to [41], the concentration for each involved species is calculated and plotted in Figure 1.5(a) for different ambient oxygen pressures. The carrier concentration is induced by electronic charges: Holes for the oxidizing, electrons for the reducing region and both near the stoichiometric point. Assuming a constant mobility, the conductance would have a "U"-shape, as it is visible in Figure 1.5(a).

Coming closer to the model for mixed-valence manganites, one can now dope the system with an acceptor A^{2+}, as formal addition of $A^{2+}O^{2-}$ to the compound. The chemical reactions for the undoped system stay valid, but the additional substitutional cations $A_M^{/}$ have to be compensated by other defects:

- Holes (oxidized): $2\,AO + \frac{1}{2}\,O_2\downarrow \xrightarrow{M_2O_3} 2\,A_M^{/} + 3\,O_O^{x} + 2\,h^{\bullet}$
- Anion vacancies (stoichiometric): $2\,AO \xrightarrow{M_2O_3} 2\,A_M^{/} + 2\,O_O^{x} + V_O^{\bullet\bullet}$

The charge neutrality equation also has to be corrected to $p + 2[V_O^{\bullet\bullet}] = n + 3[V_M^{///}] + [A_M^{/}]$. The strongly nonstoichiometric regions are not affected, but the near-stoichiometric region is replaced by the impurity controlled region, represented by the electronic and the ionic compensation when neglecting the non-dominant effects:

- Electronic compensation: Holes compensate the doping charge: $p = [A_M^{/}]$
- Ionic compensation: "Crisscross" region, where oxygen vacancies level the additional negative charge: $2[V_O^{\bullet\bullet}] = [A_M^{/}]$

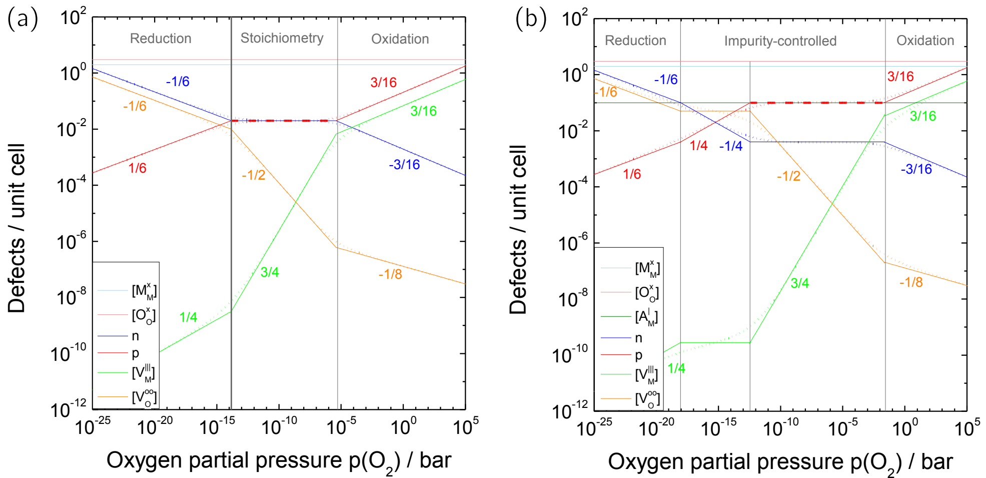

Figure 1.5: Kröger-Vink diagram of M_2O_3 and A:M_2O_3. The approximated calculations (solid lines) differ only slightly from the exact calculations (dotted lines). For the approximation the slopes for each species and regime are marked. (a) M_2O_3: Three regions can be identified for the undoped system: The reduction region, the near-stoichiometric region and the oxidation region. (b) A:M_2O_3 for $[A] = 10\,\%$: For the doped system the near-stoichiometric region is replaced by the ionic and electronic compensated impurity-controlled regions.

Using a doping concentration of 0.1 doping atoms per unit cell as example, one can again calculate the approximated and exact defect concentrations, as shown in Figure 1.5(b). For doping, the "U"-shape of the carrier concentration is widened out and in the plateau region two levels appear, as oxygen vacancies become the determining carriers over a certain pressure regime.

If the defect concentration of intrinsic or extrinsic defects reaches more than $1\,\%$ of the host material, the model of dilute solution is no longer valid. In this case, it has to be taken into account that the concentration of the host components can no longer be regarded as constant, but the number of lattice sites is unchanged within the crystal. Additionally, the distribution of defects is no longer random, but there might be cluster formation, neutralization and the formation of extended defects. Besides, interactions between point defects as associations and complex formation might occur. Because the integration of such complex processes into the current model is highly complicated, defects will still be regarded as randomly distributed and the interactions between them will be neglected.

The host components will now be considered as variables of the ambient oxygen partial pressure, so that site balance equations are needed and the picture of doping is changed to that of a solid solution of two compositions. In addition, the charges created by the ionization process are assumed to be localized at the cations, known as small polaron model (SPM) [41, 42]:

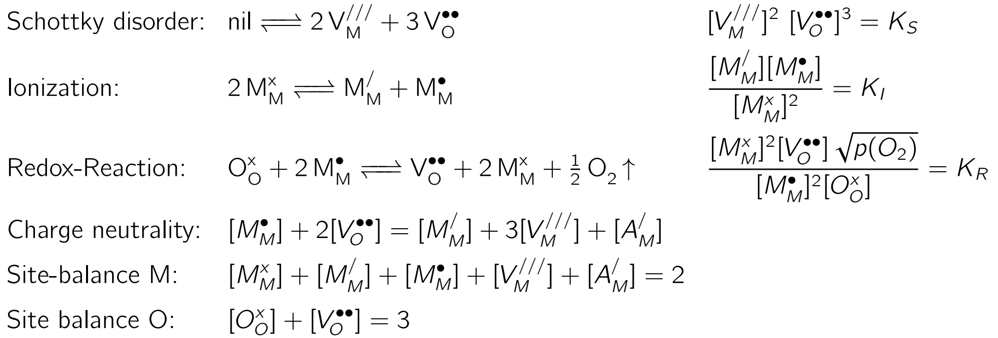

Schottky disorder: $\mathrm{nil} \rightleftharpoons 2\,\mathrm{V}_{\mathrm{M}}^{///} + 3\,\mathrm{V}_{\mathrm{O}}^{\bullet\bullet}$ $\qquad [V_M^{///}]^2\,[V_O^{\bullet\bullet}]^3 = K_S$

Ionization: $2\,\mathrm{M}_{\mathrm{M}}^{x} \rightleftharpoons \mathrm{M}_{\mathrm{M}}^{/} + \mathrm{M}_{\mathrm{M}}^{\bullet}$ $\qquad \dfrac{[M_M^{/}][M_M^{\bullet}]}{[M_M^{x}]^2} = K_I$

Redox-Reaction: $\mathrm{O}_{\mathrm{O}}^{x} + 2\,\mathrm{M}_{\mathrm{M}}^{\bullet} \rightleftharpoons \mathrm{V}_{\mathrm{O}}^{\bullet\bullet} + 2\,\mathrm{M}_{\mathrm{M}}^{x} + \frac{1}{2}\,\mathrm{O}_2\uparrow$ $\qquad \dfrac{[M_M^{x}]^2[V_O^{\bullet\bullet}]\,\sqrt{p(O_2)}}{[M_M^{\bullet}]^2[O_O^{x}]} = K_R$

Charge neutrality: $[M_M^{\bullet}] + 2[V_O^{\bullet\bullet}] = [M_M^{/}] + 3[V_M^{///}] + [A_M^{/}]$

Site-balance M: $[M_M^{x}] + [M_M^{/}] + [M_M^{\bullet}] + [V_M^{///}] + [A_M^{/}] = 2$

Site balance O: $[O_O^{x}] + [V_O^{\bullet\bullet}] = 3$

Using this set of formulas the concentrations of all six different species can be calculated in dependence of the ambient oxygen partial pressure, as shown in Figure 1.6(a) for a defect concentration of 20 %.

Moving one step further towards real systems, the compound A^{2+}: $\mathrm{R}^{3+}\mathrm{Mn}^{3+}\mathrm{O}_{3\pm\delta}^{2-}$ has to be considered. The Schottky reaction changes to $\mathrm{nil} \rightleftharpoons \mathrm{V}_{\mathrm{R}}^{///} + \mathrm{V}_{\mathrm{Mn}}^{///} + 3\,\mathrm{V}_{\mathrm{O}}^{\bullet\bullet}$ and the charge neutrality to $[\mathrm{Mn}_{\mathrm{Mn}}^{\bullet}] + 2\,[\mathrm{V}_{\mathrm{O}}^{\bullet\bullet}] = [\mathrm{Mn}_{\mathrm{Mn}}^{/}] + 3\,[\mathrm{V}_{\mathrm{R}}^{///}] + 3\,[\mathrm{V}_{\mathrm{Mn}}^{///}] + [\mathrm{A}_{\mathrm{R}}^{/}]$.
Besides, the defect-chemical processes are usually thermally activated and only contribute above their respective activation temperature:

- Low temperature regime ($T < 500\,^\circ\mathrm{C}$):
  - Ionization is activated according to the band gap E_g
  - Ion diffusion is frozen in
  - Carriers are created from dopants
  - Associates, complexes and not completely ionized defects exist
- Intermediate temperatures ($500\,^\circ\mathrm{C} < T < 1000\,^\circ\mathrm{C}$):
  - Oxygen exchange with atmosphere is activated
  - Associates, complexes and other defects are completely ionized

- High temperature regime ($T > 1000\,^{\circ}$C):
  - Schottky balance is activated

For an appropriate comparability of the theoretical considerations and real thin films deposited by PLD at 600-800 °C, the Schottky balance might have to be frozen in, because cation vacancies can be neglected to some extent. The resulting Kröger-Vink diagram is shown in Figure 1.6(b) and clearly resembles results shown in [43, 41].

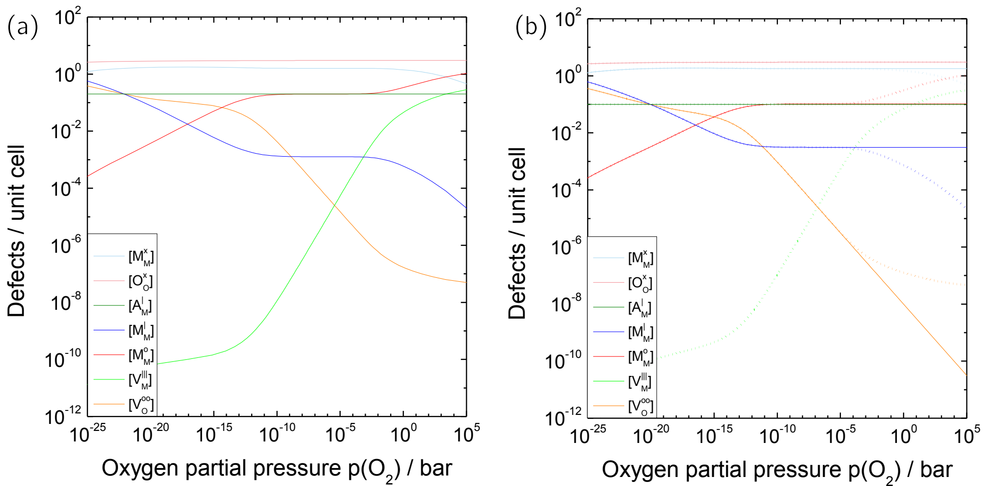

Figure 1.6: Kröger-Vink diagram of A:M_2O_3 covering site-balance: (a) For both extreme oxygen conditions even the host components are clearly affected, using $[A] = 20\,\%$. (b) When the Schottky balance is frozen in (solid lines), the region of highly oxidizing conditions is not visible, using $[A] = 10\,\%$. The dotted lines refer to calculations of the same system with activated Schottky reaction.

1.2.2 Effects of correlated electronics

As described in Section 1.2.1, the point defect chemistry in combination with the doping level determines the number and the charge of carriers in dependence of ambient oxygen pressure and temperature. For many systems, the conductivity σ follows the shape of the carrier concentrations n_i, derived from defect chemistry, under the assumption that the mobility μ_i is equal for all charge carriers and not dependent on the oxygen partial pressure, according to

$$\sigma = \sum_i q_i n_i \mu_i,$$

summing up over all different electronic and ionic carrier types i with the respective charges q_i.

For mixed valence manganites a "U"-shape carrier concentration for holes, oxygen vacancies and electrons was calculated in Section 1.2.1 for different pressure regimes and thus a similar shaped conductivity over oxygen partial pressure is predicted. The oxygen partial pressure dependence of the conductivity for $La_{0.8}Sr_{0.2}MnO_3$ (LSMO) is available in literature [44] and shown in Figure 1.7(a). The conductivity stays constant over a wide oxygen partial pressure regime and only drops under highly reducing conditions by almost two orders of magnitude.

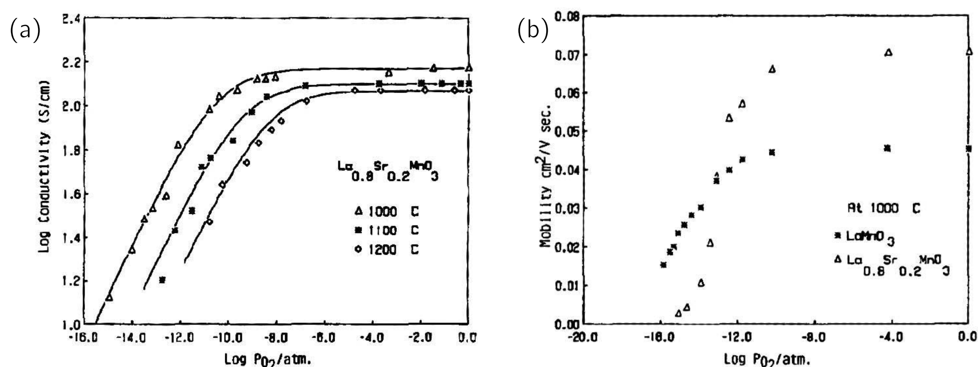

Figure 1.7: Transport properties of $La_{0.8}Sr_{0.2}MnO_3$ in dependence of the oxygen partial pressure, taken from [44]: (a) The conductivity of LSMO drops dramatically at highly reducing conditions. (b) The mobility of LSMO also drops significantly at a similar oxygen partial pressure.

A reason for this behavior might be different mobility values for each charge carriers. For reducing conditions, the hole concentration is exceeded by the oxygen vacancy concentration,

which becomes negligible for transport properties, when assuming a much lower mobility of ionic defects compared to electronic defects. Another explanation could be an oxygen partial pressure dependence of the mobility, which is available in literature for $La_{0.8}Sr_{0.2}MnO_3$ [44] (Figure 1.7(b)). It has a similar shape as the conductivity and is therefore the most probable explanation.

To understand the correlation between oxygen partial pressure and mobility of the charge carriers, it is important to look at the large variety in structural, magnetic and transport properties of mixed-valence manganites. In Figure 1.8 the phase diagrams of $Pr_{1-x}Ca_xMnO_3$ and $La_{1-x}Sr_xMnO_3$ are depicted. Figure 1.8(c) shows a more schematic sketch of the different phases of $R_{1-x}A_xMnO_3$ in general.

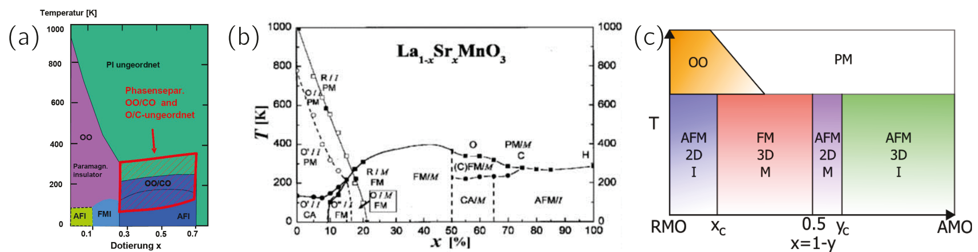

Figure 1.8: Phase diagrams of $R_{1-x}A_xMnO_3$: (a) Phase diagram of $Pr_{1-x}Ca_xMnO_3$, taken from [45]. (b) Phase diagram of $La_{1-x}Sr_xMnO_3$, taken from [46]. (c) Sketch of a general phase diagram of $R_{1-x}A_xMnO_3$: Magnetism: ferromagnetic (FM or F), antiferromagnetic (AFM, A or AF), canted antiferromagnetic (CAFM, CN, CA), paramagnetic (PM or P); Transport: metallic (M), insulating (I); Structure: cubic (C), orthorhombic (O or O'); Order: orbital-ordering (OO), charge-ordering (CO).

To explain the different properties it is crucial to first consider the end-members $RMnO_3$ and $AMnO_3$. Starting with a perfectly cubic system (Figure 1.9(a)) the oxygen ions are arranged in an octahedral coordination around the Mn cations and form a crystal field, in which the five 3d-orbitals of Mn get split (Figure 1.9(b)). Since d_{xy}, d_{xz} and d_{yz} are oriented in-between the directions of the three axial oxygen 2p-orbitals, they have a small overlap with these orbitals, therefore are energetically favored and form the energetically lowered triple t_{2g} level, where g stands for an even inversion center. The $d_{x^2-y^2}$ and d_{z^2} orbitals are oriented along the same axes as the O_{2p} and the coulomb repulsion between electron and O^{2-} lifts the two orbitals up to the double e_g-level.

For the perovskite lattice structure the sizes of the two different cations have a crucial impact on the stability of the structure. Goldschmidt defined a tolerance factor

$$T = \frac{1}{\sqrt{2}} \frac{r_A + r_O}{r_B + r_O},$$

in [47], which relates the ion radii $r_{i=A,B,O}$ of the different species of ABO_3 together and which value defines the stability and distortion of a system. At $T = 1$ the system is perfectly cubic, as it is the case for $SrTiO_3$, and for $0.8 < T < 1.0$ the system is at least stable. A deformation of the unit cell occurs for $0.75 < T < 0.90$, so that in RMO with a factor of around 0.9 the oxygen octahedra are tilted.

A similar effect is attained, if there is exactly one e_g-orbital occupied in a system, which is the case for RMO. The system tries to reverse the degeneracy of the two e_g-levels to minimize the total energy by getting distorted in a way, that the overlap between the occupied orbital and the O_{2p}-orbitals become minimized, called Jahn-Teller distortion (JT) (Figure 1.9(c)). The most plausible way is to extend the oxygen octahedra along the c-axis, when the d_{z^2}-orbital is occupied. Another possibility, which is mainly important for mixed-valence manganites as $Pr_{1-x}Ca_xMnO_3$ (Figure 1.9(d)), is the tilting of the oxygen octahedra for the occupation of the $d_{x^2-y^2}$-orbital. As two neighboring octahedra share a common oxygen ion, the deformations are not independent and the whole lattice is distorted, which is the so-called cooperative Jahn-Teller effect. Such a lattice distortion generated by a single electron is called a polaron, since the electron is localized within its own lattice distortion by coulomb forces.

For the consideration of the magnetic properties [51], Hund's rules are necessary to be beared in mind. Within one atom or ion, the spins of a partially occupied shell are oriented in one direction due to Hund's second rule. Applied to Mn, it has three t_{2g}-electrons forming the t-core with a spin of 3/2 and possibly one e_g-electron with the spin of 1/2, which must be oriented the same way.
In $RMnO_3$ Mn^{3+}([Ar]$3\,s^2 3\,d^4$) has one loosely bound e_g-electron per unit cell. If we now consider two Mn^{3+} ions, they both have one occupied e_g-level. As they are coupled by an oxygen ion with fully occupied $2d^6$ configuration, the Mn-spins are oriented antiferromagnetically (AFM) along the d_{z^2}-direction, as well as their cores due to Hund's rule, what is called super exchange (Figure 1.10(a)). As the $d_{x^2-y^2}$-orbitals are unoccupied, they can couple degeneratedly and the in-plane exchange mechanism is ferromagnetism (FM). In an easy picture, the two energetically separated e_g-states due to Jahn-Teller distortion form two bands with a certain energy gap when put into a periodic crystal. In pure $RMnO_3$ the

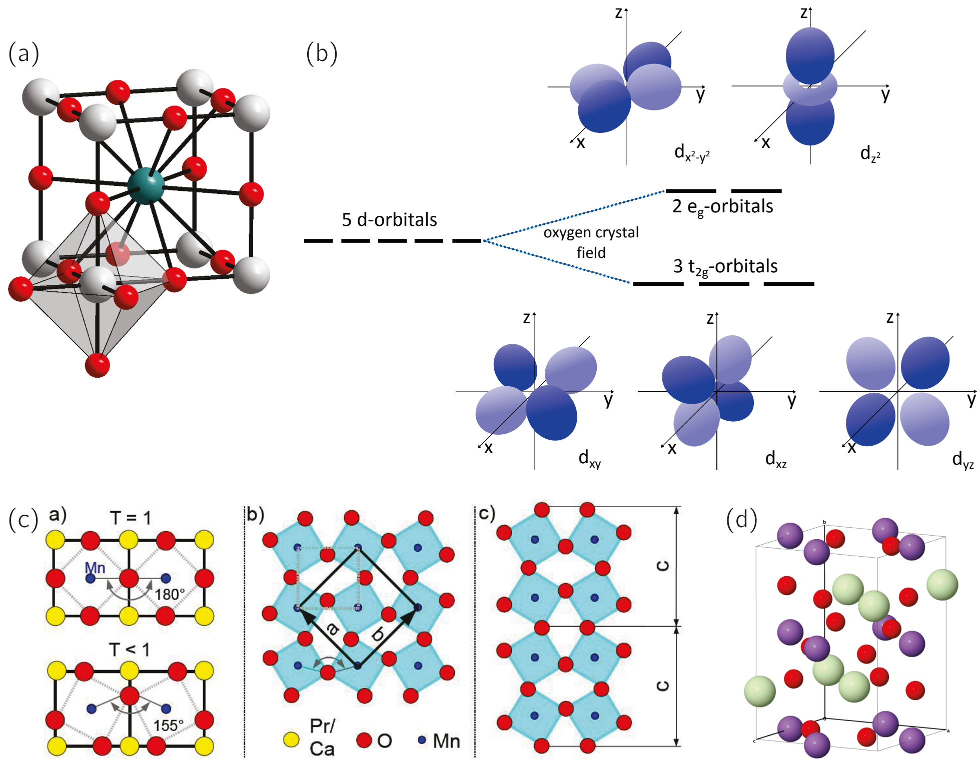

Figure 1.9: Crystal field splitting and Jahn-Teller distortion: In the crystal field of the octahedral oxygen environment in the perovskite crystal structure ABO_3 (a), taken from [48], the five d-orbitals of Mn split into two energy levels (b), based on [49]. The three t_{2g}-levels are energetically favored, as their orbitals are lying just between the oxygen p-orbitals, while the 2 e_g-orbitals are unfavored due to their large overlap with the oxygen orbitals. If only one e_g-orbital is occupied in $R_{1-x}A_xMnO_3$, the crystal tries to minimize the total energy by distorting according to Jahn-Teller (c), taken from [45]. Besides the difference between untilted and tilted oxygen octahedra, the top and side view of a distorted structure is depicted. This is the reason for an enlarged unit cell for $Pr_{0.48}Ca_{0.52}MnO_3$ (d), taken from [50].

lower band is totally occupied, while the other one is empty [52]. So the trapped electrons have no possibility to move and the system is insulating.

In $AMnO_3$ Mn^{4+}([Ar]3 s^{2}3 d^3) has no occupied e_g-orbital and only three strongly bound t_{2g}-electrons to provide the overlap with the oxygen orbitals. Therefore, there will be no JT-distortion. As the three t-core orbitals are completely equivalent, the model of super exchange is valid in all directions and the spins of the Mn cations are oriented in a 3D

antiferromagnet of type charge-exchange (CE). As the gap between the hybridized t_{2g} and the e_g-levels is rather large and there are no unbound carriers, the material behaves insulating.

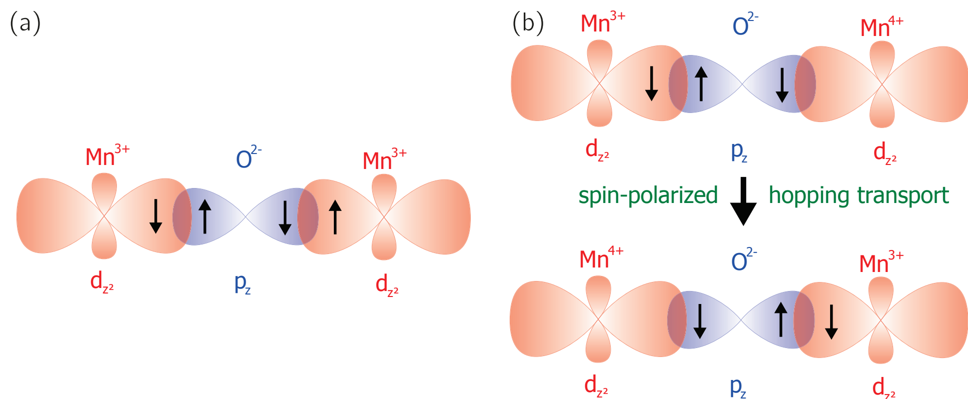

Figure 1.10: (a) Antiferromagnetic super exchange: The spins of additional e_g-electrons are oriented antiparallel due to the interaction with the mediating oxygen ions. (b) Ferromagnetic double exchange: The spin polarized hopping transport between two Mn ions with different valence state is enhanced, as the two states are degenerated.

"Doping" the $RMnO_3$-compound with $AMnO_3$ will lead to the creation of holes within the material as the acceptor-like dopants need to be compensated. Such a hole can be considered as a missing e_g-electron in the actual unit cell, where it is localized, turning the Mn^{3+} to Mn^{4+}. To understand how the magnetic exchange mechanism is coupled to the conductivity in manganites, it is crucial to consider the coupling between Mn^{3+} to Mn^{4+}, called double exchange (Figure 1.10(b)). Again Hund's second rule forces the valence electrons to be polarized the same way as the t-core. In addition, charge carriers keep their spin when hopping to a vacant neighboring site. These facts result in a possible hopping process between ferromagnetically oriented cations, while hopping is forbidden for antiparallel spins. As hopping increases the degree of disorder, which is energetically favored due to an increase in entropy, the hopping process lowers the systems total energy and ferromagnetic coupling occurs. In another picture, the two states $Mn^{3+}-O^{2-}-Mn^{4+}$ and $Mn^{4+}-O^{2-}-Mn^{3+}$ are quantum theoretically equal, so that the electron is delocalized over the whole system, the probability amplitude is uniformly distributed over the two ions and the electron is therefore mobile. As charge transfer is provided by spin-polarized electrons via so-called "zig-zag"-patterns, the conducting state is called "half-metallic".

Using the current considerations, it is possible to explain the schematic phase diagram of mixed-valence manganites (Figure 1.8(c)). Starting to dope the $RMnO_3$ system with A, the new hole-containing unit cells will be randomly distributed and the antiferromagnetism will be locally replaced by ferromagnetic coupling, in which charge exchange is allowed. With more and more doping, clusters will be formed, what can be calculated by percolation theory [53]. At a certain concentration, the system will be pierced infinitely by FM regions, which allow a macroscopic change in conductivity, while still AFM and FM regions coexist. This 3D-percolation threshold $x_c \approx 0.16$ leads to an insulator-metal transition into a metallic FM state in three dimensions, which persist up to $x = 1 - y = 0.5$.
Doping the $AMnO_3$-system with R, i.e. electrons, the picture of percolation can again be applied. Up to a 2D-percolation threshold of $y_c \approx 0.45$, the 3D insulating AFM state is conserved, in spite of the coexisting new phase. Above this insulator-metal transition, the conducting state consists of an antiferromagnetic A-structure with conducting FM-coupled planes and forbidden charge transport along the c-axis.

Going from the magnetically ordered states to higher temperatures, both FM and AFM phases show the typical phase transition to the paramagnetic phase under thermal destruction of the former arranged spins at Curie- and Néel-temperature respectively. As depicted in [54], the temperature dependence of $R_{1-x}A_xMnO_3$ for a metallic composition is dominated by the FM metallic phase for low temperature, switching at T_C into a thermally activated semiconducting behavior in the paramagnetic phase.
At elevated temperatures and certain doping levels the system can additionally adopt orbital and/or charge ordering. Orbital ordering (OO) is closely related to the cooperative JT-effect, which provides the direction of occupied orbitals. As the charge is localized within the single distorted unit cells, this phenomenon is also called polaron ordering. The alternating orientation of the oxygen octahedra often leads to an enlarged unit cell compared to the cubic structure with the lattice constant a_{cubic}, resulting in an orthorhombic structure with a unit cell of about $(\sqrt{2} \mid \sqrt{2} \mid 2) \cdot a_{\text{cubic}}$. Orbital ordering can occur only if there are enough ions with orderable orbitals Mn^{3+}, i.e. mainly near $x = 0$, with decreasing transition temperature towards $AMnO_3$.
Inter-atomic coulomb interactions cause a phenomenon that is called charge ordering (CO). Also known as Wigner crystallization, the mobile electrons (or holes) can be localized on certain manganese ions forming a regular lattice of Mn^{3+}/Mn^{4+}. This mechanism mainly occurs at doping concentrations being rational fractions.

In principle this scheme of different phases is very similar in all mixed-valance manganites, but the borders between the different regimes and the transition temperatures depend

strongly on the cation species. The tolerance factor has a large impact on the JT-distortions, as the ratio in cation radii regulates the octahedra tilting. A strong distortion of the oxygen neighborhood again decreases the strength of the double exchange, because this mechanism is optimized for untilted Mn−O−Mn chains. The ferromagnetism also controls the charge exchange and therefore the conductance mechanism.

Reducing the material by adjustment of the ambient leads to the creation of oxygen vacancies due to defect chemistry, described later-on in Section 1.2.1. A missing oxygen ion leads to the destruction of the Mn−O−Mn chains, which are responsible for magnetic order and hence conductance. Furthermore, if the material is highly reduced, the oxygen vacancies might replace the holes as compensating defects and the conductance mechanism is changed from half-metallic to the less conducting ionic type because of a hopping barrier of $\Delta E \approx 0.6 - 0.9\,\mathrm{eV}$ for oxygen vacancies and even higher values for interstitial diffusion or cation hopping [55].

This rather simple picture of mixed-valence manganites already provides the explanation of many observed phenomena, but still does not explain, for example, why these materials show p-type conductance over almost the whole doping range. Therefore a more complex view has to be taken into account. As $R_{1-x}A_xMnO_3$ can be regarded as a kind of semiconductor, it is interesting to consider the band scheme including the doping levels. Using density functional theory (DFT) calculations the density of states (DOS) can be obtained for different stoichiometries of $Pr_{1-x}Ca_xMnO_3$, as schematically depicted in Figure 1.11(a).

In Figure 1.11(b) the band structure of $Pr_{0.7}Ca_{0.3}MnO_3$ is depicted for the stoichiometric composition and an oxygen deficient composition $Pr_{1-x}Ca_xMnO_{3-\delta}$. According to these calculations the region around the Fermi level consists of oxygen vacancy levels $Mn^{3+}{-}V_O^{\bullet\bullet}{-}Mn^{4+}$. These can be filled up by charge carriers, but the mobility of the holes is so small, that they can be regarded as localized. As the mobility edge [57] is lying well below the Fermi level, the localized states act as shallow in-gap bandgap and the system does no longer behave half-metallic.

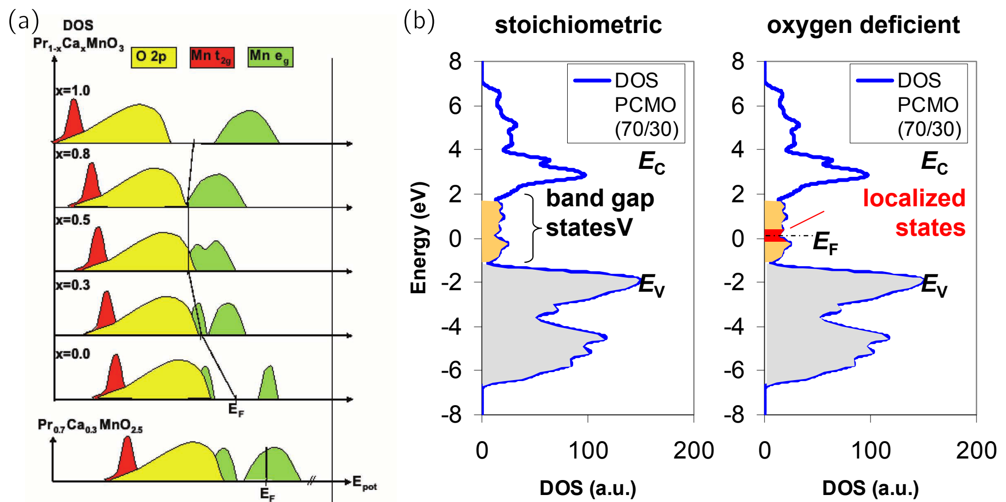

Figure 1.11: DFT calculations for $Pr_{1-x}Ca_xMnO_3$: (a) Schematic evolution of the band structure of $Pr_{1-x}Ca_xMnO_3$, which is based on DFT calculations, taken from [52]. The two end-members $CaMnO_3$ and $PrMnO_3$ are isolating, while in-gap states lead to transport for mixed systems. For oxygen depletion, additional carriers are introduced and the Fermi level is shifted to higher energies, but the carriers become immobile. (b) DOS of $Pr_{0.7}Ca_{0.3}MnO_3$ for the stoichiometric and a reduced composition, taken from [56]. Within the bandgap the DOS near the Fermi edge can be assigned to localized oxygen vacancy states.

2 Epitaxial growth of perovskite thin film heterostructures by pulsed laser deposition

In this chapter the deposition procedure of epitaxially grown thin films is described. Various perovskite materials are grown in diverse complicated layer stacks for different projects. After a short description of the background of epitaxial growth, the applied methods are introduced and the results of several heterostructures are presented.

2.1 Basics

2.1.1 Epitaxial thin film growth

For the hetero-epitaxial growth of a complex oxide material on a single-crystal substrate, the mismatch between the two different lattices has a crucial impact on the growth quality. Cubic $SrTiO_3$ is used as a substrate for many thin films, while the deposited film material can have various complex crystal structures. The crystal structure of many materials can be regarded as cubic by using only small approximations, which is the neglect of the oxygen octahedra tilting for manganites, described in Section 1.2. The newly created unit cell is called "pseudo-cubic" and in most cases denoted with *. For many common oxides the cubic/pseudo-cubic lattice constants are shown in Figure 2.1(a).

Depending on the ratio of the pseudo-cubic lattice constants of film and substrate, the mismatch strain

$$\epsilon_m = \frac{a^*_{\text{film}} - a^*_{\text{substrate}}}{a^*_{\text{film}}}$$

in the film is compressive or tensile (Figure 2.1(b)). When a critical film thickness d_c is reached, which depends strongly on the mismatch itself, the stress inside the thin film becomes too large and the material starts to relax. Relaxation is achieved by the introduction of one-, two- or three-dimensional lattice defects.

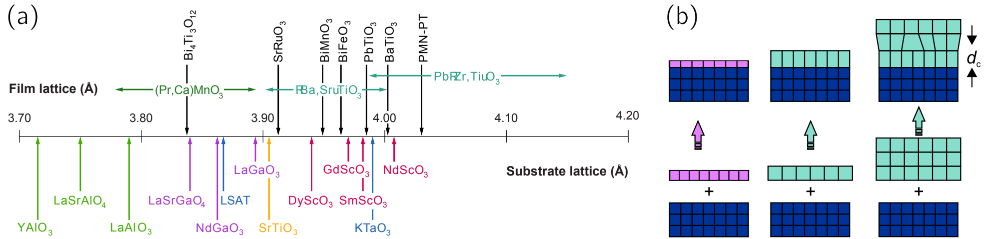

Figure 2.1: For hetero-epitaxial thin film growth, the mismatch in lattice constant results in strain: (a) (Pseudo-)cubic lattice constants of common oxide substrate and thin film materials, based on [58]. (b) Effect of tensile and compressive strain on thin films, based on [59]. For both cases the film will start to relax above a certain thickness d_c.

Beside the three-dimensional growth modes Volmer-Weber and Stranski-Krastanov, the two-dimensional growth modes Frank-van der Merve (layer-by-layer) and step-flow growth mode exist, which are desirable as they result in atomically flat surfaces.

2.1.2 Deposition and characterization methods

2.1.2.1 Pulsed laser deposition

For the deposition of complex oxides, pulsed laser deposition (PLD) is a widely used technique [60, 23, 61, 62]. The working principle is sketched in Figure 2.2(a): A short-pulsed laser is focused on the ceramic or single-crystalline target material. The absorption of the pulse instantaneously generates a plasma plume of neutral and ionized species of the composition and is directed orthogonal to the target surface. As result of the high energetic laser pulse, the ablated material is not in its thermodynamical equilibrium and even for large melting-point deviations of the individual species, the stoichiometry can be transferred into the plasma phase and later onto the substrate. The large advantage of PLD is, that with the right set of process parameters, the stoichiometry is conserved during the transfer of material between target and substrate.

In this work, a setup from TSST (Twente Solid State Technology, B.V.) was used (Figure 2.2(b)), applying a 50 W KrF excimer laser with a wavelength of $\lambda = 248$ nm, which provides a large absorption in the target. The pulse length is $t = 25$ ns and the repetition rate can be varied between $f = 1$ Hz and 50 Hz. The fluence on the target has a crucial impact on the stoichiometry on the substrate. It depends on the laser pulse energy

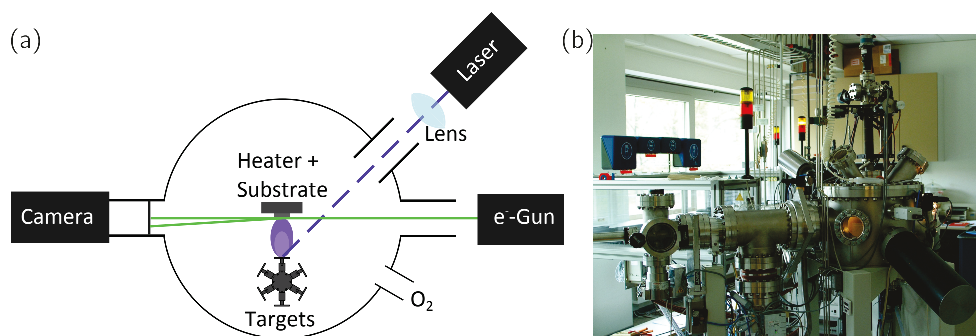

Figure 2.2: RHEED-assisted pulsed laser deposition: (a) Sketch of the PLD chamber. (b) Photo of the PLD setup from TSST.

E, which can be adjusted by a beam attenuator and measured in front of the chamber, the transmission coefficient of the window, through which the laser beam is directed, and the laser spot size on the target adjusted by the optics geometry. The background pressure in the vacuum chamber is typically 10^{-8} mbar. For the deposition, a carefully controlled oxygen ambient can be created in the chamber, which can be varied over 8 orders of magnitude in partial pressure p and has an influence on the plume expansion, the valance states of the plume particles and their kinetic energy. The substrate is glued on a heater with silver paste and is adjusted in the center of the plum in an adjustable distance d of about 6 cm. The substrate can be heated up to a maximum temperature of $T = 800\,°\mathrm{C}$, which activates the mobility of the incoming species on the surface. The stoichiometry of a thin film deposited by PLD depends strongly on the complex interaction between laser ablation and plasma plume kinetics [63]. Therefore, the adjustable parameters have to be tuned carefully and mutually to obtain high quality single crystal thin films.

2.1.2.2 RHEED

During the deposition, reflection high energy electron deflection (RHEED) is used to monitor the crystal growth in-situ. Here, a differentially pumped, high pressure TorrRHEED system by STAIB Instruments GmbH is applied. A high energetic electron beam of 25 keV hits the substrate in gracing incidence and is focused on a phosphor screen, as depicted in Figure 2.3(a) for a $SrTiO_3$ substrate. To achieve a large surface sensitivity, the incoming angle is chosen very small, so that a small part of the beam even passes the substrate. The largest part is diffracted at the periodic crystal lattice, as the wavelength of the electrons is

comparable to the atomic distances, directly reflected or scattered by the surface roughness. The penetration depth of the electrons is only a few atomic layers, so that the detected information comes mainly from the surface. On the screen, the direct beam can be observed and beside the directly reflected spot (specular spot), a characteristic material-dependent diffraction pattern arises [64].

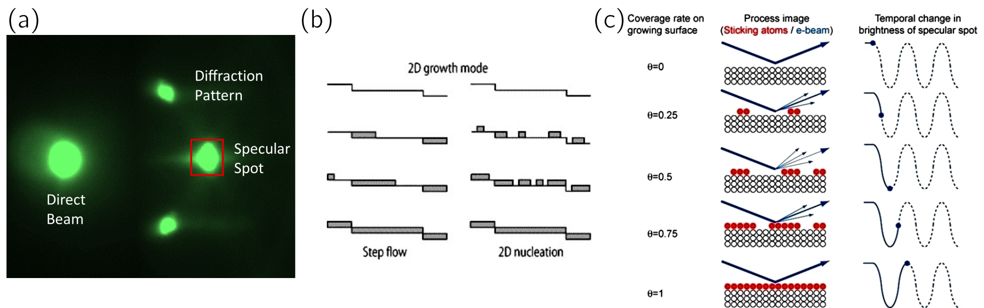

Figure 2.3: Principle of RHEED: (a) RHEED pattern of a $SrTiO_3$ substrate: Beside the direct beam, the directly reflected specular spot is visible and the specific diffraction pattern of $SrTiO_3$. The red box indicates the area, over which the intensity is integrated and measured. (b) Two different modes of 2-dimensional growth, based on [65]: In layer-by-layer growth mode, the surface is successively covered by nucleation points, while in step-flow growth mode the incoming species dock with the edges of the surface. (c) RHEED signal of layer-by-layer growth, taken from [66]: During the deposition, the scattered part of the beam changes frequently due to roughness alternations.

During the growth of one unit cell layer (ucl) of a material growing in layer-by-layer mode (Figure 2.3(b)), the monitored intensity of the specular spot runs through one oscillation (Figure 2.3(c)). Starting at an atomically flat surface of the substrate, the plane is successively covered with material. Nucleation and growth of the formed islands are competing processes, which lead to a two-dimensional growth process. For an increased coverage of the surface, the island growth process becomes dominant, until the ucl is completed. The roughness of the surface is directly determined by the coverage, as the amount of step edges crucially depends on the density of islands, and thus is minimal for a closed ucl and maximal for half a ucl. The roughness in turn determines the scattering probability of the electrons and thus the intensity of the reflected beam. A maximum in electron scattering for half of a closed ucl causes a minimum in the reflected intensity of the specular spot, so that the detected RHEED signal goes through one complete oscillation during the growth of one ucl. A detailed description can be found in [64].
Step-flow (Figure 2.3(b)) describes a growth mode, during which the incoming species are

so mobile at the surface, that they move towards a step edge of the underlying layer and stick there, while no island nucleation takes place. The corresponding RHEED intensity of the specular spot does not alter much during growth, because the roughness of the surface is not changed due to a shift of the step edges. This growth process provides a very good crystal quality and is therefore favorable, but only realizable for some materials and deposition conditions.

2.1.2.3 Target and substrate preparation

The targets used for depositions, consisting of highly compressed dense ceramic powders, were mainly bought from Praxair Surface Technologies or in several cases produced within the institute. Prior to each deposition, the target surface was sanded homogeneously.

Four different single crystal materials were used as substrates: $SrTiO_3$(001) (STO), Nb(0.5 at.%):$SrTiO_3$(001), $NdGaO_3$(110) (NGO) and $(La_{0.3}Sr_{0.7})(Al_{0.65}Ta_{0.35})O_3$(001) (LSAT). To achieve a uniform TiO_2-termination of (Nb:)$SrTiO_3$, the substrates were partially etched in buffered hydrofluoric acid (BHF, $pH = 6.5$) for 3:45 min. In order to reduce the disorder and defects, induced by the polishing procedure, an annealing step is applied, which allows the system to rearrange its lattice structure at high temperatures. Due to a natural miscut angle of the substrates, a step-terrace structure of one unit cell height is formed on the surface. The annealing procedures are listed in Table 2.1.

Material	Atmosphere	Temperature	Time
(Nb:)$SrTiO_3$	Air	950 °C	4 h
TiO_2-terminated (Nb:)$SrTiO_3$	Air	950 °C	2 h
$NdGaO_3$	Air	1000 °C	2 h
LSAT	H_2(4%)-Ar	1050 °C	60 h

Table 2.1: Annealing procedures for different substrates.

2.1.2.4 Atomic force microscopy

The surface morphology of the prepared substrates and deposited thin films was determined by atomic force microscopy (AFM). The images were measured with an SIS Pico Station by UltraObjective in tapping mode.

The work principle of an AFM is based on inter-atomic forces between probe and sample (Figure 2.4). An atomically sharp tip, which is attached to an elastic cantilever, is approached to the surface of the sample and then carefully scanned over an area of micrometer range. Atomic interactions between tip and surface atoms cause a bending of the cantilever in dependence of the surface topography. A laser is directed on the backside of the cantilever and its reflection is detected by a multiple segmented photo-diode, so that small changes in its direction are revealed. For the applied tapping mode of the AFM, the cantilever is externally oscillated at its resonance frequency, and the change in amplitude and phase due to tip-sample interaction forces are measured. More information can be found in [67].

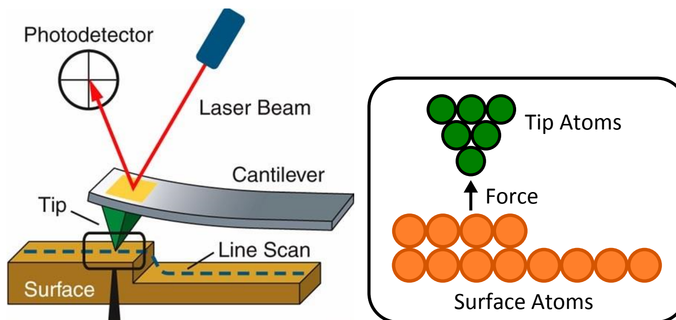

Figure 2.4: Work principle of an AFM, based on [68]: An atomically sharp tip mounted under a cantilever is scanned over a surface, while a laser beam is focused on the cantilever. The reflection of the laser beam is detected and changes of the surface are measured.

With the AFM, the surface morphology can be imaged with a vertical resolution of down to 1 Å and a lateral resolution of well below 100 nm. The scans are used to monitor the step-terrace structure of the substrates and thus their quality and how good the steps are reproduced in the epitaxial thin films. In addition, the roughness ρ of the surface can be determined as the root mean square (RMS) value of the AFM height data set.

2.1.2.5 X-ray diffraction

For the structural analysis of the thin films, X-ray diffraction (XRD) is used. X-ray radiation is suitable to resolve the crystal structure, as its small wavelength λ lies in the same range as the atomic distances in solids, and diffraction reflexes appear as a result of the periodicity of the crystal lattice. As the X-ray beam hits a crystal, it interacts with the electronic structure of the lattice constituents and is scattered. Under certain angles the diffracted radiation interferes constructively, as shown in Figure 2.5(a). As the beam hits parallel lattice planes spaced by $d_{hkl} = \frac{1}{\sqrt{(\frac{h}{a})^2+(\frac{k}{b})^2+(\frac{l}{c})^2}}$, valid for right-angled crystal systems with lattice constants a, b and c and Miller indices (hkl), observable intensity peaks appear for angles $2\theta_B$, where the Bragg-equation

$$2d_{hkl} \sin\theta_B = \lambda$$

is fulfilled and no reflexes are erased due to symmetry properties of the respective Bravais lattice.

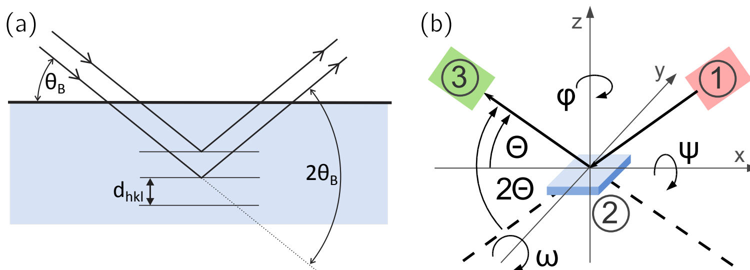

Figure 2.5: X-ray diffraction: (a) Schematic depiction of the Bragg condition, based on [69]: Parallel X-rays are diffracted at lattice planes of the distance d_{hkl} and interfere in dependence of their angle of incidence. (b) Measurement principle of XRD, based on [45]: The X-ray tube ① generates the beam, which is focused on the sample ②, while the diffracted radiation is detected ③. The sample can be moved along all three axes and the corresponding rotation angles, the detector can only be moved along one angle 2θ.

In this work a Philips PW3020 diffractometer equipped with a Cu-K_α tube of wavelength $\lambda = 1.54\,\text{Å}$ was used, which line actually splits into K_{α_1} and K_{α_2}. The schematic setup is depicted in Figure 2.5(b). The sample can be moved in all three dimensions x, y and z and rotated along the corresponding angles ψ, ω and φ. The detector can be moved by the angle 2θ, in-plane with ω.

Pure out-of-plane reflexes ($00l$) in Bragg-Brentano geometry ($\theta = \omega$) were measured as 2θ-ω scans to determine the lattice constants of the epitaxially grown thin films. ω-scans were performed at the respective 2θ-positions to obtain the width (full width at half maximum, FWHM-value) of the resulting peaks, known as "rocking curves", which give a hint on the crystallinity of the thin films. The resolution of the XRD system in the used configuration provides the lower limit of the ω-peak width for the STO substrate of $\Delta\omega = 0.025$-$0.032\,°$.

Additionally, reflexes with in-plane contribution ($h0l$) were used to image the strain effects of the lattice mismatch in so-called reciprocal space maps (RSM). For this technique an asymmetric XRD reflex is chosen, in this work the STO (103) reflex, to obtain in-plane information on the thin film in addition to the out-of-plane information, recorded in Bragg-Brentano geometry. Around the STO (103) peak a set of 2θ-ω-scans for different ω-offsets is measured and combined to a map. After converting the data set to real space lattice constants, the intensity is gained in dependence of in-plane lattice constant a^* and out-of-plane lattice constant c^*.

A method called X-ray reflection (XRR) was occasionally used to determine the thickness d of thin films. For this technique, the Bragg-Brentano geometry is used with a very small incidence angle $0\,° \leq \theta \leq 2\,°$. Now the direct beam is measured and its interference fringes caused by the reflection at the surface interacting with the one at the underlying interfaces. The difference between $n + 1$ maxima of the detected signal $\Delta(2\theta)$ is used to determine the thickness using the small-angle approximation with θ in radian measure

$$d = \frac{n \cdot \lambda}{\Delta(2\theta)}.$$

From the periodicity of these oscillations the film thickness can be calculated with an accuracy of 0.5 nm.

2.2 Growth of perovskite heterostructures

For the growth of epitaxial thin films with PLD the deposition parameters have to be adjusted individually for each material to obtain a stoichiometric transfer from the target to the substrate.
For homo-epitaxially grown films, the crucial criterion for a stoichiometric composition is the matching of the out-of-plane lattice constant, which forms a minimum at the stoichiometric point for fluence variation [63]. If the stoichiometry is not conserved during growth due to a misaligned parameter set, cation vacancies are formed, which distend the unit cell and result in an increased out-of-plane lattice constant.
This criterion is not valid for hetero-epitaxially grown films. As the bulk lattice constant of the thin film material differs from the substrate lattice constant, the film will adapt the in-plane structure of the substrate and also the out-of-plane dimension will change. From elastic deformation considerations [70] an appropriate value for the out-of-plane lattice constant can be estimated, which gives - in addition to the bulk value - the other limit for the real thin film lattice constant. In addition, the width of the rocking curve at the film Bragg reflex is a good measure for the crystal quality.
Beside the structural investigations, the surface morphology gives a hint on the stoichiometry. For a perfectly strained and near-stoichiometric film, the step-terrace structure of the substrate should be reproduced without any segregated material on its surface.

2.2.1 Growth of $SrRuO_3$

The growth properties of $SrRuO_3$ depend strongly on the surface termination of the underlying substrate [71]. The diffusion lengths of the species vary strongly between the SrO- and the TiO_2-termination, so that several nm deep holes are created during the growth of $SrRuO_3$ on an only-annealed $SrTiO_3$ substrate. Therefore, the substrates have to be prepared by the etching step discussed in Section 2.1.2.3, which in most cases improves the regularity of the terrace structure.
In addition, the parameter set has to be chosen very carefully, in order to achieve step-flow growth. Thus, the laser frequency has to be adjusted to the step length of the substrate [72]. Besides, the Ru is known to be volatile [73], so that a relatively low deposition temperature is recommended, which narrows the parameter space.
Taking into account these circumstances, the optimized parameter set for $SrRuO_3$ is $p = 0.133\,\text{mbar}$ O_2, $T = 650\,°\text{C}$, $E = 19\,\text{mJ}$, $f = 10\,\text{Hz}$ and $d = 59\,\text{mm}$. The results of a

terminated $SrTiO_3$ are shown in Figure 2.6.

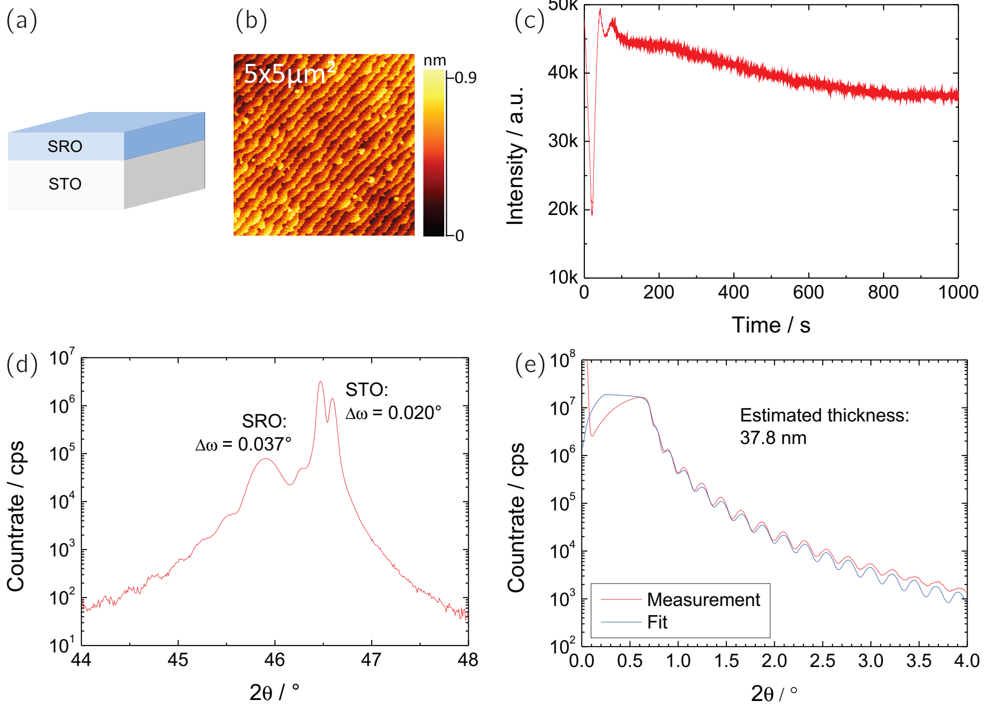

Figure 2.6: Growth of $SrTiO_3$ substrate / 40 nm $SrRuO_3$: (a) Layer stack: STO-SRO. (b) AFM image of the SRO surface, $\rho = 1.6\,\text{Å}$. (c) RHEED signal for SRO, growing in step-flow mode. The dip is the result of a termination change. (d) XRD spectrum around the STO (002) reflex of the complete stack. (e) XRR spectrum at gracing incidence. With the help of a simulation, a film thickness of 37.8 nm was determined.

As visible from the RHEED intensity evolution in Figure 2.6(c), the $SrRuO_3$ grows in almost perfect step-flow growth mode. After a very deep dip in the RHEED signal intensity, which covers the first one and a half ucl and can be ascribed to an internal termination alternation [74], the intensity reaches the initial value again and stays more or less constant at this magnitude. This behavior is typical for the step-flow growth mode, indicating that all adhered species move upon the surface, until they reach a step edge. The surface of the 40 nm thick $SrRuO_3$ film in Figure 2.6(b) shows nicely the step-terrace structure of the substrate with a roughness of $\rho = 1.6\,\text{Å}$. The straightness of the step edges has vanished as a result of the not completely perfect step-flow growth. The XRD spectrum around the

STO (002) reflex in Figure 2.6(d) shows a nicely developed $SrRuO_3$ peak beside the intense $SrTiO_3$ substrate split peak. Due to the relatively small mismatch of +0.56 %, the rocking curves are with a width well below 0.04° very sharp, indicating a good crystal quality. In the XRR-measurement in Figure 2.6(e) thickness fringes are visible beside the direct beam near the 0-position. The data set was simulated and a film thickness of ≈ 38 nm was determined from the periodicity of the oscillations.

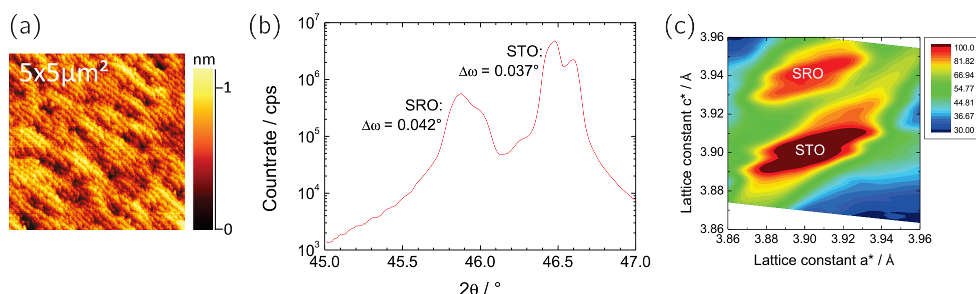

Figure 2.7: Growth of $SrTiO_3$ substrate / 100 nm $SrRuO_3$: (a) AFM image of the SRO surface, $\rho = 2.1$ Å. (b) XRD spectrum around the STO (002) reflex of the complete stack. (c) RSM around the STO (103) reflex.

In addition, a 100 nm thick $SrRuO_3$ film is grown on terminated $SrTiO_3$ and the results of the characterization are depicted in Figure 2.7. On the surface in Figure 2.7(a) the step-terrace structure is still reproduced and in the XRD spectrum (Figure 2.7(b)) the $K_{\alpha_{1/2}}$-splitting is observable even for the $SrRuO_3$ Bragg reflex. Besides, an RSM was measured around the STO (103) reflex and is depicted in Figure 2.7(c). The additional in-plane lattice parameter information shows, that even the 100 nm thick $SrRuO_3$ film is grown completely strained on top of $SrTiO_3$, as the a^* values of both reflexes match perfectly.

2.2.2 Growth of $BaTiO_3$ heterostructures

2.2.2.1 Growth of $BaTiO_3$

For the growth of $BaTiO_3$ on $SrTiO_3$ substrate, it is a complex task to find good deposition conditions, since the lattice mismatch of +2.62 % [50] is very large and results in compressive strain. For further electrical measurements, as will be presented in Chapter 3, the deposition process was optimized for 30 nm thin film grown on $SrRuO_3$/$SrTiO_3$. $SrRuO_3$ acts as BE and its deposition process is described in Section 2.2.1.

Many different parameter series were tested to find a parameter set, with which $BaTiO_3$ could be grown as nicely as $SrRuO_3$ or different manganites, which will be shown in Section 2.2.3. But for $BaTiO_3$ growth, hardly a few RHEED oscillations were visible, because the thin film starts to relax at a very small thickness. Additionally, this behavior can result in rough surfaces and bad crystal qualities.
Still, some $BaTiO_3$ thin films could be grown, which have nice properties. Here, three representative thin films are presented in Figure 2.8, which show at least one outstanding property.

The parameter set $p = 0.001$ mbar O_2, $T = 600$ °C, $E = 25$ mJ, $f = 5$ Hz and $d = 57$ mm (Figure 2.8(a)-2.8(c)) lead to pronounced RHEED oscillations, while step bunching occurs at the surface and the rocking curve of the $BaTiO_3$ reflex is extremely broad.
The conditions $p = 0.001$ mbar O_2, $T = 600$ °C, $E = 19$ mJ, $f = 5$ Hz and $d = 57$ mm (Figure 2.8(d)-2.8(f)) produced a very nice surface, but the XRD peak is not clearly visible. For this deposition the burst mode of the laser was used, implying that the calculated number of pulses for one ucl is applied within one burst of 5 Hz, with a relaxation time of 10 s in-between.
For the deposition of a sample with very good structural properties (Figure 2.8(g)-2.8(i)), the set $p = 0.001$ mbar O_2, $T = 600$ °C, $E = 27$ mJ, $f = 5$ Hz and $d = 57$ mm was used. This deposition resulted in a very rough and grainy surface.
The parameter sets do not vary much, but it has to be taken into account, that the laser optics had to be adjusted frequently and the resulting fluences are not linearly comparable to the energy values.

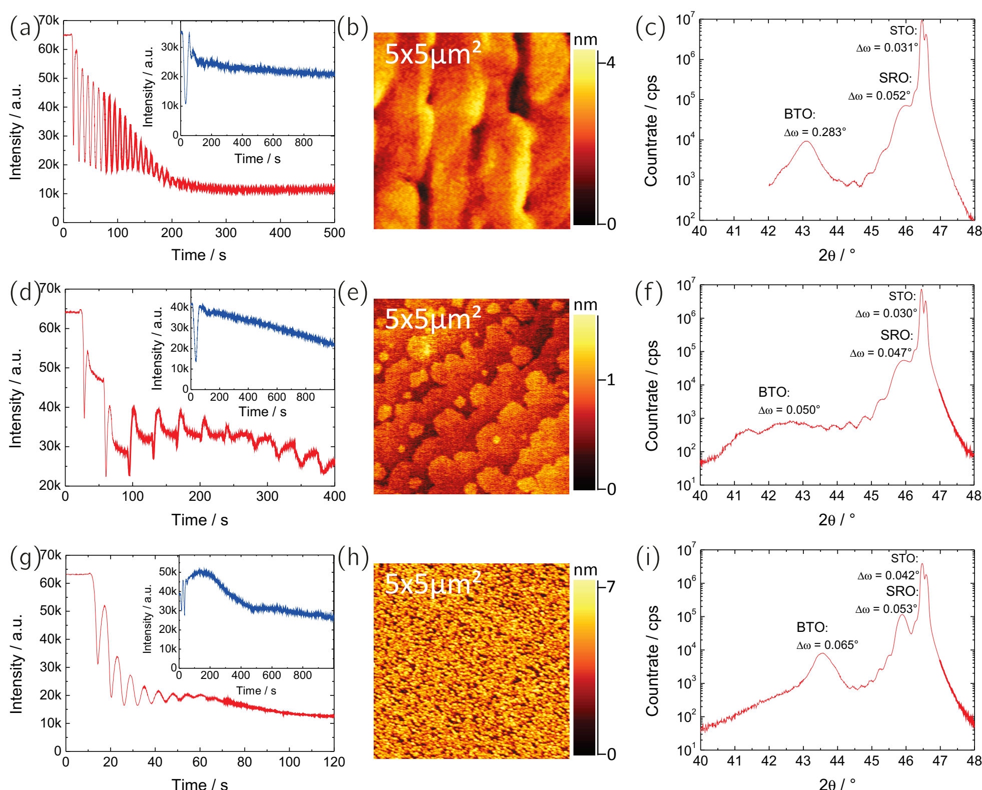

Figure 2.8: Growth of $SrTiO_3$ substrate / 30 nm $SrRuO_3$ / 30 nm $BaTiO_3$. RHEED intensity of $BaTiO_3$ (red curve) and $SrRuO_3$ (inset, blue curve), AFM image and XRD data are depicted: (a-c) $BaTiO_3$ sample with nice growth process: While many RHEED oscillations are visible, the surface shows step bunching ($\rho = 5.6$ Å) and the rocking curve of the XRD reflex for $BaTiO_3$ is very broad. (d-f) $BaTiO_3$ sample with nice topography: While the surface is atomically flat ($\rho = 2.0$ Å) and the RHEED signal from burst mode looks acceptable, there is no real XRD reflex visible. (g-i) $BaTiO_3$ sample with nice structural properties: While the Bragg reflex is nicely developed, its rocking curve is very sharp and the RHEED oscillations are acceptable, the surface morphology shows many grains with a roughness of $\rho = 12.9$ Å.

Using a parameter set, which seemed really promising, an energy series was performed, for which the other parameters were kept constant at $p = 0.01$ mbar O_2, $T = 600$ °C, $f = 5$ Hz and $d = 57$ mm. The whole series is shown in Figure 2.9 with a variation of energy between 22-42 mJ at an interval of 5 mJ.

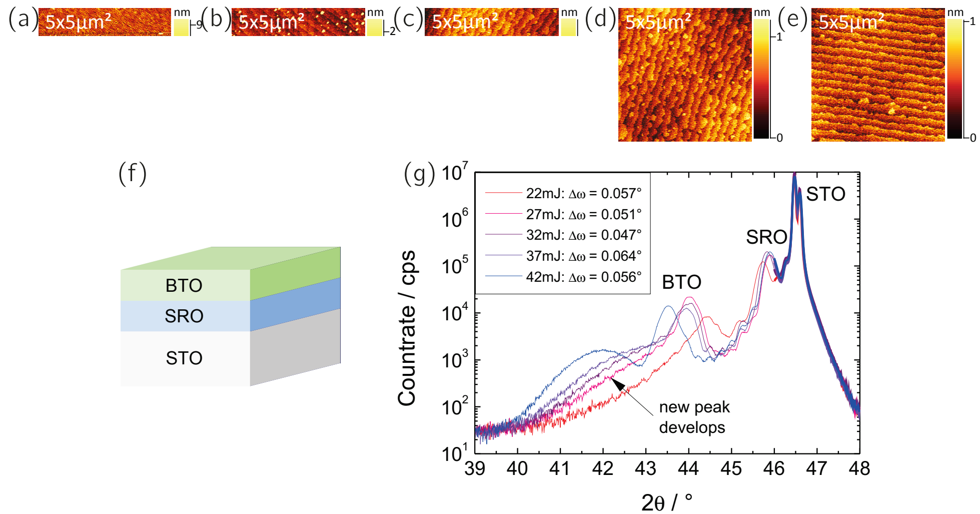

Figure 2.9: Growth of $SrTiO_3$ substrate / 30 nm $SrRuO_3$ / 30 nm $BaTiO_3$ during laser energy variation between 22-42 mJ: (a) AFM image of the BTO surface grown at $E = 22$ mJ, $\rho = 16.2$ Å. (b) AFM image of the BTO surface grown at $E = 27$ mJ, $\rho = 6.2$ Å. (c) AFM image of the BTO surface grown at $E = 32$ mJ, $\rho = 2.0$ Å. (d) AFM image of the BTO surface grown at $E = 37$ mJ, $\rho = 2.1$ Å. (e) AFM image of the BTO surface grown at $E = 42$ mJ, $\rho = 1.8$ Å. (f) Layer stack: STO-SRO-BTO. (g) XRD spectra around the STO (002) reflex of the complete stack. The $BaTiO_3$-reflex is successively shifted towards larger c-axes, while an additional peak at very small 2θ-angles develops.

Starting with the surface properties of the energy series $BaTiO_3$ thin films, a clear trend from a very rough topography (Figure 2.9(a)) towards an atomically flat surface (2.9(e)) is visible for increasing laser energy E. For the Bragg peak (Figure 2.9(g)) also a systematic change is visible, as the c-lattice constant for $BaTiO_3$ is shifted from 4.076 Å to 4.156 Å upon energy increase, what indicates the incorporation of cation vacancies to the lattice. In addition, already at 27 mJ a shoulder starts to develop at around 42°, which then finally forms an individual second peak at 42 mJ. This peak splitting could be a result of strain relaxation discussed in Section 2.1.1 [75, 76], but is unwanted. A bilayered structure of $BaTiO_3$ would not have one set of ferroelectric properties and be thus not useful for integration in functional stacks. In addition, an enlarged unit cell due to vacancy formation leads to a better conductance in titanates, which is very unfavorable for ferroelectric switching, as it will be discussed in Chapter 3. Considering the formation of cation vacancies in $SrTiO_3$ [63], the case could be similar for $BaTiO_3$. For low fluences the material is grown Sr-rich,

resulting in segregation or Ruddlesden-Popper phases, which will lead to 3D-growth. For higher fluencies, the stoichiometric point will be reached, and beyond Sr-vacancies might be formed, which flare the out-of-plane axis. Local inhomogeneities in the Sr-content could be a reason for the development of the second peak. The results of the energy series are summed up in Table 2.2.

Energy E	22 mJ	27 mJ	32 mJ	37 mJ	42 mJ
AFM: ρ	16.2 Å	6.2 Å	2.0 Å	2.1 Å	1.8 Å
c	4.076 Å	4.112 Å	4.114 Å	4.119 Å	4.156 Å
$\Delta\omega$	0.057°	0.051°	0.047°	0.064°	0.056°
2nd c	-	$\sim$ 4.20 Å	$\sim$ 4.22 Å	$\sim$ 4.25 Å	4.31 Å

Table 2.2: Energy series of $BaTiO_3$ growth.

In conclusion, while the surface becomes smoother with increasing laser energy, the strain within the material becomes larger, resulting in a relaxation of the thin film at lower film thickness. The trend already seen in Figure 2.8 is always recurring: If one property is improved, another one is deteriorated. For small laser energies a very rough surface is obtained and for large laser energies a double peak in the XRD spectrum occurs. The intermediate value of $E = 32$ mJ is a good compromise as optimized growth condition set. A more detailed characterization of this $BaTiO_3$ thin film is depicted in Figure 2.10.

A TiO_2-terminated $SrTiO_3$ substrate (Figure 2.10(b)) is used for the deposition of $SrRuO_3/BaTiO_3$ and 30 nm $SrRuO_3$ and $BaTiO_3$ are grown in-situ by PLD. $SrRuO_3$ grows nicely in step-flow growth mode (inset of Figure 2.10(d)) and $BaTiO_3$ in layer-by-layer growth mode for approximately 10 ucl, as depicted in Figure 2.10(d). The surface of $BaTiO_3$ is atomically smooth with a roughness of $\rho = 2.0$ Å (Figure 2.10(c)) and the meander structure can be explained by the step-flow growth of $SrRuO_3$. In the XRD spectrum in Figure 2.10(e) three well defined Bragg reflexes can be identified, for which all rocking curves are sharp with a FWHM of below 0.05°.

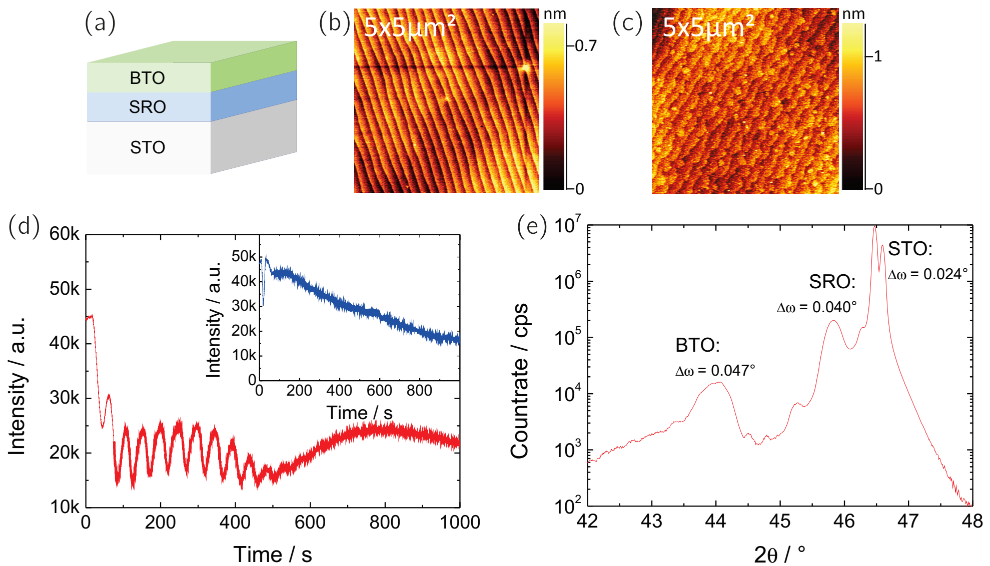

Figure 2.10: Growth of $SrTiO_3$ substrate / 30 nm $SrRuO_3$ / 30 nm $BaTiO_3$: (a) Layer stack: STO-SRO-BTO. (b) AFM image of the terminated STO substrate surface, $\rho = 1.8$ Å. (c) AFM image of the BTO surface, $\rho = 2.0$ Å. (d) RHEED signal for SRO (inset, blue) and BTO (red), growing in step-flow mode and layer-by-layer mode, respectively. (e) XRD spectrum around the STO (002) reflex of the complete stack.

2.2.2.2 Interface engineering of $BaTiO_3/SrRuO_3$ heterostructures

For the epitaxial growth of perovskites, a uniformly terminated surface is important for most materials. In particular for ferroelectrics, the screening at the interface and thereby the polarization could be influenced. Thus the identification of interface termination and possible approaches to modify it were investigated for $SrTiO_3$, $BaTiO_3$ and $SrRuO_3$.

For stacks on $SrTiO_3$ it is important to first consider the naturally formed interface structure. Different sample stacks were analyzed by scanning transmission electron microscopy (STEM) by Daesung Park at the GFE [77], RWTH Aachen. For this purpose, an electron transparent lamella was prepared out of the sample stack, which was previously covered by amorphous $SrTiO_3$ (α-STO) and Au, by focused ion beam (FIB) sectioning. The images shown here were recorded by the high-angle annular dark field (HAADF) detector in STEM mode, where the intensity is roughly proportional to the square of the atomic number Z^2 and therefore also called "Z-contrast image".
Going back to the growth of $SrRuO_3$ on $SrTiO_3$ (Section 2.2.3.1), we know from [71], that a single TiO_2-termination of $SrTiO_3$ is necessary for a homogenous growth process. In addition, as the underlying $SrTiO_3$ substrate is deliberately TiO_2-terminated, the $SrRuO_3$ layer has an SrO-termination at the atomically-sharp bottom interface. Regarding $BaTiO_3$, the same arguments explains the BaO-termination at the bottom interface for the growth on terminated $SrTiO_3$.
During the growth of $BaTiO_3$ a mixed termination of mainly TiO_2 is formed at the surface. The growth properties of $SrRuO_3$ on top of $BaTiO_3$ depend crucially on its termination, since the nucleation rates for $SrRuO_3$ differ strongly according to the local termination of $BaTiO_3$, so that for extreme cases neither step-flow nor layer-by-layer growth is possible. This can result in a very rough layer with locally strongly disordered crystallinity, as shown for a 30 nm thick film grown on non-terminated $Pr_{0.48}Ca_{0.52}MnO_3$ (Figure 2.11).

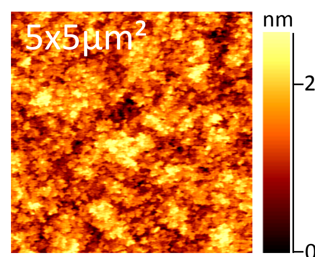

Figure 2.11: AFM image of the $SrRuO_3$ surface, grown on PCMO/SRO/STO, $\rho = 4.3\,\text{Å}$.

Using an additional annealing step prior to the $SrRuO_3$ growth, a larger part of TiO_2-terminated surface regions were achieved at the upper interface of $BaTiO_3$, proved by STEM and depicted in Figure 2.12. Although this enhanced the crystal quality of $SrRuO_3$, a reliable uniform termination for the whole interface was still not possible using this method.

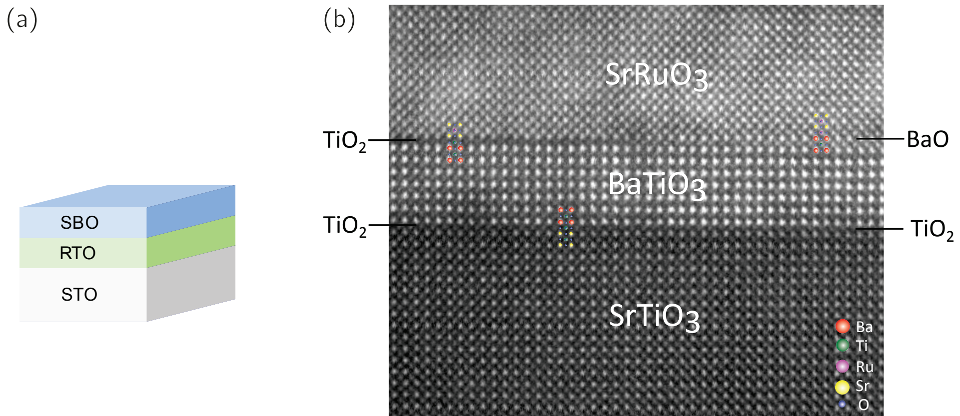

Figure 2.12: Cross-sectional STEM image of stack $SrTiO_3$ substrate / 7 ucl $BaTiO_3$ / 15 ucl $SrRuO_3$: (a) Layer stack: STO-BTO-SRO. (b) STEM image of the two $BaTiO_3$ interfaces. The TiO_2-termination of the $SrTiO_3$ substrates leads to a BaO-termination of the bottom interface, while the top interface is TiO_2/BaO-mixed terminated. Its main part is TiO_2-terminated as a result of an additional annealing step. For the deposition of this stack the normal parameter set for $SrRuO_3$ was used, while for the growth of $BaTiO_3$ $p = 0.05$ mbar O_2, $T = 800\,°C$, $E = 42$ mJ, $f = 1$ Hz and $d = 57$ mm was applied.

An approach to artificially modify the process-related TiO_2-termination of the top interface of $BaTiO_3$ actively, is to add a layer of $BaRuO_3$ with the thickness of one ucl at the $BaTiO_3/SrRuO_3$ interface. As depicted in Figure 2.13(b), $BaRuO_3$ has the A-site cation of the underlying $BaTiO_3$ and the B-site cation of the stacked $SrRuO_3$. $BaRuO_3$ would then have a BaO-termination at bottom interface due to the TiO_2-termination of $SrTiO_3$ analog to $SrRuO_3$ and $BaTiO_3$. As only one ucl is grown, the top interface will be RuO_2-terminated and thus the next atomic layer of $SrRuO_3$ will be SrO. But it is not possible to distinguish, whether the BaO-layer at the bottom interface belongs to $BaRuO_3$ or to $BaTiO_3$, as well as it is not possible to assign the top RuO_2 of $BaRuO_3$ to $BaRuO_3$ or to $SrRuO_3$. Therefore the result would be a termination change of the upper interface of $BaTiO_3$ towards BaO.

The results of this approach are shown in Figure 2.13. The BHF-etched $SrTiO_3$ substrate (Figure 2.13(c)) has a nice step-terrace structure, but at some step edges small bumps in a jagged pattern are visible, which are due to a not perfectly finished termination. These straight lines are reproduced in the $SrRuO_3$ surface in Figure 2.13(d) as line-like holes, because the whole layer stack could not be grown properly on top of these regions. Beside these $SrTiO_3$-dependent features, the surface is atomically flat with the typical step-flow

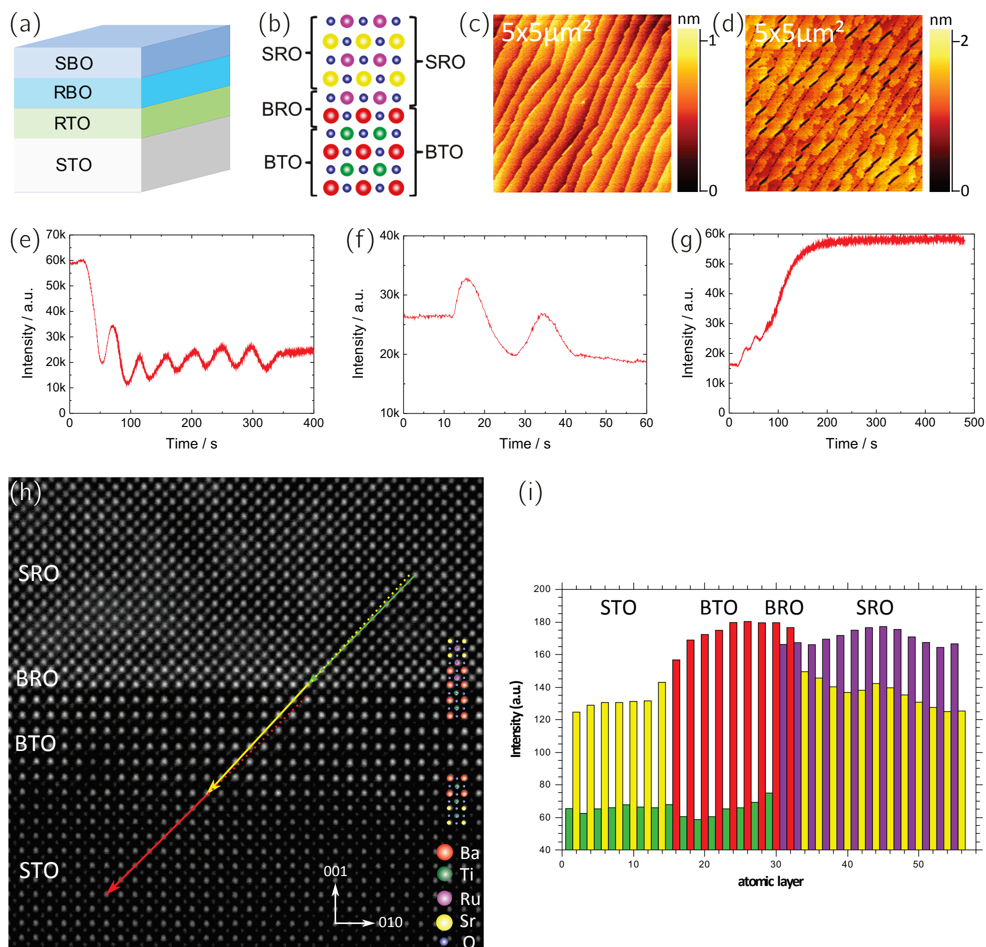

Figure 2.13: Cross-sectional STEM image of stack with $BaRuO_3$ incorporation: (a) Layer stack: STO-BTO-BRO-SRO. (b) Schematic sketch of the impact of the one ucl $BaRuO_3$ interface-layer. (c) AFM picture of the $SrTiO_3$ substrate surface, $\rho = 1.6\,\text{Å}$. (d) AFM picture of the $SrRuO_3$ surface, $\rho = 5.1\,\text{Å}$. (e) 7 RHEED oscillations = 3 nm of $BaTiO_3$, growing in layer-by-layer mode. (f) 1.5 RHEED oscillations of $BaRuO_3$, growing in layer-by-layer mode. (g) RHEED intensity of $SrRuO_3$, growing in step-flow mode. (h) Drift-corrected HAADF (STEM) image of the cross-section of the layer stack. All three interfaces are atomically sharp. In addition, the tetragonal deformation of the $BaTiO_3$ unit cells are visible, depicted by the yellow arrow joining the diagonal arranged Ba-ions. (i) Intensity profile of a vertical line-scan through the layer stack. The red arrows indicate the Ba rows, while the green ring displays the 1.5 ucl of $BaRuO_3$.

caused surface of $SrRuO_3$ growth. Figure 2.13(e) shows 7 RHEED oscillations of the $BaTiO_3$ deposition using $p = 0.001$ mbar O_2, $T = 600$ °C, $E = 19$ mJ, $f = 1$ Hz and $d = 57$ mm. For the growth of $BaRuO_3$ the $SrRuO_3$-growth conditions were used, but the temperature was set to $T = 600$ °C as for $BaTiO_3$. It was challenging to stop the laser after the right number of pulses necessary for one ucl, because in comparison to regular layer-by-layer growth the intensity of the specular spot was increased first (Figure 2.13(f)). The reason might be a not totally completed last ucl of $BaTiO_3$. As a result, not one ucl, but about 1.5 ucl of $BaRuO_3$ were grown. $SrRuO_3$ then grew - beside the holes - nicely in step-flow growth mode, as well as $BaTiO_3$ at $T = 600$ °C, as visible in Figure 2.13(g).

The cross-sectional HAADF image of the stack in Figure 2.13(h) visualizes the results more tangible. Depicted is the perfectly drift-corrected HAADF image, showing the "Z-contrast" according to Ba (Z=56, red) appearing brightest, over Ru (Z=44, purple) and Sr (Z=38, yellow) to Ti (Z=22, green) and finally O (Z=8, blue) almost not visible. In addition, the HAADF intensity profile of a vertical line-scan from the bottom (STO) to the top (SRO) is depicted for a more quantitative view on the results (Figure 2.13(i)). A peak finding algorithm in combination with Gaussian fitting was used to determine the position and intensity of the ions. For the interface between $SrTiO_3$ and $BaTiO_3$, a slight intermixing on Ba/Sr site is observed. At the upper interface, a BaO-terminated $BaTiO_3$ thin film is visible, to which a complete ucl of $BaRuO_3$ is added, before the $SrRuO_3$ layer starts. This sample shows, that in principle the BaO-termination change of $BaTiO_3$ is possible with this approach, but the thickness of $BaRuO_3$ has to be adjusted more precisely to exact one ucl. Furthermore, the $BaRuO_3$ interface-layer compensates any intermixing at the interface and results in a very sharp interface, which is uniformly BaO-terminated over the whole sample.

In addition to the termination change of $BaTiO_3$, also the lattice constants could be determined by STEM in Figure 2.13(h), using the peak finding algorithm. Averaged over five unit cells respectively, the lattice constants could be determined. The results are listed in Figure 2.3. For perfectly cubic $SrTiO_3$, the Sr cations are connected with a diagonal red arrow. The procedure is repeated for $BaTiO_3$ (yellow arrow, Ba) and $SrRuO_3$ (green arrow, Sr). The small angles between the arrows indicate the tetragonal lattice distortion of the originally cubic $BaTiO_3$ unit cell, which are quantified in Figure 2.3.

The close-up of the STEM image in Figure 2.14 shows a detail to visualize the tetragonal distortion of $BaTiO_3$. Additionally, the displacement of the Ti cation is depicted. This displacement, causing the ferroelectric polarization, is measured with the peak finding algorithm and depicted in Figure 2.15(a) for a linescan through the whole stack. No

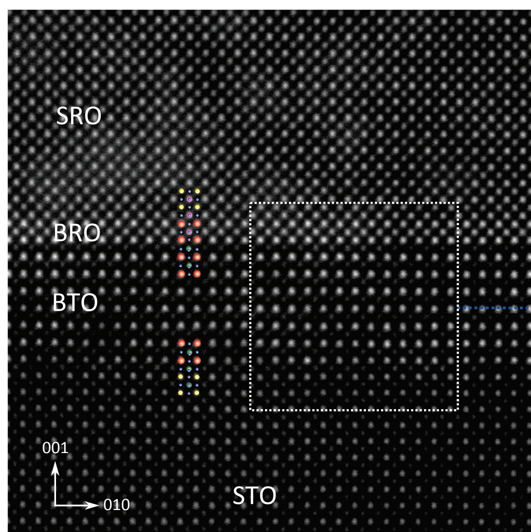

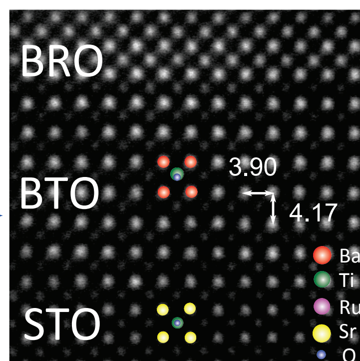

Figure 2.14: Detail of Figure 2.13(h).

significant displacement is visible for Ti in $SrTiO_3$ and Ru in $SrRuO_3$, but the Ti in $BaTiO_3$ is displaced from its central position by almost 0.3 Å, proving the ferroelectricity of the $BaTiO_3$ thin film.

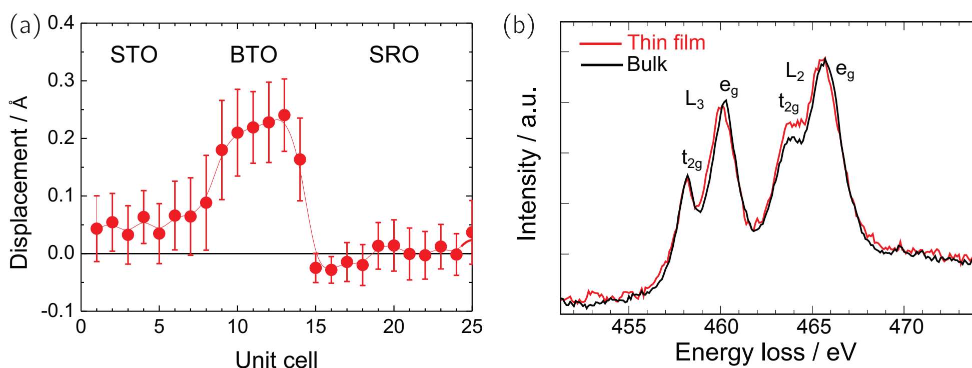

Figure 2.15: Indications for a tetragonal distortion in $BaTiO_3$: (a) Measured displacement for the B-site cations. In $BaTiO_3$ the Ti is displaced from its central position by almost 0.3 Å. (b) EELS spectra for the BTO thin film and a bulk reference.

Electron energy loss spectroscopy (EELS) was performed on the ultra-thin film using the StripeSTEM technique. In the Ti L_{23} spectrum in Figure 2.15(b) the crystal field splitting is slightly reduced compared to the BTO bulk reference. This observation corresponds to an additional reduction of symmetry from the already tetragonal structure of BTO, which is caused by the enhancement of the tetragonal distortion by epitaxial strain.

2.2.3 Growth of mixed-valence manganites

2.2.3.1 Growth of $Pr_{0.48}Ca_{0.52}MnO_3$ in various layer stacks

For the deposition of $Pr_{0.48}Ca_{0.52}MnO_3$ (PCMO) the PLD process optimization was performed for the growth on $SrTiO_3$ substrates. The lattice mismatch in the pseudo-cubic picture is about −2.39 % [50] resulting in tensile strain. Starting with a parameter set from literature [22] the adjustable parameters oxygen partial pressure p in the chamber, substrate temperature T, laser energy E (and thus the energy density on the target), laser repetition rate f and target-to-substrate distance d were varied successively and independently. To determine the quality of each grown PCMO film, three different methods were used: The growth mode and quality by the RHEED intensity development, the surface topography measured by AFM and the crystallinity gained by XRD. After identifying the best film from a variation series of one parameter, the next parameter was altered systematically. The optimal parameter set has been proven to be $p = 0.133$ mbar O_2, $T = 700$ °C, $E = 50$ mJ, $f = 5$ Hz and $d = 59$ mm. The characterization results of a 20 nm thick film grown under these conditions are shown in Figure 2.16.

20 nm PCMO was grown on a $SrTiO_3$ substrate (Figure 2.16(d)). The substrate surface is depicted in Figure 2.16(a) and shows a step-terrace structure due to the miscut angle with a natural roughness of $\rho = 1.8$ Å. During the deposition, the RHEED pattern was recorded and the intensity of the specular spot is plotted in Figure 2.16(c). The more than 50 pronounced oscillations show, that under the previously mentioned conditions, PCMO is growing mainly in the so-called layer-by-layer growth mode, in which one ucl is finished before the next is started, as described in Section 2.1.2.2. After the deposition, the PCMO-surface is scanned by AFM (Figure 2.16(b)) and the step-terrace structure of the substrate is nicely reproduced in the thin film, which is still atomically flat with a roughness of $\rho = 2.4$ Å. Figure 2.16(e) shows a 2θ-ω-overview scan along the c-axis of the system. Only the STO (001), (002) and (003) reflexes appear with additional PCMO peaks, shifted to slightly higher 2θ-values than the substrate peaks caused by a smaller out-of-plane lattice constant. As there are no peaks visible in-between, the PCMO-film seems to consist of a single phase. Zooming in the STO (002) region (Figure 2.16(f)), the out-of-plain lattice constant of PCMO could be determined to be $c^* = 3.730$ Å, which is about 2.20 % smaller than the bulk value. The rocking curve at the PCMO-peak is very sharp with a width of $\Delta\omega = 0.055$ °.

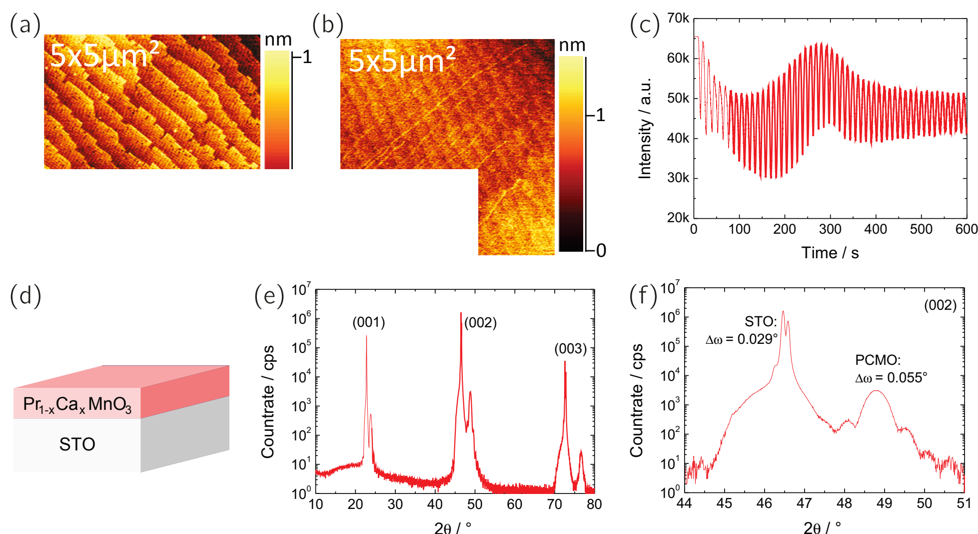

Figure 2.16: Growth of $SrTiO_3$ substrate / 20 nm $Pr_{0.48}Ca_{0.52}MnO_3$: (a) AFM image of the STO substrate surface, $\rho = 1.8$ Å. (b) AFM image of the PCMO surface, $\rho = 2.4$ Å. (c) RHEED oscillations for PCMO, growing in layer-by-layer mode. (d) Layer stack: STO-PCMO. (e) Complete XRD spectrum in Bragg-Brentano geometry. (f) XRD spectrum around the STO (002) reflex.

For electrical measurements, the PCMO active layer has to be deposited on a conducting material, acting as a bottom electrode (BE). Because a *p*-*n* junction forms at the interface to Nb:$SrTiO_3$ in the case of *p*-type half-metallic PCMO, the metallic oxide $SrRuO_3$ (SRO) is used. The results of PCMO growth on 30 nm $SrRuO_3$ are shown in Figure 2.17. For the growth procedure itself, $SrTiO_3$ and Nb:$SrTiO_3$ can be regarded as equal, as the Nb-doping seems to have a neglectable impact on the crystal structure.

Starting with the terminated Nb:$SrTiO_3$ substrate (Figure 2.17(b)), $SrRuO_3$ grows mainly in step-flow growth mode, visible from the inset in Figure 2.17(e). After the deposition of 30 nm $SrRuO_3$ the straightness of the step edges has gone, but the roughness has not changed significantly compared to the substrate (Figure 2.17(c)). The deposition of 20 nm PCMO again proceeds in layer-by-layer mode, as it can be observed from the RHEED oscillations (Figure 2.17(e)). In the AFM picture of the surface (Figure 2.17(d)) the steps are even better visible than for PCMO grown directly on $SrTiO_3$ (Figure 2.16(b)), but the roughness is comparable. From the XRD spectrum (Figure 2.17(f)) one can extract, that $SrRuO_3$ as well as PCMO was grown epitaxially on Nb:$SrTiO_3$. The very sharp peaks in

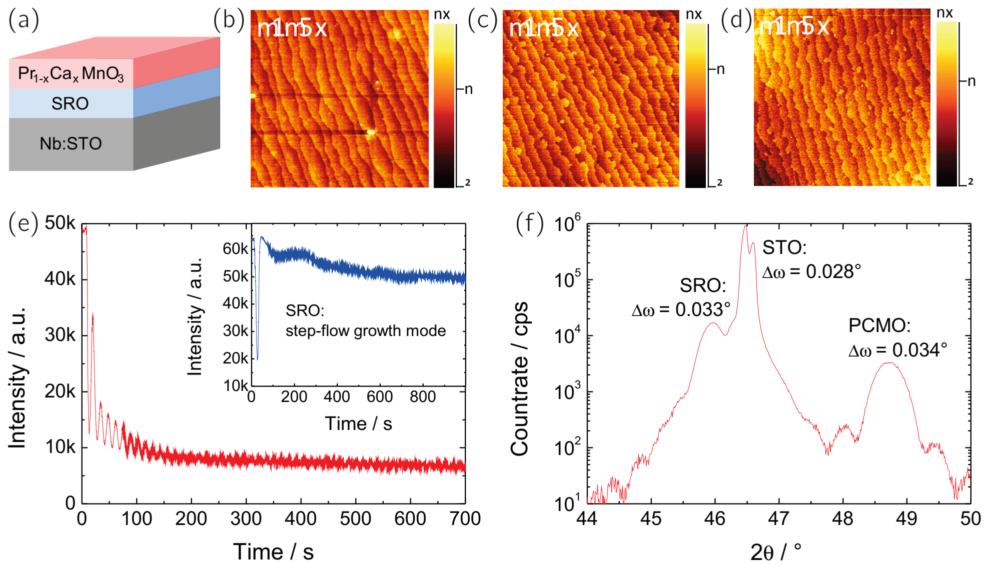

Figure 2.17: Growth of Nb:SrTiO$_3$ substrate / 30 nm SrRuO$_3$ / 20 nm Pr$_{0.48}$Ca$_{0.52}$MnO$_3$: (a) Layer stack: STO-SRO-PCMO. (b) AFM image of the terminated Nb:STO substrate surface, $\rho = 2.4$ Å. (c) AFM image of the SRO surface, $\rho = 1.7$ Å. (d) AFM image of the PCMO surface, $\rho = 2.3$ Å. (e) RHEED intensity for SRO (inset, blue) and PCMO (red), growing in step-flow mode and layer-by-layer mode, respectively. (f) XRD spectrum around the STO (002) reflex of the complete stack.

the rocking curves of less than 0.035° widths indicate very good crystal qualities of both thin films. For the PCMO film on top of SrRuO$_3$, the surface reproduces the substrate structure more pronounced and the crystal quality is even better compared to the PCMO film grown directly on SrTiO$_3$ (Figure 2.16). Thus, PCMO grown on a SrRuO$_3$-buffered SrTiO$_3$ shows a better crystal quality than PCMO grown directly on SrTiO$_3$.

Up to a thickness of 20 nm PCMO grows epitaxially on SrTiO$_3$ without any crystal quality deterioration due to relaxation effects. The situation changes slightly for the growth of a 50 nm thick layer (Figure 2.18). The surface of such a thin film is depicted in Figure 2.18(d) and still shows a reproduced step-structure of the substrate, but it becomes a bit blurred. In addition, the Bragg peak is well pronounced, but the rocking curve is relatively broad with a value of $\Delta\omega = 0.143°$ (Figure 2.18(h), red curve). A detailed investigation of the influence of film thickness will be discussed in Section 4.1.3.

To further improve the growth quality of thicker PCMO films, substrates with a smaller lattice mismatch to PCMO are used. $NdGaO_3$ and LSAT, which both form a pseudo-cubic mismatch of around −1.36 % [50], are used (Figure 2.18). $NdGaO_3$ has the big advantage, that the single crystal substrates in general have a better quality than $SrTiO_3$. LSAT is used, because … a wide oxygen … tion 4.2.4). But … cedure does not

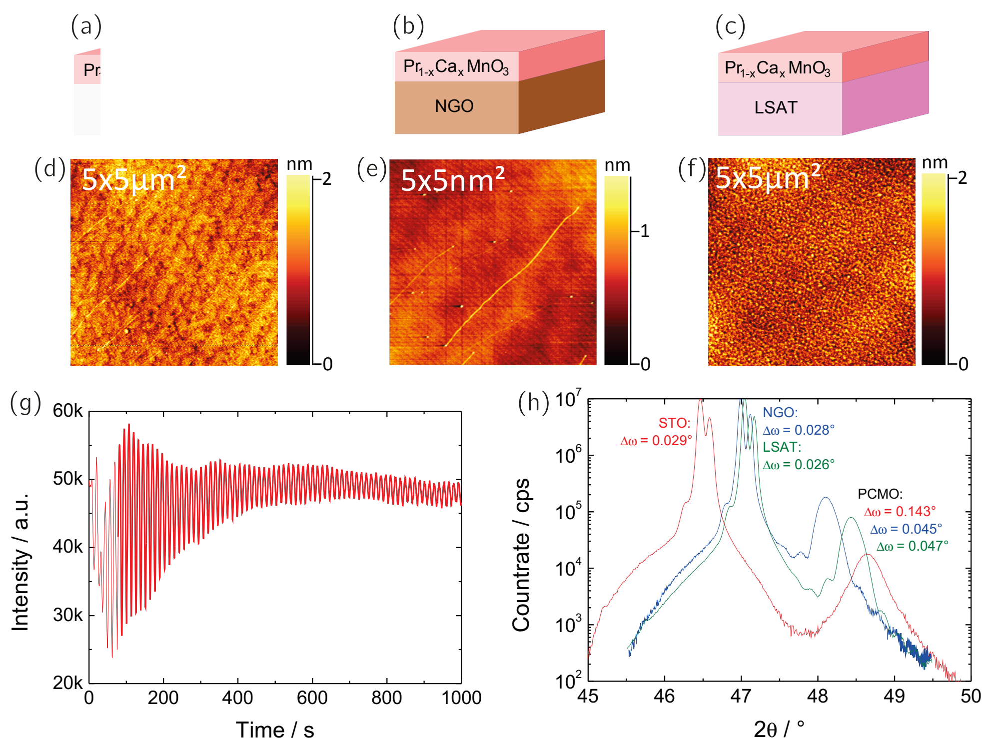

Figure 2.18: Growth of 50 nm $Pr_{0.48}Ca_{0.52}MnO_3$ on $SrTiO_3$, $NdGaO_3$ and LSAT: (a) Layer stack: STO-PCMO. (b) Layer stack: NGO-PCMO. (c) Layer stack: LSAT-PCMO. (d) AFM image of the PCMO surface on STO, $\rho = 2.8$ Å. (e) AFM image of the PCMO surface on NGO, $\rho = 2.5$ Å. (f) AFM image of the PCMO surface on LSAT, $\rho = 3.3$ Å. (g) RHEED oscillations of PCMO on NGO growth. (h) XRD spectra for 50 nm $Pr_{0.7}Ca_{0.3}MnO_3$ on different substrates: $SrTiO_3$, $NdGaO_3$ and LSAT (red, blue and green curve, respectively).

For the growth of 50 nm PCMO on $NdGaO_3$, the surface topography (Figure 2.18(e)) shows well established steps and the rocking curve is quite sharp (Figure 2.18(h), blue curve), both similar to the growth of 20 nm on $SrTiO_3$ (Figure 2.16). The RHEED oscillations from this deposition are presented in Figure 2.18(g) and show distinct layer-by-layer growth during the whole deposition process.
After the growth on LSAT, the surface of PCMO still shows a step structure (Figure 2.18(f)), but it is superimposed by an island structure on the terraces. In the XRD spectrum in Figure 2.18(h) the PCMO reflex lies in-between the ones for growth on $SrTiO_3$ and $NdGaO_3$. Due to the similar lattice mismatch to $NdGaO_3$, the PCMO should also be localized at a similar position, but in this case, the material appears to be not completely strained. The reason might be, that the surface quality of LSAT is not as optimal as for $NdGaO_3$ or $SrTiO_3$. In addition, it has been shown in [78], that the surface roughness can have an effect on strain relaxation for $SrTiO_3$ grown on $NdGaO_3$, which could also be the case for the $Pr_{0.48}Ca_{0.52}MnO_3$ growth on the relatively rough LSAT substrate. Still, the rocking curve is similar to the one for growth on $NdGaO_3$.

2.2.3.2 Chemical analysis of $Pr_{0.48}Ca_{0.52}MnO_3$

X-ray photoelectron spectroscopy (XPS) was performed on an as-deposited 50 nm thick PCMO sample. Due to the small mean free path of the electrons it is a surface-sensitive technique, for which a larger detector angle reduces the mean free path further and thus enhances the surface sensitivity. The X-ray beam was generated with an Al-K_α tube, having an excitation energy of $h\nu = 1486.6$ eV, and was vertically directed onto the sample, while the photoelectron detector was located under an angle of 45° with respect to the sample surface. A conducting Nb:$SrTiO_3$ substrate was used and connected to ground to avoid charging effects. The spectra were aligned to the C 1s peak at 284.8 eV. For the survey scan, shown in Figure 2.19(a), the relevant core level peaks from elemental components of PCMO are labeled, while the other appearing peaks can be assigned to satellites and Auger peaks, so that large impurity contents can be excluded.

The spectra around O 1s, Ca 2p, Mn 2p and Pr 4d were scanned more precisely. In addition, the sample was tilted by $-10°$ and $+30°$ to obtain different surface sensitivities according to the detector angles 35°, 45° and 75°. For the O 1s and the Ca 2p spectra significant changes upon the sample tilting were observed (Figure 2.19(b) and 2.19(c)), while the normalized spectra did not alter for Mn 2p and Pr 4d (not shown).

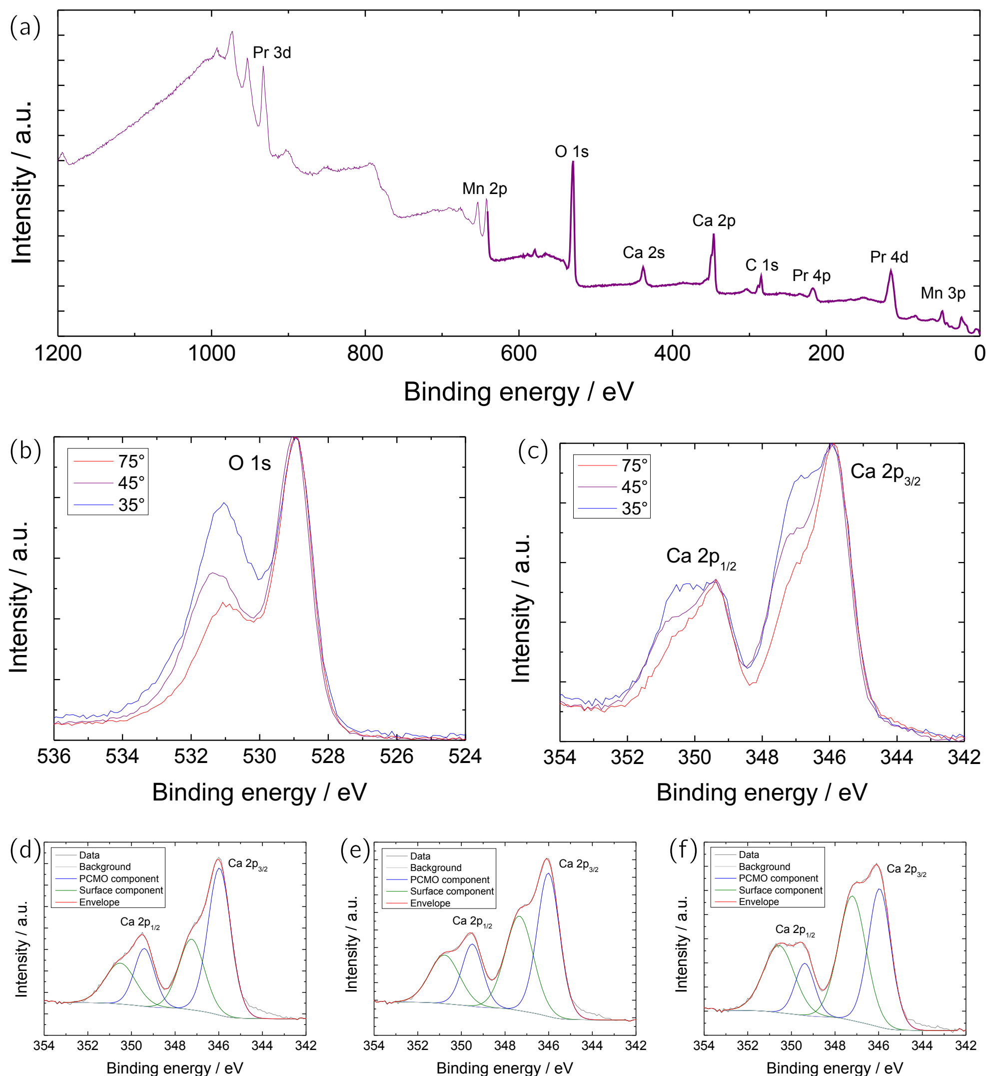

Figure 2.19: XPS measurements on PCMO: (a) Survey scan for the pristine PCMO sample with stack Nb:$SrTiO_3$ / 50 nm PCMO. (b) Normalized O 1s core level. (c) Normalized Ca 2p core level with raw data fits for (d) 75 °, (e) 45 ° and (f) 35 °. The higher energetic component increased with surface sensitivity and could be explained by a CaO surface compound.

The stoichiometry of the thin film was determined by using the integrated intensities of these peaks for a detector angle of 75° to achieve maximal bulk sensitivity. As no PCMO single crystal is available as reliable reference, the nominal atomic percentages are used and the relative error on the data has to be accounted with 10 %. The atomic percentages were determined to Pr 10.9 % (9.6 %), Ca 11.3 % (10.4 %), Mn 11.8 % (20 %) and O 66.0 % (60 %), where the values in brackets denote the nominal percentages. The value for oxygen is much higher than the nominal value, which can be explained by surface contamination due to adsorbates. For a ceramic sample this O-enrichment was removed after sputtering of the surface. The Ca/Pr ratio is nicely reproduced with a value of 1.04 (1.08). Only the Mn content is much lower than expected. With 11.8 % it is only slightly higher than for Pr and Ca, but should nominally be double the value. Here, a possible explanation would be a large Mn gradient within the film, as the content decreases with decreasing detector angle to 11.0 % for 45° and 9.2 % for 35°. In addition, the background subtraction is not unambiguous. Another reason could be a not perfectly stoichiometric transfer from the target to the thin film during the deposition or even a Mn lack already within the target material.

Having a closer look at the changes upon detector angle variation, the O 1s spectra in Figure 2.19(b) show a second peak at higher binding energies, which becomes more intense for smaller angles and thus higher surface sensitivity. For the Ca 2p doublet a second doublet develops analogously at higher binding energies. A part of the additional O 1s peak can be referred to the adsorbates on the surface. But in combination with the Ca 2p doublet, a CaO compound seems to be formed at the surface [79]. In Figure 2.19(d)-2.19(f) the Ca 2p doublet is fitted for decreasing detector angle using two components. The percentage of the integrated intensity of the surface component is increased from 40 % to 60 % upon increased surface sensitivity. But not only a pure weight transfer is observed, but also the Ca percentage is increased from 11.3 % for 75° over 12.3 % to 12.5 % for 35°. A similar CaO surface layer is reported in literature [80].
In conclusion, immediately after the deposition the PCMO thin films show an enrichment of Ca at the surface, which is mainly oxidized.

2.2.3.3 Growth of different manganite stoichiometries

Using the deposition parameter set for $Pr_{0.48}Ca_{0.52}MnO_3$ determined in Section 2.2.3.1, three additional stoichiometries of $Pr_{1-x}Ca_xMnO_3$ were grown with a thickness of 50 nm: 30 %, 40 % and 70 % Ca-doping. As well, $La_{0.7}Sr_{0.3}MnO_3$ was grown, for which the parameter set, confirmed in [81], was used.

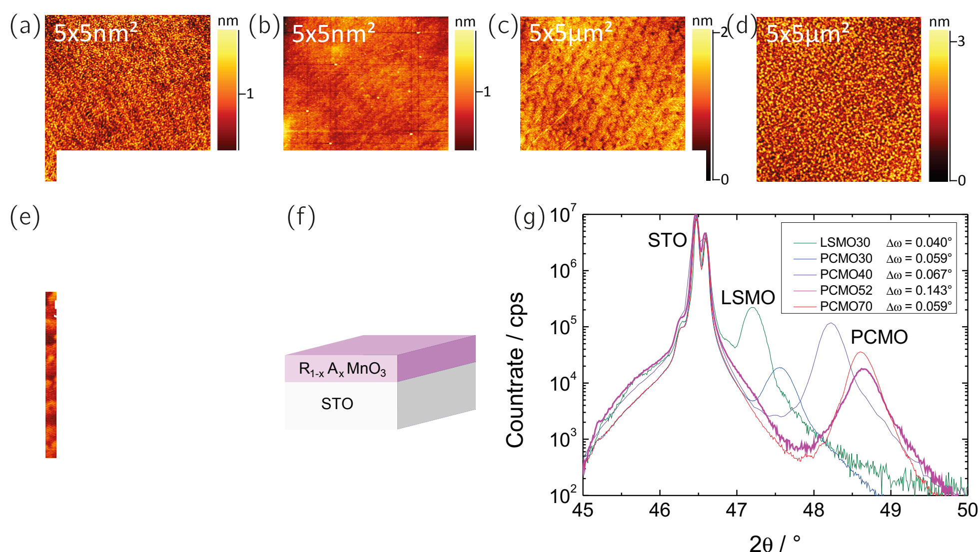

Figure 2.20: Growth of 50 nm manganite on $SrTiO_3$: Four different stoichiometries of $Pr_{1-x}Ca_xMnO_3$ (30%, 40%, 52% and 70%) (a-d) and $La_{0.7}Sr_{0.3}MnO_3$ (e): (a) AFM image of the $Pr_{0.7}Ca_{0.3}MnO_3$ surface, $\rho = 2.8$ Å. (b) AFM image of the $Pr_{0.6}Ca_{0.4}MnO_3$ surface, $\rho = 2.5$ Å. (c) AFM image of the $Pr_{0.48}Ca_{0.52}MnO_3$ surface, $\rho = 2.8$ Å. (d) AFM image of the $Pr_{0.3}Ca_{0.7}MnO_3$ surface, $\rho = 6.0$ Å. (e) AFM image of the $La_{0.7}Sr_{0.3}MnO_3$ surface, $\rho = 1.4$ Å. (f) Layer stack: $R_{1-x}A_xMnO_3$ on $SrTiO_3$. (g) XRD spectra around the STO (002) reflex for five different manganites. The manganite film peak is shifted due to the mismatch with the STO substrate.

Figure 2.20 shows the stoichiometry series of $Pr_{1-x}Ca_xMnO_3$. For the stoichiometries $Pr_{0.7}Ca_{0.3}MnO_3$, $Pr_{0.6}Ca_{0.4}MnO_3$ and $Pr_{0.48}Ca_{0.52}MnO_3$ the step terrace structure of the substrate is reproduced (Figure 2.20(a), 2.20(b) and 2.20(c)). For $Pr_{0.3}Ca_{0.7}MnO_3$ the film is too rough for the steps to be visible (Figure 2.20(d)). After the deposition of 50 nm $La_{0.7}Sr_{0.3}MnO_3$, the surface is still atomically flat as shown in Figure 2.20(e). In the XRD spectra for all five samples (Figure 2.20(g)) the manganite reflex shifts away from

the $SrTiO_3$ peak with increasing Ca-concentration and thus smaller lattice constant. A complete overview about the film properties is given in Table 2.4.

Material	Mismatch to $SrTiO_3$ [50]	AFM: ρ	XRD: c^*	XRD: $\Delta\omega$
$La_{0.7}Sr_{0.3}MnO_3$	−0.59 %	1.4 Å	3.863 Å	0.040 °
$Pr_{0.7}Ca_{0.3}MnO_3$	−1.40 %	2.8 Å	3.822 Å	0.059 °
$Pr_{0.6}Ca_{0.4}MnO_3$	−1.85 %	2.5 Å	3.772 Å	0.067 °
$Pr_{0.48}Ca_{0.52}MnO_3$	−2.39 %	2.8 Å	3.741 Å	0.143 °
$Pr_{0.3}Ca_{0.7}MnO_3$	−2.90 %	6.0 Å	3.744 Å	0.059 °

Table 2.4: Stoichiometry dependence of strain in $La_{0.7}Sr_{0.3}MnO_3$ and $Pr_{1-x}Ca_xMnO_3$. Bulk lattice constants were taken from [50].

$La_{0.7}Sr_{0.3}MnO_3$ with the smallest lattice mismatch to $SrTiO_3$ forms an epitaxial film with an atomically flat surface and a very sharp rocking curve of $\Delta\omega = 0.040\,°$. For $Pr_{1-x}Ca_xMnO_3$, with increasing mismatch, the topography becomes rougher, the XRD peak shifts to higher angles and the rocking curve is broadened. The case is different for $Pr_{0.3}Ca_{0.7}MnO_3$, as for this very high mismatch of −2.90 % the system is expected to have started to relax at a thickness of 50 nm. Thus, the Bragg reflex is shifted towards the bulk value, the surface became very rough, while the rocking curve width is reduced. The thin film seems to relax differently from the other materials which introduce defects for strain relaxation. It might have decoupled from the substrate and thus the strain is reduced.

So far, $SrRuO_3$ was only used as BE and therefore directly grown on TiO_2-terminated $SrTiO_3$ (Section 2.2.3.1). For another project, described in [82, 83], $SrRuO_3$ was grown on top of a 100 nm-thick $La_{0.7}Sr_{0.3}MnO_3$ layer on a $NdGaO_3$ substrate. $La_{0.7}Sr_{0.3}MnO_3$ was chosen, because this material can be easily etched by hydrochloride acid and $SrRuO_3$ is still supposed to act as BE for a $SrTiO_3$ thin film, but independent of a bulk single crystal. $NdGaO_3$ was chosen as substrate, as the mismatch between the two materials is only +0.41 % and thus $La_{0.7}Sr_{0.3}MnO_3$ can be grown very thick without any relaxation effects. In this configuration, $SrRuO_3$ has to be grown on top of a non-terminated thin film (Section 2.2.1). The results are shown in Figure 2.21.

The $La_{0.7}Sr_{0.3}MnO_3$ film grows nicely on top of the $NdGaO_3$ substrate (Figure 2.21(b)) in layer-by-layer growth mode, as it can be seen from the inset in Figure 2.21(d). In-situ, $SrRuO_3$ is grown on top, and the analysis of the RHEED intensity development in Figure 2.21(d) strongly indicates a step-flow-like growth mode. In addition, after 15 nm

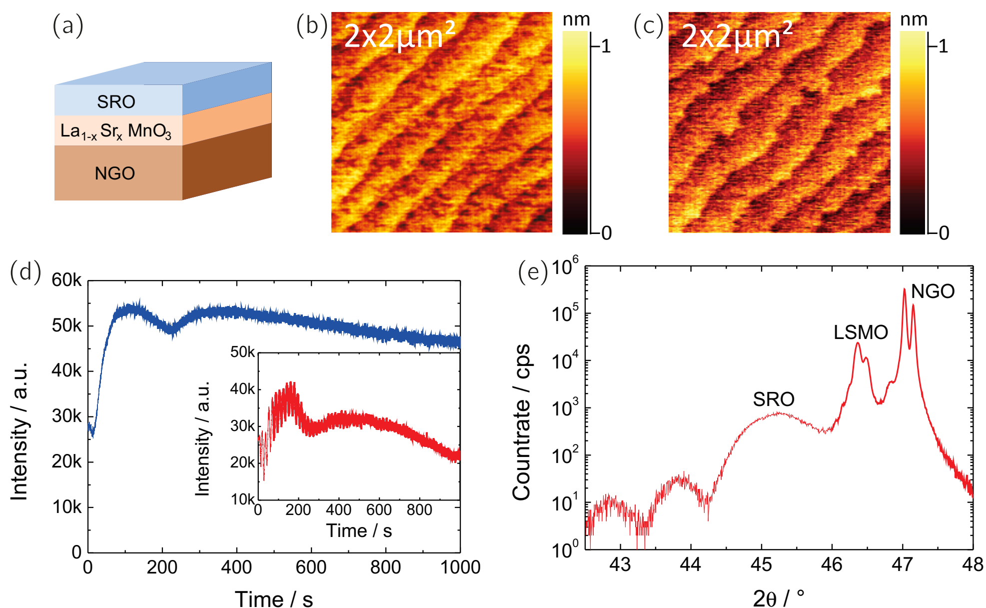

Figure 2.21: Growth of $NdGaO_3$ substrate / 100 nm $La_{0.7}Sr_{0.3}MnO_3$ / 15 nm $SrRuO_3$: (a) Layer stack: NGO-LSMO-SRO. (b) AFM image of the NGO substrate surface, $\rho = 1.8$ Å. (c) AFM image of the SRO surface, $\rho = 1.6$ Å. (d) RHEED intensity for LSMO (red) and SRO (blue), growing in layer-by-layer mode and step-flow mode, respectively. (e) XRD spectrum of the complete stack.

$SrRuO_3$ the terrace structure is still visible (Figure 2.21(c)). From the XRD spectrum in Figure 2.21(e) high thin film quality is visible. For the relatively thick $La_{0.7}Sr_{0.3}MnO_3$ layer, the splitting of the K_α-line is visible, as it is usual for the substrate, and for the thin $SrRuO_3$-layer thickness fringes are observable.

2.2.3.4 Growth of different manganites on $BaTiO_3$

$Pr_{1-x}Ca_xMnO_3$ was grown in two different stoichiometries on top of $BaTiO_3$ for electrical characterization. The great challenge in growing this layer stack epitaxially by PLD is the combination of materials differing crucially in their lattice constants. For $Pr_{1-x}Ca_xMnO_3$, the lattice mismatch to $SrTiO_3$ is up to -2.39 % leading to tensile strain, while the mismatch between $SrTiO_3$ and $BaTiO_3$ is even larger with a value of $+2.62$ % resulting in compressive strain. The nominal strain for $Pr_{0.48}Ca_{0.52}MnO_3$ on $BaTiO_3$ would then

amount to −5.14 %.

A terminated $SrTiO_3$ substrate was used and 30 nm $SrRuO_3$ were grown under the conditions $p = 0.133$ mbar O_2, $T = 650$ °C, $E = 27$ mJ, $f = 10$ Hz and $d = 59$ mm.
20 nm $BaTiO_3$ were deposited in-situ using the parameter set $p = 0.05$ mbar O_2, $T = 800$ °C, $E = 42$ mJ, $f = 1$ Hz and $d = 57$ mm.
Afterwards, each time 20 nm of $Pr_{0.48}Ca_{0.52}MnO_3$ and $Pr_{0.6}Ca_{0.4}MnO_3$ were grown with $p = 0.133$ mbar O_2, $T = 700$ °C, $E = 65$ mJ, $f = 5$ Hz and $d = 59$ mm, respectively. The results of both stacks are depicted in Figure 2.22.

For the $Pr_{1-x}Ca_xMnO_3$ compositions 52 %Ca and 40 %Ca, the surface of the stack and the RHEED signal development during the depositions are depicted in Figure 2.22(a), 2.22(d) and Figure 2.22(c), 2.22(e), respectively. For both growth processes, the surfaces show the step-terrace structure, but to some extent also island growth is observable, which leads to an increased roughness of about $\rho = 4$ Å. Regarding the RHEED signal of $SrRuO_3$, a nice step-flow-like growth mode is visible for the $Pr_{0.48}Ca_{0.52}MnO_3$-sample. In both cases, the specular spot showed several oscillations during the $BaTiO_3$ growth, but its intensity was too weak after the completion of the $BaTiO_3$ layer, so that no data is available for the $Pr_{1-x}Ca_xMnO_3$ growth. In Figure 2.22(f) the XRD spectra for both stacks are depicted for a range around the STO (002) reflex. Although the $BaTiO_3$ reflexes appear as broaden peaks, they are located at an appropriate 2θ-value. The rocking curves at each peak position shown in Figure 2.22(g) trace the still good crystal quality of all layers with a width of well below 0.1 °. The structural data of all different thin films are listed in Table 2.5.

Material	$a^{(*)}$ [50]	mismatch to $SrTiO_3$	$c^*_{52\%}$	$\Delta\omega_{52\%}$	$c^*_{40\%}$	$\Delta\omega_{40\%}$
$SrTiO_3$	3.901 Å	-	-	0.027 °	-	0.027 °
$SrRuO_3$	3.923 Å	+0.56 %	3.959 Å	0.052 °	3.974 Å	0.051 °
$BaTiO_3$	4.006 Å	+2.62 %	4.108 Å	0.069 °	4.127 Å	0.062 °
$Pr_{0.48}Ca_{0.52}MnO_3$	3.814 Å	−2.39 %	3.788 Å	0.078 °	-	-
$Pr_{0.6}Ca_{0.4}MnO_3$	3.830 Å	−1.85 %	-	-	3.813 Å	0.082 °

Table 2.5: Growth of $Pr_{0.48}Ca_{0.52}MnO_3$ and $Pr_{0.6}Ca_{0.4}MnO_3$ on $SrTiO_3/SrRuO_3/BaTiO_3$ stack.

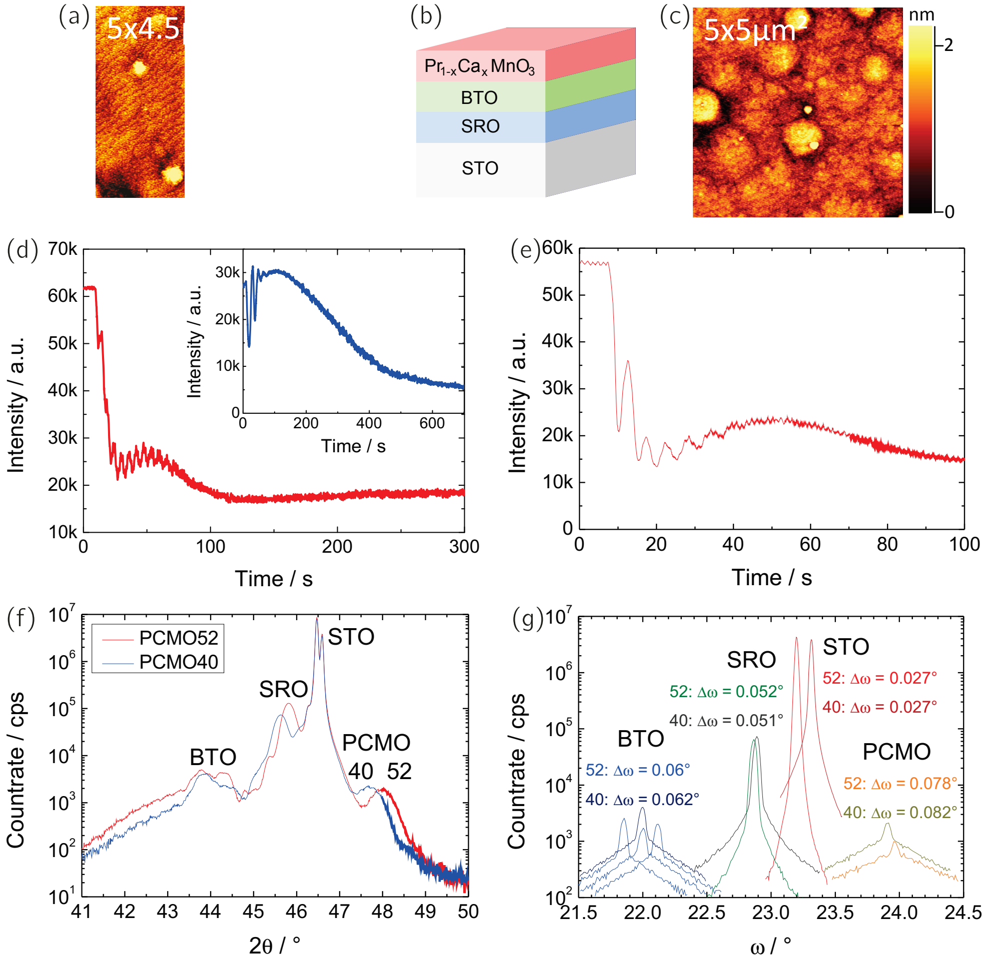

Figure 2.22: Growth of $SrTiO_3$ substrate / 30 nm $SrRuO_3$ / 20 nm $BaTiO_3$ / 20 nm $Pr_{1-x}Ca_xMnO_3$ with 52 % and 40 %: (a) AFM picture of the $Pr_{0.48}Ca_{0.52}MnO_3$ surface, $\rho = 4.0$ Å. (b) Layer stack: STO-SRO-BTO-PCMO(x). (c) AFM picture of the $Pr_{0.6}Ca_{0.4}MnO_3$ surface, $\rho = 3.9$ Å. (d) RHEED signal of $SrRuO_3$ step-flow growth (inset, blue line) and $BaTiO_3$ layer-by-layer growth (red line) for the $Pr_{0.48}Ca_{0.52}MnO_3$-sample. (e) RHEED oscillations of $BaTiO_3$ for the $Pr_{0.6}Ca_{0.4}MnO_3$-sample. (f) XRD spectra around the STO (002) reflex for both stoichiometries. (g) Rocking curves of all Bragg reflexes for both stoichiometries, respectively.

3 Electrical properties of $BaTiO_3$

$BaTiO_3$ (BTO) is one of the most well-known ferroelectric materials. In contrast to $Pb(Zr_xTi_{1-x})O_3$ (PZT), which is frequently used for application due to its large polarization, $BaTiO_3$ is lead-free and therefore interesting for environment-friendly technology. After a short introduction into the basics of ferroelectricity, the ferroelectrical characterization of $BaTiO_3$ thin films is reported. In particular, leakage effects, their causes and possible solutions to distinguish them from ferroelectric switching currents and how to avoid them are discussed.

3.1 Principle of ferroelectricity

Ferroelectricity (FE) describes a phenomenon, in which materials exhibit a remanent polarization at zero applied electrical field E. Generally, materials can be non-polar or polar, implying that dipols are existing within the material. A non-polar material can be polarized in an external electrical field, known as induced polarization, or, as a special case of it, the ions in an ionic crystal can be displaced as a result of the electrical field (ionic polarization). In polar materials, the permanent dipols become aligned in the external field, which is called orientation polarization. If in a polar material the dipols stay aligned after the external field is switched off and the polarity can be reversed by an external stimulus, it is ferroelectric. The measurable remanent polarization P_r is a quantity for the strength of the effect.

The origin of ferroelectricity is, that the sublattices of cations and anions are shifted against one another along a certain preferential direction, resulting in a spontaneously formed dipole moment. Analog to ferromagnetism, this collective behavior vanishes above the ferroelectric phase transition temperature, called Curie-temperature T_C, and merges into a paraelectric phase.

For the wide-band gap insulator BTO with $E_g = 3.2\,\text{eV}$ [84], this phase transition is connected with a structural change. At high temperatures, BTO has a cubic phase and

shows paraelectric behavior. At $T_C \approx 120\,°\mathrm{C}$ the system changes into a tetragonal structure, where the c-axis is elongated and the $a = b$ axes are shortened [85], so that a preferential direction is created and the system is ferroelectric at room temperature.

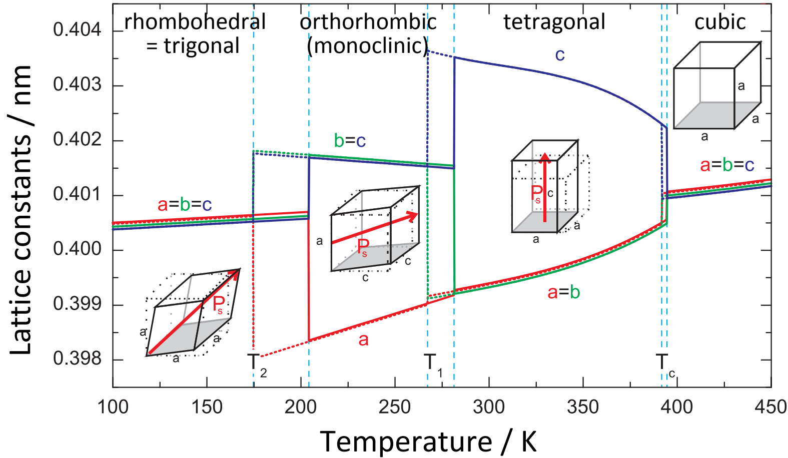

Figure 3.1: Phase transitions in BTO, based on [86]: Dependence of the pseudo-cubic lattice constants of BTO on the temperature. Dotted lines represent a decreasing temperature, while solid lines stand for increasing temperature. BTO has three ferroelectric phases and its paraelectric phase transition is at $T_C \approx 392\,\mathrm{K}$.

As depicted in Figure 3.1, BTO has three different ferroelectric phases for different temperature regimes. At $T_1 \approx 7\,°\mathrm{C}$ [85] the crystal structure is changed again into a monoclinic phase, for which $b = c$ is valid and the non-rectangular angle only slightly deviates from $90\,°$. This phase is often named orthorhombic phase, as with only small approximations the monoclinic unit cell can also be described like this [87]. At $T_2 \approx -84\,°\mathrm{C}$ a phase transition into the rhombohedral phase occurs.
For the cubic phase, depicted in Figure 3.2(a), the system is isotropic. The Ti cation is located in the center of the unit cell and the centers of positive and negative charges within the crystal structure coincide. Upon the tetragonal distortion of the unit cell during the ferroelectric transition, the c-axis becomes enlarged and the repositioning of the central Ti cation along the polar axis becomes energetically favorable. Two equivalent stable positions form, for which the Ti-lattice gets displaced with respect to the oxygen anion sublattice. In Figure 3.2(a) the displacement is simplified, but the major contribution to the polarization is based on the relative shift between the Ti ion towards its oxygen octahedron. A net polarization arises, which direction depends on the actual position of the Ti ion.

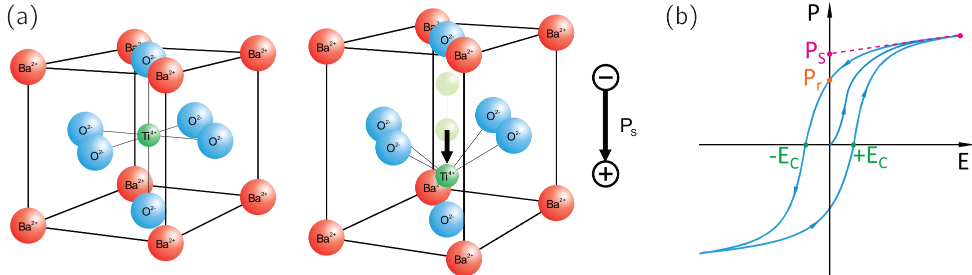

Figure 3.2: Principle of ferroelectricity in $BaTiO_3$, based on [88]: (a) Cubic and tetragonal unit cell of $BaTiO_3$. (b) Hysteresis between polarization P and electrical field E.

For a BTO bulk crystal or ceramic the complete material does not necessarily have to be polarized in the same direction. Regions of same polarization direction are called domains and especially in an electrically untreated system, the net polarization is normally zero. Upon the application of an electrical field, depicted in Figure 3.2(b), the domains become aligned with their polarization parallel to the external field by tilting the polarization of the entire domain or shifting the domain walls, which have a dimension of a few nanometers. This process is visible as the initial branch, starting at zero polarization.
For a perfect crystal, the polarization saturates at a certain electric field and is conserved down to zero field, called saturation polarization P_S, and also beyond into negative electrical fields, until the negative coercive field $-E_C$ is reached. For a real system, the measured polarization at zero field P_r is slightly lower, because impurity contents and crystal defects might relax the polarization. At the coercive field, the external field is high enough to reverse the overall polarization, which again saturates at a certain negative field. The shape of the resulting hysteresis loop, defined by P_r and E_C, determines the ferroelectric properties of a material system.

The hysteresis loop, resulting from the ferroelectricity, can be modified by other contributions to the polarization. The dielectric displacement field $D = \varepsilon E$ causes a linear contribution to the polarization according to the permittivity $\varepsilon = \varepsilon_0 \varepsilon_r$ of the material, consisting of vacuum and relative permittivity, which bends the hysteresis, as shown in Figure 3.2(b). In addition, leakage currents through the ferroelectric lead to a football-shaped polarization curve, which distends the polarization especially at zero applied field and thus leads to an apparently higher remanent polarization.

For an epitaxially grown ferroelectric thin film, the strain determines an additional distortion of the system and can enhance or reduce the markedness of ferroelectric properties. For the special case of BTO grown on STO, a tetragonal distortion with an enlarged *c*-axis is induced by the strain. Compared to the tetragonal crystal structure at room temperature, the polar axis is fixed to the *c*-direction. Thus, the domains can only be polarized out-of-plane and no in-plane contribution is expected. In addition, the tetragonal distortion caused by epitaxial strain is larger than for the relaxed tetragonal phase, which can increase the ferroelectric properties. Upon cooling, the other two phase transitions might be suppressed due to the lattice adoption to the STO substrate.

3.2 PFM measurements on $BaTiO_3$

Piezoresponse force microscopy (PFM) was performed on BTO thin films by the group of Dr. Lucien Pintilie, NIMP, Romania. This technique uses the fact that all ferroelectric materials are also piezoelectric, meaning that they react on elastic deformation with the development of an electrical voltage and, reversely, they deform under the application of a voltage. This effect is widely used for sensors, for actuators in micro- and nano-positioning systems and for high voltage sources.
PFM is a variation of atomic force microscopy (AFM), that allows imaging and manipulation of ferroelectric domains and is based on the correlation between the polarization and the deformation direction. For PFM a conducting BE is needed, which is connected to ground. A conductive tip is brought into contact with the surface of the sample, an alternating voltage is applied to the tip and induces an alternating deformation in the sample, which is detected analog to the AFM. Depending on the polarization direction of the probed domain, the piezoresponse is in-phase with the driving voltage or out-of-phase. During a scan, the topography is detected simultaneously to the amplitude and the phase signal of the piezoresponse. The most interesting signal is the phase, which has a circularly closed range of 360 ° and 0 ° means in-phase with the exciting signal and 180 ° out-of-phase. As the amplitude is similar for both polarization directions, only the domain walls protrude in the amplitude image.

For the investigation of BTO with PFM two different thicknesses 7 ucl $\approx$ 3 nm and 150 nm of BTO are grown on 30 nm conducting $SrRuO_3$ on $SrTiO_3$ substrates. The results of the piezoresponse measurements are shown in Figure 3.3. In Figure 3.3(b) the XRD data are shown for both thin films. All measured rocking curves were sharp with a width well

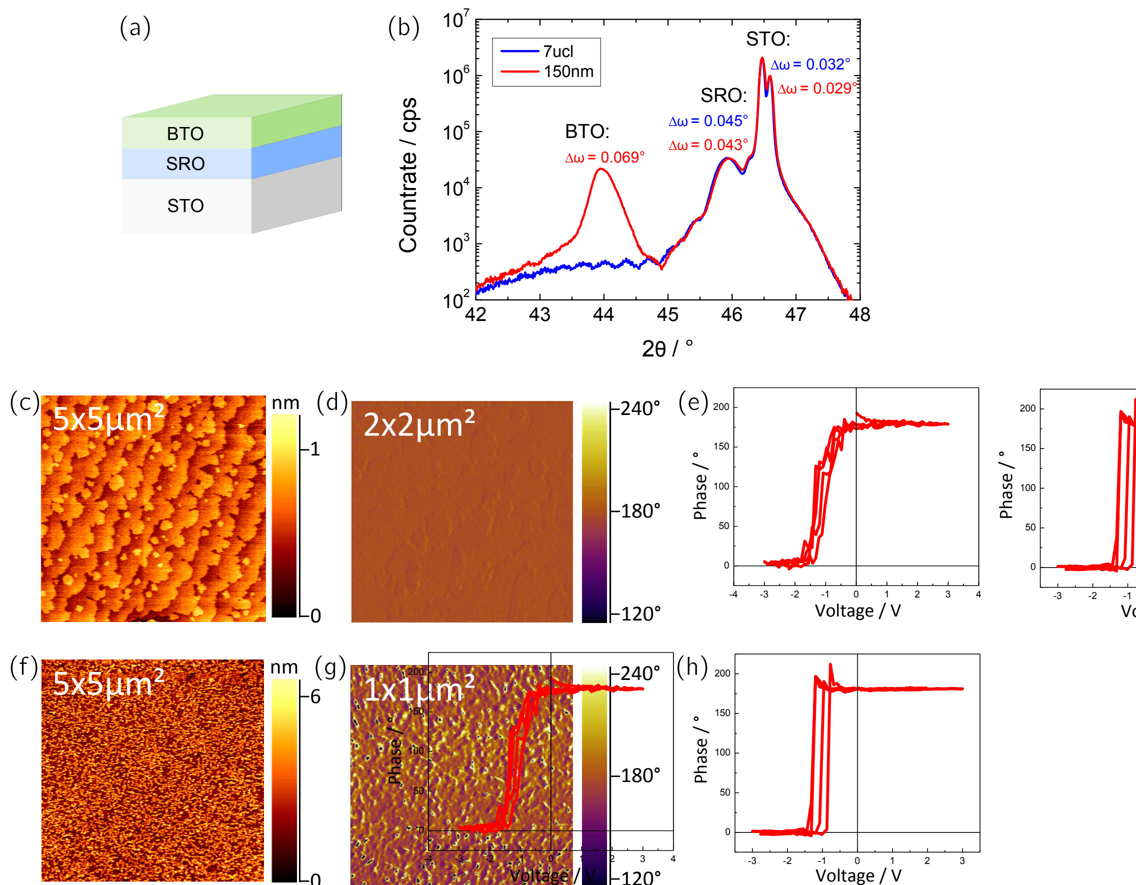

Figure 3.3: PFM measurements on BTO samples with two different BTO thicknesses: 7 ucl and 150 nm: (a) Layer stack: STO-SRO-BTO. (b) XRD spectra of both samples. (c) AFM image of the 7 ucl thick BTO surface, $\rho = 1.5$ Å. (d) PFM phase image of the 7 ucl thick BTO surface. (e) Phase signal for a voltage sweep for the 7 ucl thick BTO sample. (f) AFM image of the 150 nm thick BTO surface, $\rho = 11.5$ Å. (g) PFM phase image of the 150 nm thick BTO surface. (h) Phase signal for a voltage sweep for the 150 nm thick BTO sample.

below 0.1 °. For the 150 nm thick film, the Bragg peak is nicely developed, while for the 7 ucl thick BTO film it is hardly visible. Starting with the 7 ucl sample, the surface in Figure 3.3(c) shows the step-terrace structure of the substrate with a roughness of $\rho = 1.5$ Å, similar to the substrate itself. In the PFM phase image in Figure 3.3(d) a phase of 180 ° is detected for the entire scanning area of 2 x 2 µm^2, implying a homogenous

distribution of the polarization orientation over the whole thin film. The slight deviations from this value can be explained by the step edges of the surface, because a signal transfer between topography and piezoresponse cannot be avoided completely. To elucidate the switching behavior, the tip was located at one position on the surface and the AC voltage was superimposed by a DC voltage signal of a voltage sweep between ±3 V. The DC voltage was used to eventually switch the polarization direction of the BTO film, while the AC voltage is still needed to detect the phase signal. The result is depicted in Figure 3.3(e) and shows a polarization reversal between −1 V and −1.5 V. The hysteresis opens up only slightly, so that the coercive field is very small, but it is shifted towards negative values by 1 V, called imprint effect. The reason for this imprint is a relatively strong internal field, which acts as driving force for the system to be completely polarized downwards. A possible reason might be the asymmetry of the stack due to the bare BTO surface or termination effects at the interface to $SrRuO_3$.
For the 150 nm thick BTO sample the case is very similar. The surface in Figure 3.3(f) is relatively rough with a roughness of $\rho = 11.5$ Å, which is transferred into the PFM signal in Figure 3.3(g), where larger deviations from 180 ° are detected. For the voltage sweeps in Figure 3.3(h) the signal is less noisy than for the 7 ucl sample and the hysteresis opens up more precisely, because the signal is averaged over a 50 times thicker film.

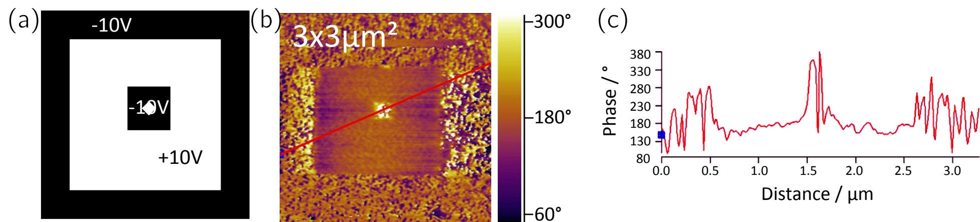

Figure 3.4: PFM writing experiments on a BTO sample: (a) Schematic poling map. (b) PFM phase image of the 150 nm thick BTO surface after application of the poling map (a). (c) Linescan through the phase image in (b).

For the 150 nm thick BTO film additional poling experiments have been performed. Due to the large imprint of the sample, a ±10 V DC voltage was used, as shown in Figure 3.4(a), and applied to the scan area. After 15 min the same area was read-out with just the AC voltage signal. The resulting phase image is shown in Figure 3.4(b). The signal of a linescan through the phase image is shown in Figure 3.4(c). For the regions, that were poled with +10 V, a phase of 180 ° is detected, but the deviations visible in Figure 3.3(g) vanished. For the −10 V regions especially the linescan shows large noise, but in average

the signal is enlarged up to 360 °, what corresponds to 0 ° and upwards polarization.

With these experiments it has been shown that BTO thin films, grown on a $SrRuO_3$ bottom electrode, are naturally polarized downwards due to strong internal fields and the resulting imprint. The film was poled and a change in the piezoresponse phase could be observed, which was conserved for at least 104 min (Section A.4).

3.3 Ferroelectric properties of $BaTiO_3$

3.3.1 Measurement setup

For the determination of the ferroelectric properties of the BTO thin films, an aixACCT TF Analyzer 2000 was used, which utilizes the virtual ground feedback method [89]. Operated in the dynamic hysteresis measurement mode (DHM), a voltage sweep is applied to the sample in capacitor geometry and the current response signal is measured.

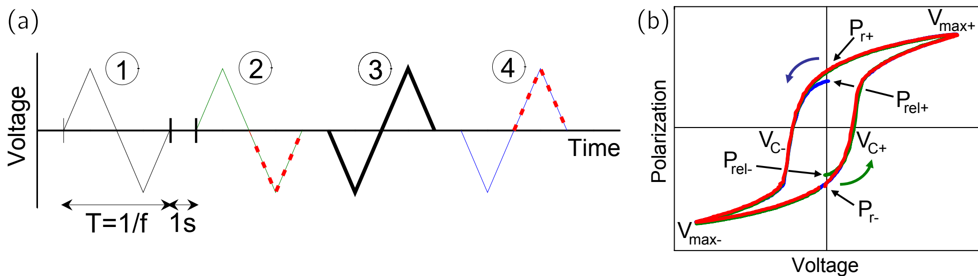

Figure 3.5: Voltage sweeps for FE characterization, based on [89]: (a) Voltage excitation signal: ① and ③ act as prepolarization pulses, while the sweeps ② and ④ are measured. The final hysteresis is calculated from the second half of ② and ④, respectively (red, dashed). (b) Corresponding *P*-*V* curves for a ferroelectric reference device.

For each measurement, four voltage cycles are stringed together, as shown in Figure 3.5(a), each separated by a 1 s relaxation time. For the cycles, the voltage amplitude $V_{max\pm}$ and the frequency f can be chosen within the ranges 0.1 V – 15 V and 0.01 Hz – 2 kHz. For a ferroelectric device, the prepolarization pulse ① establishes a defined polarization state, the negative state of relaxed remanent polarization P_{rel-}. For the followed pulse ② the current response is recorded. The next pulse ③ acts as a prepolarization pulse again, but now creates the positive relaxed remanent polarization P_{rel+}, and the consecutive pulse ④

is recorded. To avoid the influence of relaxation effects, the second halfs of sweep ② and ④ are merged into a closed current signal. The final hysteresis is then calculated from the measured current response $I(V)$ by

$$P(V) = \frac{1}{4AV_{\max}f} \oint |I(V)|\, dV - C,$$

where A is the device area and C is an integration constant, which levels the hysteresis in a way that the boundary condition $P(V_{\max+}) = -P(V_{\max-})$ is fulfilled. From the hysteresis loop in Figure 3.5(b), the coercive voltages $V_{C\pm}$ can be determined as intersection points with the V-axis, while the remanent polarizations $P_{r\pm}$ are the intersection points with the P-axis.

The DHM program is designed for ferroelectric materials, but the current response can also be obtained for other devices. In most cases, the recorded signal consists of a superposition of different terms. The I-V and P-V curves for three different single circuit elements are sketched in Figure 3.6.

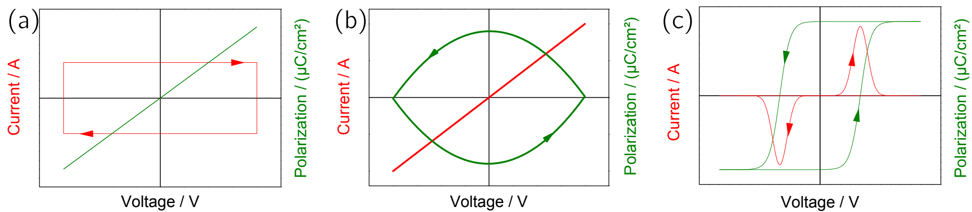

Figure 3.6: I-V and P-V curve of different circuit elements: (a) Dielectric. (b) Ohmic resistor. (c) Ferroelectric.

Figure 3.6(a) shows the characteristics of a capacitance. As each ferroelectric material has a high dielectric constant, this contribution is always observed for ferroelectrics and is visible in particular for small voltage sweeps below $V_{C\pm}$. The current response of an ohmic resistor is depicted in Figure 3.6(b). Linear or also non-linear leakage currents through the device can appear in ferroelectric capacitors. The corresponding polarization curve opens up, especially for small voltages, and should not be mixed up with ferroelectric switching [90]. In Figure 3.6(c) the characteristics of a pure ferroelectric are sketched, including domain behavior. Here, the current signal is zero until it peaks for the coercive voltage $V_{C\pm}$, at which the ferroelectric polarization is reversed and the switching current is measured. The corresponding polarization curve is the well-known hysteresis loop.
Adding a dielectric contribution to the "perfect" hysteresis loop in Figure 3.6(c) will bend

the hysteresis and additional leakage will distend the loop. In general, it is very important to cross-check both current and polarization signal, because the *P*-*V* curve, which contains the physical information, is only reasonable for a current signal with distinct switching peaks.

3.3.2 $SrRuO_3$/$BaTiO_3$/Pt devices

3.3.2.1 Separation of ferroelectricity from leakage in $BaTiO_3$ devices

For the investigation of the ferroelectric switching of BTO, a 30 nm thick thin film is grown on a 30 nm thick $SrRuO_3$ bottom electrode on a $SrTiO_3$ substrate. 30 nm thick Pt pads of size 50 x 50 μm^2 are sputtered on top through a shadow mask and the BTO is etched down to the BE at one corner of the sample.
High work function metals are used as electrode materials, as they form a rectifying Schottky contact at the interface to the naturally *n*-doped BTO. These back-to-back Schottky contacts help to suppress leakage currents through the device. The consequence of these blocking interfaces is that the voltage does not drop uniformly across the device, but the main decline occurs at the interfaces. Thus, the transformation of the applied voltage V into an electric field E is not trivial and $E = \frac{V}{d}$ with the BTO film thickness d does not lead to the effective fields within BTO. Therefore, the applied voltage is plotted instead of the electric field.

For BTO thin films grown under diverse conditions, different results were obtained for the ferroelectric characterization. One example for the current response is depicted in Figure 3.7 for a 100 nm thick film (Figure 2.8(a)-2.8(c)), which shows a measurable FE switching behavior.

In Figure 3.7(a) the measurement frequency is held constant at $f = 2$ kHz, while the voltage amplitude V_{max} is increased in steps of 1 V from 1 V to 14 V. For small voltages $V_{max} < 4$ V below the coercive voltage, mainly a dielectric contribution is visible in the current signal (Figure 3.6(a)). For an increased voltage, two peaks with positive and negative amplitude appear, which can be identified with the switching currents upon alternation of the polarization direction (Figure 3.6(c)). Concurrently, large currents are measured for the negative voltage branch. Parallel to the indirectly flowing switching current, the leakage through the BTO film is not ohmic in this case, but has a non-linear shape according to the Schottky contacts at the interfaces (Figure 3.6(b)). In conclusion, the applied voltage

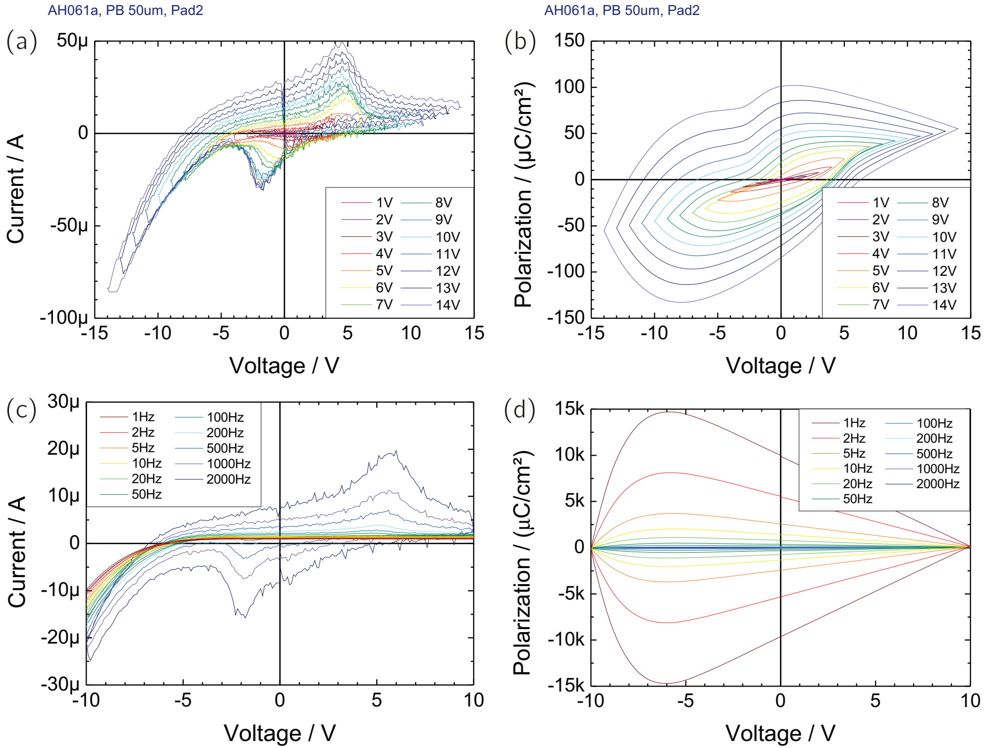

Figure 3.7: Changes in the current response: (a) Upon voltage variation between $V_{max} = 1$ V and $V_{max} = 14$ V for $f = 2$ kHz. (b) Corresponding *P*-*V* curves. (c) Upon frequency variation for $V_{max} = \pm 10$ V. (d) Corresponding *P*-*V* curves.

has to be larger than the respective coercive voltage to switch the system.
The frequency of the sweeps is varied between $f = 1$ Hz and $f = 2$ kHz for a constant voltage amplitude $V_{max} = 10$ V and the resulting current responses are depicted in Figure 3.7(c). Here, the ferroelectric as well as the dielectric contribution decrease upon decreasing frequency and finally vanish, while the leakage current does not change significantly. For a perfect insulator, also small excitation frequencies are sufficient to measure a ferroelectric signal, as di- and ferroelectric contributions decrease in the same manner. But in a leaky ferroelectric the electronic charges can compensate the dipole moments. Only for high frequencies, when the free carriers cannot follow the electrical field as fast as the ferroelectric switching occurs, the ferroelectricity is measurable. Note that for all shown current responses the leakage is too high to lead to a sensible hysteresis, which are nevertheless presented in Figure 3.7(b) and 3.7(d), respectively.

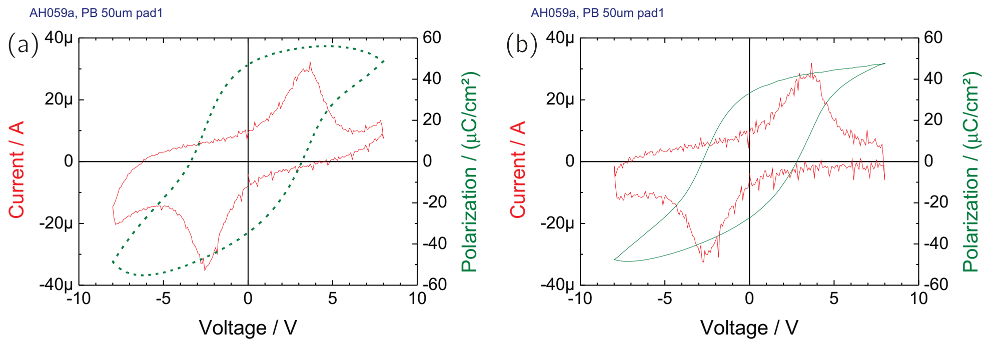

Figure 3.8: Ferroelectric switching of BTO at 2 kHz and $V_{max} = \pm 8$ V: (a) Raw data for the current and the resulting hysteresis. (b) Measurement with enabled DLCC.

Figure 3.8(a) shows the current response and the related polarization hysteresis of a 30 nm thick BTO film. Again all three different contributions to the signal, discussed in the beginning of Section 3.3, are visible. The main part of the current signal comes from the ferroelectric switching, identified with the two peaks at around ± 3 V. Additionally, the current signal does not drop to zero apart from the current peaks. Here, the dielectric contribution is visible, which also widens the I-V curve for higher voltages, where the leakage currents are visible.
A dielectric contribution is not avoidable, because each ferroelectric material has a high permittivity. But much more affecting than an additional linear contribution to the polarization is the leakage current, which inflates the hysteresis and leads to misleadingly increased remanent polarization values.

As it has been seen from Figure 3.7(c), the leakage does not significantly depend on the sweep velocity, but the FE signal does. That is why the leakage contribution can be compensated by subtracting two measurements of different frequencies. A detailed description of this method can be found in [91] and this principle is implemented in the measuring software as option called dynamic leakage current compensation (DLCC) [89]. The application of this tool is shown in Figure 3.8(b) for the same pad measured in Figure 3.8(a). Now the leakage tails vanish and only the FE capacitor properties are visible. For this current response, a calculation of the hysteresis signal is sensible.
The polarization hysteresis gives information about the strength of the ferroelectric effect. The remanent polarization, as a measure of the displacement of the sublattices against each other, is calculated to $P_r = (P_{r+} - P_{r-})/2$. A deviation of the two values only appears, because the integration constant is unknown and the offset of the hysteresis is determined

according to $P(V_{\text{max}+}) = -P(V_{\text{max}-})$. The coercive voltages $V_{C\pm}$ should generally coincide with the peak positions of the current signal. Their average $V_C = (V_{C+} - V_{C-})/2$ is a measure for the stability of the ferroelectric polarization states. In contrast to the remanent polarization, the shift between the two values $V_I = (V_{C+} + V_{C-})/2$ is called imprint and is a device related phenomenon. For the current example, $V_C \approx 3\,\text{V}$ and $V_I \approx 0.5\,\text{V}$ are extractable. The imprint effect is caused by an additional internal electrical field, which enhances one polarization direction. The reason could be the asymmetric device stack, termination effects at the interfaces or oxygen vacancies.

The DLCC tool can be applied for all measurements, but only leads to improved results, if the leakage branch and the switching peak are clearly separated in voltage. If the switching peak is covered by the leakage current, the application of the DLCC is not sensible. In addition, the DLCC-corrected data set is usually much more noisy than the raw data. As for the DLCC two measurements with comparable noise are subtracted, the resulting signal becomes smaller while the relative error is increased.
Beside the increased noise due to the DLCC, the current range of the measurement, which can be chosen in steps of one order of magnitude, crucially determines the signal-to-noise ratio. It is large, if the complete current range is used, while the noise can become comparable to small signal features, if only a small part of the current range is utilized. Depending on the purpose of the measurement, it can be useful not to measure the complete current signal, as done in Figure 3.7(a), but to let the current run into its compliance to make small features visible, as shown in Figure 3.9(a).

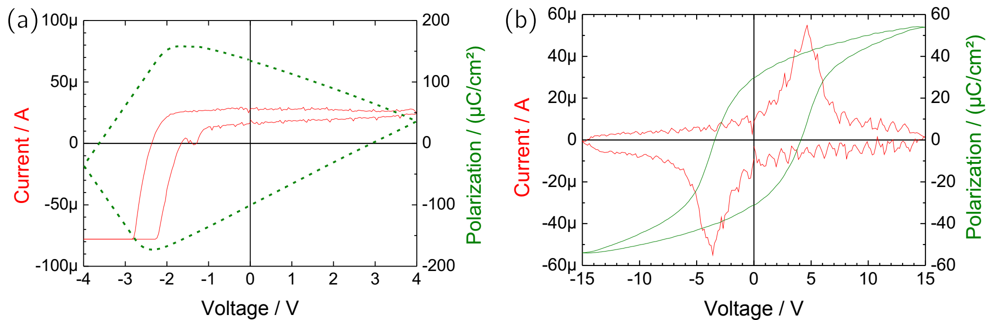

Figure 3.9: Ferroelectric switching of different BTO samples: (a) FE switching of a sample of good crystal quality with disabled DLCC and a current range of 100 µA. (b) FE switching of a sample with worse crystal quality and enabled DLCC.

In Figure 3.9 the FE switching behavior of two different 30 nm thick BTO films stacked between $SrRuO_3$ and Pt is presented. The FE properties of a sample with good crystal quality are shown in Figure 3.9(a). The growth properties have been reported in Figure 2.10 and show nice RHEED oscillations, an atomically flat surface and a distinct Bragg reflex with a sharp rocking curve. But from the FE characterization it is visible, that the film is rather leaky. One switching peak at −1.5 V is only visible, because the current range has been reduced manually to 100 µA. For this current response, the application of the DLCC does not help, because switching and leakage current overlap too much.
In contrary, the nicest switching behavior, depicted in Figure 3.9(b), has been observed for a BTO thin film, which does not have a good crystal quality, indicated by an XRD spectrum with no distinct BTO Bragg reflex, comparable to the one shown in Figure 2.8(f). With enabled DLCC the leakage branches could be reduced to zero and two nicely developed switching peaks appear. The resulting hysteresis loop does not show any inflation and the remanent polarization has a value of $P_r = 30\,\frac{\mu C}{cm^2}$, which is higher than the value reported for a single crystal $P_r = 26\,\frac{\mu C}{cm^2}$ [92].

For all BTO samples with leakage currents, the negative branch shows more conductance than the positive branch. As the system consists of two back-to-back Schottky contacts, it is possible to extract, which interface is responsible for the large leakage. In a serial circuit, the resistance is dominated by the largest resistance and thus by both blocking directions. For negative voltages, applied to the TE, the Pt/BTO interface would be blocking, but here the enlarged leakage is measured. Hence, the interface to Pt causes the main leakage contribution, although the work function of Pt $\Phi_{Pt} = 5.65$ eV is larger than that of $SrRuO_3$ $\Phi_{SRO} = 5.3$ eV.

The imprint effect as well as the unilateral leakage branch can be avoided by pad-to-pad measurements, including two capacitor devices connected by the BE (Section 3.3.2.4). In this symmetric case, the thickness of the active device is doubled, but the two imprint shifts are acting against each other and for each polarity the blocking direction of the $SrRuO_3$/BTO Schottky contact is dominant. But for some BTO devices, even this circumvention leads to too large leakage currents through the capacitor structure to obtain nice FE switching behavior.

In addition to dynamic hysteresis measurements also static hysteresis measurements (SHM) can be performed. As the frequency has a crucial impact on the measurement, as visible in Figure 3.7(c), it is interesting to exclude its influence by moving to an infinite slow voltage sweep, which requires an extremely sensitive current meter. This fact is circumvented by a

measurement method as shown in Figure 3.10(a). As reference, a complete quasi-static hysteresis is performed. Then the sweep is repeated until the measurement voltage V_{meas} is reached and held constant for a relaxation time t_{rel}, normally on second-scale. After this time, the quasi static hysteresis is continued to the next maximum voltage and the current response of this part is integrated to yield a polarization value. The difference between the polarization at the saturation voltage and the measured value then refers to the voltage V_{meas}.

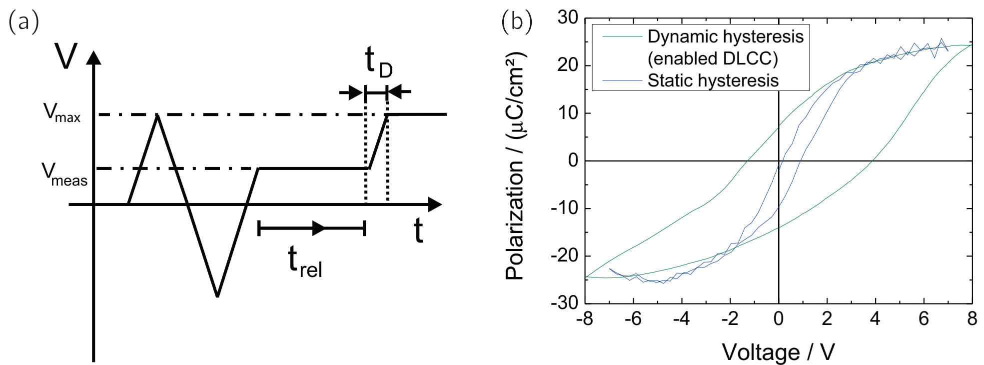

Figure 3.10: Static hysteresis measurement: (a) Measurement program, based on [93]. (b) Comparison of dynamic and static hysteresis. For the DHM the DLCC was enabled.

Both DHM and SHM have been performed on devices made of the same BTO thin film. The results are depicted in Figure 3.10(b). In comparison to the DHM, which was performed at a frequency of 2 kHz with enabled DLCC to avoid leakage influences, the coercive voltages as well as the remanent polarization values decreased dramatically for the static measurement.

3.3.2.2 Annealing series

The reason for the large leakage through the BTO thin film is thought to be charged lattice defects [93]. As BTO is connatural to $SrTiO_3$ [70], also its defect chemistry is comparable [94]. Thus, for reducing conditions, oxygen is easily removed from the system and the remaining oxygen vacancies are compensated by electrons, which lead to a thermally activated conductance through the formal insulator. Most BTO thin films are grown in a low oxygen partial pressure atmosphere (10^{-3} mbar), which could be already a

reducing condition for the thin films. In [95] post-annealing experiments in an oxygen-rich atmosphere are reported to improve the FE switching behavior.

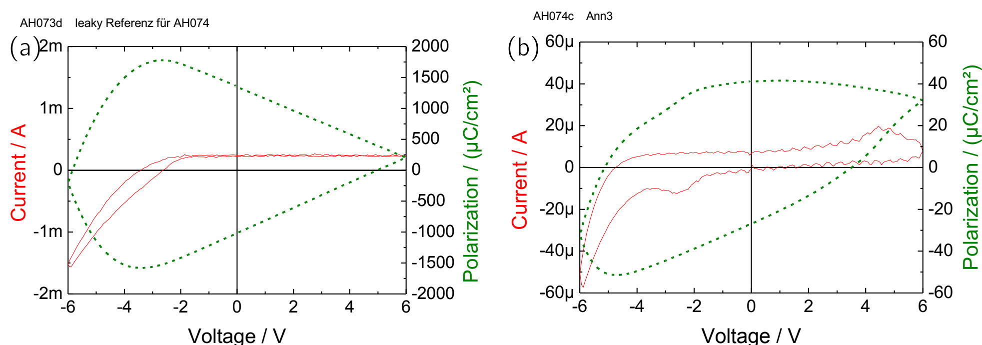

Figure 3.11: Annealing effect on FE switching of BTO: (a) Current response of a BTO device. (b) Current response of the same device after 15 h annealing in air at 400 °C.

The current response of a BTO device with a very high leakage current and no visible FE switching is shown in Figure 3.11(a). Different annealing procedures have been tested and the best has been found to be annealing in air for at least 15 h at 400 °C. The current response of the same device after the post-annealing is shown in Figure 3.11(b). Although the leakage branch is still dominant for negative voltages, two switching peaks are visible now, since the leakage current was reduced from mA to the µA regime.

Allowing the BTO thin film to exchange with an oxidizing atmosphere at elevated temperatures is concluded to suppress leakage currents, but not completely. A reason for this observation might be a natural enrichment of electrons at the surface. For $SrTiO_3$ it was found recently, that the conductivity is increased by reduction of the thin film thickness [70, 96]. A possible explanation is a natural redistribution of oxygen vacancies from the bulk to the surface. This oxygen depleted "surface core" generates an electrical potential, so that electrons are attracted and form a space charge layer, similar to a half-sided grain boundary. Calculations show that this effect is dominant for thin films with thicknesses up to 100 nm and for films thinner than 10 nm the depletion layer can be regarded as a flat-band case. As a result, even completely oxidized films in equilibrium with a high-pressure oxygen atmosphere show an oxygen depleted surface layer, which leads to an increased leakage conductance.

Within the framework of this model it can be understood, why the interface to Pt causes higher leakage than the interface to $SrRuO_3$. The deposition of Pt on top of the oxygen-depleted BTO layer does not show any impact on the oxidation. In contrast, the deposition

of an oxide as $SrRuO_3$ will lead to a shift of this space charge layer into the $SrRuO_3$, where the effect does not play a crucial role.

3.3.2.3 Low temperature measurements

The leakage currents in BTO originate from oxygen vacancies, which are compensated by electrons. These electrons can be regarded as defect charges, which can be thermally activated with an energy of $\Delta E = 0.12\,\mathrm{eV}$ [97]. As reverse conclusion, the leakage currents can be reduced by a decrease of thermal energy upon cooling.

A BTO sample with weakly pronounced switching currents, superimposed by large leakage branches, is mounted into a N_2 continuous-flow cryostat, which sample chamber can be evacuated down to 10^{-2} mbar.

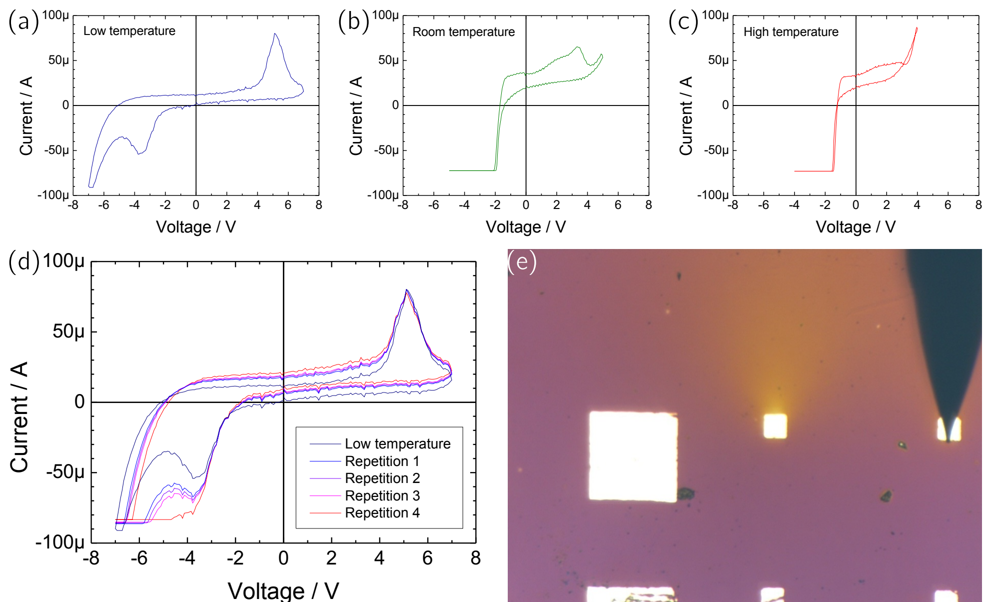

Figure 3.12: Current response on FE excitation for different temperatures: (a) Low temperature measurement at approximately $-50\,°\mathrm{C}$. (b) Room temperature measurement. (c) High temperature measurement at $100\,°\mathrm{C}$. (d) Temporal evolution of the current response at low temperatures caused by warming of the system through the tip. (e) Camera picture of the sample, the connected pad has the size 50 x 50 μm^2.

Figure 3.12 shows the results of temperature dependent FE measurements on a 30 nm thick BTO sample, stacked between $SrRuO_3$ and Pt. The room temperature current response is depicted in Figure 3.12(b), exhibiting large leakage, especially for negative voltages. Upon heating the sample stage up to 100 °C (Figure 3.12(c)) the leakage currents are enhanced and the FE switching behavior almost vanished. Upon cooling the sample with liquid nitrogen, the leakage was reduced and nicely shaped switching peaks developed, as depicted in Figure 3.12(a). Still, the leakage current is visible in the negative branch, but now clearly distinguishable from the negative switching peak. Note that for all three measurements the current runs into its compliance for negative voltages.
The measurement, shown in Figure 3.12(a) was performed directly after the tip was brought in contact with the 50 x 50 μm^2 Pt-pad. Repeated measurements with the N_2 flux held constant are shown in Figure 3.12(d) and exhibit a strong increase of conductance for negative voltages over time. This time-dependence can be identified with a temperature effect, because the tip itself is not separately cooled and warms up the sample on top of the cooled stage, so that 77 K could not be reached for the BTO thin film itself. After cooling down the system, the residual gas within the chamber condensed at the coldest part of the setup and created a thin film, which is visible through the microscope due to interference effects. Figure 3.12(e) shows a camera picture of a measured pad, where the region of the former tip position has another color due to a thinner condense film, caused by heating.

As a result, cooling of the BTO thin film devices helps to make the FE switching visible. Although leakage suppresses the switching signal at room temperature, it can reasonably be concluded that the BTO thin films are ferroelectric.

3.3.2.4 *C-V* Measurements

Another possibility to suppress the influence of leakage compared to the switching response are capacitance measurements. The capacitance also undergoes a maximum at the coercive voltage, but much higher frequencies can be used in this method to avoid leakage effects. In contrast to *P-V* measurements, the frequency ω does not refer to the sweep itself for *C-V* measurements, but - similarly to PFM - to the AC voltage signal, which is superimposed on the DC sweep on a second-time scale.

For dielectric materials, the capacitance is supposed to form a maximum at zero applied voltage, while for ferroelectrics a so-called "butterfly"-curve is measured, which consists of two different peaks, depending on the history of the device. *C-V* measurements can

only be sensibly performed, if the measured capacitor does not show too high leakage. A measure for this is the dissipation factor $\tan\delta = \omega RC$, where R is a parallel resistor, which represents the leakage, and δ refers to the phase-shift angle between real and imaginary part of the impedance. In general, $\tan\delta$ has a similar shape as the capacitance and a value well below 1, if R is small. But for higher leakage, its value can exceed 1, so that also the *C*-*V* measurement in this regime is not reliable.

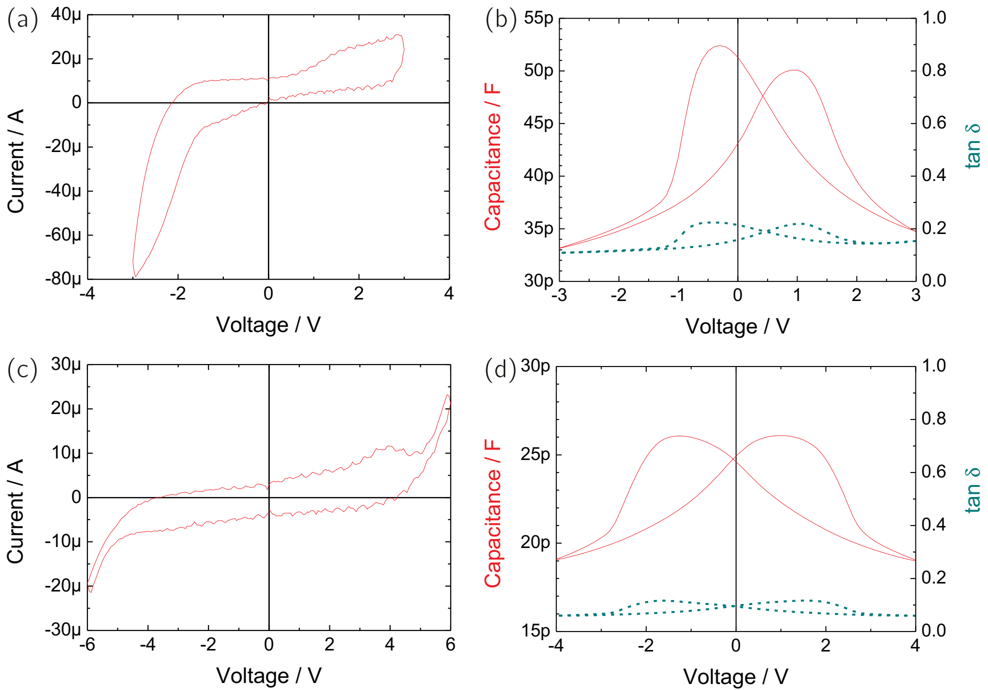

Figure 3.13: *C*-*V* measurements on BTO: (a) FE current response for pad-bottom measurement. (b) Corresponding *C*-*V* measurement. (c) FE current response for pad-pad measurement. (d) Corresponding *C*-*V* measurement.

In Figure 3.13 *P*-*V* and *C*-*V* measurements are shown for the same 30 nm thick BTO sample. Figure 3.13(a) and 3.13(b) refer to *P*-*V* and *C*-*V* measurements of a single capacitor device, while 3.13(c) and 3.13(d) show the respective curves for a pad-to-pad measurement.

The single device current response shows a strong leakage branch for negative voltages and the switching peaks can only be divined at -1 V and 2 V. However, the corresponding *C*-*V* measurement presents a nicely shaped butterfly curve with distinct switching peaks

at −0.4 V and 1 V, while the tan δ imitates this shape with values around 0.2 . For this measurement the excitation frequency was set to 1 MHz with an amplitude of 0.05 V, while the voltage sweep was performed very slowly with 1 s per data point. The very high frequency could successfully suppress the leakage compared to the *P-V* measurement and even the tan δ does not show any rise for higher voltages. The coercive voltage is decreased, as the DC sweep can be regarded as quasi-static, so that relaxation processes reduce the coercive field, analogous to the data shown in Figure 3.10.
For the symmetric back-to-back capacities the leakage in the current response is reduced, but not avoided, and the coercive voltage is enlarged to ±4 V. The corresponding *C-V* measurement shows capacitance values, which are about half of the ones for a single device, which is expected according to the serial addition of capacities. The coercive voltage appears to be around ±1.5 V.

In conclusion, high frequency *C-V* measurements can be used to prove ferroelectric behavior, even if the switching currents are superimposed by large leakage currents in the *P-V* measurements. The coercive voltages are not comparable to DHM, but fairly to SHM due to relaxation processes, and the remanent polarization cannot be determined.

3.3.3 Symmetric $SrRuO_3/BaTiO_3/SrRuO_3$ devices

To test a symmetric stack with TE and BE consisting of $SrRuO_3$, 100 nm BTO were grown by PLD on 30 nm $SrRuO_3$ on $SrTiO_3$ and in-situ 30 nm $SrRuO_3$ were deposited on top of the BTO film. The top $SrRuO_3$ and BTO film were structured by photo-lithography, as sketched in Figure 3.14(a). For the FE characterization, no DLCC application was necessary and the results are shown in Figure 3.14(b). As expected, the leakage currents vanish, as the $SrRuO_3$/BTO interfaces suppress the current much better than Pt, and the larger thickness of BTO might also impinge positively.

Additionally, for this device structure an imprint of $V_I \approx 1.5$ V is visible. A shift of the hysteresis towards positive voltages has already been noticed for the asymmetric devices. Taking into account the new information, the asymmetry in electrode material as sole reason for this shift can be excluded. For the growth of $SrRuO_3$ a strong impact of the interface termination on the film properties is known (Section 2.2.1). Grown as BE, the $SrTiO_3$ has been TiO_2-terminated, while as TE, $SrRuO_3$ is grown on the unterminated BTO film. As a result, the roughness of the surface is increased to $\rho = 12.7$ Å and the crystal quality is assumed to be reduced, although this cannot be made visible due to the

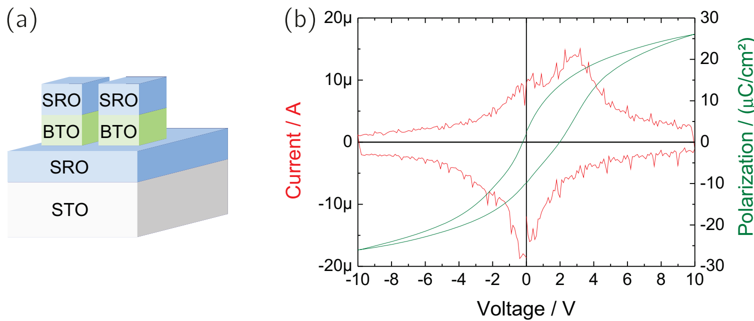

Figure 3.14: Ferroelectric switching of a symmetric BTO sample: (a) Layer stack: $SrTiO_3$ / 30 nm $SrRuO_3$ / 100 nm BTO / 30 nm $SrRuO_3$. (b) Switching behavior of the symmetric device with disabled DLCC.

high-quality $SrRuO_3$-BE. These items can influence the interface properties and lead to unequally charged interfaces, which establish an internal electrical field.

3.3.4 Discussion

Generally, it would be best to be able to deposit an epitaxial BTO thin film with high crystal quality, atomically flat surface, perfect insulating properties and a high remanent polarization. But a sample with all these properties could not be attained. In addition to the challenges of growth, discussed in Section 2.2.2.1, nicely established ferroelectricity seems to appear especially in defect-rich films. In literature, there are studies on growth of BTO [98], but when the FE properties are discussed, in most cases the structural properties are not shown, especially not the surface topography [99, 100, 101, 102, 75]. In [103] both film and FE properties are reported, but here high-pressure sputtering is used for the deposition of BTO. Thus, the impression obtrudes, that the combination of a perfectly epitaxial BTO thin film without leakage but high polarization is very challenging to obtain.

Regarding leakage, the measurement frequency has to be chosen as high as possible to suppress the leakage branch with respect to the FE switching peaks. If these peaks are separated from the leakage in voltage, a leakage compensation (DLCC) can be applied, so that a useful hysteresis is obtained. Post-annealing procedures can improve the resistive properties of the BTO thin films by the incorporation of oxygen from the environment, but will not lead to a perfect insulating system due to the formation of a space charge region. Cooling can be used to visualize the FE effect of leaky devices, as the transport through

BTO is a thermally activated process. *C-V* measurements appear to be a simple and functional tool to circumvent leakage, as the excitation frequency can easily be increased up to the MHz regime.

From the polarity of the leakage branch in $SrRuO_3/BaTiO_3/Pt$ devices and the observation of a suppressed leakage in $SrRuO_3/BaTiO_3/SrRuO_3$ devices, the usage of an oxide $SrRuO_3$ electrode for the bottom as well as for the top contact is recommended.
Still, a (positive) imprint effect is observed for these symmetric devices, which has been ascribed to unequal $BaTiO_3/SrRuO_3$ interfaces. The different terminations of $SrRuO_3$ (Section 2.2.2.2) or an accumulation of charged oxygen vacancies at one interface leads to an internal field, which is directed from bottom to top. For the asymmetric case $SrRuO_3/BaTiO_3/Pt$ this imprint effect is enhanced by the asymmetry of the electrodes.
In contrast to these observations, the imprint, which was measured with PFM on a free BTO surface (Section 3.2) has the opposite polarity, indicating an internal field directed towards the bottom electrode. Once more it becomes clear, that a free BTO thin film possesses different properties compared to an integrated layer and the configuration of the interfaces has a strong impact on the electrical properties of the device.

3.4 ReRAM switching in $BaTiO_3$

For FE measurements, the leakage currents through a BTO capacitor are unintended, as they superimpose the switching response current peaks. But the BTO devices can also be tested for resistive switching properties, where these currents are utilized.
A 30 nm thick BTO thin film stacked between $SrRuO_3$ and Pt, as unusually used for FE characterization (Figure 3.15(a)), is measured in a probe station to look for resistive switching effects.

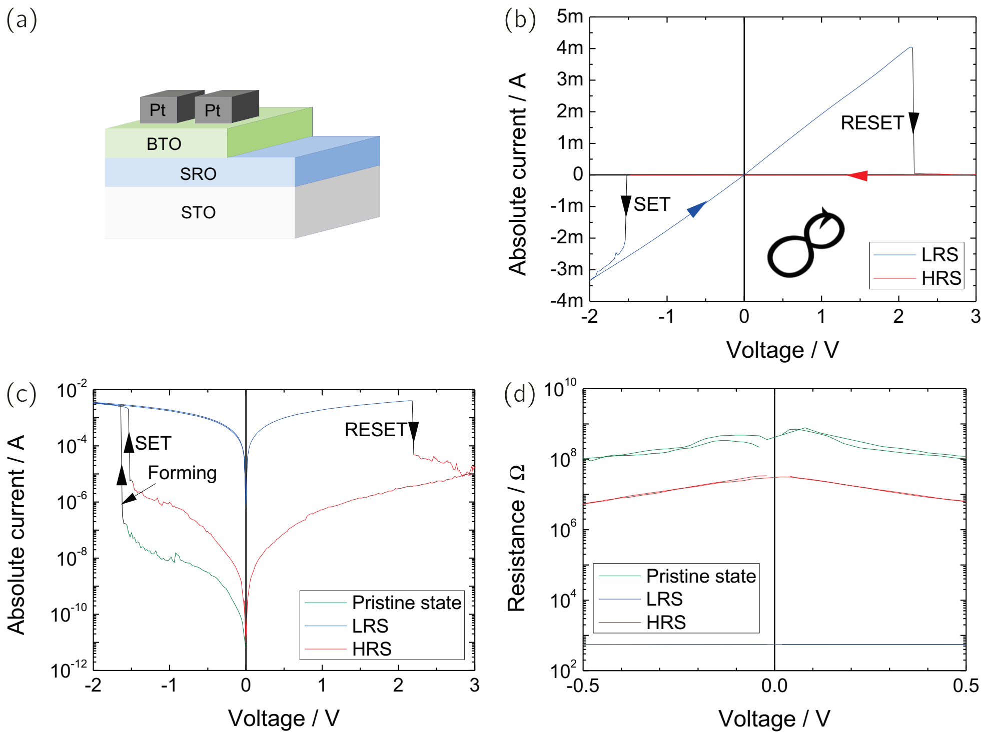

Figure 3.15: Resistive switching of a BTO device: (a) Layer stack STO-SRO-BTO-Pt. (b) Current-voltage characteristic for switching. (c) Current-voltage characteristic for forming and switching on a logarithmic scale for absolute current values. (d) Voltage dependence of the resistances.

After an initial forming step at negative voltages, a reversible resistive switching loop is obtained and plotted on a linear scale in Figure 3.15(b). The switching polarity is "counter-eight-wise", discussed in Section 1.1, implying a RESET for positive voltages. In addition, the device is initially in a very high resistive state, although the currents are

sufficiently high to interfere with the FE switching. This pristine state is formed into the LRS with a negative voltage sweep, as indicated in Figure 3.15(c), upon a sharp current increase over 5 orders of magnitude. The forming procedure looks very similar to the SET process on a linear scale and is therefore not shown. The resistive switching has a counter-eight-wise polarity and the SET as well as the RESET process appear at sharp voltage values. The ON/OFF-ratio has a value of more than 10^4 over a wide voltage range, which becomes even clearer when regarding the resistances in dependence of the voltage in Figure 3.15(d).

Note that the device shows ReRAM switching at voltages $V_{\mathrm{(RE)SET}} \approx \pm 2\,\mathrm{V}$, while an identical device made of the same BTO thin film could be switched ferroelectrically at $V_C \approx \pm 4\,\mathrm{V}$ (Section 3.3.2.3) without showing any electrical breakdown (corresponding to the SET-process). The reason for this behavior can be found in the sweep velocity. While for ReRAM testing a DC voltage sweep is applied, the FE sweep is performed with 2 kHz. According to [104], the ultra-nonlinear switching kinetics in oxide-based ReRAM devices lead to an immense increase of the SET- and RESET-voltage when going to high frequencies.

4 Transport properties of $Pr_{0.48}Ca_{0.52}MnO_3$

4.1 Interplay between structural and transport properties

4.1.1 Resistance measurements

In-plane resistance measurements in a four-point geometry can be used to determine the resistivity of the PCMO thin film material, what will be shown in detail in Section 4.2.1. For these measurements it is important, that all contacts have comparable contact resistances, so that the introduction of metallic pads on top of the PCMO films becomes necessary. Round 50 nm thick Pt-pads with a diameter of 50 µm are sputtered on top of the 50 nm thick PCMO layer, grown on insulating $SrTiO_3$, through a shadow mask. With the help of an optical microscope, these pads can be contacted by needles, which are mounted on probe heads and are thus electrically accessible.
First, all deposited contacts at the four corners of a 5 x 5 mm^2 large sample are tested in two-point geometry with a read-out *I-V* sweep of ± 1 V. A lot of in-plane Pt−PCMO−Pt measurements showed an ohmic behavior, as expected and depicted in Figure 4.1(a). But for many pads, a reproducible non-linear and rectifying *I-V* curve was measured, as shown in Figure 4.1(b). The linear *I-V* curve is expected, as PCMO is a half-metallic *p*-type conductor, which is known to form an ohmic contact to high work function metals as Pt and Au [105].

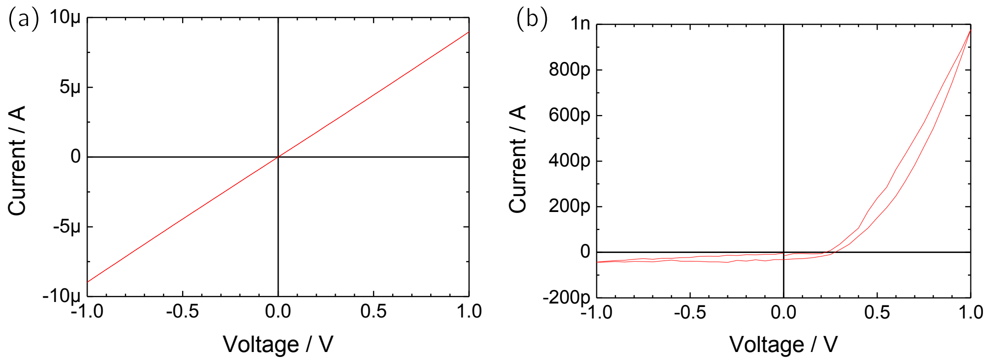

Figure 4.1: Lateral *I*-*V* measurements in PCMO: (a) A Pt–PCMO–Pt measurement, showing the expected ohmic behavior. (b) A Pt–PCMO–Pt measurement, which is extremely non-linear and rectifying.

4.1.2 Appearance of a line structure on the surface of $Pr_{0.48}Ca_{0.52}MnO_3$

During the growth parameter optimization for $Pr_{0.48}Ca_{0.52}MnO_3$ (PCMO), described in Section 2.2.3.1, a surface effect was observed. For thin films grown with a thickness of 50 nm a line structure appears at the surface, as depicted in Figure 4.2(a) and 4.2(b). The pattern varies from sample to sample, but in most cases the lines are mostly oriented parallel or perpendicular to the step edges of the underlying substrate. Moreover, the lines are approximately 2-4 nm high and about 200 nm thick, as it can be seen from a linescan through three lines on the surface in Figure 4.2(c). For very thin PCMO films, the surface topography does not show these features, but even for 20 nm thick films, sometimes very weak lines appeared, which were not yet oriented in such a checkerboard pattern (Figure 4.3(b)).

A similar line pattern is also observed for $Pr_{0.7}Ca_{0.3}MnO_3$ [106] and $LaAlO_3$ [107], where possible explanations reach from walls between different crystallographic domains up to crack formation. Furthermore, the formation of these lines from segregated material is imaginable [63]. In either case, these effects could have a strong impact on the electrical transport properties of the thin film, especially, if the lines go down through the whole film. Thus, the investigation of the checkerboard pattern could help to understand the electrical measurements in Section 4.1.1. Since the observation is a thickness effect, a thickness variation of PCMO was performed.

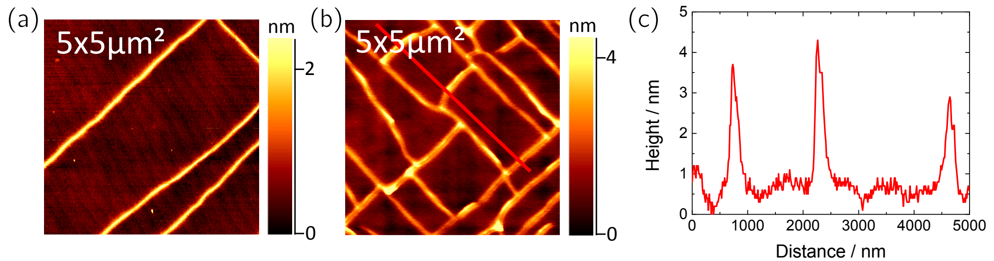

Figure 4.2: Domain structure on 50 nm thick PCMO thin films: (a) AFM image of a 50 nm thick PCMO film, $\rho = 4.3$ Å, showing the typical step terrace structure, superimposed by the checkerboard pattern. (b) AFM image of a 50 nm thick PCMO film, $\rho = 9.2$ Å, showing a more pronounced line pattern. The red line indicates the line profile shown in (c). (c) Height profile perpendicular to three lines of the checkerboard pattern on the surface of the 50 nm-thick PCMO film.

4.1.3 Thickness series of $Pr_{0.48}Ca_{0.52}MnO_3$ on $SrRuO_3$

PCMO layers of the thicknesses 10 nm, 20 nm, 50 nm and 100 nm were grown on 30 nm $SrRuO_3$, which had been deposited on terminated $SrTiO_3$ substrates, presented in Figure 4.3.

Starting with the topography of the thickness series (Figure 4.3(a)-4.3(d)), for 10 nm and 20 nm the step-terrace structure of the substrate is reproduced and for 20 nm disordered, lines start to evolve. For the 50 nm and 100 nm sample, the surface is mainly flat without any remarkable structure, although for most 50 nm thick films the step structure is visible, but superimposed by the line pattern, like in Figure 4.2(a) and 4.2(b).
XRD was performed on these samples and the spectra around STO (002) are shown in Figure 4.3(k). Beside the strong substrate peak and the well established $SrRuO_3$ peak at approximately 46 °, the PCMO peak is visible. For the very thin film of 10 nm the Bragg reflex is relatively broad as a result of the limited c-dimension. It becomes sharper with increasing thickness towards 50 nm, while the peak position stays constant. Thickness fringes are visible for all three films. For 100 nm a second peak has developed at approximately 48 ° with an enlarged out-of-plane lattice constant. The rocking curve becomes broaden with increasing film thickness.
The development of the second peak for the thicker PCMO films could be explained by strain relaxation as described in Chapter 2. To monitor this effect, reciprocal space maps (RSM) were performed for each sample. The results are depicted in Figure 4.3(e)-4.3(h), as intensity plotted in dependence of in-plane lattice constant a^* and out-of-plane lattice constant c^*. The $SrRuO_3$ peak is represented by the small peak above the strong $SrTiO_3$

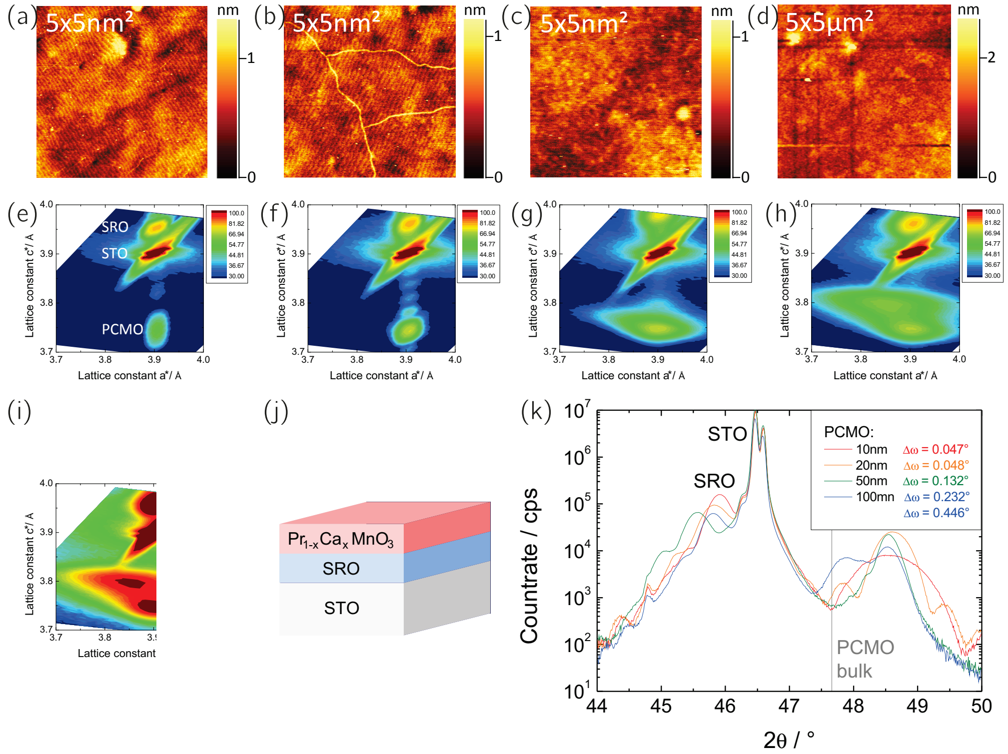

Figure 4.3: Thickness series of $Pr_{0.48}Ca_{0.52}MnO_3$ on $SrTiO_3$: 10 nm, 20 nm, 50 nm and 100 nm: (a) AFM image of the 10 nm-thick PCMO film, $\rho = 2.2$ Å. (b) AFM image of the 20 nm-thick PCMO film, $\rho = 1.7$ Å. (c) AFM image of the 50 nm-thick PCMO film, $\rho = 1.9$ Å. (d) AFM image of the 100 nm-thick PCMO film, $\rho = 5.2$ Å. (e) RSM of the 10 nm-thick PCMO film. (f) RSM of the 20 nm-thick PCMO film. (g) RSM of the 50 nm-thick PCMO film. (h) RSM of the 100 nm-thick PCMO film. (i) RSM of the 100 nm-thick film again, but using another color scale to visualize the two different film peaks for PCMO. (j) Layer stack: STO-SRO-PCMO. (k) XRD spectra around the STO (002) reflex for four different PCMO thicknesses. For 100 nm PCMO a clear double peak is visible. The rocking curves widths for the PCMO peaks for each thickness are listed in the legend. For the 100 nm thick sample the broader rocking curve was measured for the less intense peak.

substrate peak, for which the K_α-splitting is visible. As expected for 10 nm and 20 nm, the PCMO peak has the same in-plane lattice constant a^* as $SrTiO_3$ and $SrRuO_3$, meaning that the system is completely strained. In addition, the thickness fringes are also visible as weak peaks between the $SrTiO_3$ and PCMO reflex. For 50 nm the PCMO peak is becoming less circular, but somehow expands. For 100 nm the case is more clear, as beside the

strained peak a second peak at smaller in-plane, but larger out-of-plane lattice constant appears. For a more obvious view on this fact, the scale was changed for Figure 4.3(h) towards smaller countrate values and shown in Figure 4.3(i). The second peak is caused by a part of the thin film, which is relaxed from strain, as it is located near the bulk lattice constants of PCMO $a^* = c^* = 3.810\,\text{Å}$.

In addition, an even thicker sample of 120 nm was deposited. But this stack was already cracked immediately after the deposition, as can be seen from a photo taken of the sample in Figure 4.4(a). In the central part of the sample the surface is still smooth and glossy, while at the edges the thin film looks very rough. During the next few days the damage progress went on, until the whole sample was roughened. Having a closer look at this damage through an optical microscope (Figure 4.4(b)) the damage can be attributed to a certain peel-off process of the film. The PCMO film is teared in a checkerboard pattern, similar to the line structure. The peel-off region is visible in (Figure 4.4(c)), where also the line-structure can be identified at the left border.

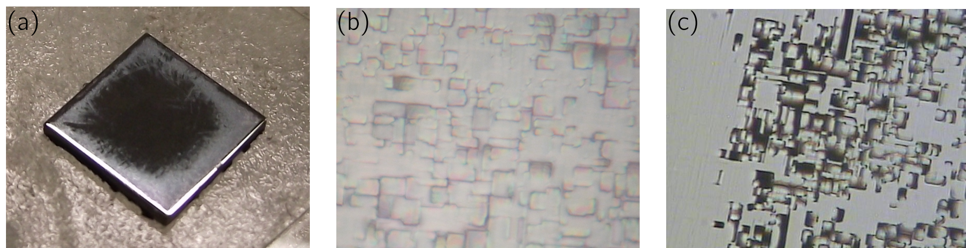

Figure 4.4: Documentation of the peel-off process of the $Pr_{0.48}Ca_{0.52}MnO_3$ thin film due to increased strain: (a) Photo of a 5 x 5 mm^2 sample, where the peel-off process started from the edges and the interior surface is still intact. (b) Photo of the peeled-off part of the sample, taken through a microscope with magnification of 200. (c) Microscope picture of the edge of the peel-off region with a magnification of 200. At the left border the checkerboard line pattern is still visible.

The reason for this behavior might be the increased stress in the PCMO thin film caused by the large mismatch and strain inside the material, which thus relaxes by cracking the predetermined breaking lines instead of introducing more defects. The XRD spectrum of this sample showed only one nicely shaped Bragg reflex for PCMO with a sharp rocking curve of $\Delta\omega = 0.075\,°$, hinting on a totally relaxed film.

4.1.4 XRD investigation: (hkl)-meshes

In [106] the line pattern is explained as domain walls between different crystallographic twin domains in PCMO. To examine, if this could also be an explanation for the observed line structure, the crystallographic orientation of a deposited thin film was investigated. Going back from the pseudo-cubic picture to a more precise consideration of the unit cell for PCMO, it has the orthorhombic crystal structure Pbnm (z=4). Due to the close symmetry relationship between PCMO and cubic $SrTiO_3$ of structure Pm$\bar{3}$m (z=1), PCMO can grow on top of $SrTiO_3$ in six different orientations. These orientations are depicted in Figure 4.5.

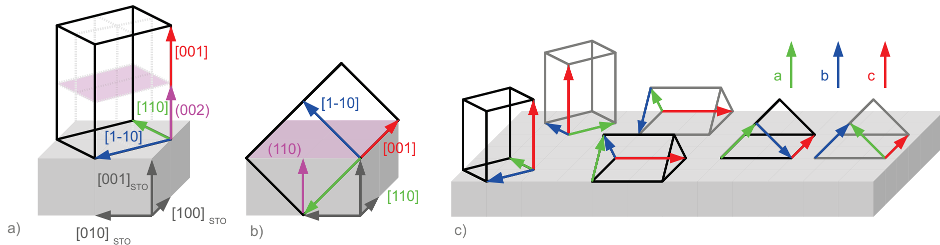

Figure 4.5: Six different orientations of the PCMO unit cell, based on [45]: (a) and (b) show two specific orientations in more detail, while all possibilities are visualized in (c).

For the assumption of completely epitaxial growth on $SrTiO_3$ without any strain relaxation, these six options reduce to three, as the two in-plane lattice constants can be regarded as equal, i.e. the same as of $SrTiO_3$. The three remaining orientations are those of the PCMO *c*-axis aligned along the *a*-, *b*- or *c*-axis of $SrTiO_3$. For each of these orientations a Bragg reflex should be visible near the $SrTiO_3$ substrate reflexes, as for example (101). But going back from the pseudo-cubic picture towards the real rhombohedral lattice (or tetragonal in case of epitaxial growth), the appearing peak would be attributed to three different (hkl)-values, depending on the relative orientation of the PCMO *c*-axis with respect to the $SrTiO_3$ lattice, as sketched in Figure 4.6. Furthermore, an additional weak reflex should appear, caused by the superstructure of the PCMO lattice with respect to the $SrTiO_3$ lattice due to the octahedra tilting. In Figure 4.6 these optional reflexes in the reciprocal lattice are depicted, colored in dependence of the relative PCMO orientation towards $SrTiO_3$.

To investigate, if there are differently oriented PCMO domains in the PLD-grown thin films, four different positions in the reciprocal (hkl)-space are chosen, and measured by XRD on a 40 nm thick PCMO film on $SrTiO_3$, with the assistance of Dr. Karen Friese, JCNS-2. The

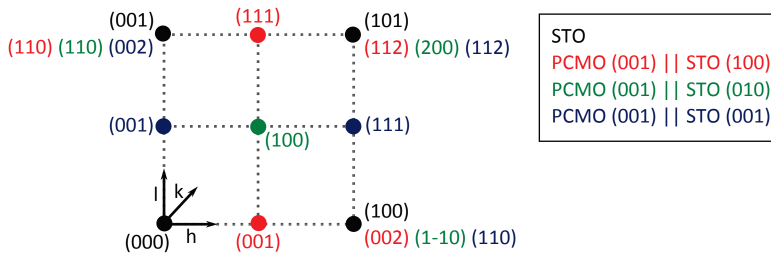

Figure 4.6: Possible reflexes for different orientations of $Pr_{1-x}Ca_xMnO_3$: Beside the reflexes near the $SrTiO_3$-spots, $Pr_{1-x}Ca_xMnO_3$ also forms additional peaks caused by the enlarged unit cell due to the oxygen octahedron tilting. Depending on the relative orientation of the c-axis of $Pr_{1-x}Ca_xMnO_3$ with respect to $SrTiO_3$, different faint reflexes should visible.

so-called *hkl*-meshes are comparable to RSMs, but they refer to the (*hkl*)-values of the underlying $SrTiO_3$ substrate. The reflex positions STO (0.5|0|1), (1|0|1), (0.5|0|0.5) and (1|0|0.5) were chosen to verify the reflex for (1|0|1) and permit a reflex for each possible orientation of PCMO, as deduced from Figure 4.6. The results of these measurements are shown in Figure 4.7.

As expected, a Bragg reflex of PCMO appears near the $SrTiO_3$ (101) peak (Figure 4.7(b)), having the same *h*-value as $SrTiO_3$, which verifies the completeness in strain. For (0.5|0|1) and (0.5|0|0.5), shown in Figure 4.7(a) and 4.7(c), respectively, no peak is visible. For (0.5|0|1) the data set was slightly modified, as reported in Section A.1. Only for (1|0|0.5) a very weak, but significant peak appears, which can be attributed to the PCMO (111) reflex.

Combining this result with the previous considerations, the conclusion is, that only one type of orientation is existing in the thin films and this is the orientation of PCMO (001) parallel to $SrTiO_3$ (001). Thus, the explanation of the line pattern as crystallographic domain walls can be excluded by these measurements.

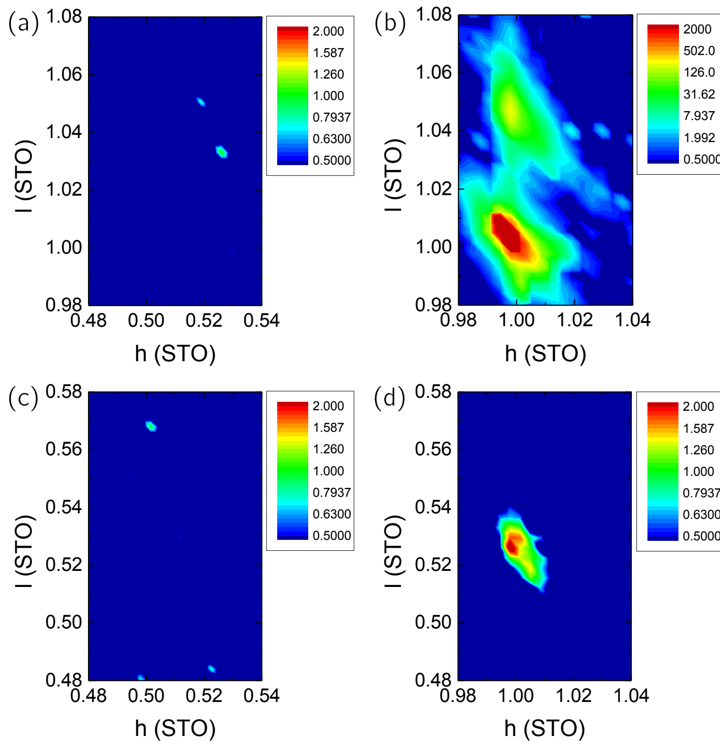

Figure 4.7: hkl-maps around four different possible superstructure reflexes of $Pr_{0.48}Ca_{0.52}MnO_3$. The color code reflects the countrate: (a) hkl-mesh around STO (0.5|0|1): There is no reflex visible. The data set is slightly modified, as result of repeated measurements reported in Section A.1. (b) hkl-mesh around STO (1|0|1): Beside the STO (101) reflex, the $Pr_{0.48}Ca_{0.52}MnO_3$ reflex is visible, confirming the completely strained thin film. This peak corresponds to the almost cubic underlying lattice and is therefore much stronger than the reflexes of the orthorhombic lattice. (c) hkl-mesh around STO (0.5|0|0.5): There is no reflex visible. (d) hkl-mesh around STO (1|0|0.5): A less intense, but significant reflex is visible, which can be identified as $Pr_{1-x}Ca_xMnO_3$ (111) reflex, giving a hint on an orientation of the $Pr_{1-x}Ca_xMnO_3$ c-axis parallel to the $SrTiO_3$ c-axis.

4.1.5 SEM-assisted micro-probe measurements

The in-plane conductance across a straight line is of crucial interest, as it might have an influence on macroscopic resistivity measurements. For these investigations a 40 nm thick PCMO film, grown on an insulating $SrTiO_3$ substrate, is used.

A special nanorobotic station [108] at the IAC, RWTH Aachen, is used for these measurements, performed by Dr. Michael Noyong. In the vacuum chamber of a scanning electron microscopy (SEM, LEO Supra 35VP) the system can be equipped with up to four nanomanipulators (Klocke Nanotechnik). For the electrical addressing of the structures, metalized AFM tips are mounted to the piezo driven nanomotors. The positioning precision is less than 1 nm. The electrical characterization was done by using a parameter analyzer.

For the investigations of the PCMO thin film, only two micro probes are used for two-point *I*-*V* measurements. The AFM tips are previously covered with a Pt/Ir (80/20) alloy to achieve the best possible electrical contact to the surface. To locate the tips at precise positions, the SEM is used, whereby the electron beam is completely blanked out by a beam blanker (Raith) to exclude parasitic current. The results are depicted in Figure 4.8.

Figure 4.8(a) shows the SEM image of the surface of the PCMO sample. The checkerboard structure is clearly visible, so that the tips can be positioned precisely onto certain domains. After several test measurements, two tips are positioned into two different domains with a straight line in-between (measurement 20, Figure 4.8(c)). The left tip is fixed at its position, while the right tip is moved. The subsequent measurement is performed with the right tip located inside the same domain as the left tip, i.e. without any domain boarder in-between (measurement 21, Figure 4.8(d)). Afterwards, both measurements are repeated successively to reproduce the measured results (Figure 4.8(e) and 4.8(f)).
The results of the corresponding *I*-*V* sweeps are shown in Figure 4.8(b). A voltage sweep of up to ± 1 V was applied for the electrical measurements, which are reproducible, as it can be seen from almost identical measurements, respectively. The small deviations can be explained by the repositioning of the right tip. In addition, thermal drift of the sample stage and noise, caused by very small currents, have an influence on the measurement. For the measurements with the tips located in two different domains, so that the current had to flow across a border, currents in the range 10-100 pA were measured. For measurements without any boarder to cross currents up to 1-10 nA were detected. For the approximately same distances between the two tips and the same applied voltages, the current across a domain wall is a factor of 100 smaller than for directly connected tips via one domain of the PCMO thin film.

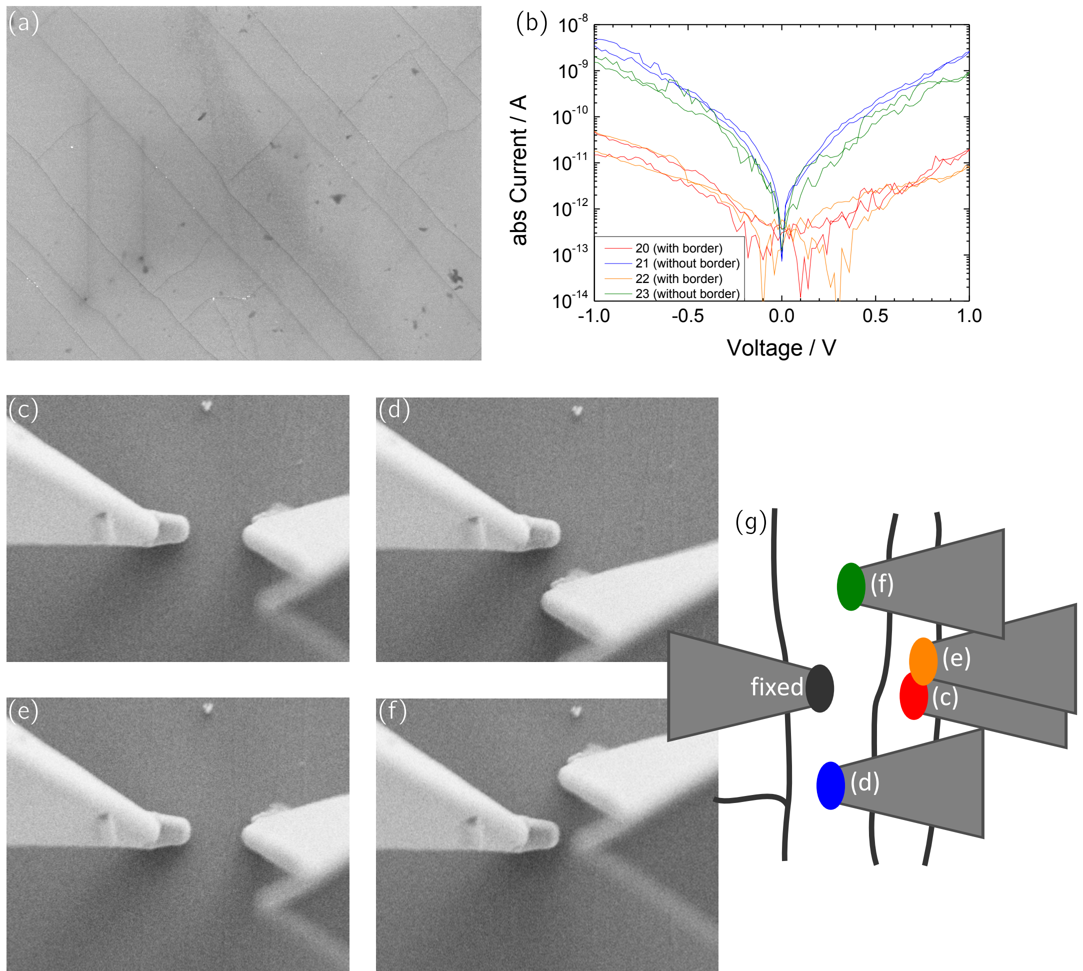

Figure 4.8: SEM-assisted micro-probe measurements of the domain structure of PCMO: (a) SEM image of the PCMO surface, where the line structure is clearly visible. Therefore, the Pt-covered AFM-tips could be carefully set into the same domain or two neighboring ones. Four successive measurements (20-23) at different tip positions were performed in an alternating way to verify the measurements. Measurement 20 and 22 were performed with the tips in two different domains, while for 21 and 23 the tips were set within one domain. (b) The I-V characteristics at four different tip positions show a large and reproducible change of two orders of magnitude in current. (c)-(f) The corresponding SEM images for measurements 20-23 show, that the left tip was left at the same position, while the right tip was moved. (g) As the lines in the SEM images (c)-(f) are hardly visible, the sketch shows the tip positions relative to the line structure. The color code refers to (b).

From this information one can conclude, that the checkerboard structure is not a surface effect, but the lines, which are visible on the surface, go through the whole film down to the bottom interface. Thus, the line pattern as a pure surface effect is disproved as well, so that the formation of cracks is left as a possible explanation.

For further investigation of the line-pattern on top of thicker PCMO thin films, local-conductivity AFM (LC-AFM) measurements were performed. The addressed question for experiments using this setup is the out-of-plane conductance, i.e. from the surface to the bottom. As the results did not contribute to a deeper understanding, they are shown in the Appendix in Section A.2.

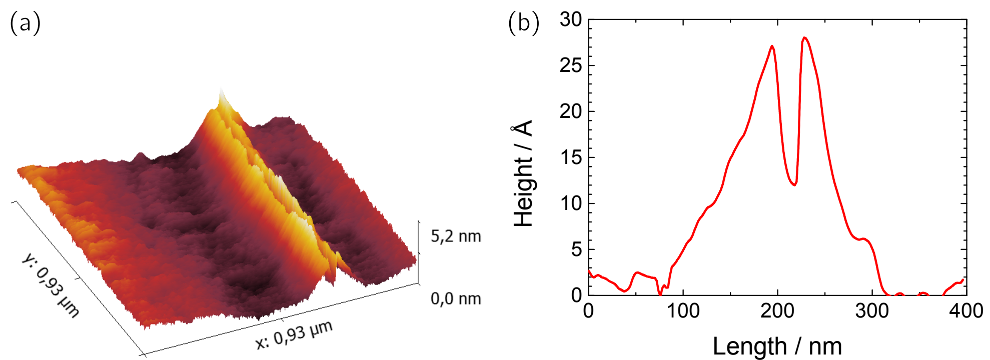

Figure 4.9: LC-AFM measurements in non-conducting mode: (a) Topography of a 50 nm thick PCMO layer grown on top of $SrRuO_3/SrTiO_3$, measured with LC-AFM using a non-conducting tip in contact mode. The surface shows one line of the checkerboard pattern. (b) Line-scan of 4.9(a) perpendicular to the line-pattern. In these vacuum conditions, also a gap within the ridge is observable.

As a first test for LC-AFM, a non-conducting AFM tip was used to scan the topography of the PCMO film. The result of a 1 x 1 μm^2 scan is shown in Figure 4.9(a), which covers a straight line of the checkerboard pattern. Compared to the AFM pictures, taken with the usually used AFM in air and tapping mode, the lateral resolution is much better, because the tip is sharper and a vacuum of the order of 10^{-9} mbar prevents the surface of quick coverage with adsorbates. A linescan perpendicular to this ridge is plotted in Figure 4.9(b). The lateral and vertical dimensions of the lines, assessed in Section 4.1.2, are verified with this measurement. In addition, a deep gap within the line is observable with this technique, although the minimum value might be at a lower value, as the tip might have been too thick to scan the gap correctly. This measurement points clearly on the formation of cracks.

4.1.6 TEM investigations of domain walls

To check the assumption of crack formation at the line structure, transmission electron microscopy (TEM) investigations were performed by Kerry O'Shea, University of Glasgow. As described in Section 2.2.2.2, the surface of a 40 nm thick PCMO film is carefully covered by evaporated Pt and a thin lamella is cut out by FIB. The results of TEM and diffraction measurements on this cross-section, as well as high resolution scanning transmission electron microscopy (HR-STEM) are depicted in Figure 4.10.

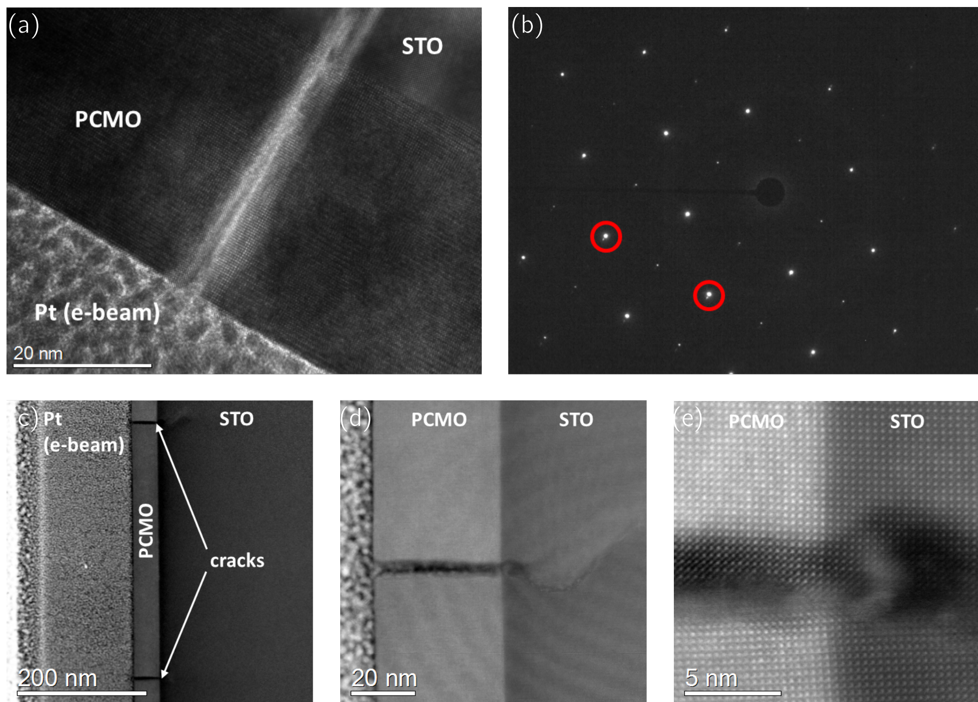

Figure 4.10: TEM/HR-STEM investigations on PCMO showing the line pattern: (a) Bright field TEM image of one crack. (b) Diffraction pattern of the whole stack. Spot splitting due to different crystallographic orientations on either side of the crack is visible (red cycles). (c) HR-STEM image of two cracks within the whole stack. (d) HR-STEM zoom-in to one crack within the PCMO, propagating into the $SrTiO_3$. (e) HR-STEM close-up at the PCMO/$SrTiO_3$ interface.

An overview TEM bright field image of the cross-section underneath one line on PCMO is shown in Figure 4.10(a). An obvious crack perpendicular to the PCMO film surface can be observed. The polycrystalline Pt has a grainy structure, while PCMO and $SrRuO_3$

are perfectly single crystalline, apart from the crack, which is lying just below the line on top of PCMO. The crack extends through the full thickness of the PCMO layer and also proceeds into the $SrTiO_3$ substrate. Where the PCMO broke, the gap has been filled with Pt during the TEM preparation. An electron diffraction pattern was additionally recorded in the TEM (Figure 4.10(b)). As a result of the slightly different crystallographic orientations on either side of the crack, the diffraction spots got split. The HR-STEM images Figure 4.10(c)-4.10(e) show the stack in the surrounding of the line structure on PCMO a bit more precisely and Figure 4.10(d) reveals the strain field upon crack formation. In Figure 4.10(e) even the small disorientation of PCMO is visible, which goes together with the crack formation and causes the spot splitting in the diffraction pattern (Figure 4.10(b)). The spacing between the cracks is in the µm-scale.

The results gained by TEM and HR-STEM now clearly verify the previous assumption. Instead of the formation of more and more dislocations and defects within the crystal upon an increase in stress, caused by the lattice mismatch to $SrTiO_3$, PCMO reacts to this strain by the formation of microscopic cracks. Thus the lusterless surface of thick PCMO films shown in Section 4.1.3 can be explained. The material becomes detached from the substrate at those positions, where the sharp gaps have been for smaller film thickness. In addition, the cracks can easily explain the two orders of magnitude decrease in conductance upon integration of a line into the direct current path, reported in Section 4.1.5, and thus the non-linear current signal, shown in Section 4.1.1. The cracks act as additional serial resistances. For some pads, a percolation path will be found without crossing any boarder, so that the resulting characteristic is ohmic. But if, by chance, such a path does not exist, the current is blocked by one ore more domain walls and thus the *I*-*V* curve gets non-linear or even rectifying.

It has become visible in Section 4.1.3 that not all thicker PCMO films show the line structure on the surface, which is identified with crack formation. Thus the question arises, how the strain is reduced in these films. Therefore, a smooth 50 nm thick PCMO film on $SrTiO_3$ has been additionally investigated by (HR-)STEM and the results are shown in Figure 4.11.

Figure 4.11(a) shows a HR-STEM image of size 12.5 x 12.5 nm^2 at the interface between $SrTiO_3$ and PCMO. By masking relevant frequencies in the Fourier transform of this image, as depicted in Figure 4.11(b), an edge dislocation within the PCMO layer is identified, which is located near the $SrTiO_3$ interface with a distance of about 1.5 nm (red box). A detailed explanation of this technique can be found in Section A.3. A larger section of

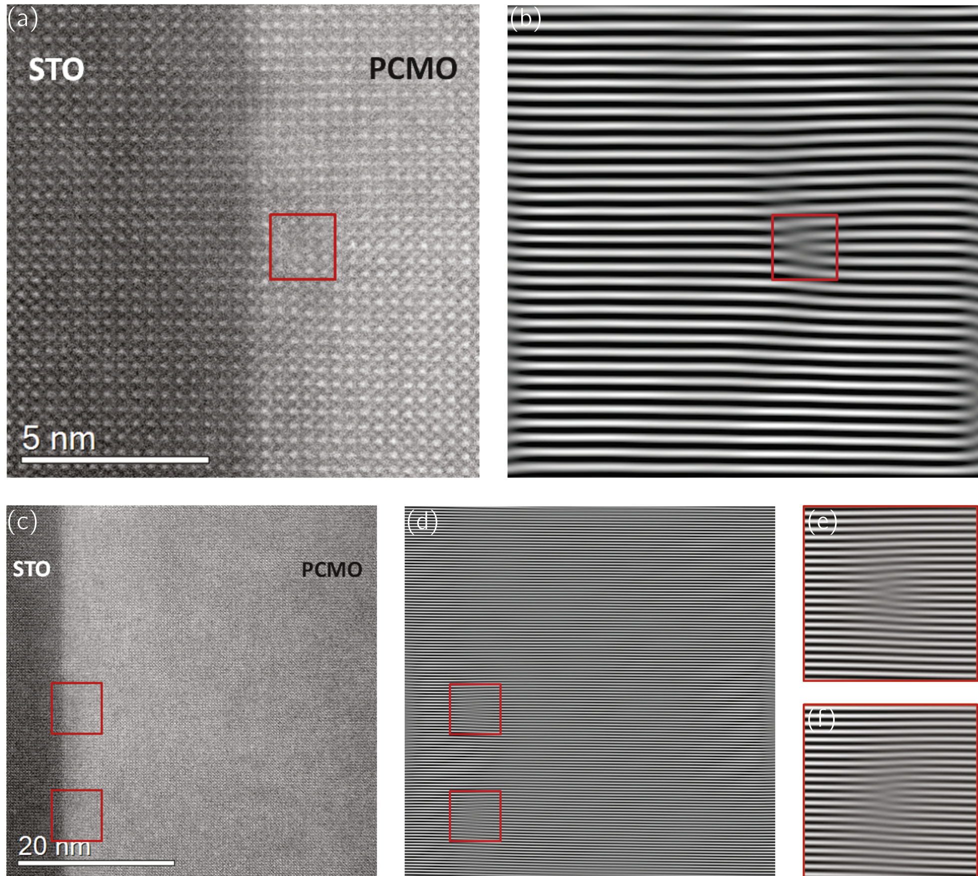

Figure 4.11: TEM/HR-STEM investigations on PCMO having a smooth surface: (a) HR-STEM image of size 12.5 x 12.5 nm^2. (b) Corresponding image after Fourier analysis, uncovering an edge dislocation. (c) STEM image of size 50 x 50 nm^2. (d) Corresponding image after Fourier analysis. (e),(f) Close-ups of the two visible edge dislocations.

50 x 50 nm^2 of the cross-section is presented in Figure 4.11(c) and the corresponding Fourier analyzed image in Figure 4.11(d) with close-ups of both appearing dislocations in 4.11(e) and 4.11(f). Here again the critical thickness for the dislocation formation appears to be $d_c \approx 1.5$ nm.

The density of dislocations, which is necessary to relax the system completely, can be calculated from geometrical considerations [109]. For the assumption of a very thick PCMO film with $d \gg d_c$, which is valid in this case, the dislocation density can be calculated

according to

$$\rho_d = \frac{a_{\text{STO}} - a^*_{\text{PCMO}}}{a_{\text{STO}} \cdot a^*_{\text{PCMO}}}.$$

For the PCMO thin film on $SrTiO_3$ a value of $\rho_d \approx 0.06\,\frac{1}{\text{nm}}$ is obtained, leading to 3 dislocations within the window of 50 nm. This value fits to the observed number of dislocations, as they are not homogeneously distributed over the entire thin film.

4.1.7 Discussion of the line structure

A similar line structure was also observed for $La_{1-x}Ca_xMnO_3$ (LCMO) thin films with $x = 0.5$ and $x = 0.66$ [110]. The pattern is identified with cracks as well and attributed to the thermal expansion mismatch between the substrate $SrTiO_3$ and the LCMO film.
Actually, the thermal expansion coefficients for $SrTiO_3$ and mixed-valence manganites at room temperature do not vary much. For $SrTiO_3$ a volumetric thermal-expansion coefficient around $\alpha_V \approx 3 \cdot 10^{-5}\,\frac{1}{\text{K}}$ is reported [111]. Assuming a cubic lattice structure for $SrTiO_3$, the system expands isotropically upon heating and thus the linear thermal-expansion coefficient is approximately $\alpha_L \approx 1 \cdot 10^{-5}\,\frac{1}{\text{K}}$ [112].
For different manganites, linear thermal-expansion coefficients slightly below $\alpha_L \approx 1 \cdot 10^{-5}\,\frac{1}{\text{K}}$ are reported [113, 114]. Although for orthorhombic manganites a large deviation between the linear expansion coefficients is known between the *c*-axis and the *a*- and *b*-axes, which can also exhibit negative coefficients [115], the average volumetric expansion is comparable to the value for $SrTiO_3$. Besides, manganites show a sharp peak in their thermal-expansion coefficient for the (anti)ferromagnetic phase transition temperature, which could lead to an increased stress within the material. But this transition is well below room temperature and therefore not responsible for the crack formation.

A likely explanation for the crack formation can be found in the elastic deformation of the epitaxially grown thin film itself [116, 117].
As discussed in Section 2.1.1, tensile strain ϵ_m results from the elastic mismatch between the smaller thin film lattice constant compared to the substrate and arises for the growth of manganites and $LaAlO_3$ on $SrTiO_3$. The elastic properties of a thin film determine, if a material is more ductile or brittle, and the elastic biaxial modulus M_{film} is the relevant measure for it. The occurring stress $\sigma_m = \epsilon_m \cdot M_{\text{film}}$ is the product of the strain and the elastic modulus. The strain energy per atom $E_{\text{atom}} = M_{\text{film}} \cdot \epsilon_m^2 \cdot a_{\text{film}}^3$ with the film lattice parameter a_{film}, which is stored within the thin film due to the elastic stress, is constant, so that the total strain energy is increased during the thin film growth. Since the elastic energy

is the driving force for strain relaxation, crack formation starts as soon as its threshold energy is reached. Over all, the elastic material properties determine, to which extent the system is stressed by a certain strain and thus at which thickness the elastic energy exceeds the energy for crack formation.
Cracks only form for tensile strained materials, as for compressively strained thin films such as $BaTiO_3$ and $SrRuO_3$, grown on $SrTiO_3$, cracks would not release the stress. Thus, these materials tend to form dislocations and extended defects to relax the built-up stress (Figure 2.1(b)).

It has been observed that for PCMO film thicknesses above 40 nm the line structure on the surface can appear (Figure 4.2), but is not necessarily visible (Figure 4.3). After stress relaxation is found to be the origin for crack formation in tensile strained thin films, also the case of smooth surfaces has to be considered. The TEM results in Figure 4.11 show that the regular incorporation of edge dislocations is the origin of strain relaxation in thicker PCMO films, which do not exhibit the checkerboard pattern.
In addition, for the PCMO thickness series in Figure 4.3 the rocking curve width increased with increasing thickness, while the damaged sample in Figure 4.4 showed a very sharp peak in the ω-scan. Combining theses results, the rocking curve of the films could provide a detailed view on the relaxation.

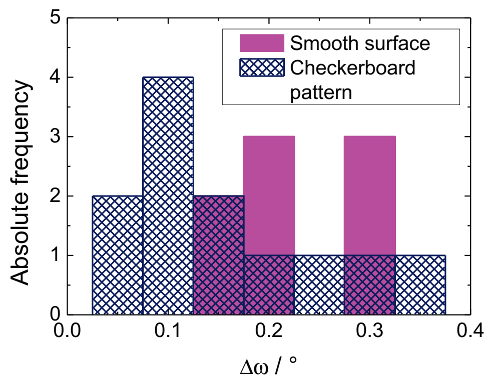

Figure 4.12: Statistics on 50 nm thick PCMO thin films: For 20 samples the rocking curve widths are shown in a histogram of 0.05° intervals. Previously they were classified by their surface structure using the AFM images.

Figure 4.12 presents the statistical distribution of rocking curve widths for 50 nm thick PCMO samples with and without checkerboard pattern. Although the statistics are not really large with an overall number of 20 samples, a remarkable difference is visible between

samples showing the line pattern or not. In general, the crystal quality seems to improve, when the checkerboard pattern appears. For these samples, an almost Gaussian distribution around $\Delta\omega \approx 0.1^\circ$ is observed, while for the samples with smooth surface structure an average value of $\Delta\omega \approx 0.2^\circ$ is measured.

A broader rocking curve is the fingerprint for the formation of crystal imperfections such as dislocations. Thus, the broad rocking curves result from the incorporated edge dislocations near the bottom interface to $SrTiO_3$. For a PCMO film with the line structure, the crack formation leads to a relaxation of the residual stress, so that no incorporation of defects is needed and the rocking curves appears sharper. Thus, one has to distinguish between two different competing relaxation mechanisms in tensile strained manganites: Generation of crystal defects and crack formation.

The question, which parameter is responsible for the type of strain relaxation, is hard to address, because the deposition parameters have not been changed. In [117] the oxygen partial pressure during growth is suggested to have the largest impact on the actual stress within the thin film. But the pressure can be controlled very precisely during the deposition, as reported in Section 2.1.2.1. A hidden parameter, which cannot be manually accessed during growth, seems to determine the kind of relaxation process in PCMO.
From these results, the appearance of the line structure seems to be an alternative to the formation of edge dislocations of the thin film to relax its residual stress.

4.2 Bulk transport in $Pr_{0.48}Ca_{0.52}MnO_3$

4.2.1 Resistivity measurements at room temperature

The sheet resistance R_S can be determined for any closed and homogeneous thin film of arbitrary shape with the so-called van-der-Pauw method [118]. The big advantage of this 4-point measurement is that the influence of Pt-contacts and cables on the measured resistance is avoided, because different pads are used for the application of the current and the measurement of the voltage drop. With a known film thickness d, the resistivity ρ is given by $\rho = R_S \cdot d$.
The sheet resistance R_S is determined by the combination of two different measurements, for which current and voltage measurement are decoupled. A current I is swept between the contacts 1 and 2, while the voltage drop is measured between contacts 3 and 4 at the opposite side of the sample, as shown in Figure 4.13. Subsequently, an identical current sweep is applied between contact 1 and 4 and the voltage is measured between 2 and 3. After the determination of the two resistance values $R_{12:34}$ and $R_{14:23}$ as the inverse values of the slopes of linear regressions to the current-voltage characteristics, the sheet resistance can be calculated to

$$R_S = \frac{\pi}{2\ln 2} \cdot F(Q) \cdot (R_{12:34} + R_{14:23}).$$

$F(Q)$ is the symmetry factor, taking into account the geometric anisotropy. The quality factor Q is defined as

$$Q = \begin{cases} \frac{R_{12:34}}{R_{14:23}} & \text{for} \quad R_{14:23} \leq R_{12:34} \\ \frac{R_{14:23}}{R_{12:34}} & \text{for} \quad R_{14:23} \geq R_{12:34}. \end{cases}$$

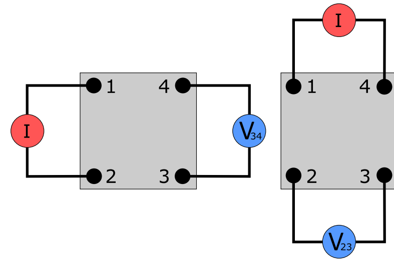

Figure 4.13: Sketch of the two different setups in van-der-Pauw geometry: (12:34) and (14:23).

For $Q < 10$, $F(Q)$ can be approximated by $F(Q) \approx 1 - 0.34657\left(\frac{Q-1}{Q+1}\right)^2 - 0.009236\left(\frac{Q-1}{Q+1}\right)^4$ [118]. For the ideal case of a square, homogeneous thin film with punctiform contacts in the corners, $Q = F = 1$ is valid.

From Section 4.1 the obstacle of cracks within the PCMO thin films and their consequence on the resistance is known. For the van-der-Pauw method, the two-point resistance measurements between each of the four pads on one sample need to show ohmic behavior (Figure 4.1(a)) for the measurement to be appropriate. In other words, if one of the

two-point measurements has a non-ohmic behavior (Figure 4.1(b)) due to crack formation discussed in Section 4.1, the van-der-Pauw measurement cannot be performed. Nevertheless, some samples did show ohmic behavior for all four pads and thus could be used to determine the resistivity of PCMO.

From reliable resistivity measurements on PCMO with a quality factor of $1.2 - 1.5$, a resistivity of $\rho = 30\text{-}40 \cdot 10^3$ µΩcm was determined in van-der-Pauw geometry. This value is comparable to the literature value of $\rho \approx 20 \cdot 10^3$ µΩcm [119].

For comparison, elementary metals range from 1.6-96.1 µΩcm [120] for the best conducting metal silver and less good conducting liquid mercury, respectively.

For the used BE $SrRuO_3$, a resistivity of $\rho = 300$ µΩcm was measured, which is a factor of 100 less then for the active layer, but only factor 3 more than for the metal Hg. This implies, that $SrRuO_3$ is very useful as perovskite (high work function) metal electrode.

For $La_{0.7}Sr_{0.3}MnO_3$ the literature values reach from $\rho = 300\text{-}2000$ µΩcm [54, 53]. For the samples, produced in this work, a resistivity of $\rho = 1000$ µΩcm was measured, which is comparable to literature and enables this material for usage as BE as well.

4.2.2 Hall measurements

In addition to the van-der-Pauw measurements, from which the resistivity of the material can be calculated, Hall measurements were performed by Hajo Molegraaf, MESA+, University of Twente. With this technique, the carrier type and concentration can be determined.

The same sample geometry as for van-der-Pauw measurements can be used, but the contacts have to be connected in a different way. A current I is driven through contacts 1 and 3, diagonally through the sample (Figure 4.13). Simultaneously, a constant magnetic field B is applied, which is directed perpendicular to the surface of the thin film of thickness d. Between the contacts 2 and 4 the Hall voltage V_H is measured, which results from the sidetracking of carriers due to the Lorentz force:

$$V_H = R_H \cdot \frac{I \cdot B}{d} \qquad \text{with the Hall constant } R_H = \frac{1}{n \cdot q}.$$

The determination of the Hall constant R_H is the aim of the measurement, because n is the carrier concentration and $q = \pm ie$ is the charge of one carrier of valence i. The Hall constant can be calculated to $R_H = \frac{V_H \cdot d}{I \cdot B}$, if a constant current is applied, and to $R_H = R_{13:24} \cdot \frac{d}{B}$, if a current sweep is performed (Figure 4.13).

For the Hall measurement, a 50 nm thick PCMO film was grown on $SrTiO_3$ and 50 nm thick Pt-contacts were sputtered on top through a shadow mask in van-der-Pauw geometry.

The magnetic field was altered between ±9 T at room temperature and the corresponding resistance $R_{13:24}$ perpendicular to the applied voltage was measured. The result is depicted in Figure 4.14(a).

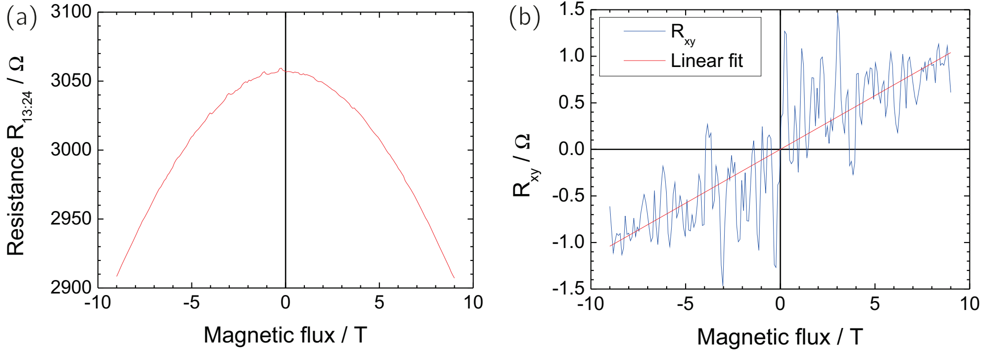

Figure 4.14: Hall measurements on PCMO: (a) Resistance perpendicular to the applied current, measured for an altered magnetic flux. (b) Hall-resistance of PCMO.

In general, the measured resistance is a superposition of the resistance caused by the Hall-effect R_{xy} and the magneto-resistance of the material R_{xx}. For most materials, the Hall effect caused by the magnetic field is much larger than its impact on the sheet resistance, so that the linear (centrically symmetric) dependence of the hall resistance is only slightly modulated by the axially symmetric B-field dependence of the sheet resistance. For PCMO, the situation is the other way around, as the measured resistance $R_{13:24}(B) = R_{xy}(B)+R_{xx}(B)$ in Figure 4.14(a) has an almost completely axially symmetric shape around $B = 0$. Using the different symmetries of both terms, the Hall-term can be obtained by the subtraction $\frac{1}{2}[R_{13:24}(B) - R_{13:24}(-B)] = \frac{1}{2}[R_{xy}(B) + R_{xx}(B) - R_{xy}(-B) - R_{xx}(-B)] = R_{xy}(B)$, shown in Figure 4.14(b). The large carrier concentration in PCMO, discussed in Section 1.2, reduces R_{xy}, while the resistivity is relatively high for a highly doped semiconductor. That is the reason for the large noise on the calculated signal.
The slope of the linear fit $m = \frac{R_{xy}}{B}$ multiplied with the film thickness d is the Hall constant $R_H = d \cdot \frac{R_{xy}}{B} = \frac{1}{n \cdot q}$. Assuming an electronic charge transport with $q = \pm 1 \cdot e$, the carrier density can be calculated to $n = \frac{1}{e \cdot d \cdot m}$. The slope of R_{xy} is determined to $m = +0.12\,\frac{\Omega}{\mathrm{T}}$. The positive sign of the slope implies that the charge of the carriers is positive and thus hole transport is verified as transport mechanism. In addition, the carrier concentration is determined to $n_h = p = 1.04 \cdot 10^{21}\,\frac{1}{\mathrm{cm}^3}$. For a repetition of the measurement a value of $p = 1.49 \cdot 10^{21}\,\frac{1}{\mathrm{cm}^3}$ was obtained, hinting on the large error of this carrier concentration

caused by the noise on the measured signal, so that the determined value should be regarded as rough estimation.
The obtained result is approximately a tenth of $p = \frac{0.52}{(3.810\,\text{Å})^3} = 9.4 \cdot 10^{21}\,\frac{1}{\text{cm}^3}$, which results from the simple calculation of the doping level with respect to the unit cell volume.

4.2.3 Temperature dependence of resistance

Beside the room-temperature resistance measurements, also temperature-dependent transport measurements were performed for three different manganites.
50 nm thick manganite thin films were grown on $SrTiO_3$ and Pt contacts were sputtered on top in van-der-Pauw geometry. The samples were mounted into a He^4 continuous-flow cryostat, which sample chamber can be evacuated down to 10^{-5} mbar to avoid impairment of the measurement by water or nitrogen condensation. The Helium flux through the cryostat can be adjusted, while the sample stage can be heated simultaneously to obtain a good temperature control. For the measurement, the sample temperature was decreased in discrete steps and it was waited for the temperature to stabilize. For each temperature, two read-out *I*-*V* sweeps in van-der-Pauw geometry were performed and the sheet resistance and thus the resistivity was determined.
The results for those temperature-dependent resistivity measurements for $La_{0.7}Sr_{0.3}MnO_3$, $Pr_{0.48}Ca_{0.52}MnO_3$ and $Pr_{0.6}Ca_{0.4}MnO_3$ are depicted in Figure 4.15.

The resistivity of $La_{0.7}Sr_{0.3}MnO_3$ at room temperature is about 1000 µΩcm and drops down to 270 µΩcm upon decreasing the temperature to 30 K, as shown in Figure 4.15(b). Beside the large deviations from a linear dependency for higher temperatures, the resistivity shows a clear metallic behavior with a linear temperature coefficient of $\alpha = 2.7 \cdot 10^{-3}\,\text{K}^{-1}$, which is comparable to metals.
For $Pr_{1-x}Ca_xMnO_3$ the case is different. For both stoichiometries $Pr_{0.48}Ca_{0.52}MnO_3$ (Figure 4.15(c)) and $Pr_{0.6}Ca_{0.4}MnO_3$ (Figure 4.15(d)) the resistivity at room temperature is about $90 \cdot 10^3$ µΩcm and $800 \cdot 10^3$ µΩcm, respectively, and increases upon cooling by up to 4 orders of magnitude. This behavior is typical for semiconductors according to

$$\rho(T) = \rho_0 \cdot e^{\frac{\Delta E}{k_B T}},$$

where ρ_0 is a pre-exponential factor, k_B is the Boltzmann constant and ΔE is the specific activation energy [121]. From the respective Arrhenius plot in the insets, this activation energy could be extracted by linear regression. For $Pr_{0.48}Ca_{0.52}MnO_3$, most data points are

(a)

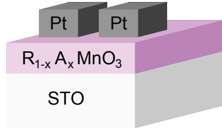

(b)

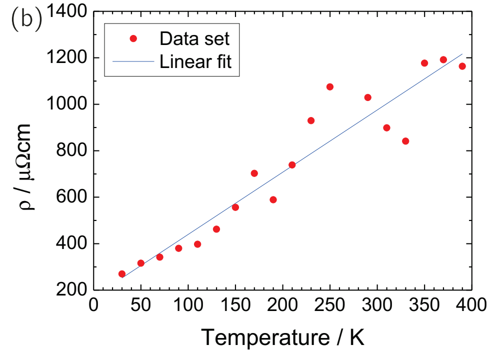

(c)

(d)

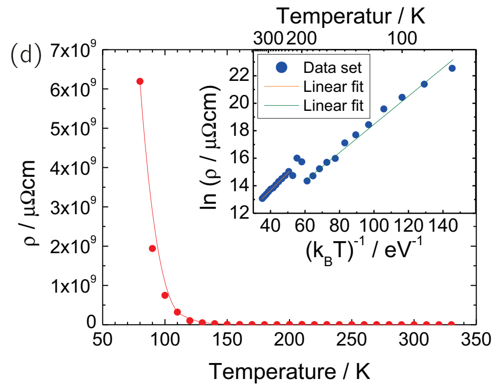

Figure 4.15: Temperature dependence of the resistivity for three different stoichiometries: (a) Layer stack: STO-RAMO-Pt. (b) $La_{0.7}Sr_{0.3}MnO_3$: The resistivity drops with decreasing temperature. This behavior is typical for metallic materials. (c) $Pr_{0.48}Ca_{0.52}MnO_3$: The resistivity is dramatically increased upon temperature decrease down to 133 K. The reliable data set is shown in an Arrhenius plot in the inset. (d) $Pr_{0.6}Ca_{0.4}MnO_3$: A similar behavior of the resistivity is observed as for PCMO. The inset shows again the Arrhenius plot.

arranged in one straight line, so that the activation energy was calculated to $\Delta E = 0.12\,\text{eV}$, comparable to literature [122, 123, 60], while for $Pr_{0.6}Ca_{0.4}MnO_3$ two slopes could be found
green line).
For classical semiconductors, this activation energy can be attributed to half of the band gap or the distance of the dopant state to the band edge. For manganites, not the carrier concentration is thermally activated, but the mobility of the charge carriers. Thus the activation energy has to be identified with the energy barrier for polaron hopping.

4.2.4 High temperature measurements in miscellaneous oxygen ambience

The resistance of PCMO after equilibration at high temperatures in different oxygen partial pressures was measured in the high temperature equilibrium conductance (HTEC) measurement setup. For this experiment, 100 nm thick Pt contacts are deposited by sputter deposition through a shadow mask in four-point geometry to avoid the influence of contact resistances. The pads are connected to the sample holder with wrapped Pt wire, which is mounted into an yttria-stabilized zirconia (YSZ) tube. This tube is used as an oxygen pump, which allows a continuous adjustment of the oxygen partial pressure between 1000 mbar and 10^{-20} mbar. The YSZ pump is located in a Al_2O_3 tube furnace, which provides high temperatures between 550 °C and 1000 °C. A detailed description of the HTEC setup and working principle can be found in [70].

As a first test, a 40 nm thick PCMO film grown on $SrTiO_3$ was used for high temperature equilibrium measurements. The deposition temperature of 700 °C was applied and the conductance was monitored. As soon as the signal did not change any more over time, the equilibrium with the atmosphere was reached and the data were recorded. The results of these measurements are shown in Figure 4.16(a).
For these measurement, the conductance and not the conductivity or resistivity is depicted, because the measurement has to be regarded as a parallel circuit between the thin film and the substrate. The substrates, which are insulating at room temperature and atmospheric pressure, can become conducting at high temperatures upon high or low oxygen partial pressure, according to their defect chemistry. Therefore, for each measurement, a reference measurement of an equal substrate is shown as open circles and the overall sheet conductance is plotted.
For the PCMO film on $SrTiO_3$, a large deviation from the substrate reference can be observed for high oxygen partial pressures down to 10^{-8} mbar. Then, both curves lie on top of each other, so that the conductance of the substrate is larger than the signal from the thin film, which is of interest but cannot be revealed. Starting at 1 mbar, what is even more oxidizing than the deposition condition, the conductance of the PCMO film is almost one order of magnitude larger than the substrate conductance. During the reduction of ambient oxygen partial pressure, the conductance drops by 1.5 orders of magnitude, until the $SrTiO_3$ conductance is reached. This drop resembles the literature data for $La_{0.8}Sr_{0.2}MnO_3$ shown in Figure 1.7(a) and can be explained by the introduction of oxygen vacancies to the PCMO lattice, which disturb the conducting chains (Section 1.2). In the range, where only the substrate is visible in the conductance, the PCMO becomes less

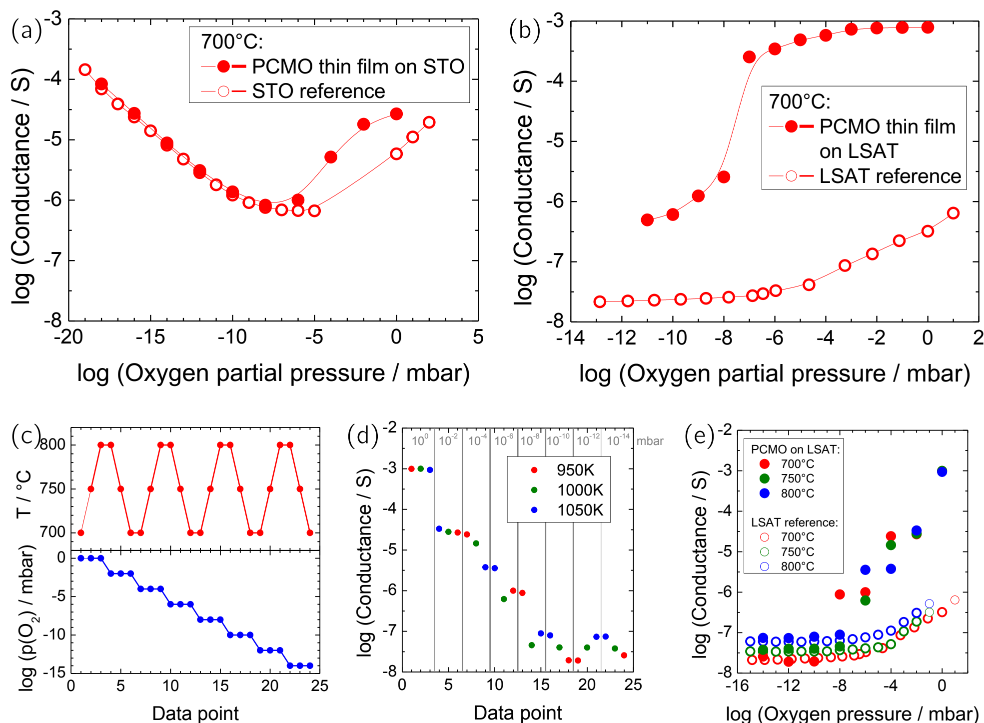

Figure 4.16: High temperature conductance measurements on PCMO: (a) Conductance of 40 nm PCMO grown on $SrTiO_3$, measured at 700 °C. (b) Conductance of 50 nm PCMO grown on LSAT, measured at 700 °C. (c) Measurement protocol for a 50 nm thick PCMO film on LSAT, measured at different temperatures. (d) Results of the measurements from (c). (e) Conductance of 50 nm PCMO grown on LSAT, measured according to (c).

conducting and decomposes. After running through the whole oxygen pressure regime, the PCMO film was completely decomposed. The film is no longer dark, but appears now transparent with a small yellow tinge, as shown in Figure 4.17(a). XRD measurements before and after the experiments prove this assumption (Figure 4.17(b)).

To avoid the influence of the substrate on the conductance in further measurements, LSAT is used as substrate. In comparison to the "U"-shaped conductance of $SrTiO_3$, LSAT is less conducting, especially in the low pressure regime. For a 50 nm thick PCMO film, grown on LSAT, an extensive measurement program was performed, as depicted in Figure 4.16(c). Different temperatures were approached, while a wide range of oxygen partial pressures was applied. The measured data are shown in Figure 4.16(d) and 4.16(e). For this sample,

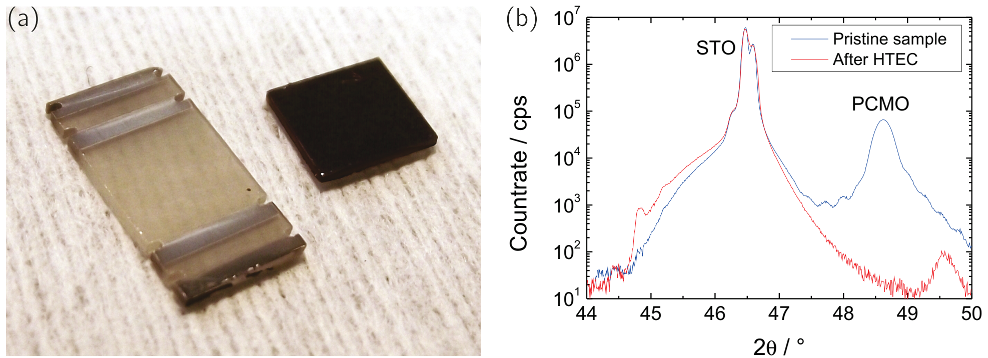

Figure 4.17: Decomposition of PCMO thin film: (a) Photo of the 5 x 10 mm^2 PCMO sample after the HTEC measurements (left side), compared to a pristine 5 x 5 mm^2 PCMO sample (right side). (b) XRD spectra of the same sample, before and after the HTEC experiments.

a similar trend as for the PCMO thin film on $SrTiO_3$ is observed. The relatively high conductance of PCMO drops upon an oxygen pressure decrease of 8 orders of magnitude and then adopts the conductance of LSAT, which is very low in reducing atmosphere. As shown, the effects of pressure and temperature variation interfered and no deconvoluted conclusion can be obtained. In addition, the sample decomposed as well.

The measurement was repeated with a new sample of the same stack. A constant equilibrium temperature of 700 °C was applied and the pressure was decreased in smaller steps. Additionally, the measurement was stopped at higher oxygen pressure in order to avoid the decomposition. The results are shown in Figure 4.16(b). During this measurement, the thin film conductance stays right above the substrate conductance. For high oxygen partial pressures, the conductance of PCMO is decreased slightly upon decreasing pressure. At 10^{-8} mbar a sharp drop was recorded, similar to $La_{0.8}Sr_{0.2}MnO_3$. After stopping the measurement at 10^{-11} mbar, the starting value could not be recovered and the thin film was decomposed.

The noticed decomposition of the PCMO thin films has also been observed for ceramic $Pr_{1-x}Ca_xMnO_3$ samples with different stoichiometries [124]. For $La_{1-x}Sr_xMnO_3$ the phase diagram [125] confirms the assumption of decomposition at very reducing conditions. For $La_{0.7}Sr_{0.3}MnO_3$ at 1100 °C the composition is stable down to 10^{-8} mbar and then decomposes into different components. A similar behavior is expected for $Pr_{1-x}Ca_xMnO_3$, so that the reliability of the data set is not given for very reducing conditions. From these measurements it cannot be concluded with absolute certainty, that the sharp drop in

conductance, which could be observed for all samples, is attributed to the decomposition, but at least these are strong hints supporting this fact. As soon as the decomposition starts, the measured conductance does no longer belong to the manganite PCMO, but to some of its components.

5 Resistive switching of $Pr_{0.48}Ca_{0.52}MnO_3$

After the documentation of the growth process in Section 2.2.3 and the electrical investigations of the bulk transport in Chapter 4, PCMO is now examined in a metal - insulator (oxide) - metal (MIM) structure, stacked between two metal electrodes. The devices are always biased at the top electrode while the bottom electrode is grounded. After the consideration of the transport properties through different interfaces of PCMO, the resistive switching effect at the Ti/PCMO interface is discussed in detail.

5.1 Surface and interface contacts of $Pr_{0.48}Ca_{0.52}MnO_3$

5.1.1 LC-AFM measurements

During the LC-AFM measurements, described in Section 4.1.5 and A.2, a conducting tip is used to analyze the material. Directly after the scan with the non-conducting tip, i.e. approximately 2 h after the sample was loaded to the vacuum chamber, an I-V sweep was measured at one arbitrary point on the surface. The result is shown in Figure 5.1(b) as a red curve. The non-linearity can be attributed to the *p*-*n* junction between the *n*-type semiconductor tip and the PCMO layer and to an inhomogeneous field distribution. The same measurement was repeated approximately 20 h after the sample was loaded to the chamber and the result is striking (blue curve): Much higher voltages are needed to get a current through the PCMO thin film. The reason for this behavior is explained in Section 1.2.1. Although no elevated temperature was applied to the PCMO film to activate oxygen exchange with the environment, the topmost layer of PCMO has been reduced over time as a result of oxygen exchange with the vacuum. As the Mn−O−Mn chains got split, the conductance dropped, as explained in Section 1.2.

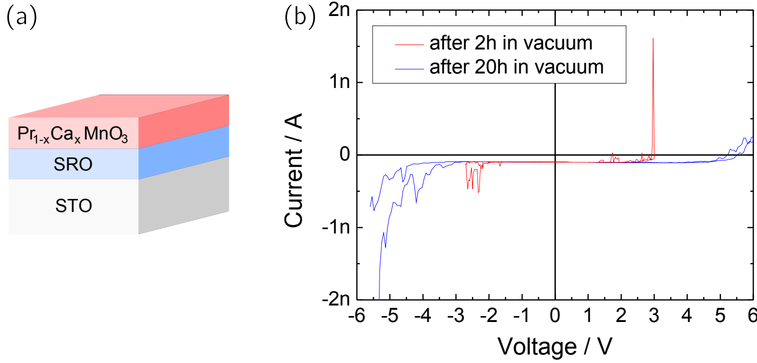

Figure 5.1: LC-AFM measurements: (a) Layer stack: STO-SRO-PCMO. (b) *I*-*V* sweeps at one point of the surface, measured at two different time intervals after loading the sample to the vacuum chamber.

5.1.2 Nb:$SrTiO_3$/$Pr_{0.48}Ca_{0.52}MnO_3$

Nb:$SrTiO_3$ is a commonly used substrate, which can also act as a bottom electrode (BE). With a doping level of 0.5 at.% on the Ti-site, the material is a doped *n*-type semiconductor with a band gap of $E_g = 3.2\,\mathrm{eV}$ and an electron affinity of $\chi_{\mathrm{Nb:STO}} = 4.0\,\mathrm{eV}$ [126] and it forms an ohmic contact to other *n*-type oxides and low work function metals.
In contact with the *p*-type semiconductor PCMO, formally a *p*-*n* junction is formed. Actually PCMO is doped by approximately 50 at.% and thus a factor of 100 more than the used Nb:$SrTiO_3$, so that the depletion layer within the PCMO is a factor of 100 thinner than within the Nb:$SrTiO_3$ and can be neglected. Thus, the interface can be considered as a Schottky-contact.

For the measurement of an *I*-*V* sweep across this interface, a 20 nm thick PCMO film is grown on an annealed Nb:$SrTiO_3$ substrate. Pt-contacts are ex-situ sputtered on top through a shadow mask and act as top electrode (TE). Pt with a high work function of $\Phi_{Pt} = 5.65\,\mathrm{eV}$ [105] forms an ohmic contact at the interface to PCMO and has already been used for the electrical in-plane investigations in Section 4.2. For this stack, the interface PCMO/Nb:$SrTiO_3$ will have the largest contribution in the overall measured resistance and can thus be analyzed. The resulting *I*-*V* curve is shown in Figure 5.2.

The current through the PCMO/Nb:$SrTiO_3$ junction will be described by the thermionic emission-diffusion theory [67, 127, 128], under the assumption that the barrier height Φ_B

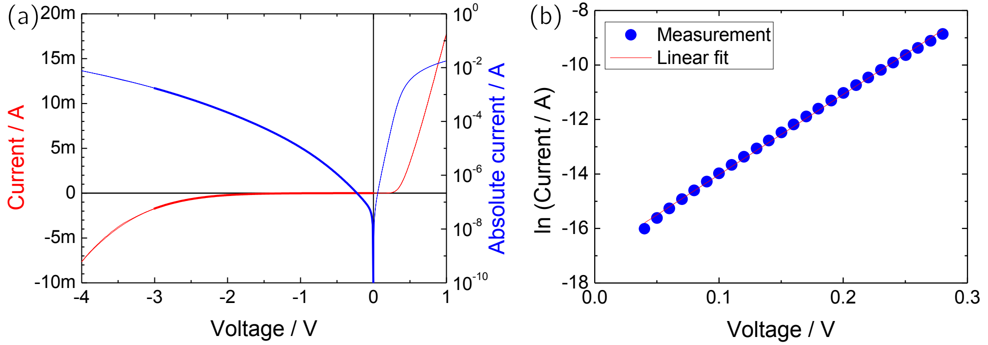

Figure 5.2: Electrical characterization of the *p*-*n* junction of PCMO to Nb:STO: (a) $Pr_{0.48}Ca_{0.52}MnO_3$: *I*-*V* characteristic on linear and logarithmic scale. (b) $Pr_{0.48}Ca_{0.52}MnO_3$: Linear regression for the linear part of $\ln(I)$ for the forward direction.

is much larger than $k_B T$:

$$I = J_S A e^{\frac{eV}{nk_B T}},$$

with pad area A, ideality factor n, Boltzmann constant k_B and temperature T. The saturation current density J_S is approximated by

$$J_S = A^* T^2 e^{-\frac{e\Phi_B}{k_B T}},$$

where an effective Richardson constant of $A^* = 120\,\frac{\mathrm{A}}{\mathrm{cm^2K^2}}$ is applied. At room temperature $T = 293\,\mathrm{K}$ and with an area of a circular pad of 100 µm in diameter, the ideality factor n and the effective barrier height Φ_B can be determined by the linear regression in Figure 5.2(b). With the calculated ideality factor of 1.34, the contact barrier was determined to $\Phi_B = 0.60\,\mathrm{eV}$. The barrier height can in general be calculated as the difference of the two electron affinities $\Phi_B = \chi_{\mathrm{PCMO}} - \chi_{\mathrm{Nb:STO}}$. Using the calculated barrier height, the electron affinity of PCMO can be determined to 4.60 eV.
In literature, the work function of $Pr_{0.7}Ca_{0.3}MnO_3$ was determined to $\chi_{\mathrm{PCMO}} = 4.9\,\mathrm{eV}$ by Kelvin probe measurements [129]. Here, the barrier would be $\Phi_B = 0.9\,\mathrm{eV}$, showing a significant deviation from our measurements. By temperature dependent current density measurements and investigations of the capacitance in the reverse bias region, a barrier of $\Phi_B = 0.7\,\mathrm{eV}$ was obtained [128], which is much closer to our results.

For $Pr_{0.6}Ca_{0.4}MnO_3$ and $La_{0.7}Sr_{0.3}MnO_3$ similar measurements were performed (Figure 5.3(a) and 5.3(b)) and the barrier heights were determined analog to PCMO. For $Pr_{0.6}Ca_{0.4}MnO_3$ a barrier of $\Phi_B = 0.51\,\mathrm{eV}$ was calculated, leading to $\chi_{\mathrm{PCMO(40\%)}} =$

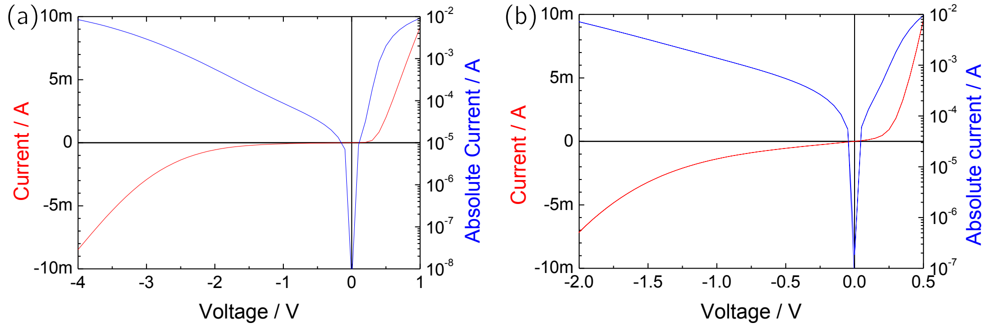

Figure 5.3: Electrical characterization of the *p*-*n* junction of $Pr_{0.6}Ca_{0.4}MnO_3$ (a) and $La_{0.7}Sr_{0.3}MnO_3$ (b) to Nb:STO.

4.9 eV, while for $La_{0.7}Sr_{0.3}MnO_3$ a barrier of $\Phi_B = 0.44$ eV and an electron affinity of $\chi_{LSMO(30\%)} = 4.44$ eV were received.

5.1.3 High and low work function metals

PCMO as a *p*-type semiconductor with half-metallic transport properties is assumed to form a Schottky contact at the interface to metals. For high work function metals with $\Phi_M > \chi_{PCMO} = 4.9$ eV, the Schottky contact should show an ohmic current-voltage characteristic. For low work function metals with $\Phi_M < 4.9$ eV a rectifying interface is expected due to a formed Schottky barrier Φ_B [127].

The interface between PCMO and Pt is already known to show an ohmic contact, as used in Section 4.2 for the investigation of the PCMO bulk transport properties. Within the class of metals, Pt has one of the largest work functions with a value of $\Phi_{Pt} = 5.65$ eV [105]. $SrRuO_3$ with a work function $\Phi_{SRO} = 5.3$ eV [20] slightly smaller than Φ_{Pt} is also expected to form an ohmic contact to PCMO. Due to its perovskite lattice structure, $SrRuO_3$ can be used as bottom electrode. For measuring the *I*-*V* characteristic, different metals are used as top electrode. The results for platinum, gold, SRO, tungsten, aluminum and titanium are shown in Figure 5.4.

For all *I*-*V* measurements a stack of $SrTiO_3$/30 nm $SrRuO_3$/20 nm PCMO is used, but the TE differ in their geometry. Most materials were sputtered with a thickness of 30-50 nm through a shadow mask, while for Ti and SRO photo-lithography was applied and for W only a needle was used as contact. The measured curves were normalized to a uniform TE

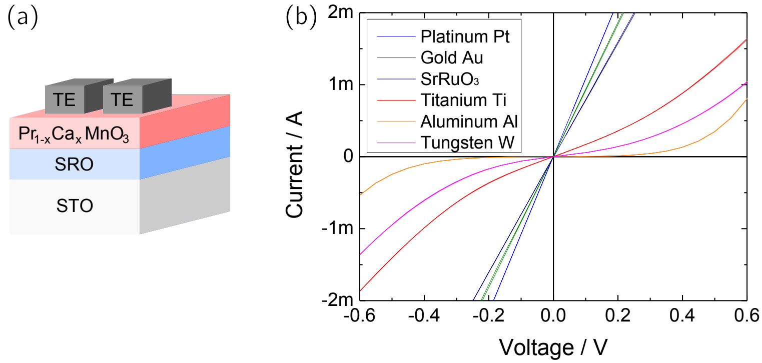

Figure 5.4: *I*-*V* characteristic for different top electrodes on PCMO: (a) Layer stack: STO-SRO-PCMO-TE with TE = Pt, Au, SRO, Ti, Al, W. (b) *I*-*V* characteristics for different top electrodes.

pad area with a certain error, but nevertheless the curve shapes are qualitatively correct. However, one clear trend is visible in Figure 5.4. For Pt, Au and SRO the *I*-*V* curves show a linear behavior, while for the other materials a clear non-linearity is observed. According to the explanations above, the high work function materials with $\Phi_{Pt} = 5.65\,eV$, $\Phi_{SRO} = 5.3\,eV$ and $\Phi_{Au} = 5.1\,eV$ lead to an ohmic contact. The low work function metals with $\Phi_{W} = 4.55\,eV$, $\Phi_{Ti} = 4.33\,eV$ and $\Phi_{Al} = 4.28\,eV$ [105] show a non-ohmic interface contact.

In contradiction to the expectations, the non-linearity of the curves does not show a rectifying behavior. This observation can be explained by the assumption, that low work function metals get easily oxidized and a native metal oxide is formed at the interface to an oxide layer, what changes the transport properties of the stack. This effect will be discussed in detail in Section 5.2.

5.2 Forming and switching in PCMO/Ti devices

For the forming as well as for the switching of VCM devices, ions have to be moved within the device. Hence, large electric fields are indispensable to generate the conditions for ion motion [130]. For ohmic contacts, the field perpendicular to the device is distributed constantly, so that a large voltage has to be applied to activate ion movement, but simultaneously the large current would cause a thermal breakdown. For devices with a non-linear voltage drop over the entire current path, smaller voltages are sufficient, because the field is enhanced at the blocking or rectifying interface. Thus, low work function metals are suitable to observe resistive switching at the PCMO interface, as they form a Schottky barrier-like contact, as discussed in Section 5.1.3. In this work, Ti is used as active top electrode.

For resistive switching experiments on $Pr_{0.48}Ca_{0.52}MnO_3$, 20 nm PCMO were grown epitaxially on 30 nm $SrRuO_3$ on a $SrTiO_3$ substrate, as reported in Section 2.2.3.1. $SrRuO_3$ acts as bottom electrode (BE) and is connected to a Pt pad on the Si "carrier" by aluminum wire bonding, as sketched in Figure 5.5(a). A 15 nm thick polycrystalline Ti film is deposited by sputter deposition as top electrode (TE) and capped in-situ by a 20 nm thick Pt layer. The Pt prevents the Ti layer from oxidation at the surface. Either the metal top electrode or the entire stack down to the bottom electrode is structured by photo-lithography.

The non-destructive read-out *I-V* sweep for such a stack in its pristine state (PS) has already been shown in Section 5.1.3. For switching, higher voltages are needed and the resulting current-answer is depicted in Figure 5.5(b). The current is increased with increasing voltage, for this particular device up to 3 V, then the current signal flattens and finally even drops by a factor of 5 during a voltage increase (green line), caused by a suddenly increased resistance. After this electroforming process, the device is in a less conducting formed state (FS). This curve is not reproducible for this device and activates the following switching effect.

After the forming, a positive voltage does not affect the device state at all, but with a negative voltage, the SET process can be observed for approximately −2.5 V, as explained in general in Section 1.1. Here, the current follows a smooth curve and is abruptly increased by more than one order of magnitude upon switching into the low resistance state (LRS or ON state). Applying a positive voltage again, the system is gradually reset into a high resistive state (HRS or OFF state) between 1.5 V and 3 V. PCMO shows a clear "counter-eight-wise" switching behavior.

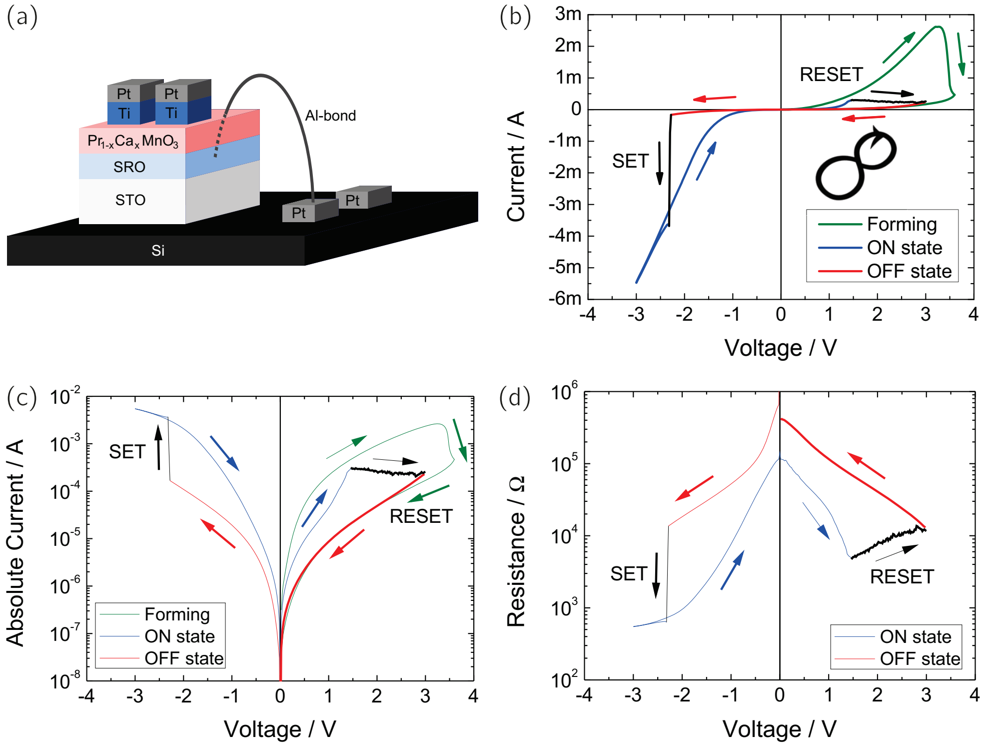

Figure 5.5: Electroforming and resistive switching of a PCMO/Ti device: (a) Layer stack and electrical connection: The source is connected to a Pt pad on the surface of PCMO, while $SrRuO_3$ is grounded via an aluminum wire bond to a Pt pad on the Si "carrier". (b) Current-voltage characteristic of forming and switching. A soft forming step is needed and then "counter-eight-wise" switching is observed. (c) Current-voltage characteristic on a logarithmic scale for absolute current values. (d) Resistance-voltage plot. A counter-clockwise switching is visible.

Due to the large difference in resistance, that has to be shown, the low-current regime is hardly visible, when the high-current regime is nicely scaled. Thus, the data set is additionally plotted on a logarithmic scale in Figure 5.5(c). Here, the absolute value of the current is regarded.

The resistance is plotted in dependence of the stimulating voltage (Figure 5.5(d)). A counter-clockwise resistance switching is observed. The $R_{\mathrm{ON}}/R_{\mathrm{OFF}}$ ratio of 4 is relatively small at zero applied field, although the hysteresis opens up by more than a factor of 10 for higher voltages.

5.3 The forming process of $Pr_{0.48}Ca_{0.52}MnO_3$/Ti

5.3.1 Impedance spectroscopy

Having a closer look at the forming procedure and its origin, a more detailed electrical characterization of the device is necessary. Going back to the pristine state of the sample, before any electrical treatment was applied, impedance spectroscopy was performed, as depicted in Figure 5.6.

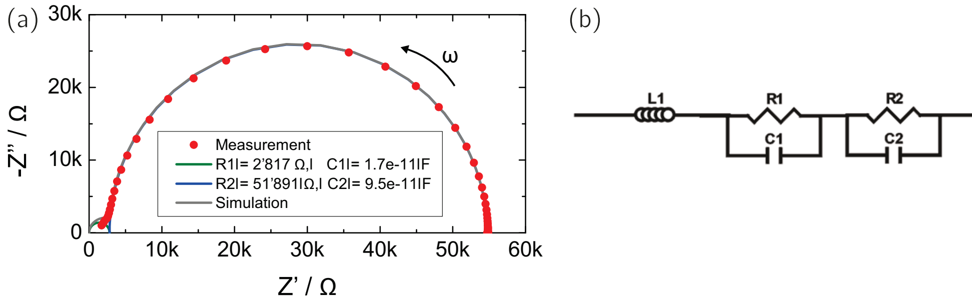

Figure 5.6: Impedance spectroscopy on a PCMO device: (a) Cole-Cole plot for frequency variation. (b) Equivalent circuit diagram, which simulates the data set.

In the so-called Cole-Cole plot in Figure 5.6(a) the imaginary part of the impedance Z'' is plotted in dependence of the real part Z' for angular frequencies ω between $10^{-2}\,\frac{1}{s}$ and $3 \cdot 10^{6}\,\frac{1}{s}$. A typical semi-circle shaped curve is measured. The data set is modeled with equivalent circuits to obtain the suitable configuration, which fits best with the measured result. The best result was received for two parallel RC-elements in series with a very small inductance L, depicted in Figure 5.6(b) (gray line). The impedance of a single parallel RC-element is determined to

$$Z = Z' + iZ'' = \frac{R}{1 + (\omega RC)^2} - i\frac{\omega R^2 C}{1 + (\omega RC)^2},$$

while the impedances are added for different RC- and L-elements in a serial circuit. The two RC-elements were determined to $R1 = 2817\,\Omega$; $C1 = 1.7 \cdot 10^{-11}$ F and $R2 = 51891\,\Omega$; $C2 = 9.5 \cdot 10^{-11}$ F and can be attributed to the bulk of the PCMO thin film (1) and the interface to Ti (2). They are also drawn in Figure 5.6(a) as two single circles (green and blue line). As a result, the interface contribution to the overall resistance is much larger than the bulk resistance of PCMO and thus is the determining part.

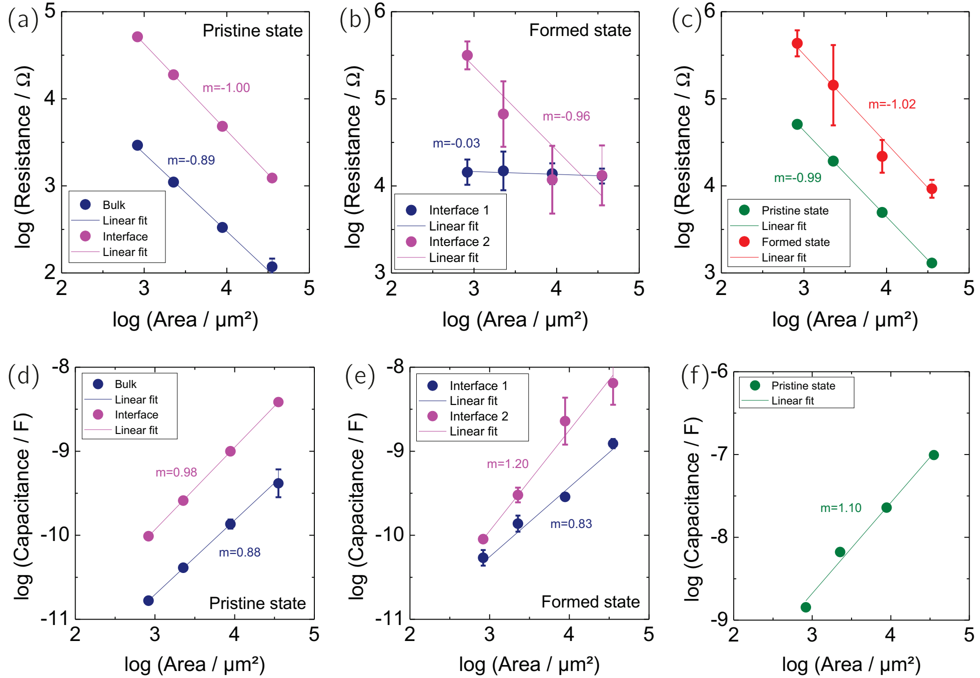

Figure 5.7: Area dependence of the pristine and formed state with slope m: (a) Resistance of the two circuit elements bulk and interface for the pristine state. (b) Resistance of the two interfacial circuit elements for the formed state. (c) Overall resistance for the pristine and the formed state. (d) Capacitance of the two circuit elements bulk and interface for the pristine state. (e) Capacitance of the two interfacial circuit elements for the formed state. (f) Overall capacitance for the pristine state.

Impedance spectroscopy has been performed on the pristine and formed PCMO devices for different top electrode areas A and was evaluated each time according to the equivalent circuit in Figure 5.6(b). The results for both resistances and capacities are shown in Figure 5.7.

The resistances of the pristine state are plotted in Figure 5.7(a). The interface resistance is one order of magnitude higher than the bulk resistance and both show a clear area dependence with slope $m \approx -1$ according to $R = \rho \cdot \frac{d}{A}$. The corresponding capacities are depicted in Figure 5.7(d) and, as well, show a clear area dependence with slope $m \approx 1$, according to $C = \varepsilon_0 \varepsilon_r \cdot \frac{A}{d}$, where ε_0 and ε_r are the vacuum and the relative permittivity. The interface between PCMO and Ti has a 10 times higher resistance and capacitance

than the bulk of PCMO.
The resistances and capacities of the formed devices in dependence of the device area are depicted in Figure 5.7(b) and 5.7(e). Again, two semi-circles could be identified, but the resistances are too high to be referred to the bulk resistance and thus they are identified with two interface components. Resistance and capacitance are strongly area dependent for one component, whereas the resistance in the other component changes only slightly with the area.
The overall resistances R of the devices for the pristine and formed samples are shown in Figure 5.7(c). As already known from the switching experiments in Figure 5.5, the resistance increases upon forming, in particular by almost one order of magnitude. The overall capacitance could only be determined for the pristine state (Figure 5.7(f)). In general, these values are quantified according to $Z = Z' + iZ'' = R - i\frac{1}{\omega C}$, so that the capacities also have an influence on the overall resistance and the resistors on the overall capacity. The very interesting result is, that the area dependence of $m \approx -1$ is conserved upon forming. That implies, that the forming procedure affects the device homogeneously.

5.3.2 TEM investigations

A likely explanation for the forming effect and its homogeneity is the oxidation of the Ti layer at the interface to PCMO [23]. However, the local effects within the device structure and especially at the electrode-oxide interface region are not properly understood. To approach this topic, TEM measurements were performed on layered PCMO heterostructures by the group of Jo Verbeeck, EMAT, University of Antwerp. Two cross-section electron transparent lamellas were prepared by FIB out of a pristine and a formed PCMO device with $SrTiO_3$ / 30 nm $SrRuO_3$ / 20 nm PCMO / 15 nm Ti / 20 nm Pt sample stack. High-angle annular dark-field scanning transmission electron microscopy (HAADF-STEM) and electron energy-loss spectroscopy (EELS) were performed using a JEOL 3000 transmission electron microscope, operated at 300 kV.

The TEM and HAADF-STEM images of the cross-sections of the two devices are depicted in Figure 5.8(a) and 5.8(b). As additional information the corresponding EELS data are shown in Figure 5.8(c) and 5.8(d), respectively. This analysis provides atomic spatial resolution upon the cross-sectional elemental distributions for Ti, Pr, Ca, Mn and O and shows that both systems contain an intermixing region of about 8.5 nm. The intensities are normalized to the maximum of each curve.
For the pristine device just after sputter deposition of the top electrode material (Fig-

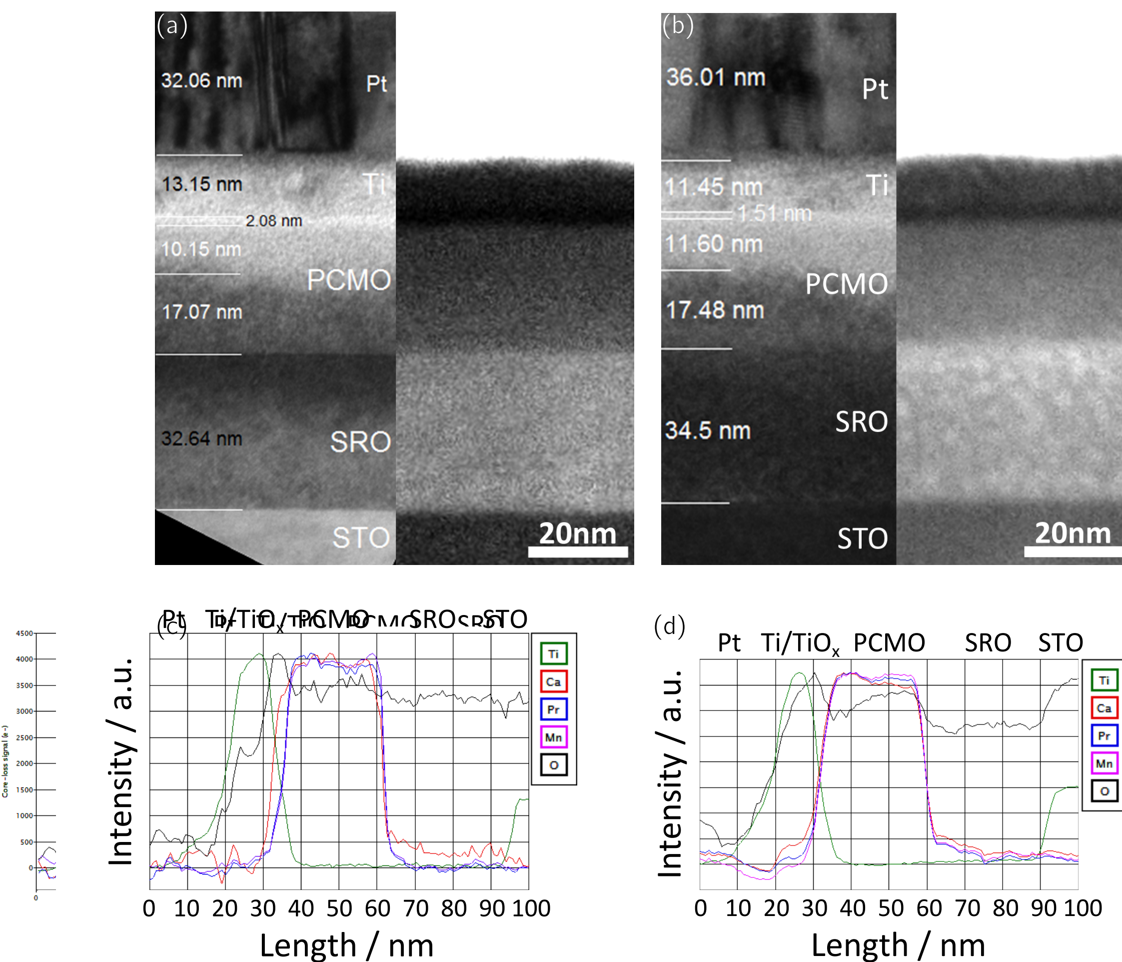

Figure 5.8: (a)-(b): Cross-section of PCMO devices: TEM (left side) and HAADF-STEM (right side), respectively: (a) Pristine state: An amorphous layer is formed at the PCMO/Ti interface. (b) Formed state: The amorphous layer is only slightly changed during the forming process. (c)-(d): EELS data of the cross-section: (c) Pristine state: An intermixing region is visible at the PCMO/Ti interface. (d) Formed state: Almost the complete Ti layer is oxidized.

ure 5.8(c)), an oxygen signal can be received from the region of the Ti layer. A thin part of the film remains metallic titanium, but most of it is at least partially oxidized. In addition, at the interface a very thin layer is formed, which contains mainly Ti, Ca and O, because the Ca signal does not drop like the Pr and Mn signal, but reaches a bit further into the Ti layer. This Ca excess at the upper PCMO interface arises already during the deposition of the PCMO film, as reported in Section 2.2.3.2, and does not coincide with the deposition of the titanium layer.
The formed device (Figure 5.8(d)) shows no increased Ca content at the interface. But the oxygen signal is now present over the entire Ti layer, while it is lowered in the upper part of the PCMO layer.

5.3.3 HAXPES experiments

To get a closer insight into the chemical processes, which take place during electroforming, hard X-ray photoelectron spectroscopy (HAXPES) was performed by the group of Francesco Borgatti, University of Bologna, as nondestructive analysis tool for deep regions and buried interfaces. With this technique, high-energetic X-ray photons knock photoelectrons out from the core levels of the investigated material, which are analyzed with regard to their kinetic energy. Because of the large footprint of the synchrotron beam, single devices are not suitable for investigation. Thus, in this experiment the average signal over a large area is measured. As many devices are measured simultaneously, the statistical distribution of the resistances is of great interest. The resistance was read-out for 135 equal pads in the pristine state. Then a threshold DC forming automated system was used, in which a constant voltage of 10 V was applied to the device and the measurement was terminated as soon as the threshold resistance of 5 kΩ had been reached. The results of this measurement are depicted in Figure 5.9(a).

The resistance distribution is very sharp for the pristine states, whereas the resistances differ over more than two orders of magnitude for the formed state. Nevertheless, this accuracy should be sufficient to see chemical changes upon electroforming, if the process takes place homogeneously. The sample geometry used for HAXPES investigations is shown in Figure 5.9(b). The top electrode of the sample was structured by photo-lithography into several arrays of 100 x 100 μm^2 pads with 10 µm spacing. Unlike in Figure 5.5(a), the PCMO is also structured this time to prevent the signal from the pure PCMO from interfering, so that the gaps between the pads and arrays show $SrRuO_3$ on the surface.

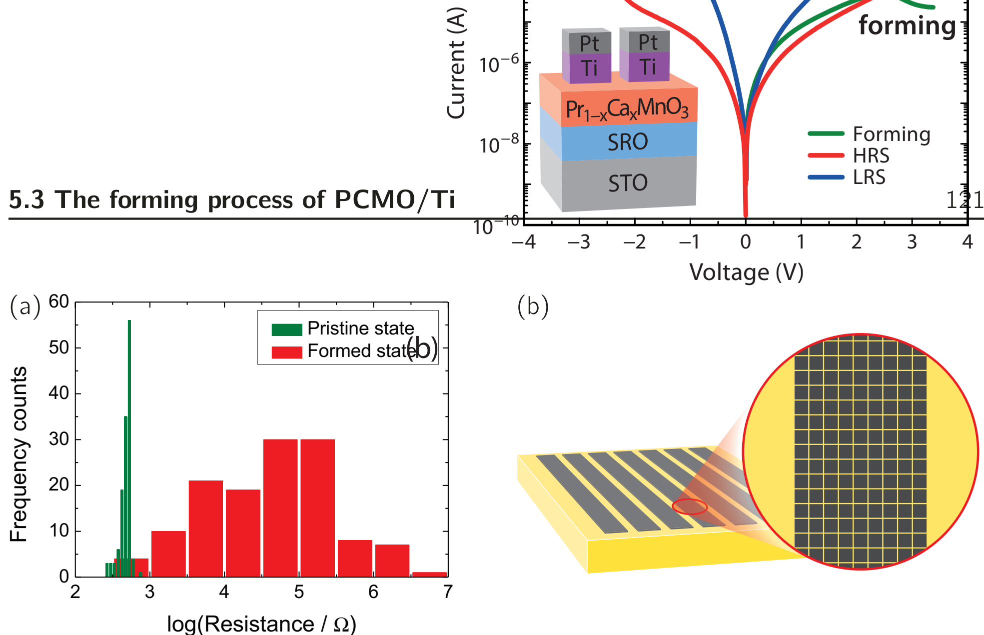

Figure 5.9: (a) Resistance distribution of the pristine and formed state. (b) Sample geometry for HAXPES experiments.

HAXPES measurements were performed at the BL15XU beam-line of the Spring-8 synchrotron radiation source in Japan. The X-ray beam was directed onto the sample with gracing incidence of 2°, leading to a beam footprint on the sample surface of about 3000 x 100 μm^2. The photon energy was set to 5950.14 eV and the overall resolution was 0.25 eV. With this method the binding energy of core electrons is measured, which alters for different elements and also with their valence. As Pt possesses a very high absorption in the X-ray regime, the capping layer thickness was reduced to 4 nm to provide enough intensity. The electron inelastic mean free path for the hard X-ray excitation regime is typically 8 nm. Thus, the thickness of the Ti top electrode material was set to 7 nm and 10 nm for two different samples, so that different depths of the buried region could be addressed. As reference, a 50 nm thick PCMO film was deposited on $SrTiO_3$ and a region between two arrays was investigated to obtain a reference for $SrRuO_3$. The survey scans for the sample with 7 nm Ti are shown in Figure 5.10(a).

Beside the large range survey scans, highly resolved measurements were performed around core levels of high interest. As Ti has already been proven to be involved in the forming process, its 2p spectra are shown in Figure 5.10(b) and a closeup on the Ti $2p_{3/2}$ in Figure 5.10(e). Additionally, the PCMO-related core levels of Pr 3d (Figure 5.10(c)), Ca 2p (Figure 5.10(d)), Mn 2p (Figure 5.10(f)), and O 1s (Figure 5.10(g)) are shown.
The Ti 2p core level spectra, depicted in Figure 5.10(b), are normalized to the background intensity. Because of the partial overlap of the Ti $2p_{1/2}$ with the Ru $3p_{3/2}$, only the spectral region of the Ti $2p_{3/2}$ component is clearly distinguishable and plotted in Figure 5.10(e) as a close-up. There, two distinct features at 454 eV and 459 eV are visible and can be

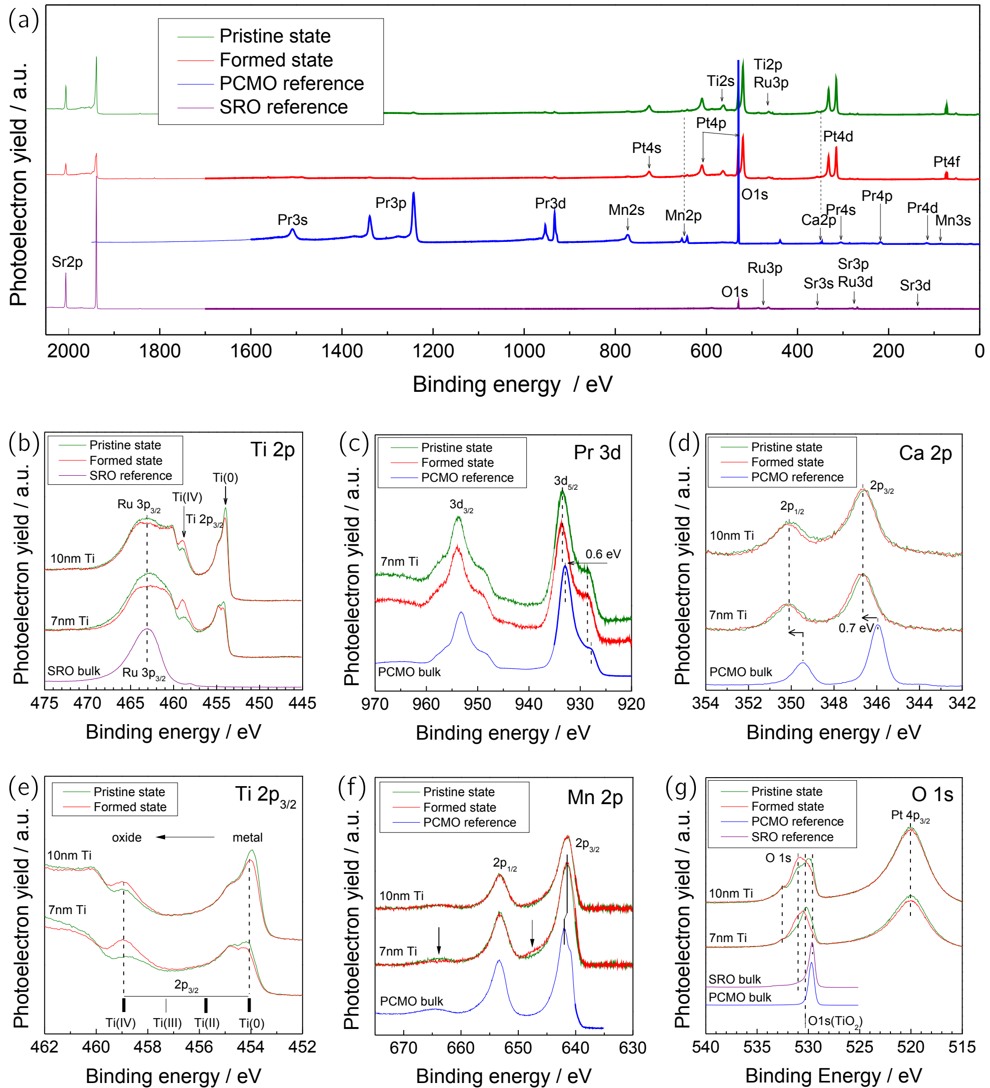

Figure 5.10: HAXPES results on electroforming: Ti and PCMO related core-level spectra of the pristine (green curves) and formed (red curves) device array: (a) Survey scans for the PCMO sample with stack $SrTiO_3$ / 30 nm $SrRuO_3$ / 20 nm PCMO / 7 nm Ti / 4 nm Pt. Core level spectra of specific elements: (b) Ti 2p level. (c) Pr 3d level. (d) Ca 2c level. (e) Ti $2p_{3/2}$ level. (f) Mn 2p level. (g) O 1s level.

associated with metallic Ti^0 and fully oxidized Ti^{4+} cation valence states. In general, the peak for metallic Ti is much more pronounced for the sample with 10 nm Ti on top, while more oxidized Ti^{4+} is detected for 7 nm Ti, where the photons reach deeper into the device. For both samples the electroforming procedure changes the spectra clearly with a redistribution of the Ti towards higher valences.
The core-level spectra of the PCMO-related elements in Figure 5.10(c), 5.10(d) and 5.10(f) all exhibit a shift of the binding energy with respect to the reference spectrum. For Pr 3d and Ca 2p the peaks are shifted to higher binding energies by 0.6-0.7 eV, while for Mn 2p they are shifted to lower binding energies by 0.2 eV. Being very similar for both states, they denote a stable change of the electronic structure in PCMO upon the integration of the Ti top electrode. This behavior strongly resembles the binding energy shift in $Pr_{1-x}Ca_xMnO_3$ as a function of the Ca doping level and can thus be related to a lowering of the PCMO chemical potential at the Ti interface [131]. The opposite direction of the Mn 2p shift can be interpreted as the progressive change of the Mn^{4+} species to lower valence states Mn^{3+} due to a reduction of the material at the interface to Ti. For O 1s shown in Figure 5.10(g), the spectra clearly differ from the $SrRuO_3$ and the PCMO references. With a broadening of the peak, at least three well defined features appear. The complexity of the line-shapes is attributed to the overlap of different contributions from the oxygen atoms belonging to PCMO, the oxidized Ti top electrode and the surface oxidation of the Pt layer. The stable shoulder at the left side of the O 1s peak is due to the Pt oxidation, while the other two features redistribute their intensity upon electroforming, so that the lower energetic peak can be related to PCMO states and the higher energetic one to TiO_x states.

Having a closer look at the Ti top electrode material, all four data sets for 7 nm/10 nm Ti thickness and the pristine/formed state, respectively, were fitted using the Ru 3p level and four different Ti valences for each Ti 2p energy level: Ti^0 (metallic), Ti^{1+} (Ti_2O), Ti^{2+} (TiO), Ti^{3+} (Ti_2O_3) and Ti^{4+} (TiO_2). The results of the fits are shown in Figure 5.11.

In conclusion, PCMO undergoes minor changes during the electroforming process, while the main chemical changes in the device structure occur in the titanium oxide interface layer. Thus, the electroforming step mainly takes place at the PCMO/Ti interface and the oxidation of the Ti is strongly involved in the mechanism. The results on the electroforming procedure of the PCMO/Ti switching devices have been published in [132].

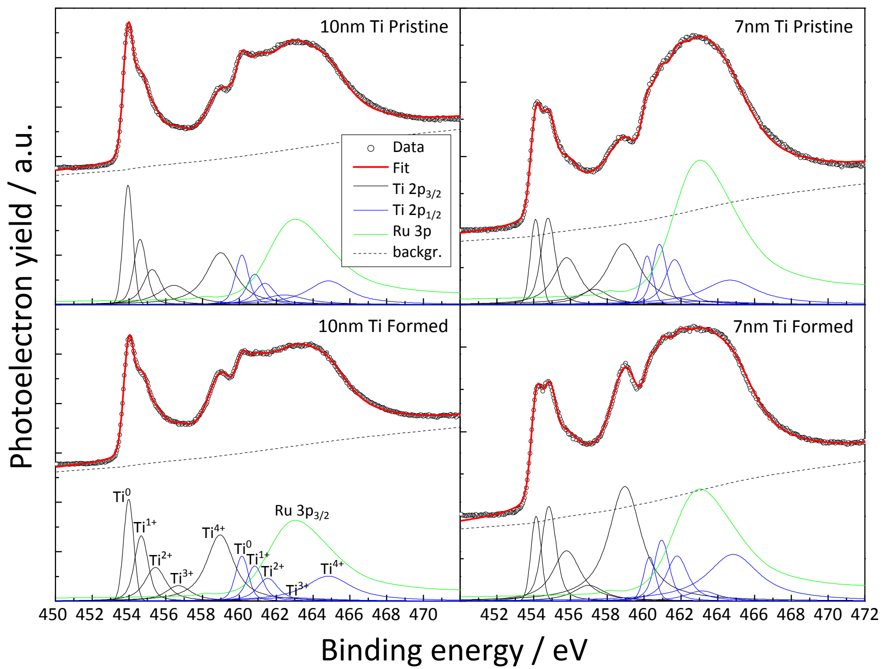

Figure 5.11: Evaluation of Ti 2p core levels: Four different valence states were used for each Ti 2p energy level and the Ru 3p level.

5.4 The switching process of $Pr_{0.48}Ca_{0.52}MnO_3$/Ti

From the current knowledge it is clear, that the Ti top electrode material is heavily involved in the electroforming mechanism [132]. However, up to now there is no chemical insight into the resistance switching process itself.

To investigate this effect further, HAXPES measurements (Section 5.3) were performed for each of the four resistive states. A sample stack of TiO_2-terminated $SrTiO_3$ / 30 nm $SrRuO_3$ / 20 nm PCMO / 7 nm Ti / 3 nm Pt was used. The top electrode was structured by photo-lithography using the array structure in Figure 5.9(b), consisting of 50 x 50 μm^2 electrodes with 10 μm spacing, arranged in strips of size 7 x 0.8 mm^2.

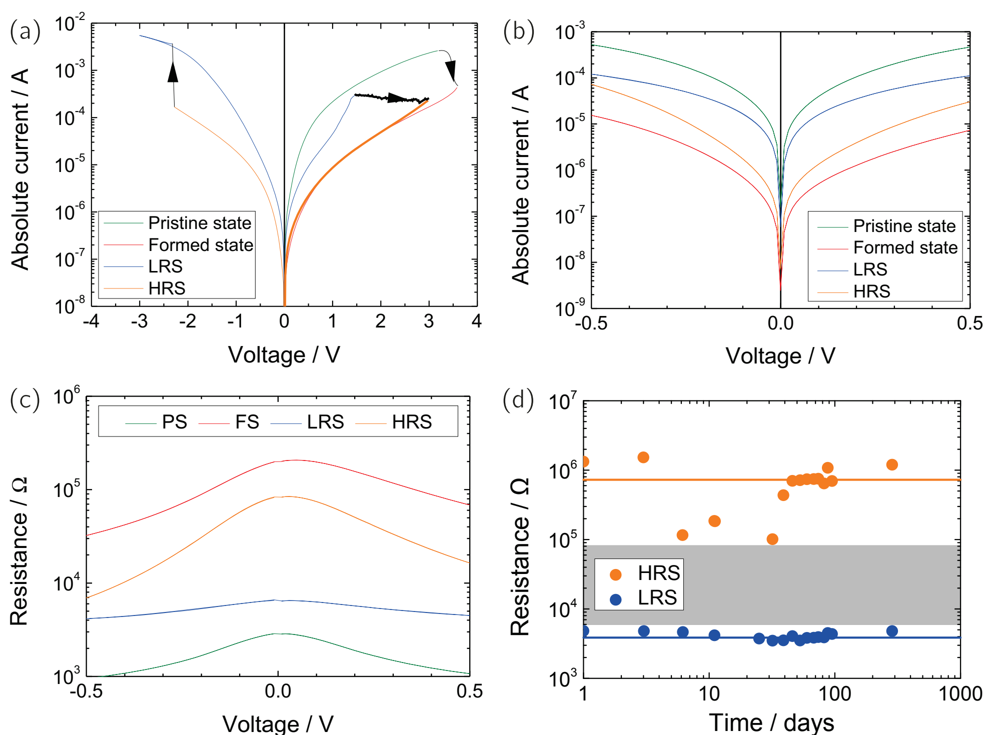

Figure 5.12: Resistive switching: (a) Forming and switching *I*-*V* curves. (b) Read-out sweeps. (c) Voltage dependence of the resistances. (d) Retention measurements on LRS and HRS.

The electrical treatment of the array pads can be understood with the help of Figure 5.12(a). For the array with pristine states, the pads were left untreated. For the formed state, a positive voltage was applied, which exceeds the positive forming threshold voltage. To set

the devices into the LRS states, the forming sweep was extended by a sweep to negative voltages to allow the SET process. The HRS was finally achieved by a forming sweep, a set sweep and an additional reset sweep at positive voltages again. Afterwards, pads of each array were read-out by a non-destructive low-voltage sweep of ± 500 mV to confirm the alternation of the states, shown in Figure 5.12(b). The corresponding resistances and their voltage dependencies are shown in Figure 5.12(c). According to their resistances, the four states can be ordered as PS $<$ LRS $<$ HRS $<$ FS. For a comparable sample, retention measurements were performed. As depicted in Figure 5.12(d), the resistance values were stored for at least 300 days, so that the written states were conserved for the HAXPES investigations.

5.4.1 HAXPES experiments

The HAXPES measurements were performed by the group of Francesco Borgatti, University of Bologna, at beamline P9, Petra III, HASYLAB, Germany. The X-ray beam with a photon energy of 6 keV was focused on the sample under a gracing angle of 2°. To maximize the bulk sensitivity, the electron analyzer was set to an angle of 90° with respect to the X-ray beam. The measurements were performed at room temperature and an overall resolution of 0.35 eV was achieved. As results, the Ti 2p spectra of the TE material as well as the Mn 2p spectra of PCMO and the O 1s spectra consisting of both contributions are depicted in Figure 5.13.

The Ti 2p spectra in Figure 5.13(a) are of major importance, as they contain information about the Ti valence states and thus the oxidation state. For the pristine sample the Ti 2p spectrum exhibits two distinct features at a binding energy of 454 eV and 459 eV, which can be identified as the Ti $2p_{3/2}$ emission lines of metallic Ti^0 and fully oxidized Ti^{4+}. For a good reproduction of the spectral envelope, a least-squares fitting analysis with one spin-orbit split doublet pair for each possible oxidation state of Ti was performed. The area ratio of the doublet peaks was set to 2 : 1 and also the doublet separation was kept fixed. A minor contribution from the underlying $SrRuO_3$ bottom electrode, arising from the area between the electrodes, was accounted for by a single peak, corresponding to the Ru $3p_{3/2}$ line at 463.4 eV. With increasing resistance state, a spectral weight transfer from the low binding energy components to the high binding energy components of Ti 2p is observed. The area percentages of all Ti oxidation states are shown in Figure 5.13(b). While the dominant Ti^{4+} component spectral line shows a monotonous increase with resistance, the part of the metallic Ti^0 line is decreased gradually. In a similar manner, Figure 5.13(c)

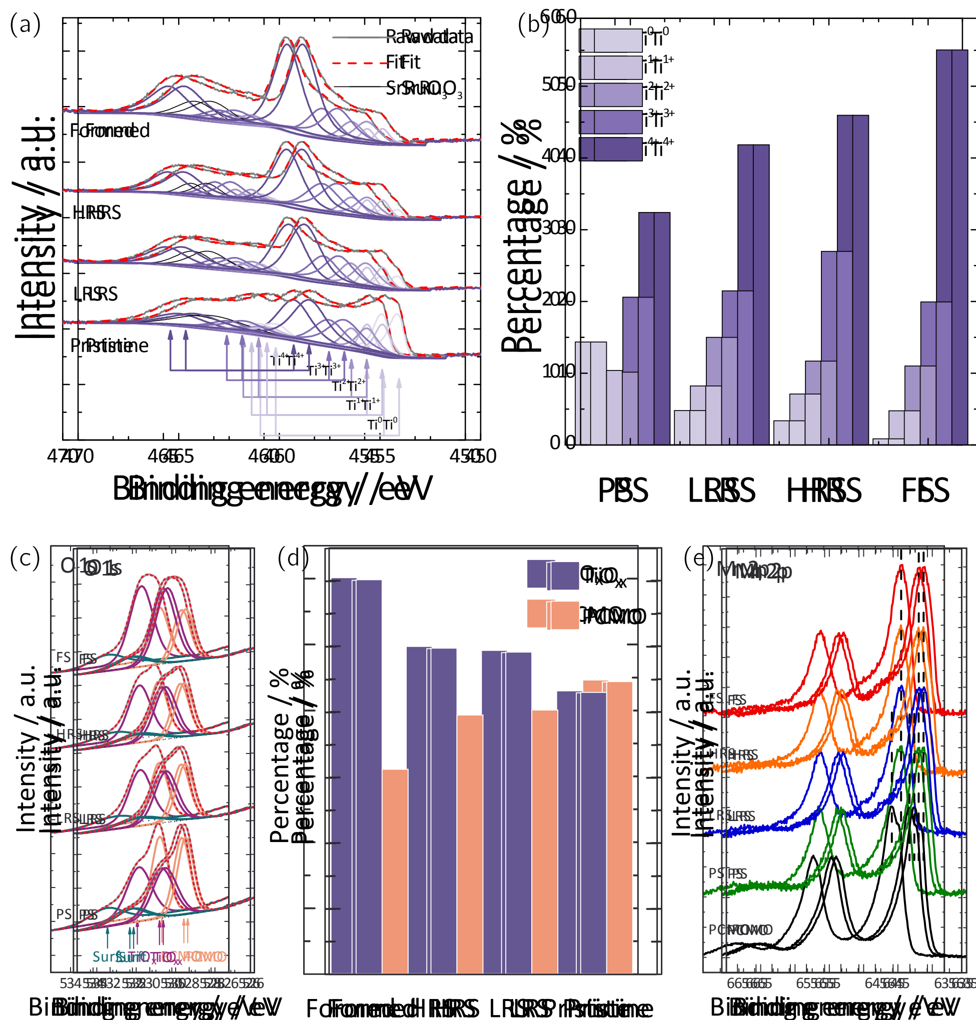

Figure 5.13: HAXPES spectra for resistively switching devices PCMO/Ti: (a) Ti 2p data sets with fits. (b) Ti 2p percentages. (c) O 1s data sets with fits. (d) O 1s percentages. (e) Mn 2p data sets.

and 5.13(d) depict the O 1s spectra and area percentage of three contributing peaks. Two peaks can be assigned to PCMO and TiO_x, while the third one is a result of surface contamination. In analogy to the trend observed in the Ti spectra, a spectral weight transfer is observed from PCMO to TiO_x upon increased resistance states. The Mn 2p emission doublet in Figure 5.13(e) is shifted towards lower binding energies for all resistance states in comparison to the PCMO reference sample. This indicates a shift of the average Mn valence towards Mn^{3+} according to

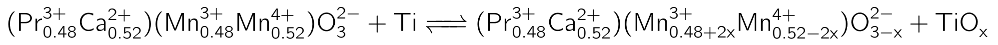

$$(Pr^{3+}_{0.48}Ca^{2+}_{0.52})(Mn^{3+}_{0.48}Mn^{4+}_{0.52})O^{2-}_{3} + Ti \rightleftharpoons (Pr^{3+}_{0.48}Ca^{2+}_{0.52})(Mn^{3+}_{0.48+2x}Mn^{4+}_{0.52-2x})O^{2-}_{3-x} + TiO_x$$

The photoemission spectra of the Ti 2p, O 1s and Mn 2p lines clearly show that a redox-reaction is induced through electrical biasing, influencing the resistance of both the Ti electrode and the PCMO layer. The monotonous increase of electrode oxidation with stack resistance implies a direct role of the interfacial oxide layer in the resistance change. The clear involvement of the Ti electrode during electroforming is confirmed by these measurements. Additionally, a significant difference between LRS and HRS could be shown, because the switching mechanism does take place distributed over the entire electrode area. So the chemical evidence for the resistive switching has been found for the system PCMO/Ti.

5.4.2 Modeling of read-out sweeps

In addition to these chemical analyses, electrical data have been evaluated to investigate, if the electrode oxidation alone determines the resistance of the multilayer stack. Regarding the low-voltage characteristics of the four resistive states in Figure 5.12(b), all curves show a non-linear behavior. However, for the PS and LRS the curves are almost centrically symmetric, while for the FS and HRS a notable asymmetry is observed. Taking into account the complex multilayer structure of the system, a qualitative analysis of the dominating conduction mechanisms during switching was performed.

For the symmetric read-out data for PS and LRS a field-acceleration of the polaron hopping was assumed as transport mechanism according to [133]

$$I_\Delta(V_\Delta) = \frac{nea\omega A}{\pi} e^{-\frac{\Delta E}{k_B T}} \sinh\left(\frac{ea}{2k_B T r} \cdot V_\Delta\right),$$

where T is the temperature, r the thickness of the hopping region, a the hopping distance, n the polaron density, ω the hopping frequency, A the device area, ΔE the activation energy

for hopping, k_B the Boltzmann constant and e the electronic charge. As the fitting of the pure hopping mechanism did not provide a good agreement with the measured data, a serial ohmic resistance R was added as . Beside the feed lines, the Pt top electrode and $SrRuO_3$ bottom contact, as well as the suboxides of the Ti [134] will contribute to this circuit element. In a serial circuit the current through each element is conserved according to $I_{sym} = I_\Delta = I_\Omega = I$, while the voltages are added accordingly as $V_{sym}(I) = V_\Delta(I) + V_\Omega(I)$. Thus, the inverse functions $V_\Delta(I)$ and $V_\Omega(I)$ have to be added as

$$V_{sym}(I) = V_\Delta(I) + V_\Omega(I) = \frac{2k_B T r}{ea} \operatorname{arcsinh}\left(\frac{\pi}{nea\omega A} e^{\frac{\Delta E}{k_B T}} \cdot I\right) + R \cdot I.$$

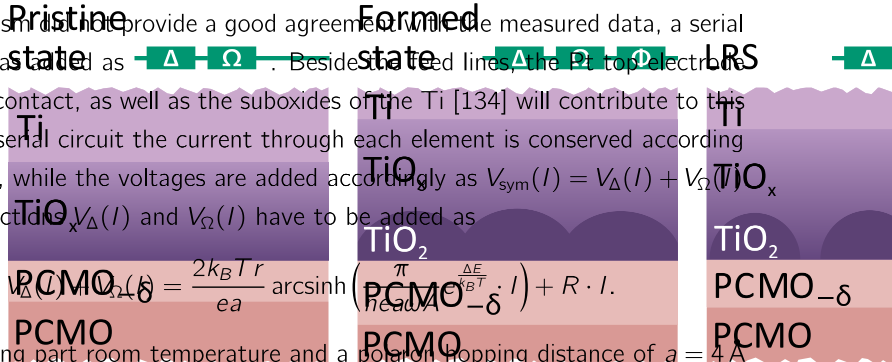

For the polaron hopping part room temperature and a polaron hopping distance of $a = 4$ Å according to the Mn-Mn distance was assumed. The pad area is $A = (50\,\mu m)^2$ and the polaron density $n = 0.78\,\frac{1}{nm^3}$, due to the results of the Hall-measurements in Section 4.2.2. The attempt rate for hopping was set to $\omega = 10^{13}$ Hz corresponding to the phonon frequency, so that two independent fitting parameters r and ΔE are left, as well as the serial resistance R. With the current model the two symmetric I-V curves could be fitted reasonably, as shown in Figure 5.14(a) and 5.14(c). For both fits the barrier for hopping transport was consistently determined to $\Delta E = 0.41$ eV, which is much higher than the energy barrier of $\Delta E = 0.12$ eV determined in Section 4.2.3 from temperature dependent resistance measurements, which is also confirmed in [133] for a completely oxidized thin film. In addition, a thickness of the hopping region r of below 1 nm was received, so that the results of the fitting procedure indicate, that only a thin part of the PCMO film near the Ti layer accounts for the non-linearity of the hopping region. Here, the hopping barrier is increased, as a reduction of this part leads to interrupted Mn-O-Mn chains, while the rest of the 20 nm thick PCMO thin film retains the ohmic conductance mechanism and thus contributes to R.

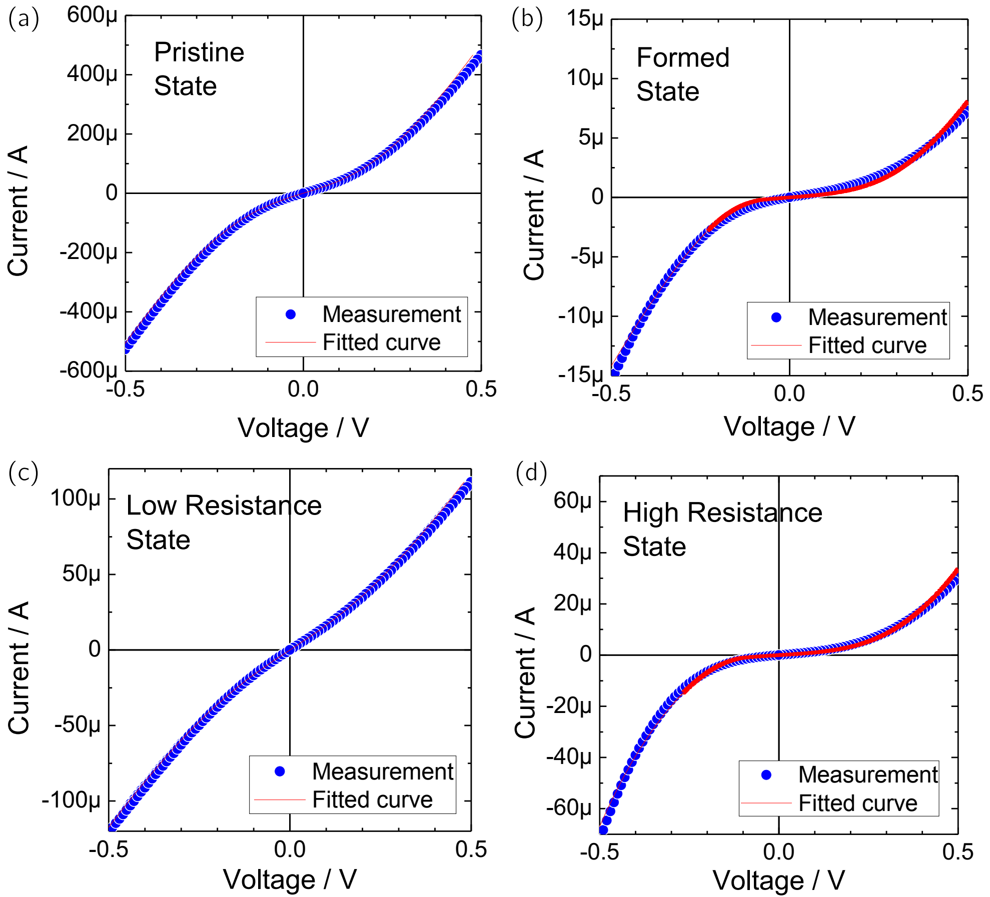

Figure 5.14: Read-out-*I*-*V* sweeps and fitted curves: (a) Pristine state: Symmetric *I*-*V* curve with high currents. (b) Formed state: Asymmetric *I*-*V* curve with low currents. (c) Low resistance state: Symmetric *I*-*V* curve. (d) High resistance state: Asymmetric *I*-*V* curve.

For the asymmetric read-out sweeps for FS and HRS, the model needs to be expanded by an additional asymmetric circuit element. As the HAXPES data show a larger amount of Ti^{4+} for these states, it is conceivable that an interfacial TiO_2 layer acts as a tunnel barrier for charge carrier transport at the Ti/TiO_x/TiO_2/PCMO interface region. For a trapezoidal tunnel barrier with two different barrier heights $\varphi_1 < \varphi_2$ and thickness d, described in [135], asymmetry can only be found for voltages higher than the specific barrier height $\varphi_{1/2}$. For lower voltages a symmetric function has to be applied:

$$I_\Phi(V_\Phi{=}V) =$$
$$\begin{cases} \dfrac{1.1eA(eV{+}\varphi_2{-}\varphi_1)^2}{4\pi h\varphi_2 d^2}\left[\mathrm{e}^{-\frac{23\pi\sqrt{m}d\varphi_2^{3/2}}{6h(eV+\varphi_2-\varphi_1)}} - \left(1+\dfrac{2eV}{\varphi_2}\right)\mathrm{e}^{-\frac{23\pi\sqrt{m}d\varphi_2^{3/2}\sqrt{1+\frac{2eV}{\varphi_2}}}{6h(eV+\varphi_2-\varphi_1)}}\right] & eV < \text{-}\varphi_1, \\ \dfrac{eA}{4\pi hd^2}\left[(\varphi_1{+}\varphi_2{-}eV)\mathrm{e}^{-\frac{4\pi d\sqrt{m}}{h}\sqrt{\varphi_1+\varphi_2-eV}} - (\varphi_1{+}\varphi_2{+}eV)\mathrm{e}^{-\frac{4\pi d\sqrt{m}}{h}\sqrt{\varphi_1+\varphi_2+eV}}\right] & e|V| \leq \varphi, \\ \dfrac{1.1eA(eV{-}\varphi_2{+}\varphi_1)^2}{4\pi h\varphi_1 d^2}\left[\mathrm{e}^{-\frac{23\pi\sqrt{m}d\varphi_1^{3/2}}{6h(eV-\varphi_2+\varphi_1)}} - \left(1+\dfrac{2eV}{\varphi_1}\right)\mathrm{e}^{-\frac{23\pi\sqrt{m}d\varphi_1^{3/2}\sqrt{1+\frac{2eV}{\varphi_1}}}{6h(eV-\varphi_2+\varphi_1)}}\right] & eV > \varphi_2. \end{cases}$$

m is the effective mass and h the Planck constant. The range of validity for the symmetric part of the function for intermediate voltages depends on the the specific barrier heights $-\varphi_1 \leq eV \leq \varphi_2$. For higher voltages applied to the PCMO devices the positive voltage branch $eV > \varphi_2$ is correlated with the reverse direction and the negative one $eV < -\varphi_1$ with the forward direction of the current.

For the devices, this tunnel circuit element is added in series to the two symmetric ones as —Δ—Ω—Φ—, so that again the relations $I_{asy} = I_\Delta = I_\Omega = I_\Phi = I$ and $V_{asy}(I) = V_\Delta(I) + V_\Omega(I) + V_\Phi(I)$ are valid. An inversion of formula $I_\Phi(V_\Phi)$ is analytically not possible. To circumvent this problem, the voltage V_Φ was varied in small increments and the current $I_\Phi(V_\Phi)$, flowing through the tunnel barrier, was calculated. As the current in a serial circuit is conserved with $I_\Phi = I$, the resulting voltage drop at the polaron hopping region $V_\Delta(I)$ and the ohmic resistance $V_\Omega(I)$ could be calculated, and all three voltages were added to obtain the overall voltage drop $V_{asy}(I)$. Using these calculations, an effective mass of $m = 1.19 \cdot m_e$ and the already obtained hopping energy of $\Delta E = 0.41$ eV, suitable parameter sets were found for both FS and HRS, resulting in good fits as shown in Figure 5.14(b) and 5.14(d), respectively.

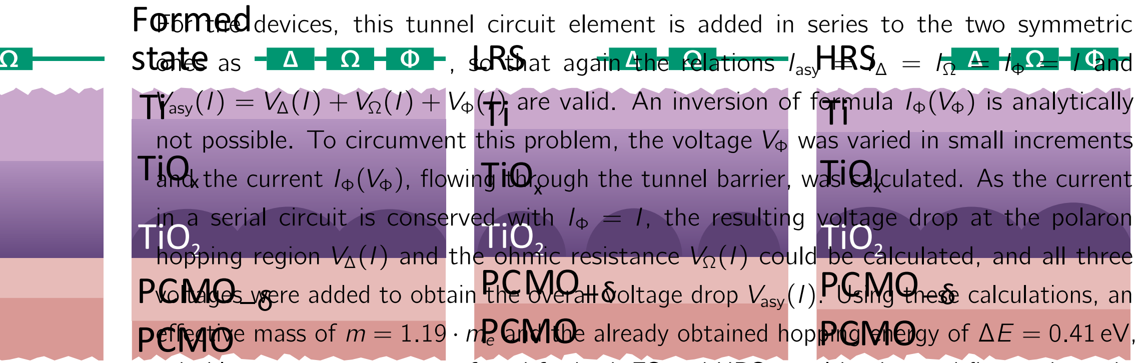

From these two different serial circuits necessary to reproduce the experimental data, charge carrier transport across the multilayer stack is concluded to be not determined by a single conduction mechanism, but rather by a combination of several mechanisms and their respective contribution to the total resistance. The fitting parameters for all four different resistance states are summarized in Table 5.1.

Taking into account the HAXPES results and the parameters obtained by appropriate fitting of equivalent circuits to each state, the transition between PCMO and TiO_2 as the dominating contribution to the stack resistance can now be understood as depicted in Figure 5.15.

State	Pristine	Formed	LRS	HRS
Hopping region thickness r	0.65 nm	1.60 nm	0.79 nm	0.95 nm
Hopping barrier ΔE	0.41 eV	(0.41 eV)	0.41 eV	(0.41 eV)
Ohmic resistance R	450 Ω	11′000 Ω	2′371 Ω	700 Ω
Tunnel barrier thickness d		2.94 nm		2.84 nm
Barrier height φ_1		0.080 eV		0.100 eV
Barrier height φ_2		0.915 eV		0.850 eV

Table 5.1: Fit parameters for the read-out sweeps for four different resistance states.

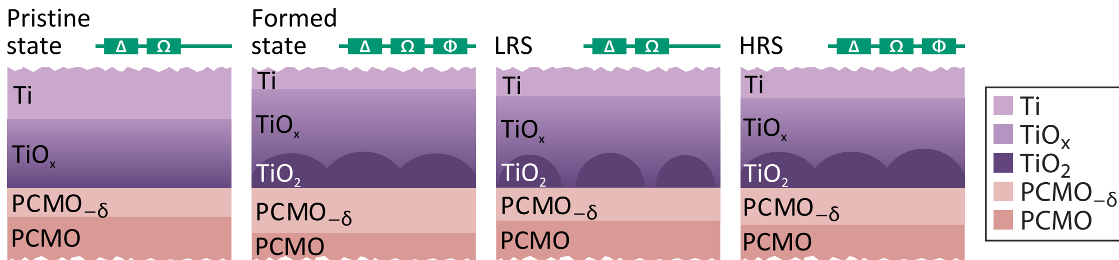

Figure 5.15: Model for resistive switching in a PCMO/Ti device: During the electroforming process a TiO_2 tunnel barrier is formed, which is bridged and restored during switching. In the equivalent circuit diagrams Δ symbolizes the polaron hopping region, Ω represents the ohmic resistance and Φ stands for the Simmons tunnel barrier.

Prior to the deposition of the Ti top electrode material, the PCMO is a highly doped *p*-type semiconductor with half-metallic behavior. During the deposition of the Ti top layer, the topmost PCMO layer is reduced, while the Ti is oxidized. The Ti oxidation is visible with TEM and HAXPES, but the suboxide formation only affects the serial ohmic resistance R. In contrast, the reduction of the topmost 1 nm PCMO causes an interruption of the double-exchange chains along the Mn−O−Mn bonds, increases the activation energy for hopping immensely and thus leads to a field-acceleration of the polaron hopping in this region before any operation has been applied to the device.
During electroforming, a positive voltage is applied to the top electrode and oxygen anions migrate from the PCMO towards the Ti and form a closed TiO_2 layer at the interface. The almost 3 nm thick TiO_2 acts as an asymmetric tunnel barrier, because it is sandwiched between two electrodes with different work functions/electron affinities. In addition, the $PCMO_{3-\delta}$ layer is increased in thickness and also the suboxide formation proceeded, which

results in a huge increase of the serial resistance. The TiO_2, having a formal electron affinity of $\chi_{TiO_2} = 4.0\,eV$ [136], forms a barrier of almost $\varphi_2 = 1\,eV$ at the interface to the reduced PCMO with $\chi_{PCMO} = 4.9\,eV$ [129]. At the interface to the Ti suboxides, which work functions might slightly differ from $\Phi_{Ti} = 4.33\,eV$ [105], a barrier of $\varphi_1 = 0.1\,eV$ is received. Despite the fact that the oxidation is homogeneous across the entire electrode, it is conceivable that the oxidation front shows in-plane inhomogeneities on the nanometer scale, as sketched in Figure 5.15 by bulges. Such inhomogeneities might be a consequence of the polycrystalline structure of the electrode, or due to the a nanoscale roughness of the oxygen diffusion front formed during electroforming.

When a negative bias is applied to the formed device for the SET process, the nanoscale roughness leads to a local reduction of the TiO_2 layer. As sketched in Figure 5.15, the tunnel barrier is percolated by reduced conductive $TiO_{2-\delta}$ channels. On the one hand, the tunnel barrier is not needed to fit the symmetrical electrical data, on the other hand in the HAXPES spectra the Ti^{4+} component is still strongly visible. The high serial resistance can be understood, as most of the device area is still covered with the TiO_2 and only a minor part contributes to the ohmic conductance.

For the RESET process by a positive voltage, the tunnel barrier is restored. The switching effect can then be understood according to chemical redox processes

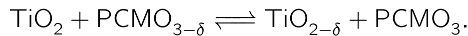

$$TiO_2 + PCMO_{3-\delta} \rightleftharpoons TiO_{2-\delta} + PCMO_3.$$

The oxygen depleted PCMO region acts as oxygen supply, but does not change its conductance behavior significantly, whereas the tunnel barrier is formed and bridged reversibly. The results are submitted for publication [137].

5.5 Second forming step and switching

The positive voltage sweep for forming in Figure 5.5(b) leads to a gradual decrease in current upon the forming process. When the voltage is increased further, a sharp increase in current is detected, as shown in Figure 5.16(a). As this irreversible procedure also activates a stable resistance switching behavior in the device, depicted in Figure 5.16(b), it is referred to as "second forming".

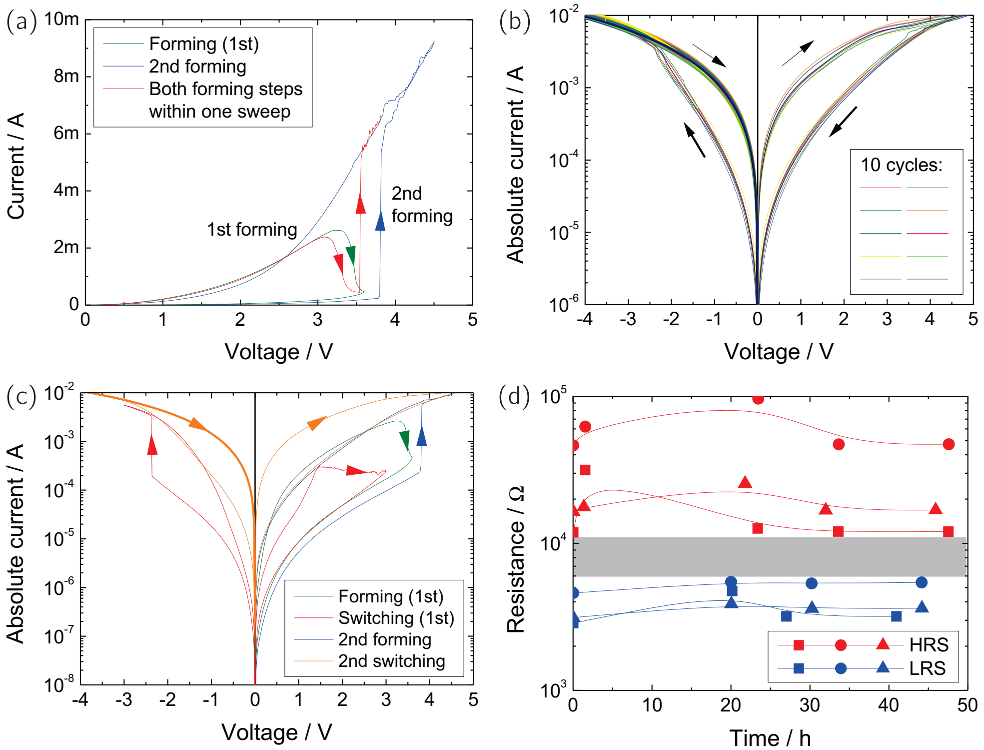

Figure 5.16: Second forming and switching: (a) Forming (first) and second forming sweep. (b) Resistive switching after the second forming. (c) Direct comparison of both forming and switching processes. (d) Retention measurements on the second switching in PCMO/Ti.

The activated resistive switching process after the second forming is taking place "counter-eight-wise" as well and is very stable, as visible in Figure 5.16(b) for 10 cycles. The hysteresis opens up by a factor of 10 already for small read-out voltages. In comparison to the first switching (Figure 5.16(c)), the second one is much more symmetric and the SET

and RESET are passed without any abrupt resistance changes.
The second forming was not possible for all PCMO/Ti devices. Especially for the larger pad sizes, no second forming appeared, so that no clear statement can be given for the homogeneity of the switching effect. From the two area sizes, where second switching was observed, no scaling with the area was measured, hinting on a filamentary switching mechanism. One possible explanation for these observations is the further oxidation of the complete Ti electrode. Upon further increase of the voltage, oxygen could be removed from the TiO_2 layer, leading to conducting paths through the TiO_2 layer and a sharp resistance decrease. In this scenario, the second switching could be the pure filamentary switching of the TiO_2 at the interface to Pt, while the rest of the former tunnel barrier is bridged by these channels. But further experiments are needed to confirm this explanation.
However, retention data are available for the second switching. For the LRS and HRS, three different pads were set/reset by a voltage pulse of ± 4 V, respectively, and afterward read-out with a voltage pulse of -0.1 V after four different time periods. The corresponding data are depicted in Figure 5.16(d) and show a gap of a factor of 6 between HRS and LRS.

6 Conclusions

In this work, the topic of interface effects in complex oxides has been addressed within the framework of novel data storage functionalities according to the "Beyond CMOS" concept. The modification of interfaces determines the growth behavior of epitaxial heterostructures, the homogeneous switching of ReRAM materials and the screening of dipols in ferroelectrics.

The epitaxial growth process by non-equilibrium pulsed laser deposition technique was studied for miscellaneous ruthenate, titanate and manganite compounds in various layer stack combinations. For all oxides, high quality thin films with atomically flat surfaces and rocking curve widths of below 0.05° were obtained as a result of differentiated parameter series.

The growth of ferroelectric $BaTiO_3$ was optimized to obtain a stable depolarization field. For ultra-thin $SrRuO_3$-$BaTiO_3$ stacks, the interface termination was studied in dependence of the deposition parameters. A mixed termination of TiO_2 and BaO was observed, which could be changed towards an almost complete TiO_2-termination by an additional annealing step. The introduction of one unit cell layer of $BaRuO_3$ was proved to change the termination to a uniform BaO-layer, which enables the step-flow growth mode for $SrRuO_3$. Embedded between two electrodes in capacitor structure, the $BaTiO_3$ devices exhibit large leakage currents, which on the one hand suppress the switching currents during the measurement and on the other hand might screen the dipole moments, which disables the depolarization field. It could be shown that high work function oxide electrode material is the best choice to minimize leakage. Anyhow, in stacks with a pure metal top electrode the leakage could be reduced by post-annealing, while the residual leakage can be avoided by low-temperature measurements and ultra-fast measurements. If the residual leakage current is separated from the switching signal, leakage compensating measurement programs can be applied and a remanent polarization of $30\,\frac{\mu C}{cm^2}$ was observed for $BaTiO_3$, exceeding the literature value of $26\,\frac{\mu C}{cm^2}$ due to an increased tetragonal distortion of the unit cell by compressive strain.

The lattice mismatch between the $Pr_{0.48}Ca_{0.52}MnO_3$ thin film and the substrate leads to

mechanical stress and thus strain within the thin film. For $Pr_{0.48}Ca_{0.52}MnO_3$, having a mismatch to $SrTiO_3$ of $-2.39\,\%$, the tensile strain energy is preserved within the material up to a thickness of 40 nm, where the system starts to relax. Two concurring relaxation processes could be identified in this work: The incorporation of randomly distributed edge dislocations near to the interface to $SrTiO_3$ and the formation of cracks all-through the thin film into the substrate. The type of relaxation process determines crucially the structural properties and furthermore the transport properties of the material.

Completely strained $Pr_{0.48}Ca_{0.52}MnO_3$ thin films were investigated with respect to their transport properties. Polaron hopping of holes with an activation energy of 0.12 eV was proved to be the conduction mechanism in bulk $Pr_{0.48}Ca_{0.52}MnO_3$. In accordance to these findings, the transport properties are mainly determined by effects of correlated electrons rather than by defect chemistry considerations. It was found, that under very reducing conditions, $Pr_{0.48}Ca_{0.52}MnO_3$ decomposes into its insulating constituents.
Stacked into a capacitor structure, $Pr_{0.48}Ca_{0.52}MnO_3$ shows resistive switching properties in combination with a low work function metal like titanium as active oxidizable electrode. After an initial electroforming step using a positive bias, the system can be switched stably between two states of a resistance ratio of one order of magnitude. Because the achieved retention time of at least 300 days was rather good, a further stabilization of the states by a ferroelectric was postponed to future investigations.
As the forming and switching mechanisms are occurring homogeneously over the entire interface between $Pr_{0.48}Ca_{0.52}MnO_3$ and Ti, electron microscopic and X-ray spectroscopic methods could be used to investigate the chemical changes during the different electrical treatments. Both forming and switching processes could be proved to be based on redox-reactions involving an oxygen transfer from the $Pr_{0.48}Ca_{0.52}MnO_3$ to the Ti, whereby the main changes appear in the valence state of the Ti electrode material. The electrical data could successfully be fitted by combining a polaron hopping contribution, containing an increased activation energy for the oxygen-depleted $Pr_{0.48}Ca_{0.52}MnO_3$ layer, with a serial ohmic resistor for the pristine and the low resistive state. For the formed and high resistive state, the equivalent circuit had to be supplemented by an additional serial tunnel barrier of trapezoidal shape, which could be proved to represent a thin TiO_2 layer. Combining the electrical and chemical information about the forming and switching effects in interface-type switching $Pr_{0.48}Ca_{0.52}MnO_3$-Ti devices, a coherent model for the switching effect is presented, which mainly bases on the formation and bridging of a TiO_2 tunnel barrier, leading to a reversible alternation between tunneling and polaron hopping as dominant transport mechanism [132, 137].

A Appendix

A.1 Additional information to Section 4.1.4

The raw data set of the (hkl)-mesh around STO (0.5|0|1) (Figure 4.7(a)) is depicted in Figure A.1(a). Here, four relatively intense spots are visible, which even almost exceed the countrate of the real Bragg reflex in the STO (1|0|0.5)-map. As only exactly one data point has this high value and the surrounding is less intense, respectively, it is very likely, that the spots are just an effect of the noise background of the signal. Nevertheless, the measurement in the spotty region of the map was repeated, as shown in Figure A.1(b). For this measurement, only the usual background noise is visible, so that the presumption is verified. To avoid confusion when viewing the results, the four data points were deleted for the presentation in the real document.

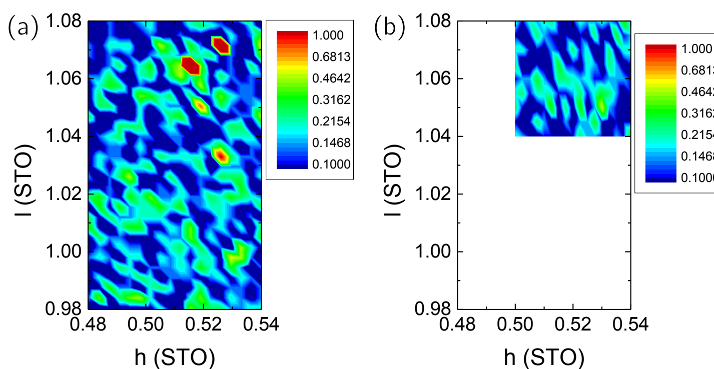

Figure A.1: Repetition of the scan around $SrTiO_3$ (0.5|0|1): As the intense spots in the unchanged map of this reflex (a) are not reproduced in the repeated measurement of the spotty region of the hlk-map (b), they can be regarded as background noise.

A.2 LC-AFM measurements on $Pr_{0.48}Ca_{0.52}MnO_3$

For further investigation of the line-pattern on top of thicker PCMO thin films in Section 4.1, local-conductivity AFM (LC-AFM) measurements were performed. The addressed question for experiments using this setup is the out-of-plane conductance, i.e. from the surface to the bottom. For this method, a conducting tip is used, which is brought in contact with the thin film surface, while a conducting substrate or, in this case, the bottom electrode $SrRuO_3$ is grounded. An adjustable voltage can be applied to the tip and for the measurement either the tip is set on a certain potential and scanned over the surface in contact mode, while the current is measured, or the tip is located at one position and the voltage is altered. A detailed description of this method can be found in [63]. The results of these measurements for a 50 nm thick PCMO layer on $SrRuO_3/SrTiO_3$ are shown in Figure A.2.

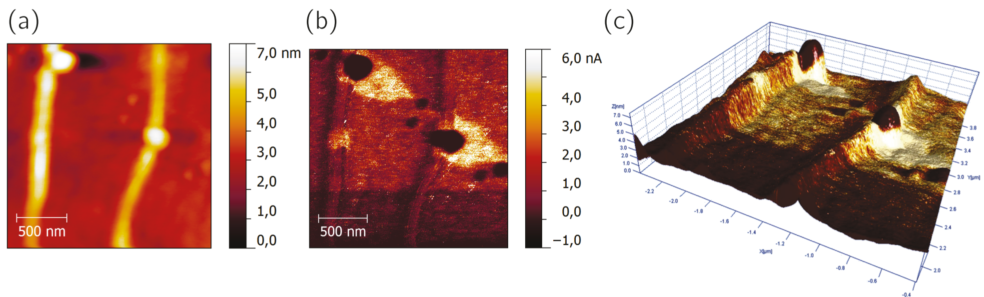

Figure A.2: LC-AFM measurements: (a) Topography scan of the LC-AFM with a conducting tip in contact mode. (b) Simultaneous current scan. (c) Overlaying of both topography and current signal.

The conducting tip is used to scan over the surface to measure the local conductivity of the PCMO layer. Applying a voltage of 2 V to the tip, the topography and flowing current were measured simultaneously at a part of the PCMO surface, where two lines are visible. The results are shown in Figure A.2(a) and A.2(b), respectively. The height signal is not as well resolved as the morphology measured with the non-conducting tip, but still two distinct lines are observable, which have two additional bumps on top. In the corresponding current signal, the scan was started from the bottom with an applied voltage of 1.5 V and after a third of the scan increased to 2 V, which explains the change in current. The two lines can be recognized, but not as a very good or bad conducting region compared to the environment. Only their shadow seems to be reproduced. The reason is not an actual change in conductance, but an effect of the topography. As the tip is scanning

perpendicular to the lines, which are bulged out, the tip is pressed with more force onto the surface at the up-going side, while the force is smaller at the down-going side, which is reproduced in the current signal. A real effect is visible for the bumps, which have a much smaller conductivity than the rest of the sample. In addition, in a defined region next to each bump, the conductivity is clearly increased. The bumps could be insulating segregated material, but the good conducting parts cannot be explained so far. For a more illustrative view, the two signals were superimposed in Figure A.2(c), so that the topography covers the height signal, while the color code represents the current signal. In this combination, the factual coincidence is monitored.
Overall, the lines do not differ anyhow in their out-of-plane conductivity compared to the domain areas.

A.3 Additional information to Section 4.1.6

The Fourier analyzed image of Figure 4.11(a) is shown in Figure 4.11(b). To illustrate the applied technique, the two missing images of the Fourier transform are added in Figure A.3.

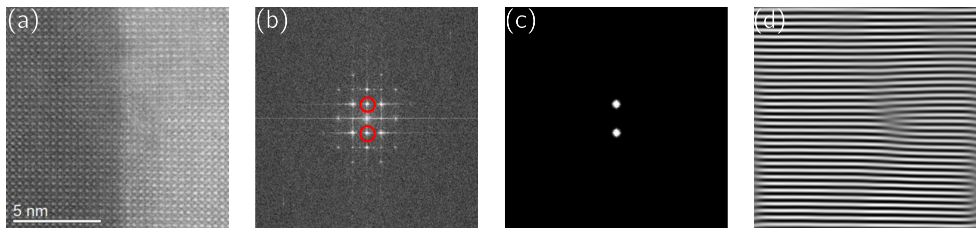

Figure A.3: Method of a Fourier analysis for a STEM image, exemplary for Figure 4.11(a): (a) Original HR-STEM image. (b) Fourier transformed image. (c) Fourier image after application of a mask to select specific frequencies. (d) STEM image after inverse Fourier transformation, identifying an edge dislocation.

In Figure A.3(a) the raw data of the HR-STEM image of a 50 nm thick PCMO film on $SrTiO_3$ is shown. A Fourier transform of this image is created by using the Fast Fourier Transform algorithm available on the TEM software package Digital Micrograph^{TM} and depicted in Figure A.3(b). To select specific frequencies in the frequency domain, a mask was applied to the FFT image (Figure A.3(c)). To return to the spatial domain, an inverse Fourier transform was taken, which enables an easy identification of the edge dislocation within the PCMO thin film, as shown in Figure A.3(d).

A.4 Additional information to Section 3.2

After the application of the poling map (Figure 3.4(a)), the same area was read-out with just the AC voltage signal. The resulting phase image after 14 min is shown in Figure 3.4(b). In Figure A.4 the same 3 x 3 μm^2 read-out phase image is presented for different time periods after the poling procedure. The phase scale is not shown, as a drift in phase has been observed.

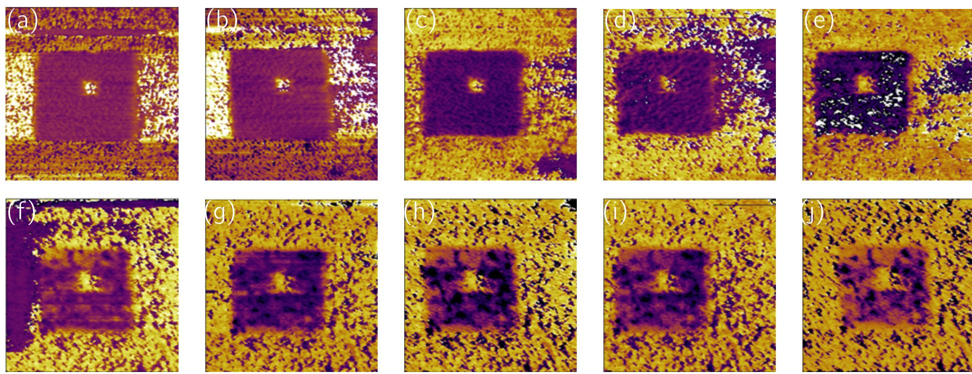

Figure A.4: Temporal evolution of written FE states: (a) 14 min. (b) 23 min. (c) 32 min. (d) 40 min. (e) 49 min. (f) 69 min. (g) 78 min. (h) 86 min. (i) 95 min. (j) 104 min.

A.5 Electrical properties of $Pr_{1-x}Ca_xMnO_3/BaTiO_3$ stack

Two different manganite stoichiometries of $Pr_{1-x}Ca_xMnO_3$ have been grown on $BaTiO_3$/ $SrRuO_3/SrTiO_3$, as reported in Section 2.2.3.4. Additional Pt top electrodes were deposited by sputter deposition through a shadow mask (Figure A.5(a)) and the devices have been tested for ferroelectricity.

Figure A.5 shows the results of *P*-*V* and *C*-*V* measurements of 20 nm $Pr_{0.48}Ca_{0.52}MnO_3$ and $Pr_{0.6}Ca_{0.4}MnO_3$ grown on 20 nm $BaTiO_3$, respectively. A ferroelectric hysteresis could not be measured, as for both samples no switching peaks have been observed in the current response. As depicted in Figure A.5(b) for $Pr_{0.48}Ca_{0.52}MnO_3$ exemplarily, the current response at $f = 2$ kHz did consist of the leakage current and an additional dielectric contribution. In the *C*-*V* measurement with an excitation signal frequency of 1 MHz, the pad-to-pad measurements are shown for both samples. Although the $\tan\delta$ has a very high

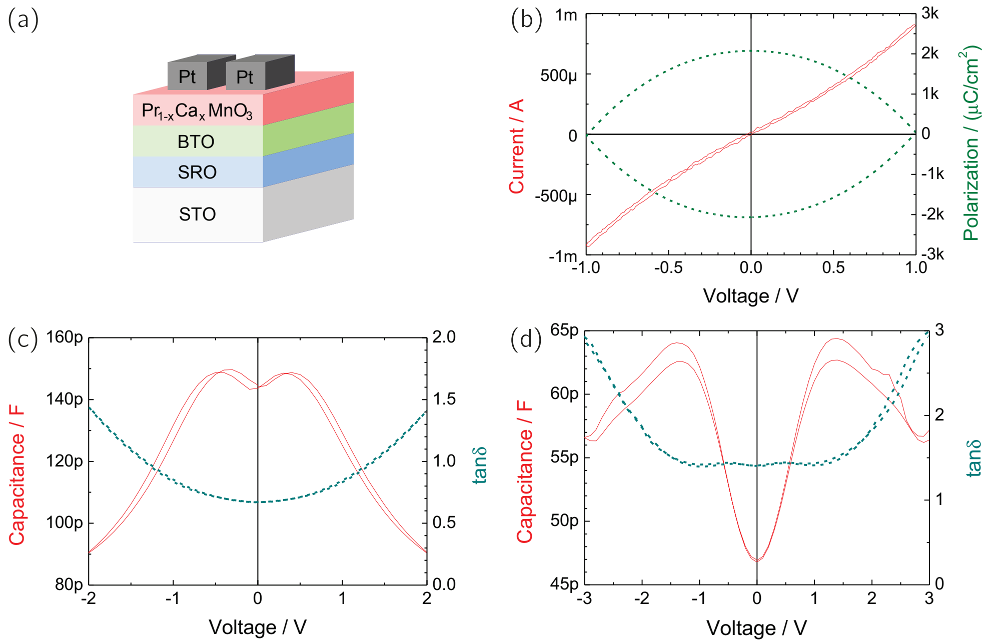

Figure A.5: Ferroelectric characterization on BTO-PCMO stacks: (a) Layer stack $SrTiO_3$ / 30 nm $SrRuO_3$ / 20 nm $BaTiO_3$ / 20 nm $Pr_{1-x}Ca_xMnO_3$. (b) *P-V* measurement on stack with $Pr_{0.48}Ca_{0.52}MnO_3$. (c) *C-V* measurement on stack with $Pr_{0.48}Ca_{0.52}MnO_3$. (d) *C-V* measurement on stack with $Pr_{0.6}Ca_{0.4}MnO_3$.

value $\gtrsim 1$, at least for small voltages the capacitance seems to be measurable. For both samples a double peak is observed, which does not depend on the history of the device as for ferroelectrics. The origin of this curve shape has not been illuminated yet.

Figures

1.1 Principle of resistive RAM. 6
1.2 Polarity of switching in RRAM 7
1.3 Classification of VCM 8
1.4 Resistive switching via homogeneous oxygen movement 10
1.5 Kröger-Vink diagram of M_2O_3 and A:M_2O_3 14
1.6 Kröger-Vink diagram of A:M_2O_3 covering site-balance 16
1.7 Conductivity and mobility of LSMO 17
1.8 Phase diagrams of $R_{1-x}A_xMnO_3$ 18
1.9 Crystal field splitting and Jahn-Teller distortion 20
1.10 Magnetic super and double exchange 21
1.11 DFT calculations for PCMO 24

2.1 Strain effects in hetero-epitaxial growth 26
2.2 RHEED-assisted pulsed laser deposition 27
2.3 Principle of RHEED 28
2.4 Work principle of an AFM 30
2.5 X-ray diffraction 31
2.6 Growth of STO/SRO 34
2.7 Growth of STO/SRO 35
2.8 Growth of STO/SRO/BTO 37
2.9 Energy series of BTO growth 38
2.10 Growth of STO/SRO/BTO 40
2.11 AFM image of the SRO surface, grown on PCMO. 41
2.12 Cross-sectional STEM image of STO/BTO/SRO stack 42
2.13 Cross-sectional STEM image of stack with BRO incorporation 43
2.14 Detail of Figure 2.13(h) 45
2.15 Indications for a tetragonal distortion in BTO 45
2.16 Growth of STO/20nm PCMO 47

2.17 Growth of Nb:STO/SRO/PCMO . . . 48
2.18 Growth of PCMO on STO, NGO and LSAT . . . 49
2.19 XPS measurements on PCMO . . . 51
2.20 Growth of different manganites on STO . . . 53
2.21 Growth of NGO/LSMO/SRO . . . 55
2.22 Growth of STO/SRO/BTO/PCMO with 52% and 40% . . . 57

3.1 Phase transitions in BTO . . . 60
3.2 Principle of ferroelectricity in BTO . . . 61
3.3 PFM measurements on BTO samples . . . 63
3.4 PFM writing experiments on a BTO sample . . . 64
3.5 Voltage sweeps for FE characterization . . . 65
3.6 *I-V* and *P-V* curves of different circuit elements . . . 66
3.7 Dependence of switching on frequency and voltage . . . 68
3.8 Ferroelectric switching of BTO . . . 69
3.9 Ferroelectric switching of different BTO samples . . . 70
3.10 Static hysteresis measurement . . . 72
3.11 Annealing effect on FE switching of BTO . . . 73
3.12 Temperature dependent measurement of FE properties of BTO . . . 74
3.13 Capacitance measurements on BTO . . . 76
3.14 Ferroelectric switching of a symmetric BTO sample . . . 78
3.15 Resistive switching of a BTO devices . . . 80

4.1 Lateral I-V measurements in PCMO . . . 84
4.2 Domain structure on PCMO surface . . . 85
4.3 Thickness series of PCMO on STO . . . 86
4.4 Documentation of the peel-off process of the PCMO thin film due to increased strain . . . 87
4.5 Different orientations of the PCMO unit cell . . . 88
4.6 Possible reflexes for different orientations of PCMO . . . 89
4.7 hkl-meshes around four different possible superstructure reflexes of PCMO 90
4.8 SEM-assisted micro-probe measurements of the domain structure of PCMO 92
4.9 LC-AFM measurements in non-conducting mode . . . 93
4.10 TEM/HR-STEM investigations on PCMO showing the line pattern . . . 94
4.11 TEM/HR-STEM investigations on PCMO having a smooth surface . . . 96
4.12 Statistics on 50nm thick PCMO samples . . . 98

4.13 Sketch of the setups in van-der-Pauw geometry 100
4.14 Hall measurements on PCMO 102
4.15 Temperature dependence of the resistivity for PCMO and LSMO 104
4.16 High temperature conductance measurements 106
4.17 Decomposition of PCMO thin film 107

5.1 LC-AFM measurements: I-V sweeps 110
5.2 Electrical characterization of the p-n junction of PCMO to Nb:STO . . . 111
5.3 Electrical characterization of the p-n junction of manganites to Nb:STO . 112
5.4 I-V characteristic for different top electrodes on PCMO 113
5.5 Electroforming and resistive switching of a PCMO/Ti device 115
5.6 Impedance spectroscopy on a PCMO device 116
5.7 Area dependence of the pristine and formed state 117
5.8 TEM and EELS cross-section of PCMO devices 119
5.9 Resistance distribution and sample geometry for HAXPES 121
5.10 HAXPES results on electroforming 122
5.11 Evaluation of Ti 2p core levels 124
5.12 Resistive switching 125
5.13 HAXPES spectra for resistively switching devices PCMO/Ti 127
5.14 Read-out I-V sweeps and fits 130
5.15 Model for resistive switching in a PCMO/Ti devices 132
5.16 Second forming and switching 134

A.1 Repetition of the scan around STO (0.5|0|1) 139
A.2 LC-AFM measurements 140
A.3 Method of a Fourier analysis for a STEM image 141
A.4 Temporal evolution of written FE states 142
A.5 Ferroelectric characterization on BTO-PCMO stacks 143

Tables

2.1 Annealing procedures for different substrates 29
2.2 Energy series of BTO growth 39
2.3 Lattice constants determined by STEM 45
2.4 Stoichiometry dependence of strain in PCMO 54
2.5 Growth of PCMO in two stoichiometries on BTO 56

5.1 Fit parameters for read-out sweeps 132

References

[1] Moore, G.E.: Cramming more components onto integrated circuits. In: *Electronics 38, 8, 114–117* (1965). http://dx.doi.org/10.1109/JPROC.1998.658762 1

[2] http://www.nanofunction.eu/data/document/introduction.pdf 1

[3] http://www.semicon.panasonic.co.jp/en/products/microcomputers/mn101l 1

[4] Xing, Z.W. ; Wu, N.J. ; Ignatiev, A.: Electric-pulse-induced resistive switching effect enhanced by a ferroelectric buffer on the $Pr_{0.7}Ca_{0.3}MnO_3$ thin film. In: *Appl. Phys. Lett. 91, 052106* (2007). http://dx.doi.org/10.1063/1.2759476 2, 11

[5] Schmelzer, S.: *Ultra Thin Oxide Films for Dielectric and Resistive Memory Applications*, Rheinisch-Westfälische Technische Hochschule Aachen, Diss., 2013 5

[6] *The International Technology Roadmap for Semiconductors. 2011 Edition*. http://www.itrs.net/Links/2011ITRS/2011Chapters/2011ERD.pdf. Emerging Research Devices 5

[7] Waser, R. ; Dittmann, R. ; Staikov, G. ; Szot, K.: Redox-Based Resistive Switching Memories - Nanoionic Mechanisms, Prospects, and Challenges. In: *Adv. Mater. 21, 2632–2663* (2009). http://dx.doi.org/10.1002/adma.200900375 6, 7, 8

[8] Tsymbal, E.Y. ; Kohlstedt, H.: Applied physics - Tunneling across a ferroelectric. In: *Science 313, 5784, 181-183* (2006). http://dx.doi.org/10.1126/science.1126230 6, 7

[9] Loertscher, E. ; Ciszek, J.W. ; Tour, J. ; Riel, H.: Reversible and controllable switching of a single-molecule junction. In: *Small 2, 8–9, 973–977* (2006). http://dx.doi.org/10.1002/smll.200600101 6

[10] Wuttig, M. ; Yamada, N.: Phase-change materials for rewriteable data storage. In: *Nat. Mater. 6, 11, 824–832* (2007). http://dx.doi.org/10.1038/nmat2009 6

[11] Waser, R.: *Redox-Based Switching - the Next Step of Moore's Law?*, DPG Spring Meeting, Invited Talk, 2009 6

[12] Waser, R.: *Nanoelectronics and Information Technology - Advanced Electronic Materials and Novel Devices*. Viley-VCH Verlag & Co.KGaA, 2012 7

[13] Muenstermann, R. ; Menke, T. ; Dittmann, R. ; Waser, R.: Coexistence of Filamentary and Homogeneous Resistive Switching in Fe-Doped $SrTiO_3$ Thin-Film Memristive Devices. In: *Adv. Mater. 22, 43, 4819–4822* (2010). http://dx.doi.org/10.1002/adma.201001872 7

[14] Gibbons, J.F. ; Beadle, W.E.: Switching Properties of Thin NiO Films. In: *Solid-State Electron. 7, 11, 785* (1964). http://dx.doi.org/10.1016/0038-1101(64)90131-5 7

[15] Kozicki, M.N. ; Mitkova, M.: *Nanoelectronics and Information Technology - Advanced Electronic Materials and Novel Devices*. Viley-VCH Verlag & Co.KGaA, 2012 7

[16] Simmons, J.G. ; Verderbe, R.R.: New Conduction and Reversible Memory Phenomena in Thin Insulating Films. In: *Proc. R. Soc. London Ser. A 301, 1464, 77* (1967). http://dx.doi.org/10.1098/rspa.1967.0191 7

[17] Sawa, A. ; Fujii, T. ; Kawasaki, M. ; Tokura, Y.: Interface resistance switching at a few nanometer thick perovskite manganite active layers. In: *Appl. Phys. Lett. 88, 23, 232112* (2006). http://dx.doi.org/10.1063/1.2211147 7, 10

[18] Asamitsu, A. ; Tomioka, Y. ; Kuwahara, H. ; Tokura, Y.: Current switching of resistive states in magnetoresistive manganites. In: *Nature 388, 50* (1997). http://dx.doi.org/10.1038/40363 7, 9

[19] Jooss, C. ; Wu, L. ; Beetz, T. ; Klie, R.F. ; Beleggia, M. ; Schofield, N.A. ; Schramm, S. ; Hoffmann, J. ; Zhu, Y.: Polaron melting and ordering as key mechanisms for colossal resistance effects in manganites. In: *PNAS 104, 34, 13597–13602* (2007). http://dx.doi.org/10.1073/pnas.0702748104 7, 9

[20] Sawa, A.: Resistive switching in transition metal oxides. In: *Mater. Today 11, 6, 28* (2008). http://dx.doi.org/10.1016/S1369-7021(08)70119-6 8, 9, 10, 112

[21] Quintero, M. ; Levy, P. ; Leyva, A.G. ; Rozenberg, M.J.: Mechanism of Electric–Pulse-Induced Resistance Switching in Manganites. In: *Phys. Rew. Lett. 98, 116601* (2007). http://dx.doi.org/10.1103/PhysRevLett.98.116601 9

[22] Sawa, A. ; Fujii, T. ; Kawasaki, M. ; Tokura, Y.: Hysteretic current-voltage characteristics and resistance switching at a rectifying $Ti/Pr_{0.7}Ca_{0.3}MnO_3$ interface. In: *Appl. Phys. Lett. 85, 18, 4073* (2004). http://dx.doi.org/10.1063/1.1812580 9, 46

[23] Asanuma, S. ; Akoh, H. ; Yamada, H. ; Sawa, A.: Relationship between resistive switching characteristics and band diagrams of Ti/$Pr_{1-x}Ca_xMnO_3$ junctions. In: *Phys. Rev. B 80, 235113* (2009). http://dx.doi.org/10.1103/PhysRevB.80.235113 10, 26, 118

[24] Tsubouchi, K. ; Ohkubo, I. ; Kumigashira, H. ; Oshima, M. ; Matsumoto, Y. ; Itaka, K. ; Ohnishi, T. ; Lippmaa, M. ; Koinuma, H.: High-Throughput Characterization of Metal Electrode Performance for Electric-Field-Induced Resistance Switching in Metal/$Pr_{0.7}Ca_{0.3}MnO_3$/Metal Structures. In: *Adv. Mater. 19, 1711–1713* (2007). http://dx.doi.org/10.1002/adma.200601957 10

[25] Liao, Z.L. ; Wang, Z.Z. ; Meng, Y. ; Liu, Z.Y. ; Gao, P. ; Gang, J.L. ; Zhao, H.W. ; Liang, X.J. ; Bai, X.D. ; Chen, D.M.: Categorization of resistive switching of metal-$Pr_{0.7}Ca_{0.3}MnO_3$-metal devices. In: *Appl. Phys. Lett. 94, 253503* (2009). http://dx.doi.org/10.1063/1.3159471 10

[26] Shono, K. ; Kawano, H. ; Yokota, T. ; Gomi, M.: Origin of Negative Differential Resistance Observed on Bipolar Resistance Switching Device with Ti/$Pr_{0.7}Ca_{0.3}MnO_3$/Pt Structure. In: *Appl. Phys. Express 1, 55002* (2008). http://dx.doi.org/10.1143/APEX.1.055002 10

[27] Kawano, H. ; Shono, K. ; Yokota, T. ; Gomi, M.: Enhancement of Switching Capability on Bipolar Resistance Switching Device with Ta/$Pr_{0.7}Ca_{0.3}MnO_3$/Pt Structure. In: *Appl. Phys. Express 1, 101901* (2008). http://dx.doi.org/10.1143/APEX.1.101901 10

[28] Shono, K. ; Kawano, H. ; Yokota, T. ; Gomi, M.: Effect of Electron Injection at the Pt-interface on a Bipolar Resistance Switching Device with Ta/$Pr_{0.7}Ca_{0.3}MnO_3$/Pt Structure. In: *Appl. Phys. Express 2, 071401* (2009). http://dx.doi.org/10.1143/APEX.2.071401 10

[29] Kohlstedt, H. ; Pertsev, N.A. ; Contreras, J.R. ; Waser, R.: Theoretical current-voltage characteristics of ferroelectric tunnel junctions. In: *Phys. Rew. B 72, 125341* (2005). http://dx.doi.org/10.1103/PhysRevB.72.125341 10

[30] Meyer, R. ; Waser, R.: Hysteretic resistance concepts in ferroelectric thin films. In: *J. Appl. Phys. 100, 051611* (2006). http://dx.doi.org/10.1063/1.2337078 10

[31] Chanthbouala, A. ; Crassous, A. ; Garcia, V. ; Bouzehouane, K. ; Fusil, S. ; Moya, X. ; Allibe, J. ; Dlubak, B. ; Grollier, J. ; Xavier, S. ; Deranlot, C. ; Moshar, A. ; Proksch, R. ; Mathur, N.D. ; Bibes, M. ; Barthélémy, A.: Solid-state memories

based on ferroelectric tunnel junctions. In: *Nature Nanotech. 7, 101* (2011). http://dx.doi.org/10.1038/NNANO.2011.213 10

[32] Chanthbouala, A. ; Garcia, V. ; Cherifi, R.O. ; Bouzehouane, K. ; Fusil, S. ; Moya, X. ; Xavier, X. ; Yamada, H. ; Deranlot, C. ; Mathur, N.D. ; Bibes, M. ; Barthélémy, A. ; Grollier, J.: A ferroelectric memristor. In: *Nature Mater. 11, 860* (2012). http://dx.doi.org/10.1038/NMAT3415 10

[33] Tsymbal, E.Y. ; Gruverman, A. ; Garcia, V. ; Bibes, M. ; Barthélémy, A.: Ferroelectric and multiferroic tunnel junctions. In: *MRS Bulletin 37, 138* (2012). http://dx.doi.org/10.1557/mrs.2011.358 10

[34] Tsurumaki, A. ; Yamada, H. ; Sawa, A.: Impact of Bi Deficiencies on Ferroelectric Resistive Switching Characteristics Observed at p-Type Schottky-Like Pt/$Bi_{1-\delta}FeO_3$ Interfaces. In: *Adv. Funct. Mater. 22, 1040–1047* (2012). http://dx.doi.org/10.1002/adfm.201102883 10

[35] Bourim, E.M. ; Park, S. ; Liu, X. ; Biju, K.P. ; Hwang, H. ; Ignatiev, A.: Ferroelectric Polarization Effect on Al-Nb Codoped $Pb(Zr_{0.52}Ti_{0.48})O_3/Pr_{0.7}Ca_{0.3}MnO_3$ Heterostructure Resistive Memory. In: *Electroochem. Solid State Lett. 14, 5, H225–H228* (2011). http://dx.doi.org/10.1149/1.3556977 11

[36] Sadaf, S.M. ; Bourim, E.M. ; Liu, X. ; Choudhury, S.H. ; Kim, D.W. ; Hwang, H.: Ferroelectricity-induced resistive switching in $Pb(Zr_{0.52}Ti_{0.48})O_3/Pr_{0.7}Ca_{0.3}MnO_3$/Nb-doped $SrTiO_3$ epitaxial heterostructure. In: *Appl. Phys. Lett. 100, 113505* (2012). http://dx.doi.org/10.1063/1.3694016 11

[37] Liu, X. ; Biju, K.P. ; Park, J. ; Park, S. ; Shin, J. ; Kim, I. ; Sadaf, S.M. ; Hwang, H.: Low-Power and Controllable Memory Window in Pt/$Pr_{0.7}Ca_{0.3}MnO_3$/Yttria-Stabilized Zirconia/W Resistive Random-Access Memory Devices. In: *J. Nanosci. Nanotchnol. 12, 4, 3252–3255* (2012). http://dx.doi.org/10.1166/jnn.2012.5606 11

[38] Malavasi, L.: The physics of manganites: Structure and transport. In: *Rev. Mod. Phys. 73, 583–628* (2001). http://dx.doi.org/10.1103/RevModPhys.73.583 12

[39] Smyth, D.M.: *The Defect Chemistry of Metal Oxides*. Oxford University Press, Inc., 2000 12

[40] Kroeger, F.A. ; Vink, H.J.: Relations between the Concentrations of Imperfections in Solids. In: *J. Phys. Chem. Solids 5, 3, 208–223* (1958). http://dx.doi.org/10.1016/0022-3697(58)90069-6 12

[41] Poulsen, F.W.: Defect chemistry modelling of oxygen-stoichiometry, vacancy concentrations, and conductivity of $(La_{1-x}Sr_x)MnO_{3\pm\delta}$. In: *Solid State Ionics 129, 145–162* (2000). http://dx.doi.org/10.1016/S0167-2738(99)00322-7 13, 15, 16

[42] Malavasi, L.: Role of defect chemistry in the properties of perovskite manganites. In: *J. Mater. Chem. 18, 3295–3308* (2008). http://dx.doi.org/10.1039/B800099A 15

[43] Nowotny, J. ; Rekas, M.: Defect Chemistry of $(La,Sr)MnO_3$. In: *J. Am. Ceram. Soc. 81, 1, 67–80* (1998). http://dx.doi.org/10.1111/j.1151-2916.1998.tb02297.x 16

[44] Kuo, J.H. ; Anderson, H.U. ; Sparlin, D.M.: Oxidation-Reduction Behavior of Undoped and Sr-Doped $LaMnO_3$: Defect Structure, Electrical Conductivity, and Thermoelectric Power. In: *J. Solid State Chem. 87, 55–63* (1990). http://dx.doi.org/10.1016/0022-4596(90)90064-5 17, 18

[45] Moschkau, P.: *Defektabhängige Transporteigenschaften von Praseodym-Kalzium-Manganat*, Georg-August-Universität zu Göttingen, Diss., 2009 18, 20, 31, 88

[46] Istomin, K.: *Interplay between Charge, Spin and Orbital Ordering in $La_{1-x}Sr_xMnO_3$ Manganites*, Rheinisch-Westfälische Technische Hochschule Aachen, Diss., 2003 18

[47] Goldschmidt, V.M.: Die Gesetze der Krystallochemie. In: *Die Naturwissenschaften 21, 477–485* (1926). http://dx.doi.org/10.1007/BF01507527 19

[48] http://de.academic.ru/pictures/dewiki/75/Kristallstruktur_Perovskit.png 20

[49] http://grund-wissen.de/_downloads/d-orbitale.svg 20

[50] http://www.fiz-karlsruhe.de/icsd.html 20, 36, 46, 49, 54, 56

[51] Goodenough, J.B.: Theory of the Role of Covalence in the Perovskite-Type Manganites [La, M(II)]MnO_3. In: *Phys. Rev. 100, 2, 564–573* (1955). http://dx.doi.org/10.1103/PhysRev.100.564 19

[52] Raabe, S. ; Mierwaldt, D. ; Ciston, J. ; Uijttewaal, M. ; Stein, H. ; Hoffmann, J. ; Zhu, Y.M. ; Blöchl, P. ; Jooss, C.: In Situ Electrochemical Electron Microscopy Study of Oxygen Evolution Activity of Doped Manganite Perovskites. In: *Adv. Funct. Mater. 22, 16, 3378–3388* (2012). http://dx.doi.org/10.1002/adfm.201103173 20, 24

[53] Gor'kov, L.P. ; Kresin, V.Z.: Mixed-valence manganites: fundamentals and main properties. In: *Phys. Rep. 400, 149–208* (2004). http://dx.doi.org/10.1016/j.physrep.2004.08.003 22, 101

[54] Coey, J.M.D ; Viret, M. ; Molnár, S. von: Mixed-valence manganites. In: *Adv. Phys. 48, 2, 167–293* (1999). http://dx.doi.org/10.1080/000187399243455 22, 101

[55] Peña, M.A. ; Fierro, J.L.G.: Chemical Structures and Performance of Perovskite Oxides. In: *Chem. Rev. 101, 1981–2017* (2001). http://dx.doi.org/10.1021/cr980129f 23

[56] Meyer, R.: *Wenn sich "nichts" bewegt - Thermodynamik und Kinetik von Punktdefekten; Tunnel RRAM - Device Features and 1R True Cross-Point Implementation*. EMRL seminar talks, 2013. – Standford University; RAMBUS Inc. 24

[57] Mott, N.: The mobility edge since 1967. In: *J. Phys. C: Solid State Phys. 20, 3075–3102* (1987). http://dx.doi.org/10.1088/0022-3719/20/21/008 23

[58] Schlom, D.G. ; Chen, L.Q. ; Eom, C.B. ; Rabe, K.M. ; Streiffer, S.K. ; Triscone, J.M.: Strain Tuning of Ferroelectric Thin Films. In: *Annu. Rev. Mater. Res. 37, 589–626* (2007). http://dx.doi.org/10.1146/annurev.matsci.37.061206.113016 26

[59] Opel, M.: Spintronic oxides grown by laser-MBE. In: *J. Phys. D: Appl. Phys. 45, 033001* (2012). http://dx.doi.org/10.1088/0022-3727/45/3/033001 26

[60] Schlom, D.G. ; Chen, L.-Q. ; Pan, X. ; Schmehl, A. ; Zurbuchen, M.A.: A Thin Film Approach to Engineering Functionality into Oxides. In: *J. Am. Ceram. Soc. 91, 8, 2429–2454* (2008). http://dx.doi.org/10.1111/j.1551-2916.2008.02556.x 26, 104

[61] Huijben, M. ; Rijnders, G. ; Blank, D.H.A. ; Bals, S. ; Aert, S. van ; Verbeeck, J. ; Tendeloo, G. van ; Brinkman, A. ; Hilgenkamp, H.: Electronically coupled complementary interfaces between perovskite band insulators. In: *Nature Mater. 5, 556* (2006). http://dx.doi.org/10.1038/nmat1675 26

[62] Hwang, H.Y. ; Iwasa, Y. ; Kawasaki, M. ; Keimer, B. ; Nagaosa, N. ; Tokura, Y.: Emergent phenomena at oxide interfaces. In: *Nature Mater. 11, 103* (2012). http://dx.doi.org/10.1038/NMAT3223 26

[63] Wicklein, S.: *Defect Engineering of $SrTiO_3$ thin films for resistive switching applications*, Christian-Albrechts-Universität zu Kiel, Diss., 2013 27, 33, 38, 84, 140

[64] Rijnders, A.J.H.M.: *The Initial Growth of Complex Oxides: Study and Manipulation*, University of Twente, Enschede, The Netherlands, Diss., 2001 28

[65] http://img.springerimages.com/Images/SpringerBooks/PUB=Springer_Berlin_Heidelberg-Berlin,_Heidelberg/BSE=284003/BOK=978-3-540-47055-7/CHP=

1_10.1007-978-3-540-47055-7_1/MediaObjects/WATER_978-3-540-47055-7_1_Fig11_HTML.jpg 28

[66] http://www.pascal-co-ltd.co.jp/solutions/index.html 28

[67] Menke, T.: *Investigation of the electroforming and resistive switching mechanisms in Fe-doped* $SrTiO_3$ *thin films*, Rheinisch-Westfälische Technische Hochschule Aachen, Diss., 2009 30, 110

[68] http://www.home.agilent.com/upload/cmc_upload/ck/zz-other/images/AFM_schematic.gif 30

[69] Friedrich, I.: *Optische Datenspeicherung mit Phasenwechselmedien - Präparation und Charakterisierung von GeSbTe-Schichten*, Rheinisch-Westfälische Technische Hochschule Aachen, Diss., 2000 31

[70] Gunkel, F.: *The role of defects at functional interfaces between polar and non-polar perovskite oxides*, Rheinisch-Westfälische Technische Hochschule Aachen, Diss., 2013 33, 72, 73, 105

[71] Menke, T. ; Mi, S. ; Jia, C. ; Park, D. ; Mayer, J. ; Schützendorf, P. ; Dittmann, R.: *Growth mode adjustment of ultrathin heteroepitaxial* $Ba_xSr_{1-x}TiO_3$ *films exploiting strain and kinetic limitation*, MRS Fall Meeting, Poster Presentation, 2010 33, 41

[72] Hong, W. ; Lee, H.N. ; Yoon, M. ; Christen, H.M. ; Lowndes, D.H. ; Suo, Z. ; Zhang, Z.: Persistent Step-Flow Growth of Strained Films on Vicinal Substrates. In: *Phys. Rev. Lett. 95, 095501* (2005). http://dx.doi.org/10.1103/PhysRevLett.95.095501 33

[73] Shin, J. ; Kalinin, S.V. ; Lee, H.N. ; Christen, H.M. ; Moore, R.G. ; Plummer, E.W. ; Baddorf, A.P.: Surface stability of epitaxial $SrRuO_3$ films. In: *Surface Science 581, 118–132* (2005). http://dx.doi.org/10.1016/j.susc.2005.02.038 33

[74] Choi, J. ; Eom, C.B. ; Rijnders, G. ; Rogalla, H. ; Blank, D.H.A.: Growth mode transition from layer by layer to step flow during the growth of heteroepitaxial $SrRuO_3$ on (001) $SrTiO_3$. In: *Apply. Phys. Lett. 79, 10, 1447* (2001). http://dx.doi.org/10.1063/1.1389837 34

[75] Kan, D. ; Shimakawa, Y.: Controlled cation stoichiometry in pulsed laser deposition-grown $BaTiO_3$ epitaxial thin films with laser fluence. In: *Appl. Phys. Lett. 99, 081907* (2011). http://dx.doi.org/10.1063/1.3628461 38, 78

[76] He, J.Q. ; Vasco, E. ; Dittmann, R. ; Wang, R.H.: Growth dynamics and strain

relaxation mechanisms in $BaTiO_3$ pulsed laser deposited on $SrRuO_3/SrTiO_3$. In: *Phys. Rew. B 73, 125413* (2006). http://dx.doi.org/10.1103/PhysRevB.73.125413 38

[77] Park, D.: *The investigation of ferroelectric materials using Transmission Electron Microscopy*, Rheinisch-Westfälische Technische Hochschule Aachen, Diss., 2013. – to be published 41

[78] Lenser, C.: *Investigation of Resistive Switching in Fe-doped $SrTiO_3$ by Advanced Spectroscopy*, Rheinisch-Westfälische Technische Hochschule Aachen, Diss., 2013 50

[79] Doveren, H. van ; Verhoeven, J.A.T.: XPS Spectra of Ca, Sr, Ba and their Oxides. In: *J. Electron Spectrosc. Relat. Phenom. 21, 3, 265–273* (1980). http://dx.doi.org/10.1016/0368-2048(80)85055-9 52

[80] Lampis, N.: *Characterization of epitaxial thin films and multilayers of manganites*, Università degli Studi di Napoli Federico II, Diss., 2008. http://www.fedoa.unina.it/3050/1/Tesi_Nathascia_Lampis.pdf 52

[81] Kim, O.: *Optimierung des PLD-Wachstumsprozesses von Manganat-Dünnschichten für ReRAM-Anwendungen*, Rheinisch-Westfälische Technische Hochschule Aachen, Bachelorarbeit, 2011 53

[82] Wasmund, H.C.: *Untersuchung resistiv schaltender Bauelemente mittels Transmissions-Röntgenmikroskopie*, Rheinisch-Westfälische Technische Hochschule Aachen, Diplomarbeit, 2013 54

[83] Koehl, A. ; Wasmund, H. ; Herpers, A. ; Guttmann, P. ; Werner, S. ; Henzler, K. ; Du, H. ; Mayer, J. ; Waser, R. ; Dittmann, R.: Evidence for multifilamentary valence changes in resistive switching $SrTiO_3$ devices detected by transmission X-ray microscopy. In: *APL Mater. 1, 042102* (2013). http://dx.doi.org/10.1063/1.4822438 54

[84] Wemple, S.H.: Polarization Fluctuations and the Optical-Absorption Edge in $BaTiO_3$. In: *Phys. Rev. B 2, 7, 2679–2689* (1970). http://dx.doi.org/10.1103/PhysRevB.2.2679 59

[85] Shebanov, L.A.: X-Ray Temperature Study of Crystallographic Characteristics of Barium Titanate. In: *Phys. Status Solidi A 65, 1, 321–325* (1981). http://dx.doi.org/10.1002/pssa.2210650137 60

[86] Pantel, D.: *Dielektrische und magnetische Eigenschaften multifunktionaler Dünnschichtstrukturen*, Technische Universität München, Diplomarbeit, 2008 60

[87] Kwei, G.H. ; Lawson, A.C. ; Billinge, S.J.L. ; Cheong, S.W.: Structures of the Ferroelectric Phases of Barium Titanate. In: *J. Phys. Chem. 97, 10, 2368–2377* (1993). http://dx.doi.org/10.1021/j100112a043 60

[88] Kaiser, A.: *Elektronentunneln durch ultradünne ferroelektrische Schichten*, Universität zu Köln, Diplomarbeit, 2006 61

[89] aixACCT Systems GmbH (Hrsg.): *TF Analyzer 2000E - Hysteresis Software Version 2.3*. Talbotstr. 25, 52068 Aachen, Germany: aixACCT Systems GmbH, 2012. www.aixacct.com 65, 69

[90] Scott, J.F.: Ferroelectrics go bananas. In: *J. Phys.: Condens. Matter 20, 021001* (2008). http://dx.doi.org/10.1088/0953-8984/20/02/021001 66

[91] Meyer, R. ; Waser, R. ; Prume, K. ; Schmitz, T. ; Tiedke, S.: Dynamic leakage current compensation in ferroelectric thin-film capacitor structures. In: *Appl. Phys. Lett. 86, 142907* (2005). http://dx.doi.org/10.1063/1.1897425 69

[92] Jona, F. ; Shirane, G.: *Ferroelectric Crystals*. Pergamon Press, New York, 1962 http://www.ph2.uni-koeln.de/fileadmin/Lehre/Fortgeschrittenenpraktikum/JonaShirane.pdf 71

[93] Trithaveesak, O.: *Ferroelektrische Eigenschaften von Kondensatoren mit epitaktischen $BaTiO_3$-Dünnschichten*, Rheinisch-Westfälische Technische Hochschule Aachen, Diss., 2004 72

[94] Katsu, H.: *Crystal- and Defect-Chemistry of Fine Grained Thermistor Ceramics on $BaTiO_3$ Basis with BaO-Excess*, Rheinisch-Westfälische Technische Hochschule Aachen, Diss., 2011 72

[95] Contreras, J.R.: *Ferroelectric Tunnel Junctions*, Universität zu Köln, Diss., 2004 73

[96] De Souza, R.A. ; Gunkel, F. ; Hoffmann-Eifert, S. ; Dittmann, R.: Finite-size vs. interface-proximity effects in thin-film, epitaxial $SrTiO_3$. In: *submitted to Phys. Rew. Lett.* (2013) 73

[97] Lewis, G.V. ; Catlow, C.R.A.: Defect studies of doped and undoped barium-titanate using computer-simulation techniques. In: *J. Phys. Chem. Solids 47, 1, 89–97* (1986). http://dx.doi.org/10.1016/0022-3697(86)90182-4 74

[98] Shin, J. ; Kalinin, S.V. ; Borisevich, A.Y. ; Plummer, E.W. ; Baddorf, A.P.: Layer-by-layer and pseudo-two-dimensional growth modes for heteroepitaxial $BaTiO_3$ films by exploiting kinetic limitations. In: *Appl. Phys. Lett. 91, 202901* (2007). http://dx.doi.org/10.1063/1.2790477 78

[99] Abe, K. ; Yanase, N. ; Kawakubo, T.: Asymmetric Switching of Ferroelectric Polarization in a Heteroepitaxial $BaTiO_3$ Thin Film Capacitor. In: *Jpn. J. Appl. Phys. 39, 4059–4063* (2000). http://dx.doi.org/10.1143/JJAP.39.4059 78

[100] Choi, K.J. ; Biegalski, M. ; Li, Y.L. ; Sharan, A. ; Schubert, J. ; Uecker, R. ; Reiche, P. ; Chen, Y.B. ; Pan, X.Q. ; Gopalan, V. ; Chen, L.Q. ; Schlom, D.G. ; Eom, C.B.: Enhancement of ferroelectricity in strained $BaTiO_3$ thin films. In: *Science 306, 5698, 1005–1009* (2004). http://dx.doi.org/10.1126/science.1103218 78

[101] Kim, Y.S. ; Jo, J.Y. ; Kim, D.J. ; Chang, Y.J. ; Lee, J.H. ; Noh, T.W. ; Song, T.K. ; Yoon, J.G. ; Chung, J.S. ; Baik, S.I. ; Kim, Y.W. ; Jung, C.U.: Ferroelectric properties of $SrRuO_3/BaTiO_3/SrRuO_3$ ultrathin film capacitors free from passive layers. In: *Appl. Phys. Lett. 88, 072909* (2006). http://dx.doi.org/10.1063/1.2174100 78

[102] Petraru, A. ; Kohlstedt, H. ; Poppe, U. ; Waser, R. ; Solbach, A. ; Klemradt, U. ; Schubert, J. ; Zander, W. ; Pertsev, N.A.: Wedgelike ultrathin epitaxial $BaTiO_3$ films for studies of scaling effects in ferroelectrics. In: *Appl. Phys. Lett. 93, 072902* (2008). http://dx.doi.org/10.1063/1.2972135 78

[103] Petraru, A. ; Pertsev, N.A. ; Kohlstedt, H. ; Poppe, U. ; Waser, R. ; Solbach, A. ; Klemradt, U.: Polarization and lattice strains in epitaxial $BaTiO_3$ films grown by high-pressure sputtering. In: *J. Appl. Phys. 101, 114106* (2007). http://dx.doi.org/10.1063/1.2745277 78

[104] Menzel, S. ; Waters, M. ; Marchewka, A. ; Böttger, U. ; Dittmann, R. ; Waser, R.: Origin of the Ultra-nonlinear Switching Kinetics in Oxide-Based Resistive Switches. In: *Adv. Funct. Mater. 21, 23, 4487–4492* (2011). http://dx.doi.org/10.1002/adfm.201101117 81

[105] Michaelson, H.B.: The work function of the elements and its periodicity. In: *J. Appl. Phys. 48, 11, 4729–4733* (1977). http://dx.doi.org/10.1063/1.323539 83, 110, 112, 113, 133

[106] Fujimoto, M. ; Koyama, H. ; Nishi, Y. ; Suzuki, T. ; Kobayashi, S. ; Tamai, Y. ; Awaya, N.: Crystallographic Domain Structure of an Epitaxial $(Pr_{0.7}Ca_{0.3})MnO_3$ Thin Film Grown on a $SrTiO_3$ Single Crystal Substrate. In: *J. Am. Ceram. Soc. 90,*

7, 2205–2209 (2007). http://dx.doi.org/10.1111/j.1551-2916.2007.01686.x 84, 88

[107] Thiel, S.P.: *Study of Interface Properties in $LaAlO_3/SrTiO_3$ Heterostructures*, Universität Augsburg, Diss., 2009 84

[108] Noyong, M. ; Blech, K. ; Rosenberger, A. ; Klocke, V. ; Simon, U.: In situ nanomanipulation system for electrical measurements in SEM. In: *Meas. Sci. Technol. 18, N84–N89* (2007). http://dx.doi.org/10.1088/0957-0233/18/12/N02 91

[109] Speck, J.S. ; Pompe, W.: Domain configurations due to multiple misfit relaxation mechanisms in epitaxial ferroelectric thin films. I. Theory. In: *J. Appl. Phys. 76, 1, 466–476* (1994). http://dx.doi.org/10.1063/1.357097 96

[110] Peng, H.B. ; Zhao, B.R. ; Xie, Z. ; Lin, B.Y. ; Zhu, B.Y. ; Hao, Z. ; Tao, H.J. ; Xu, B. ; Wang, C.Y. ; Chen, H. ; Wu, F.: Ordered Surface Structure in $La_{1-x}Ca_xMnO_3$ Films. In: *Phys. Rew. Lett. 82, 2, 362* (1999). http://dx.doi.org/10.1103/PhysRevLett.82.362 97

[111] Ligny, D. de ; Pichet, P.: High-temperature heat capacity and thermal expansion of $SrTiO_3$ and $SrZrO_3$ perovskites. In: *Phys. Rew. B 53, 6, 3013* (1996). http://dx.doi.org/10.1103/PhysRevB.53.3013 97

[112] Wang, H.S. ; Wertz, E. ; Hu, Y.F. ; Li, Q. ; Schlom, D.G.: Role of strain in magnetotransport properties of $Pr_{0.67}Sr_{0.33}MnO_3$ thin films. In: *J. Appl. Phys. 87, 10, 7409* (2000). http://dx.doi.org/10.1063/1.373002 97

[113] Zhao, G.M. ; Hunt, M.B. ; Keller, H.: Strong Oxygen-Mass Dependence of the Thermal-Expansion Coefficient in the Manganites $(La_{1-x}Ca_x)_{1-y}Mn_{1-y}O_3$. In: *Phys. Rew. Lett. 78, 5, 955* (1997). http://dx.doi.org/10.1103/PhysRevLett.78.955 97

[114] Tatsi, A. ; Papadopoulou, E.L. ; Lampakis, D. ; Liarokapis, E. ; Prellier, W. ; Mercey, B.: Raman study of anharmonic effects in $Pr_{0.5}Ca_{0.5}MnO_3$ thin films. In: *Phys. Rew. B 68, 024432* (2003). http://dx.doi.org/10.1103/PhysRevB.68.024432 97

[115] Ibarra, M.R. ; De Teresa, J.M. ; Blasco, J. ; Algarabel, P.A. ; Marquina, C. ; García, J. ; Stankiewicz, J. ; Ritter, C.: Lattice effects, stability under a high magnetic field, and magnetotransport properties of the charge-ordered mixed-valence $La_{0.35}Ca_{0.65}MnO_3$ perovskite. In: *Phys. Rew. B 56, 13, 8252* (1997). http://dx.doi.org/10.1103/PhysRevB.56.8252 97

[116] Freund, L.B. ; Suresh, S.: *Thin Film Materials: Stress, Defect Formation and*

Surface Evolution. Cambridge University Press, 2004 http://dx.doi.org/10.1017/CBO9780511754715 97

[117] Wang, Y. ; Kim, S.G. ; Chen, I.W.: Control of strain relaxation in tensile and compressive oxide thin films. In: *Acta Mater. 56, 18, 5312–5321* (2008). http://dx.doi.org/10.1016/j.actamat.2008.07.010 97, 99

[118] Pauw, L.J. van d.: A method of measuring specific resestivity and hall effect of discs of arbitrary shape. In: *Philips Res. Repts. 13, 1–9* (1958) 100

[119] Tomioka, Y. ; Asamitsu, A. ; Kuwahara, H. ; Moritomo, Y. ; Tokura, Y.: Magnetic-field-induced metal-insulator phenomena in $Pr_{1-x}Ca_xMnO_3$ with controlled charge-ordering instability. In: *Phys. Rev. B 53, 4, R1689–R1692* (1996). http://dx.doi.org/10.1103/PhysRevB.53.R1689 101

[120] http://hyperphysics.phy-astr.gsu.edu/hbase/Tables/rstiv.html 101

[121] Chaneliere, C. ; Autran, J.L. ; Devine, R.A.B.: Conduction mechanisms in Ta_2O_5/SiO_2 and Ta_2O_5/Si_3N_4 stacked structures on Si. In: *J. Appl. Phys. 86, 1, 480* (1999). http://dx.doi.org/10.1063/1.370756 103

[122] *Manganese-based perovskites*. http://www.springermaterials.com/docs/pdf/10037300_40.html?queryterms=%22manganese-based%20perovskites%22. SpringerMaterials, The Landolt-Börnstein Database, New Series III/27F1α, 5.1.6, 123–199 104

[123] Pollert, E. ; Krupicka, S. ; Kuzmicova, E.: STRUCTURAL STUDY OF $Pr_{1-x}Ca_xMnO_3$ AND $Y_{1-x}Ca_xMnO_3$ PEROVSKITES. In: *J. Phys. Chem. Solids 43, 12, 1137–1145* (1982). http://dx.doi.org/10.1016/0022-3697(82)90142-1 104

[124] Geßenich, M.: *Influence of temperature and partial pressure of oxygen on the electrical conductivity of praseodymium calcium manganite ceramics*, Rheinisch-Westfälische Technische Hochschule Aachen, Diplomarbeit, 2013 107

[125] Cherepanov, V.A. ; Barkhatova, L.Y. ; Voronin, V.I.: Phase Equilibria in the La-Sr-Mn-O System. In: *J. Solid State Chem. 134, 1, 38–44* (1997). http://dx.doi.org/10.1006/jssc.1997.7532 107

[126] Yang, H. ; Luo, H.M. ; Wang, H. ; Usov, I.O. ; Suvorova, N.A. ; Jain, M. ; Feldmann, D.M. ; Dowden, P.C. ; DePaula, R.F. ; Jia, Q.X.: Rectifying current-voltage characteristics of $BiFeO_3$/Nb-doped $SrTiO_3$ heterojunction. In: *Appl. Phys. Lett. 92, 10, 102113* (2008). http://dx.doi.org/10.1063/1.2896302 110

[127] Sze, S.M. ; Kwok, K.N.: *Physics of Semiconductor Device*. Wiley-Interscience, 2007 110, 112

[128] Sawa, A. ; Fujii, T. ; Kawasaki, M. ; Tokura, Y.: Highly rectifying $Pr_{0.7}Ca_{0.3}MnO_3/SrTi_{0.9998}Nb_{0.0002}O_3$ p-n junction. In: *Appl. Phys. Lett. 86, 11, 112508* (2005). http://dx.doi.org/10.1063/1.1883336 110, 111

[129] Reagor, D.W. ; Lee, S.Y. ; Li, Y. ; Jia, Q.X.: Work function of the mixed-valent manganese perovskites. In: *J. Appl. Phys. 95, 12, 7971–7975* (2004). http://dx.doi.org/10.1063/1.17378022 111, 133

[130] Meyer, R. ; Schloss, L. ; Brewer, J. ; Lambertson, R. ; Kinney, W. ; Sanchez, J. ; Rinerson, D.: Oxide dual-layer memory element for scalable non-volatile cross-point memory technology. In: *Proc. NVMTS, 1–5* (2008). http://dx.doi.org/10.1109/NVMT.2008.4731194 114

[131] Ebata, K. ; Wadati, H. ; Takizawa, M. ; Fujimori, A. ; Chikamatsu, A. ; Kumigashira, H. ; Oshima, M. ; Tomioka, Y. ; Tokura, Y.: Chemical potential shift and spectral-weight transfer in $Pr_{1-x}Ca_xMnO_3$ revealed by photoemission spectroscopy. In: *Phys. Rev. B 74, 064419* (2006). http://dx.doi.org/10.1103/PhysRevB.74.064419 123

[132] Borgatti, F. ; Park, C. ; Herpers, A. ; Offi, F. ; Egoavil, R. ; Yamashita, Y. ; Yang, A. ; Kobata, M. ; Kobayashi, K. ; Verbeeck, J. ; Panaccione, G. ; Dittmann, R.: Chemical insight into electroforming of resistive switching manganite heterostructures. In: *Nanoscale 5, 3954–3960* (2013). http://dx.doi.org/10.1039/c3nr00106g 123, 125, 138

[133] Schramm, S. ; Hoffmann, J. ; Jooss, C.: Transport and ordering of polarons in CER manganites PrCaMnO. In: *J. Phys.: Condens. Matter 20, 395231* (2008). http://dx.doi.org/10.1088/0953-8984/20/39/395231 128, 129

[134] Harada, S. ; Tanaka, K. ; Inui, H.: Thermoelectric properties and crystallographic shear structures in titanium oxides of the Magnèli phases. In: *J. Appl. Phys. 108, 83703* (2010). http://dx.doi.org/10.1063/1.3498801 129

[135] Simmons, J.G.: Electric Tunnel Effect between Dissimilar Electrodes Separated by a Thin Insulating Film. In: *J. Appl. Phys. 34, 9, 2581* (1963). http://dx.doi.org/10.1063/1.1729774 130

[136] Nosaka, Y. ; Norimatsu, K. ; Miyama, H.: The function of metals in metal-compounded semiconductor photocatalysts. In: *Chem. Phys. Lett. 106, 1–2, 128–131* (1984). http://dx.doi.org/10.1016/0009-2614(84)87025-6 133

[137] Herpers, A. ; Lenser, C. ; Park, C. ; Offi, F. ; Borgatti, F. ; Panaccione, G. ; Menzel, S. ; Waser, R. ; Dittmann, R.: Memristive Properties of Metal/Manganite Devices: Correlation of Charge-Carrier Transport and Redox-State at the Interface. In: *submitted to Adv. Mater.* (2013). http://dx.doi.org/ 133, 138

Acknowledgements

This thesis would never have been possible without the assistance and support of numerous people:

First of all, I would like to thank Professor Dr. Rainer Waser for the opportunity to perform my research at the Institut für Festkörperforschung 6 / Peter Grünberg Institut 7 and for his first readership.

I want to thank Professor Dr. Manfred Martin for agreeing to be my second reader.

Special thanks go to my supervisor Professor Dr. Regina Dittmann, who guided and supported me during my entire time as a PhD student.

Thanks to Maria Garcia, Michaela Ott and Martina Heinz for the help in administrative questions during my time at the institute.

This work would not have been possible without the help of numerous colleagues with technical background. Special thanks go to Marcel Gerst, René Borowski and my fellow-support in PLD-related problems Georg Pickartz.

I would like to thank Dr. Tobias Menke for the introduction into the field of ReRAM and the supervision at the beginning of my work as well as for his effort and patience during this time.

I would like to thank all former and current members of the PLD group for the rich support and fruitful discussions in both technical and scientific questions, as well as for a pleasant atmosphere in the labs and the office. Special thanks go to Chanwoo Park for various electrical measurements on PCMO devices, Dr. Christian Lenser for the evaluation of the HAXPES data and all spectroscopy-related questions, Annemarie Köhl for XPS measurements, Dr. Felix Gunkel for Hall and HTEC measurements, Dr. Sebastian Wicklein for LC-AFM measurements and Katharina Skaja for HTEC measurements.
Additionally, I would like to thank my former Bachelor student Oksana Kim and my Master student Raheleh Azmi for their support of and interest in my research.

Thanks to Dr. Paul Meuffels, who supported my work with critical questions and fruitful discussions and who always made time for various problems.

I also received help from members of the IWE II in Aachen, especially from Inka Müller in ferroelectric characterization methods, Astrid Marchevska, who supported my simulation of defect chemistry, Dr. Stephan Menzel and Dr. Eike Linn for help with the modeling of ReRAM devices and the combination of ReRAM with FE components.

I would like to say thank you to all members of both institutes in Jülich and Aachen for their help in various questions and the pleasant work atmosphere. Special thanks to all people who took part in the daily coffee round and made the time much more entertaining. Thanks also for my ride sharing and a cheerful time on my way to work and back, especially to Ninet Babajani.

I would like to thank all collaborators within the research center Jülich and the RWTH for fruitful research, especially Daesung Park and Professor Dr. Joachim Mayer from the GFE, RWHT, for the investigation of ultra-thin films and interface effects, Dr. Michael Noyong from the IAC, RWTH, for the micro-probe measurements and Dr. Karen Friese and Paul Zakalek for special XRD measurement.

Thanks go also to Twente Solid State Technology B.V. (TSST) for the continuous support with our PLD system and Bernd Reichenberg, aixACCT Systems GmbH, for a competent support in FE questions.

Thanks to the IFOX (Interfacing Oxides) project, funded by the European Union Council under the 7th Framework Program (grant no. 246102), which made this work possible. Special thanks go to the project partners Dr. Francesco Borgatti and Dr. Giancarlo Panaccione from Consiglio Nazionale delle Richerche (ISMN) for HAXPES investigations, Ricardo Egoavil and Jo Verbeeck from EMAT, Universiteit Antwerpen, for TEM measurements, Dr. Lucian Pintilie, National Institute of Materials Physics Bucharest (NIMP), for PFM measurements, Hajo Moolegraaf, Universiteit Twente, for Hall- and resistivity measurements and Kerry O-Shea, University of Glasgow, for STEM measurements.

I would like to thank all of my friends for their moral support and the patience they have shown with me. Special thanks go to Annika Seufert, Bendikt Arndt and Nicolas Raab for correcting this thesis.

Finally, this work would not have been possible without the support of my parents, Marianne Herpers and Hans Aust, during my whole studies and the following PhD period. Thanks to Malte Linn for the emotional backing in all times.

Schriften des Forschungszentrums Jülich
Reihe Information

Band / Volume 18
Crystal- and Defect-Chemistry of Fine Grained Thermistor Ceramics on $BaTiO_3$ Basis with BaO-Excess
H. Katsu (2011), xxvii, 163 pp
ISBN: 978-3-89336-741-2

Band / Volume 19
Flächenkontakte zu molekularen Schichten in der Bioelektronik
N. Sanetra (2012), XIII, 129 pp
ISBN: 978-3-89336-776-4

Band / Volume 20
Stacked device structures for resistive memory and logic
R. D. Rosezin (2012), 137 pp
ISBN: 978-3-89336-777-1

Band / Volume 21
Optical and electrical addressing in molecule-based logic circuits
M. Manheller (2012), XIV, 183 pp
ISBN: 978-3-89336-810-5

Band / Volume 22
Fabrication of Nanogaps and Investigation of Molecular Junctions by Electrochemical Methods
Z. Yi (2012), 132 pp
ISBN: 978-3-89336-812-9

Band / Volume 23
Thermal Diffusion in binary Surfactant Systems and Microemulsions
B. Arlt (2012), 159, xlvi pp
ISBN: 978-3-89336-819-8

Band / Volume 24
Ultrathin Gold Nanowires - Chemistry, Electrical Characterization and Application to Sense Cellular Biology
A. Kisner (2012), 176 pp
ISBN: 978-3-89336-824-2

Band / Volume 25
Interaction between Redox-Based Resistive Switching Mechanisms
C. R. Hermes (2012), iii, 134 pp
ISBN: 978-3-89336-838-9

Schriften des Forschungszentrums Jülich
Reihe Information

Band / Volume 26
Supported lipid bilayer as a biomimetic platform for neuronal cell culture
D. Afanasenkau (2013), xiv, 132 pp
ISBN: 978-3-89336-863-1

Band / Volume 27
15th European Workshop on Metalorganic Vapour Phase Epitaxy (EWMOVPE XV) June 2-5, 2013, Aachen, Germany
A. Winden (Chair) (2013)
ISBN: 978-3-89336-870-9

Band / Volume 28
Characterization, integration and reliability of HfO_2 and $LaLuO_3$ high-κ/metal gate stacks for CMOS applications
A. Nichau (2013), xi, 177 pp
ISBN: 978-3-89336-898-3

Band / Volume 29
The role of defects at functional interfaces between polar and non-polar perovskite oxides
F. Gunkel (2013), X, 162 pp
ISBN: 978-3-89336-902-7

Band / Volume 30
Parallelisation potential of image segmentation in hierarchical island structures on hardware-accelerated platforms in real-time applications
S. Suslov (2013), xiv, 211 pp
ISBN: 978-3-89336-914-0

Band / Volume 31
Carrier mobility in advanced channel materials using alternative gate dielectrics
E. Durğun Özben (2014), 111 pp
ISBN: 978-3-89336-941-6

Band / Volume 32
Electrical characterization of manganite and titanate heterostructures
A. Herpers (2014), ix, 165 pp
ISBN: 978-3-89336-948-5

Weitere ***Schriften des Verlags im Forschungszentrum Jülich*** unter
http://wwwzb1.fz-juelich.de/verlagextern1/index.asp

Information / Information
Band / Volume 32
ISBN 978-3-89336-948-5